Diamond
at the
Brain-Machine Interface

Robert Edgington

This thesis is submitted for the degree of Doctor of Philosophy

Department of Electronic and Electrical Engineering
University College London
University of London
2012

Declaration

The work in this thesis is the result of research carried out at University College London, London Centre for Nanotechnology, Diamond Electronics Group. I, Robert Edgington, declare it to be my own work unless referenced to the contrary in the text.

Acknowledgements

"You'll never have a more fun three years than doing your Ph.D" was the opening gambit of Professor Richard Jackman at the start of my Ph.D in 2008, and (apart from writing this thesis) I am happy to say he was right. I would like to thank Richard for playing a central role in all the fun memories I have made during my Ph.D: on the many group-socials, conferences and infamous Christmas parties that make the Diamond Electronics Group what it is; and, almost more importantly, I would like to express my profound gratitude for his support during the darker hours of my Ph.D, and for entrusting me with the perfectly balanced, double-edged sword of Freedom and Direction – without which the trials of this Ph.D would have been much greater.

Of course, the Diamond Electronics Group is no island, and I would like to thank all of the recent past and present DEG members: Dr. Haitao Ye, Dr. Niall Tumilty, Dr. Rezal Ahmad, Aysha Chaudhary, Joseph Welch, Ana Carolina Parada, Fang Zhao, Mohammad Golsharifi, Suguru Amakubo and Thuong Thuong Nyugen, for many good times shared and also for their invaluable scientific discussions during my Ph.D. Also, I would particularly like to thank Joseph Welch for his benevolent assistance in performing many of the experiments found in this thesis. Similarly, Steve Hudziak from the Department of Electronic and Electrical Engineering and the staff of the LCN cleanroom: Dr Takashi Matsuura, Steven Etienne, David Malone, Kevin Lee, Mike Cresswell, and Alan Sasnovski, are thanked for their practical assistance. The UK Engineering and Physical Sciences Research Council (EPSRC) is also acknowledged for its financial support.

During my Ph.D I was very lucky to be able to visit Waseda University, Tokyo, Japan, for six months on a Japanese Society for the Promotion of Science (JSPS) Short Term Postdoctoral Fellowship and Furusato Award, and I would like

to thank JSPS for the opportunity and funding to do so. I would like to express thanks to Professor Hiroshi Kawarada for welcoming me into his lab and for his supervision and support during my time in Japan, and also to his group for their support and patience during my stay. Special thanks goes out to Ruslinda A. Rahim, Syunsuke Sato, Yuichiro Ishiyama, Shoji Ibori and Takuma Kobayashi for their unwavering assistance and making my stay in Japan so memorable. Along these lines, I would also like to thank Kenta Sugitate, Varun Penmatsa, Gregg Burrow, John Wesley Quiles, Stewart Guethlein, and all the friends I made in Japan for making it such an unforgettable experience.

Back home, I would like to thank my housemates, friends and family for their friendship, company, love and support throughout my thesis, Ph.D and always. Finally, my deepest gratitude goes to Sarah Powell, my loving girlfriend, for the love and support she has shown me throughout my Ph.D, and for literally being behind me every step of the way during my thesis. She has been my source of motivation and inspiration, and I could not have written this thesis without her.

Abstract

Electrodes at the Brain Machine Interface (BMI) must fulfil tall specifications: They must have excellent electrical properties to transduce electrogenic activity, be highly biocompatible and not degrade in a saline environment over the lifetime of the patient. In this respect, diamond is an excellent BMI material. In this thesis, the application of diamond at the BMI is investigated.

Results Chapter 5 discusses the use of nanodiamond (ND) monolayers to promote the formation of functional neuronal networks. Neurons cultured on ND-coated substrates perform remarkably well, and similar to those grown on standard protein-coated materials with respect to their initial cell attachment, outgrowth, neuronal excitability and functionality of the resulting networks. NDs bypass the necessity of protein coating and show great potential for chronic medical implants. Chapter 6 describes the fabrication of nanocrystalline diamond (NCD) Micro-Electrode Arrays (MEAs) for the recording of electrogenic cells. MEAs are fabricated with metallic boron-doped nanocrystalline diamond (BNCD) and passivated with NCD, $SiO_2/Si_3N_4/SiO_2$ stacks and SU-8 epoxy. The recording of electrogenic activity of HL-1 cardiac cells is demonstrated with high signal-to-noise ratios and low signal loss.

Chapter 7 and Chapter 8 describe the development of boron δ-doped (111) diamond Solution Gate Field-Effect Transistors (SGFETs). In Chapter 7 an optimised Plasma Enhanced Chemical Vapour Deposition (PECVD) δ-doping recipe using the (111) diamond plane is presented. AC Hall characterisation yields desirable sheet carrier densities for FET application with enhanced carrier mobilities, and Impedance Spectroscopy (IS) measurements divulge metallic electrical properties with low activation energies, indicative of heavily doped

diamond as confirmed by Secondary Ion Mass Spectroscopy (SIMS). Chapter 8 describes the fabrication of boron δ-doped (111) diamond SGFETs (δ-SGFETs). δ-SGFETs show improved I-V characteristics in comparison to previous similar devices, whereby the enhancement mode operation, channel pinch-off and current saturation are achieved within the electrochemical window of diamond. Considering the biocompatibility of diamond towards cells, δ-SGFETs are promising for recording electrogenic cells.

Table of Contents

Figures and Tables

List of Abbreviations

AFM	Atomic Force Microscopy
$(B/C)_{gas}$	Boron-to-Carbon ratio (gas)
aCSF	artificial Cerebrospinal Fluid
AM	Adhesion Molecule
AP	Action Potential
ATR	Attenuated Total internal Reflectance
BMI	Brain-Machine Interface
BNCD	Boron-doped Nanocrystalline Diamond
CCP	Capacitively Coupled Plasma
CNT	Carbon Nanotube
CP	Coil Power
CPD	Critical Point Drying
CVD	Chemical Vapour Deposition
D-APV	D-2-amino-5-phosphonovalerate
DI	Deionised
DIV	Days *in vitro*
DND	Detonation Nanodiamond
ECM	Extracellular Matrix
EDS	Energy Dispersive X-Ray Spectroscopy
EDTA	Ethylenediaminetetraacetic acid
FBS	Fetal Bovine Serum
FEG	Field Emission Gun
FESEM	Field Emission SEM
FET	Field-Effect Transistor
FLIG	Floating Low energy Ion Guns
FTIR	Fourier Transform Infrared (Spectroscopy)
GFAP	Glial Fibrillary Acidic Protein

H-SCC	Hydrogen Surface Conductive Channel
HBSS	Hank's Buffered Salt Solution
HDMS	Hexamethyldisilazane
HEPES	4-(2-hydroxyethyl)-1-piperazineethanesulfonic acid
HFBPCD	Hot Filament Black PCD
HFCVD	Hot Filament CVD
HPHT	High Pressure High Temperature
ICP	Inductively Coupled Plasma
IHP	Inner Helmholtz Plane
IPA	Isopropanol Alcohol
IS	Impedance Spectroscopy
ISFET	Ion-Sensitive FET
LN	Laminin
LOR	Lift-off Resist
MAP2	Microtubule Associative Protein 2
MBE	Molecular Beam Epitaxy
MEA	Micro-electrode Array
MEM	Minimal Essential Medium
mEPSC	miniature Excitatory Post-Synaptic Current
MIT	Metal-to-Insulator Transition
MWPECVD	Microwave Plasma Enhanced CVD
NBQX	2,3-dihydroxy-6-nitro-7-sulfamoyl-benzo[f]quinoxaline-2,3-dione
NCD	Nanocrystalline Diamond
ND	(Detonation) Nanodiamond
NIRIM	National Institute for Research in Inorganic Materials
OHP	Outer Helmholtz Plane
ONO	$SiO_2/Si_3N_4/SiO_2$
p-ORN	Poly-DL-ornithine
PBS	Phosphate Buffered Saline
PCD	Polycrystalline Diamond
PEB	Post Exposure Bake
PL	Photolithography
PP	Platen Power

RF	Radio Frequency
RGD	Arginine-Glycine-Aspartic Acid
RIE	Reactive Ion Etching
S	Selectivity
SC	Single Crystal
SCD	Sodium Cacodylate Buffer
SEM	Scanning Electron Microscopy
SGFET	Solution Gate FET
SNR	Signal to Noise
TMB	Trimethylborane
TRITC	Tetramethylrhodamine-5-(and-6)-isothiocyanate
TTX	Tetrodotoxin
uleSIMS	ultra low energy Secondary Ion Mass Spectroscopy
VBM	Valence Band Maximum
VdP	Van der Pauw
WPCD	White PCD

Chapter 1 Introduction

One of the grand challenges we face today is an aging population, and a large consequence of this is the increased occurrence of neurodegenerative diseases caused by the age-related natural deterioration of the body. Diseases such as Parkinson's disease, macular degeneration, retinis pigmentosa and also non-degenerative injuries of the nervous system pose a major challenge on healthcare because the traditional therapeutic approaches used to restore tissue function in the body are not effective on the brain, central and peripheral nervous systems where cell regeneration is limited. Instead, artificial prosthetic devices are increasingly being used to restore lost function caused by neurodegenerative diseases. Pacemakers and cochlear implants [1] are well established neural prosthetics [2], and neural prosthetics such as artificial retina [3-5] are currently subject to intensive research; however, if chronic implantation of such electrodes is to be realised, more biocompatible materials are needed at the Brain-Machine Interface (BMI) in order to reduce electrode failure caused by the debilitating immune response [6,7] of neuronal tissue to less biocompatible materials. In this context, diamond is a very promising material due to its inert chemistry, outstanding biocompatibility [8-10] and excellent electrochemical [11] and electrical [12] properties. This thesis investigates the use of many forms of diamond as biocompatible coatings and electrode materials at the BMI.

Chapter 2 introduces diamond as a material, wherein a picture of diamond is built up atomistically and its resulting properties are discussed. The historical development and current state-of-the-art of diamond synthesis is then reviewed, followed by a discussion on the doping of diamond. Finally, the different crystalline forms of diamond that are relevant to this thesis are discussed. Chapter 3 goes on to introduce neuronal biomaterials, and the

relevant surface properties of diamond and other materials that are attributed to enhanced neuronal biocompatibility. Neuronal BMIs are then reviewed, focusing on the electrode structures of neuronal prosthetic devices, and the development of diamond-based microelectrode arrays and field-effect transistors for the recording and stimulation of neurons are reviewed. Chapter 4 reviews the experimental methods and techniques used in this thesis.

In the first results chapter, Chapter 5, the use of nanodiamond monolayers to promote the formation of functional neuronal networks is presented. The materials of glass, silicon, polycrystalline diamond (PCD) and nanocrystalline diamond (NCD) – with and without coatings of extra cellular matrix proteins and/or nanodiamond monolayers – are used to investigate the attachment and maturation of dissociated murine hippocampal neuron cultures on nanodiamond monolayers using confocal and scanning electron microscopy. The electrical characteristics of cultured neurons are then characterised using a variety of electrophysiological techniques and nanodiamond monolayers are characterised using Atomic Force Microscopy (AFM) and Fourier Transform Infrared Spectroscopy (FTIR). To finish, possible reasons for the remarkable attachment of neurons on nanodiamond monolayers are discussed. This chapter describes a major novel contribution to the field of neuronal prosthetics, wherein nanodiamond monolayer coatings are demonstrated for the first time to be excellent substrates for interfacing with neuronal cells. Nanodiamond coatings are easily deposited at low cost on a variety of materials, and could be easily coated onto existing or novel neuronal prosthetic devices in order to improve their biocompatibility, which makes nanodiamond a very promising material for use at the BMI.

Chapter 6 describes the development of highly boron-doped nanocrystalline diamond (BNCD) Microelectrode Arrays (MEAs) for the *in vitro* recording of electrogenic cells. The optimisation of a diamond reactive ion etching recipe and the fabrication of 8 by 8 microelectrode arrays using BNCD as an electrode material is described, followed by the passivation of electrode tracks using the three materials of NCD, $SiO_2/Si_3N_4/SiO_2$ stacks and SU-8 epoxy.

The ability of diamond-based MEAs to record electrogenic activity is subsequently investigated using HL-1 cardiac cells cultured on top of diamond MEAs and comparisons are made to standard MEA devices. This chapter develops a useful toolbox of processes for fabricating diamond-based MEAs and makes the important novel contribution to the BMI field by demonstrating, in comparison to conventional electrode materials, the superlative ability of boron-doped diamond electrodes to record electrogenic activity *in vitro* whilst also being exceptionally biocompatible.

Chapter 7 and Chapter 8 together describe the development of an enhanced carrier mobility boron δ-doped conductive channel in (111) diamond and its subsequent fabrication into a Solution Gate Field-Effect Transistor (SGFET). In Chapter 7, an optimised Plasma Enhanced Chemical Vapour Deposition (PECVD) protocol for δ-doping diamond is presented, using the possibly advantageous (111) diamond plane as a substrate for diamond growth. AC Hall Effect and Dielectric Impedance Spectroscopy (IS) measurements are performed to obtain the mobilities, sheet carrier densities and estimated boron concentrations of δ-doped conductive layers – the latter of which are compared to boron concentration measurements obtained using ultra low energy Secondary Ion Mass Spectroscopy (uleSIMS). This chapter contributes to the field of diamond doping by describing the novel use of single crystal (111) diamond substrates and a novel optimised PECVD protocol to deposit δ-doped channels with enhanced electrical properties and resultant conductive channels that are suitable, for the first time, to fabricate SGFET with enhancement-mode, saturated current-voltage characteristics, as described in Chapter 8.

Chapter 8 goes on to describe the fabrication and testing of oxidised boron δ-doped (111) diamond SGFETs. The fabrication of SGFET is described, SGFET are characterised using current-voltage (I-V) measurements and their performance in comparison to previous similar devices fabricated on (100) and polycrystalline diamond is discussed. Following SGFET I-V characterisation, the pH sensitivity of a boron δ-doped (111) diamond SGFET is determined and its figures of merit are discussed with respect to theoretical models of pH

sensitivity. This chapter describes the novel contribution of an enhancement-mode, saturated SGFET using oxidised boron δ-doped (111) diamond as a conductive channel. Pertinently, this device performs similarly to hydrogen-terminated diamond SGFETs, but does not suffer from the issue of unstable hydrogen termination that is associated with these devices. This makes oxidised boron δ-doped (111) diamond SGFETs suitable for chronic, physiological application and a promising device for recording electrogenic activity at the BMI.

Chapter 9 summarises the results achieved in this thesis and the future direction of each study is discussed. Finally, the impact of these results and the suitability of diamond at the Brain-Machine Interface is discussed. The following publications have resulted from work contained within this thesis:

Journal Papers

Thalhammer, A., Edgington, R. J., Cingolani, L. A., Schoepfer, R., & Jackman, R. B. (2010). The use of nanodiamond monolayer coatings to promote the formation of functional neuronal networks. *Biomaterials*, *31*(8), 2097–2104.

Maybeck, V., Edgington, R., Bongrain, A., Welch, J., Bergonzo, P., Jackman, R. B., Offenhaüser, A. (Manuscript in preparation). BNCD MEAs for monitoring cardiac action potentials.

Edgington, R., Sato, S., Ishiyama, Y., Morris, R., Jackman, R. B., & Kawarada, H. (2012). Growth and electrical characterisation of δ-doped boron layers on (111) diamond surfaces. *Journal of Applied Physics*, *111*(3), 033710–033710–7.

Edgington, R., Ruslinda, A. R., Sato, S., Ishiyama, Y., Tsuge, K., Ono, T., Kawarada, H., et al. (2012). Boron δ-doped (111) diamond solution gate Field-Effect transistors. *Biosensors and Bioelectronics*. *33*(1), 152-157.

Conference Oral Presentations

The use of nanodiamond monolayers for the formation of functional neuronal networks:

Diamond 2009, Athens.
Symposium J, MRS Fall Meeting 2009, Boston.

pH sensing on δ-doped Solution Gate Field-Effect Transistor devices:

Diamond 2010, Budapest
MRS Fall Meeting 2010, Boston.
NDNC 2011, Matsue, Japan
IMRCXX 2011, Cancun.

Chapter 2 Diamond and its forms

2.1 The many bonds of carbon

Carbon is an extraordinary element. Upon simple inspection of the electron ground state configuration of carbon ($1s^2$ $2s^2$ $2p_x^1$ $2p_y^1$, Figure 2.1a), valence bond theory would suggest that carbon could only form two covalent bonds via its half-filled p-type orbitals; however, the existence of molecules such as methane suggests otherwise. Of course, it is well understood that carbon, situated in Group IV of the periodic table with an atomic number of 6, can form up to 4 covalent bonds. This is achieved by molecular orbital hybridisation, which was first proposed by Linus Pauling in 1931 [13]. In the case of carbon, molecular orbital hybridisation is a result of the excitation of an electron from a 2s orbital causing a redistribution of nuclear core potential and electrons into energetically favoured orbitals that are 'mixed' or hybridised s-type and p-type orbitals into 4 σ sp^3 bonds (Figure 2.1a,b). Furthermore, sp^2 bonds can be formed where only 2 p-type orbitals are hybridised with an s-type orbital to form planar π-bonds that make up materials such as carbon nanotubes or graphene, or sp bonds can be formed where only one p-type orbital is hybridised.

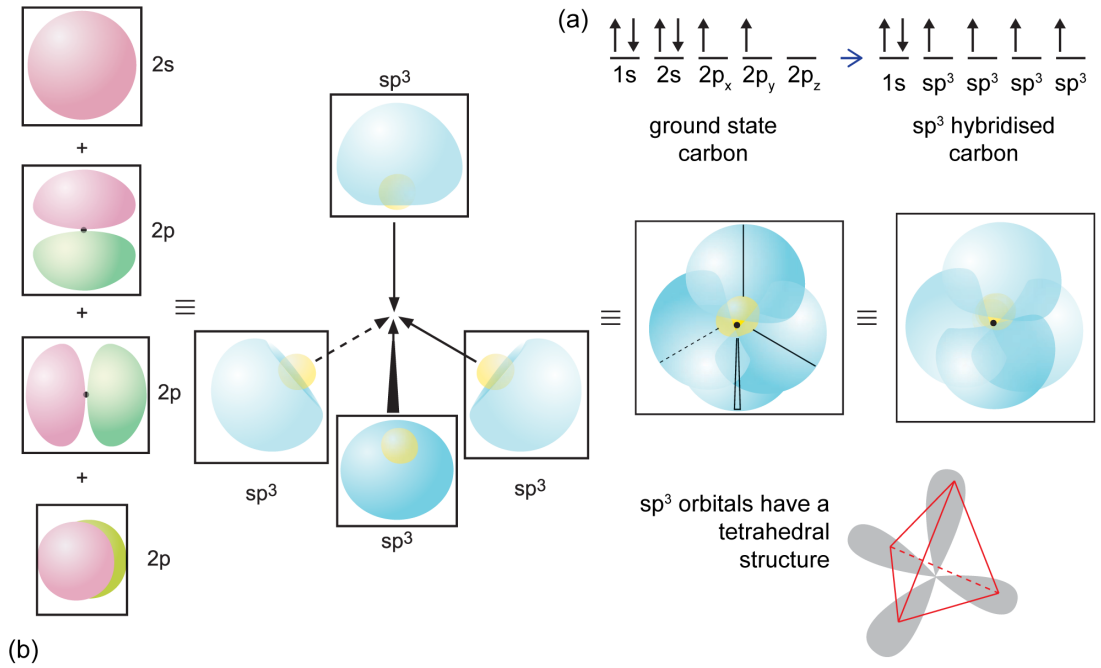

Figure 2.1: a) Distribution of electrons at carbon's ground state and for sp^3 hybridised carbon. b) Schematic of the hybridisation of s-type and p-type orbitals into sp^3 hybrid orbitals, adapted from [14]. Different complementary colours of orbitals indicate the orbital wave function to be of the opposite phase to its counterpart.

Carbon's ability to form a multitude of bonds via sp, sp^2 and sp^3 hybridisation gives rise to the many different allotropes of carbon and allows the formation of long chain organic molecules, such as peptides and DNA, with sufficient complexity and dynamism to form the molecular backbone of life as we know it. Pertinently, the sp^3 hybridisation bonding of carbon with other carbon atoms results in the tetrahedral carbon structure we know as diamond, and the nature of sp^3 bonding in carbon is responsible for many of diamond's exceptional properties (see section 2.3).

The crystal structure of diamond [15] consists of a face-centred cubic lattice with 8 C atoms per unit cell (Figure 2.2a). The additional carbon atoms are located at a_0(¼,¼,¼), a_0(¾,¾,¼), a_0(¼,¾,¾) and a_0(¾,¼,¾), where a_0 is the lattice constant (3.657 Å, [15]). Diamond has the highest atomic density of all known materials (1.76 x 10^{23} atoms/cm^3), which explains why diamond is the stiffest, hardest and least compressible of all substances. The diamond unit cell is

cubic with a side length, a_0, approximately equal to 3.567 Å at room temperature. The C–C bond length, d, is equal to ¼ of the cubic body diagonal, so that $d = \sqrt{3}a_0/4 = 1.53$ Å [16]. Within the cubic lattice of diamond there are three crystallographic Miller planes that can be used to describe its structure, and often the surfaces of diamond samples; (100), (110) and (111) (Figure 2.2b).

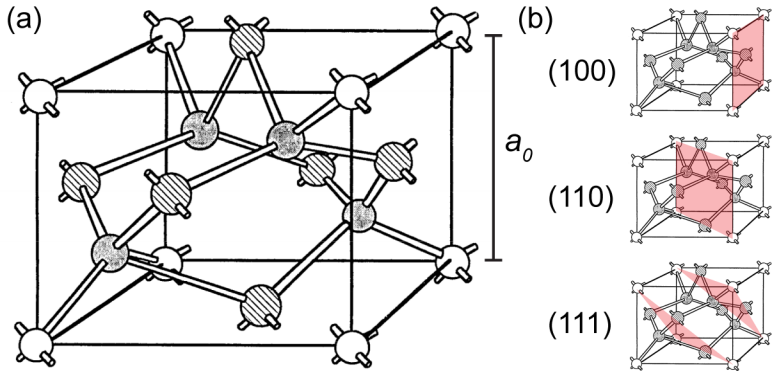

Figure 2.2: a) Face Centred Cubic structure of diamond adapted from [17], b) and the (100), (110) and (111) Miller planes. Note the high density of atoms along the (111) plane.

2.2 Forming diamond

Whilst the sp^3 carbon bond is one of the strongest bonds (711 kJ/mol [15,18]), the sp^2 bond (524 kJ/mol) sits energetically lower than the sp^3 bond by 2.87 kJ/mol [15], making diamond a metastable allotrope of carbon. As a result, very high temperatures and pressures are required to overcome the large kinetic barrier and thermodynamically unfavourable reaction of sp^2 to sp^3-bonded carbon in order to be able to form diamond (Figure 2.3) from graphite or other carbon phases. Conversely, diamond is persistent under standard conditions due to the large kinetic barrier between sp^2/sp^3 phases also requiring very high temperatures (ca. 1620˚C at room pressures) to break the 711 kJ/mol sp^3 bonds.

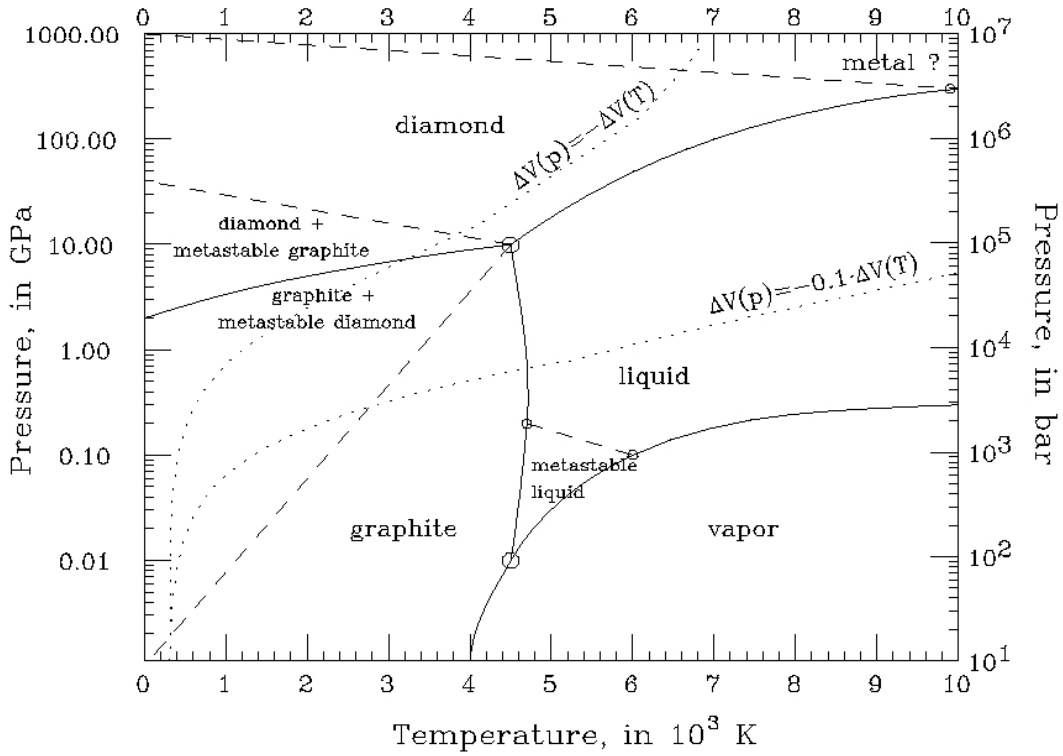

Figure 2.3: Carbon phase diagram from [19].

2.2.1 High Pressure High Temperature Synthesis

Diamond synthesis has been a goal of chemists since 1772 when Lavoisier [20] and Tennant [21] established that diamond was a crystalline form of carbon. Subsequent growth attempts set out to mimic nature's diamond formation process that occurs 150 km below the Earth's surface at high pressures and high temperatures (HPHT); however, after centuries of failed attempts, it was not until the 1950s that the first unquestioned synthesis of diamond was achieved both in the U.S., General Electric, GE, 1954 [22]; in Sweden, AESA, 1960; and in the Soviet Union, Institute for High-Pressure Physics, using a catalyzed HPHT method [23-26]. The catalyzed HPHT method, developed simultaneously by GE and ASEA, consists of using transition metal-solvent catalysts to dissolve carbon and transport it to the growing (diamond) surface where it crystallises into diamond at conditions where diamond is thermodynamically stable. Employing a transition metal catalyst such as iron, cobalt, chromium, nickel, platinum or palladium, the kinetic barrier of the graphite-to-diamond transition is reduced allowing diamond formation at temperatures and pressures of ca. 55 kbar and

1600 K [27]. Without catalysis, growth conditions of >130 kbar and ca. 3300 K are necessary for diamond formation to proceed at any observable rate, which is difficult and costly to achieve. Currently, approximately 75 tons of synthetic diamond are sold throughout the world each year [27] using the HPHT method.

2.2.2 Chemical Vapour Deposition

The first synthesis of diamond by chemical vapour deposition (CVD) was first achieved before HPHT diamond synthesis in 1953 by Eversole of the Union Carbide Corporation [26] but only first reported in 1962 [28]. This work described the CVD of diamond using a methyl-containing gas at relatively low temperatures of 900 to 1100˚C and lower pressures of 70 to 140 bar [28]; however, continual growth interruptions were needed in order to remove the accumulating sp^2 black carbon on the diamond seeds. This work was confirmed and expanded upon by Angus and Deryagin [27,29], and the use of atomic hydrogen to etch graphitic deposits and its use during growth to permit high rate nucleation of diamond on non-diamond substrates followed [26]; however, growth rates were too slow to be of commercial interest [27]. It was not until the Japanese research group at the National Institute for Research in Inorganic Materials (NIRIM) in Tsukuba, Japan, revealed details of CVD processes for diamond deposition on non-diamond substrates at commercially significant rates [30,31] using relatively low temperatures of 700 to 1100˚C [27] and low pressures of 20 to 30 Torr [32] that diamond became the international research topic it is today. The first reactor type demonstrated by NIRIM was the hot filament CVD (HFCVD) system [30], whereby a tungsten filament is used to generate hydrogen and methyl radicals above a substrate. The basis of diamond CVD consists of creating hydrogen and methyl radicals above an atomic template of sp^3 carbon in order to deposit sp^3 carbon in a piecewise fashion, where hydrogen serves to etch away graphitic carbon that is deposited during CVD. (For a fuller discussion on this topic the reader is referred to section 4.12.1). This HFCVD system was initially popular due to its simple design. A year later a Microwave plasma enhanced CVD (MWPECVD) reactor type (NIRIM type reactor,

see section 4.12.1) was presented [31] that generated radicals via MW power, which improved on HFCVD reactors by eliminating the contaminating filament from the growth chamber. Since then improvements in MWPECVD technology have lead to MWPECVD being the growth method of choice for high quality, large area diamond film deposition; however, HFCVD reactors are still widely used and various other CVD diamond synthesis methods are possible, which are summarised in Table 2.1 below.

CVD method	Rate (μm/h)	Area (cm^2)	Quality (Raman)	Substrate Material	Pros	Cons
Hot-filament	0.3–40	100–400	+++	Si, Mo, silica, Al_2O_3, etc.	Simple, large area	Contamination, stability
DC discharge (low P)	<0.1	70	+	Si, Mo, silica, Al_2O_3, etc.	Simple, area	Quality, rate
DC discharge (medium P)	20–250	<2	+++	Si, Mo, Al_2O_3,	Rate, quality	Area
DC plasma jet	10–930	2–100	+++	Si, Mo, W, Ta, Cu, Ni, Ti, stainless steel	Highest rate, quality	Stability, homogeneity
RF (low P)	<0.1	1–10	-/+	Si, Mo, silica, BN, Ni	Scale-up	Quality, rate, contamination
RF (thermal, 1 atm)	30–500	3–78	+++	Mo	Rate	Stability, homogeneity
Microwave (0.9-2.45 GHz)	1 (low P), 30 (high P)	40	+++	Si, Mo, silica, WC, etc.	Quality, area, stability	Rate
Microwave (ECR 2.45 GHz)	0.1	<40	-/+	Si	Area, low P	Quality, rate, cost, contamination
Flame (combustion)	30–200	1–100	+++	Si, Mo, Al_2O_3, TiN	Simple, rate	Stability, uniformity

Table 2.1: Table from [33] showing a comparison of diamond CVD methods. "-" indicates poor quality and "+" excellent quality.

2.3 The properties of diamond

Many of the superlative properties of diamond derive from the remarkable C-C sp^3 bond. Its large strength gives diamond its famous hardness and chemical inertness, which lays the foundation of diamond's exceptional biocompatibility. Its high bond strength, tetrahedral structure and short bond length [16] result in a dense, non-polar, high mass crystal with high phonon velocity [34]. These properties give diamond a very high thermal conductivity and low thermal expansion coefficient [16], as well as the long acoustic phonon relaxation times and high optical phonon energies that give rise to the extraordinarily high mobilities measured in diamond [34,35]. In a simplistic picture, the binding of the four sp^3 bonds of carbon to four other sp^3 carbon bonds creates eight new orbitals from binding/antibonding interactions: 4 bonding (lower energy) and 4 antibonding (higher energy). Electrons occupy the lower energy levels whilst the antibonding energy levels remain empty, creating a band gap between the states. The large difference in the energy levels between sp^3 bonding and antibonding states gives diamond its wide band gap of ca. 5.5 eV, giving diamond a very large breakdown voltage and low band-to-band generation–recombination noise of carriers which makes diamond an attractive material for high power devices or low noise sensors, respectively. At the surface of diamond sp^3 bonds are terminated with atomic or molecular groups such as hydrogen or oxygen (hydroxyl, ether moieties, etc. [36]) and the high strength of these bonds gives diamond its strong polarisability and wide chemical window (-0.75 to 2.35 V) [11,37,38]. Furthermore, the diamond surface can be tailored in its chemical composition to be more biocompatible to proteins [39,40] or cells [10,41].\][

Property		Si	GaAs	SiC (6H)	SiC (4H)	GaN	Diamond
Band gap (eV)		1.12	1.42	2.86	3.26	3.39	5.47
Thermal conductivity ($W\ cm^{-1}\ K^{-1}$)		1.15	0.46	3.6	3.6	2	21.9
Carrier mobility ($cm^2\ V^{-1}\ s^{-1}$)	electron (hall)	1450	8500	370	981	1245	660
	electron (t.o.f.)	–	–	–	–	–	4500
	hole (hall)	370	400	100	120	24	1650
	hole (t.o.f.)	–	–	–	–	–	3800
Dielectric constant		11.9	13.1	9.7, 10.03	9.7, 10.03	10.4	5.7
Saturation velocity ($cm\ s^{-1}$)	electron (calc)	10^7	2×10^7	2×10^7	2.2×10^7	2.5×10^7	1.5×10^7
	electron	–	1.9×10^7	2×10^7	–	2.5×10^7	2.5×10^7
	hole	10^7	–	–	–	–	1.1×10^7
Breakdown field ($MV\ cm^{-1}$)		0.3	0.4	3	2.7	2.7	10-20

Table 2.2: Table adapted from [12] showing the electrical properties of diamond in comparison to other semiconductor materials. "t.o.f." indicates time of flight measurements.

2.4 Doping of diamond

Whilst the sp^3 carbon bond is responsible for many of diamond's superlative properties, the sp^3 bond leaves diamond at a disadvantage with respect to incorporating dopant atoms. Firstly, diamond's metastability means it cannot be heated to temperatures at which vacancies and interstitial atoms form by thermal excitation; therefore, any diffusion process of dopant atoms that relies on these defects as carriers is not possible. For this reason, it is difficult to introduce dopant atoms into diamond by in-diffusion, as is the case with silicon,

and viable doping methods are limited to dopant uptake during growth or dopant injection by means of ion implantation. Even using such doping methods, the doping of diamond remains limited due to the short bond length of the C-C sp^3 that makes it difficult to incorporate dopant atoms into diamond via substitutional doping, resulting in dopants with large activation energies.

2.4.1 p-type: during growth

p-type diamonds occur in nature and are a blue colour. They are classified as type IIb and are extremely rare, and the most famous example of a (dark) blue diamond is the Hope diamond, which currently resides in Smithsonian Natural History Museum in Washington, D.C., USA, and is insured for an estimated $250 million. The blue colour of the Hope diamond comes from the boron included in its lattice, which is also the shallowest p-type acceptor dopant in diamond. At moderate doping densities, due to the short lattice constant of diamond, boron has a large activation energy of 0.37 eV [42]. This is the smallest activation energy of the p-type (and n-type) dopants. The first boron doped diamond was synthesised in 1959 by Wentorf [43] using a catalysed HPHT synthesis method wherein boron was added into the metal catalyst mixture; however, due to the large impurity incorporation associated with the method, poor electrical characteristics were obtained. Since then, improvements in diamond growth using MWPECVD have resulted in large mobilities of 1870 $cm^2/V.s$ at 292 K, ca. 10^{16} cm^{-3} boron concentration, [B] [44] (ascribed to oxygen in the gas mixture); 1620 $cm^2/V.s$ at 290 K, ca. $4x10^{14}$ cm^{-3} [B] [45]; ca. 2000 $cm^2/V.s$ at 290 K, ca. $5x10^{13}$ cm^{-3} [B] [46] and 1840 $cm^2/V.s$ at 290 K, ca. $2.3x10^{14}$ cm^{-3} [B] [47] being reported for boron-doped single crystal homoepitaxial diamond. Due to the large activation energy of boron acceptors in diamond (0.37 eV), only 1 % of dopant atoms are activated at room temperature. It is well established that increasing the dopant concentration reduces the activation energy of boron [42], and at ca. $3x10^{20}$ cm^{-3} boron concentration, it has an activation energy of ca. 0 eV or in the meV range due to the formation of a metallic impurity band between adjacent boron acceptors [48]. However, with increased impurities and carriers in the

diamond lattice, hole mobility is reduced, and by $3x10^{20}$ cm^{-3}, where the metallic impurity band forms [49], the mobility has dropped to <3 $cm^2/V.s$ [42]. Diborane [50]; Trimethylborane [47]; boron oxide [51]; boric acid [52] and solid boron [42] can be used as boron additives. The influence of MWPECVD parameters on boron doping is discussed further in Chapter 7. Boron (and other elements) can also be implanted using ion implantation as reviewed extensively by Kalish [53]. Whilst ion implantation allows the precise control of dopants, it results in crystal damage and low mobility carriers.

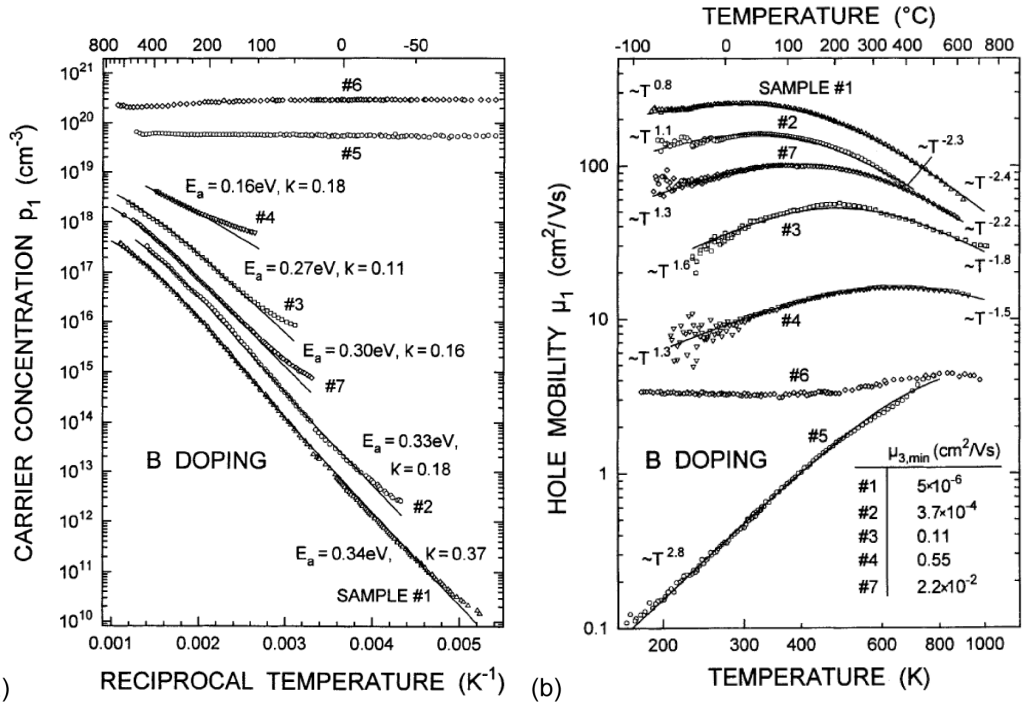

Figure 2.4: Hall effect measurements showing a) carrier concentration and b) hole mobility of single crystal Ib and IIa boron doped diamond grown in a NIRIM-type MWPECVD reactor over a range of temperatures and boron concentrations [42].

2.4.2 p-type: Hydrogen surface conductivity

The second type of p-type conductivity in diamond is hydrogen surface conductivity, which was first discovered by Landstrass and Ravi in 1989 [54]. Hydrogen-induced surface conductivity occurs due to the surface transfer doping

of electrons from the valence band of diamond into an adsorbed electrolyte [55]. For surface transfer doping to occur, the redox couple bands of the adsorbed electrolyte must have their lowest unoccupied electronic state below the valence band maximum (VBM) of diamond. It has been proposed by Foord et al. that the reduction of oxygen in the adsorbate layer acts as an electron sink [56], and since the ($O2/OH^-$) redox couple is below the VBM of diamond for all pH [57] (where O_2 is the empty state and OH^- is the filled state; $O_2 + 2\ H_2O + 4\ e^- \rightarrow 4\ OH^-$), hydrogen surface conductivity takes place in all electrolytes. Due to the corrosion resistance of diamond, oxidative dissolution of diamond does not occur and a thermal equilibrium is reached between the diamond and electrolyte, and the electron transfer and upward band bending of diamond forms a surface conductive channel of holes in diamond. Hydrogen surface conductivity exhibits sheet carrier densities in the region of 10^{13} cm^{-2} and mobilities of 10 to 100 $cm^2/V.s$, and is fabricated by MWPECVD treatments with an H_2 plasma [57] (Figure 2.5c); however, it is unstable at high temperatures and undergoes anodic oxidation after prolonged use, ultimately making it unsuitable for commercial application.

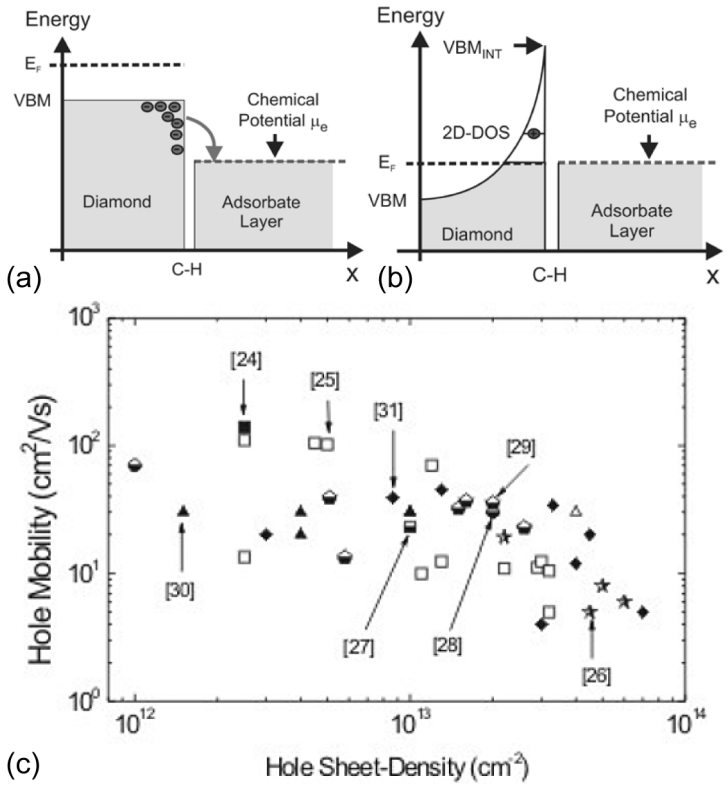

Figure 2.5: Schematic description of the diamond/adsorbate heterojunction when a) non-equilibrated and b) equilibrated. Electrons from the valence-band tunnel into empty electronic states of the adsorbate layer as long as the chemical potential μ_e is lower than the Fermi energy E_F. c) Summary of hole mobilities and hole sheet-densities as detected at room temperature on a variety of films. All panels are adapted from [57].

2.4.3 n-type: during growth

n-type doping of diamond has been historically difficult to achieve [58]. Out of the potential Group V donor dopants of diamond only nitrogen and phosphorous fit in the diamond lattice, and as for other elements only a few (S, As, Sb [58]) are predicted to be suitable donors for substitutional doping in diamond. Nitrogen is the natural candidate for n-type doping in diamond and is abundant in natural diamond; however, it's deep activation energy of 1.7 eV [59], make it highly insulating at room temperature and useless for electronic applications. Phosphorous is the next most suitable donor for diamond. Initial attempts proved difficult to incorporate phosphorous into diamond due to its

large atomic radius (1.06 Å) and high positive formation energy (6.67 eV) [60]; however, by using the non-equilibrium process of MWPECVD, Koizumi et al. [61] managed to incorporate phosphorous into diamond with an activation energy of 0.46 eV (0.4-0.6 eV) and room temperature mobilities of ca. 15 $cm^2/V.s$ (600 ppm PH_3/CH_4). Since then, room temperature mobilities of 240 $cm^2/V.s$ (500 ppm) [62,63] and 420 $cm^2/V.s$ ($2.8x10^{16}$ cm^{-3} [P]) [64] have been reported with activation energies of 0.56 eV, and theory predicts activation energies of 0.2 eV [65,66] to 0.4 eV [67] are obtainable, which makes phosphorous diamond's most promising n-type dopant.

2.5 Detonation Nanodiamond

Whilst most natural diamonds on earth originate from deep within the Earth's mantle, this is not the only place natural diamond is formed. Nano-sized diamond, a.k.a. nanodiamonds, can be found in ancient sedimentary cores that were formed in the high pressure and temperature shockwaves of large meteorites re-entering the Earth's atmosphere [68]. Detonation Nanodiamonds (DNDs, or NDs) were first produced on earth in the shockwaves of controlled explosions performed by Du Pont de Nemour et al. in the 1960s [69] and later using a more efficient method by Russian scientists during the Cold War era in the 1980s [70]. By exploding carbonaceous explosives (TNT, RDX, etc. [70,71]) in oxygen deficient environments, diamond particles were found to be formed as the Chapman-Jouguet point of the shockwave passed [71], allowing the crystallisation of sp^3 carbon for only a few microseconds. The resulting soot contained strongly-aggregated ND clusters of ca. 5 nm primary particle size; however, few results were published [69] and it was not until after the fall of the Iron Curtain that these results were first presented [70] research expanded internationally [71] and a process was developed to deaggregate the strongly bound NDs into mono-dispersed ND colloids [72] (stirred-media milling with micron-sized ceramic beads) that NDs became of significant interest to the wider scientific community. NDs comprise of an sp^3 diamond core surrounded by some sp^2 graphitic carbon [18,73] and are terminated with a variety of organic

functionalities that are predominantly C-OH terminations due to the oxidative acidic purification step of ND processing (Figure 2.6) [18,74]. NDs are nitrogen doped due to the high nitrogen content of TNT and RDX and are highly insulating [75]. NDs are extremely biocompatible, inciting little or no immunological responses when interacting with cells [76-78] and adsorb proteins with a high affinity [79].

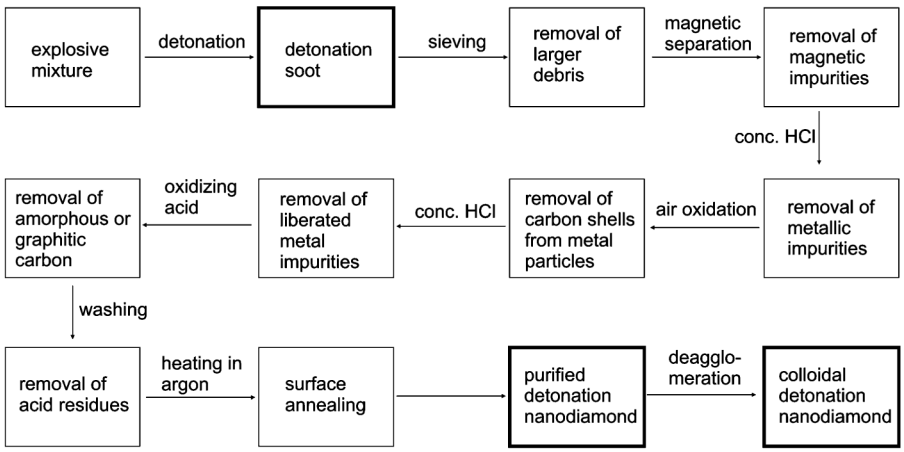

Figure 2.6: Example scheme taken from [79] describing the purification process of detonation soot for the production of detonation nanodiamond.

2.6 Nanocrystalline diamond

Depositing large-scale single crystal diamond films is difficult due to the lack of suitable substrates for homoepitaxy, and single crystal heteroepitaxy is still in its infancy of development. As a suitable alternative heteroepitaxial nanocrystalline diamond (NCD) films can be grown over large areas and possess similar properties to single crystal diamond (Table 2.3). Standard heteroepitaxy of diamond films consists of growing diamond from nucleation sites, such as nanodiamonds deposited on silicon surfaces (see section 4.12.1). As the different facetted nano-metric nucleation sites grow, faster growing diamond-facets overtake and swallow up slower diamond facets, resulting in a thick diamond film (polycrystalline diamond, PCD) that has gradually increasing crystal grain sizes (micron sized) and a rough but more orientated surface [27]. This survival

of the fittest growth model was first proposed by Van Der Drift [80] (Figure 2.7a), and results from the different growth rates of diamond facets under different growth conditions [27,81] (Figure 2.7b).

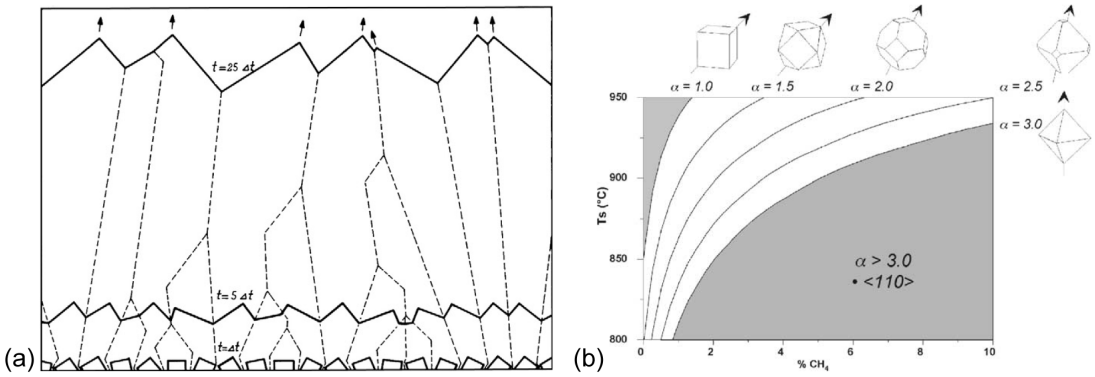

Figure 2.7: a) Evolution of columnar growth from random-orientated crystals as predicted by Van Der Drift [80]. b) Variations of the α-parameter as function of CH_4 % and T_s at 23 W cm^{-3}, where $\alpha = \sqrt{3}\,v_{100}/v_{111}$ [81], which describes the ratio of growth rates (v_{xxx}) normal to the diamond facet indicated in the subscript and determines the probable dominant growth facet for those conditions [82].

NCD growth differs from standard polycrystalline diamond growth in that a relatively high percentage of methane is used that causes a continual re-nucleation processes during MWPECVD growth [83]. This gives NCD its nanocrystalline nature with grain sizes of less than 100 nm in size, allowing thinner films to be grown with a lower surface roughness, making NCD suitable for integration into micromachining processes. A disadvantage of NCD is its higher grain-boundary density and larger sp^2 content (<0.1 % sp^2 [84]), which increases carrier scattering, decreases the mobility of carriers in NCD (10-90 cm^2/V.s) [84,85]. NCD is typically grown with 5 to 20 % methane, and NCD growth is extensively reviewed in [83,84]. NCD can also be grown at low methane percentages and high power to suppress re-nucleation [83], but retain its NCD status by stopping growth at thin film thicknesses before large grain sizes have evolved.

Property	Single-crystal diamond	NCD (grown in high methane)	NCD (highest quality)
Growth chemistry	H_2/CH_4	H_2/CH_4	H_2/CH_4
Young's modulus (GPa)	1100	500–900	1120
Hardness (GPa)	100	80	–
Macroscopic friction coefficient	0.01–0.02	0.02–0.05	0.02–0.05
Surface roughness, R_a, (nm)	depends on preparation	50–100	5-30 (depends on film thickness)
Grain size (nm)	1–10,000	50–100	5-100 (depends on film thickness)
Bonding character	sp^3	up to 50 % sp^2	<0.1 % sp^2

Table 2.3: Comparison of different forms of NCD films and single crystal diamond [84].

In summary, whilst SC diamond displays the most superlative properties of diamond, such as high room temperature carrier mobility, growing large SC wafers has yet to be achieved. Instead, for large area or heteroepitaxial applications, crystalline materials such as NCD or PCD can be used that retain many of the superlative chemical, physical and mechanical properties of SC diamond; however, due to the inclusion of grain boundaries in such materials, their electrical properties, such as carrier mobility, are adversely affected. Whilst crystalline diamond materials cannot match SC diamond's repertoire of electrical properties, for biological applications, where the high-specification electrical performance of the material is not paramount to the application, crystalline materials such as NDs, NCD and PCD have been found to be very suitable for biological application due to their ease of deposition, inert chemistry and resulting high biocompatibility (see section 3.2).

Chapter 3 Neuronal Biomaterials and Devices

3.1 Neuronal Biomaterials

During the 1960s and 70s the 1st generation of biomaterials were specifically developed to be implanted into the human body [86]. These 1st generation biomaterials were designed to reduce to a minimum the biological response of the host tissue to the biomaterial. By the 1980s, advancements in biomaterials science had lead to materials being developed that were bioactive, eliciting a controlled action and reaction in the physiological environment [87]. At the same time, resorbable biomaterials, which safely degraded over time to be replaced by the host's cells, were developed. These bioactive or resorbable biomaterials ushered in a 2nd generation of biomaterials [86,87]. Today, a 3rd generation [88] of biomaterials exists, which combines the bioactive and resorbable nature of 2nd generation biomaterials with nanoscale molecular engineering that is designed to stimulate specific cellular responses at the level of molecular biology [89,90]. These biomaterials form the basis of biomaterials used in the burgeoning field of regenerative medicine. The converging direction of biomaterials in the last few decades has been to provide biomimetic resorbable scaffolds for tissue repair; however, for neuronal biomaterials, where cellular regeneration is very limited [91], chronic electrically active artificial implants are now being increasingly used to restore lost neuronal function from trauma or neurodegenerative diseases [1,92]. Such biomaterials cannot be resorbable or bioactive without sacrificing electrical prowess and, in this context, whilst some electrodes have some 3rd generation capabilities [93], neuronal biomaterials under development for the Brain-Machine-Interface can be chiefly

categorised as 1st generation biomaterials, except with the additional electrical functionality and, with the advent of nanotechnology, nanoscale physicochemical properties [94,95] that aim to mimic the properties of tissue.

Neurons are one of the most environmentally demanding cell types. Due to their remarkable ability to generate action potentials and electrically communicate with their neighbours, their extreme differentiated phenotype leaves them with little resilience to physiological stress. For this reason, neurons are protected behind the blood brain barrier and have their own hypersensitive immune system that is tended by glial cells. Unlike the sophisticated targeted immune system of the rest of our bodies, the glial immune system aggressively attacks any foreign body it encounters [96,97], and implanted materials and electrodes often incite such an immune response and result in a process called gliosis [7]. Gliosis, or glial scarring, is where insulating glial tissue surrounds and progressively isolates implanted devices from neurons. This increase in impedance renders the implant incapacitated and gliosis accounts for a significant contribution to most neural prosthesis failures [98,99]. Therefore, neuronal biomaterials must meet very high specifications if they are to achieve neuronal biocompatibility and only select materials can promote the formation of functional neuronal networks on their surfaces (e.g. flat or unmodified glass, polystyrene, sapphire, iridium oxide, silicon, metal oxides, polymers [100], diamond [8] and platinum, as reviewed in [101]). For those that can, many of the surface properties of these biomaterial are paramount to achieving biocompatibility, and the following section discusses some of the salient identified surface properties that are conducive to neuronal growth and attachment.

3.2 Surface properties of neuronal biomaterials

First and foremost, neuronal biomaterials must have an inert chemistry in physiological media in order to not be toxic to cells. Beyond this, specific surface functionalities have been found to promote cellular attachment on materials

[102]. For example, Patel et al. showed that silane moieties have an adverse effect on neuronal attachment [103]. In the case of neurons growing on diamond, its typical hydrogen or oxygen based functionalities have been found to be of little difference to cell proliferation [8,10,104], except for flat homoepitaxial diamond (as opposed to NCD) where hydrophilic oxygenated diamond has been found to be more conducive to neuronal attachment [10]. Chen et al. [105] found that neural stem cells grown on hydrogen terminated ultra-nanocrystalline diamond (UNCD) spontaneously differentiated into neurons while the cells grown on oxygen terminated UNCD films exhibited a preference towards oligodendrocyte (insulating glia cells) differentiation. Although surface chemistry effects cellular attachment – and positively charged surfaces can cause initial (but short lived [106]) cell adhesion via electrostatic bonding with negatively charged cell membranes [107] – direct cell-biomaterial interaction has not been observed, and supposed surface chemical dependencies are often dependent on a mediatory protein adsorption on a biomaterial that brings about cellular attachment. In order to perform neuronal cell cultures *in vitro*, a coating of extracellular matrix (ECM) proteins is typically used for cellular attachment [89,101,108]. ECM proteins, such as laminin and fibrinogen, form the molecular scaffolding of cells and contain specific peptide sequences (e.g. RGD) from which cells obtain biochemical cues to initiate various developmental processes via integrin membrane protein binding [109-111]. Such sequences can also be artificially synthesised and functionalised onto biomaterial surfaces in order to promote neuronal adhesion [112,113]. With respect to the common surface terminations (H/O) and ECM protein adsorption on diamond, Rezek et al. [39] have shown the orientation of serum proteins to be dependent on surface termination, which could explain the slight chemical selectivity of neurons on diamond, but also explain the more apparent selectivity of other cells such as osteoblasts on hydrophilic oxygenated diamond surfaces [114]. In fact, out of the chemical-related metrics of diamond as a biomaterial, Rezek et al. [39] suggest wetting angle and hydrophobicity to be the most important metric for cell growth on diamond, which incorporates fundamental properties such as surface chemistry, but also topographical properties such as surface roughness [115,116] and porosity [117]. Curtis and Wilkinson [118] state that when both

chemical patterns and topographic ones are offered to cells, topography tends to have a greater effect than chemical patterns, and the nano- and microstructure of surfaces has been established as a decisive factor affecting neuron morphology and adhesion. Fan et al. found that surface roughness of 20-50 nm promoted neuronal adhesion (central neural cells, substantia nigra) on silicon substrates, and surfaces of below 10 nm and above 70 nm roughness adversely affected adhesion [119,120]. Similarly, Khan et al. [121] found rat primary cortical neurons to adhere well onto surfaces of 10-100 nm roughness. Whilst nano-roughness is known to affect neuronal adhesion, micro-roughness determines neuron morphology. Clark et al. showed chick cerebral neurons to align to 2 μm groves [122], and various other studies on neuronal guidance using micro-scale topography have been carried out showing neurons to be guided by micro-scale ridges [123], grids [124] and grooves as extensively reviewed in [101,125]. Aside from the absolute roughness or relatively large micro-scale structures of biomaterials, the shape and curvature of surfaces can strongly effect neuronal attachment. This is most likely due to the functional conformation and orientation of proteins adsorbed onto nano-textured surfaces being affected by the curvature of the surface [102,126-128] via the balance of electrostatic and hydrophobic adsorption forces, which in turn effects the degree of cell attachment on biomaterial surfaces. Other properties, such as high porosity [129] and high elasticity [130] have been shown to enhance neuronal proliferation on biomaterials, both of which mimic the properties of neuronal tissue.

Considering the metrics of modern biomaterials, diamond is a promising candidate for chronic neuronal biomaterials. Its extreme chemical inertness yet ability to be stably functionalised with a variety of molecular and macromolecular functionalities (H/O, DNA, proteins, etc. [9,131-133]) allow the tailoring of its biocompatibility towards cells. Moreover, nanodiamond coatings are a promising biomaterial due to their additional properties to those of single- and polycrystalline diamond of increased curvature and nano-roughness, ease of deposition, porosity and a high affinity for protein adsorption [134,135], where adsorbed proteins remain in their functional state [136,137]. Furthermore, the

wide chemical window and strong polarisability of diamond [11] and its impressive electrical properties (see section 2.3) make it a very suitable material for the stimulation and recording of neurons.

3.3 Neuronal Devices

3.3.1 Wire electrodes

The simplest and oldest neuronal prosthetics are thin wire electrodes, and one of the first published examples was demonstrated by Strumwasser in 1958 [138], who implanted four stainless steel electrodes into the brain of a California ground squirrel and was able to record discharges of single neurons for one week or more. Metal wires of iridium, platinum, nichrome and stainless steel were used in these early studies as reviewed in [139,140]. Micro-wire electrodes remain in use today, giving long-lasting, single-neuron recordings for more than a year in some cases, and one particular advantage is that they can be used to access deep brain structures [99].

3.3.2 Micro-electrode Arrays

By the 1960s, with the development of photolithographic techniques and silicon etching technologies, a new tool set for fabricating recording electrodes became available and the first silicon-based arrays were fabricated. One of the first silicon-based micro-electrode arrays (MEAs) were made by Wise, Starr, and Angell [141,142]. These structures have evolved into the arrays commonly known as the Michigan Array (Figure 3.1a,b), which consist of multiple electrodes set along single or multiple shaft electrodes, and the linear arrangement of recording sites along a single shank facilitates layer-by-layer analysis of brain tissue. 3D arrays of up to 1024 electrodes have since been fabricated [143], and the development and some example uses of Michigan arrays are reviewed extensively in [98,99]. Another type of silicon-based array was developed by the University of Utah, USA; the Utah Array, which is a 3D

electrode array consisting of 100 conductive sharpened silicon needles, each of which is electrically isolated from its neighbours (Figure 3.1c,d). The sharpened tip of each needle is coated with platinum and the shanks are insulated with polyimide [98,99]. As an alternative to semiconductor-based probes, ceramic probes were developed to decrease crosstalk between recording sites and reduce shunt capacitance between the metallisation layer and the substrate [98,99,144].

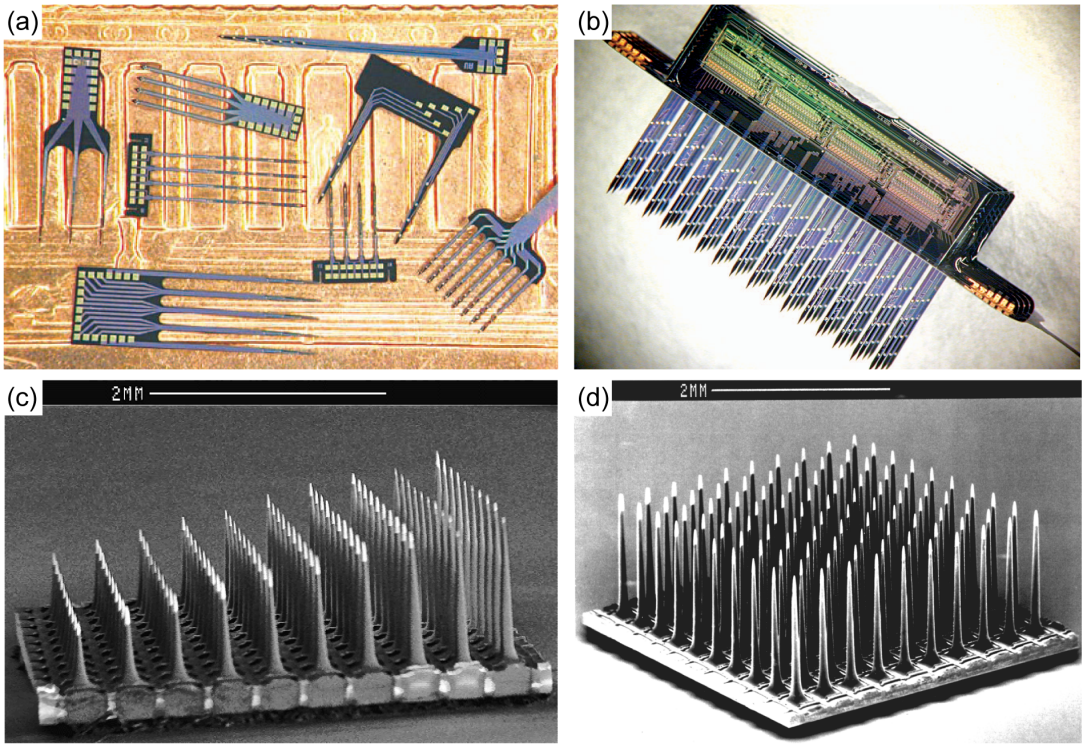

Figure 3.1: a) A selection of 2D Michigan Arrays on the back of a US penny and b) a 3D Michigan Array of four 64-site stimulating probes with shanks on 400-µm centers (both from [143]). SEM image of c) a slanted Utah Array and d) a standard 100 micro-electrode Utah Array (both from [145]).

Although rigid micro-electrodes have long been used for recording, the mechanical mismatch between the stiff probe and soft biological tissue can aggravate inflammation at the implantation site. Silicon has a Young's modulus of ca. 170 GPa and the brain of ca. 3 kPa [99]. A better electrode design would be one that has a Young's Modulus closer to that of the implantation site; therefore, flexible planar MEAs have been developed. To fabricate flexible MEAs, electrodes

are deposited and patterned on sacrificial substrates, fixed into a flexible material (typically a polymer such as Polyimide or Parylene [100]) and released from the rigid substrate by dissolving the sacrificial layer [99,146].

Most of the advances that increase biocompatibility can be attributed to novel materials, coatings, optimised geometries, and electrochemical or mechanical stability. Whilst these have increased the lifespan of neuronal MEAs to several years as opposed to the months, weeks, or days of their predecessors, no micro-electrode array design has managed to evade the host immune response and remain fully functional [7,98]. The fate of implants is often determined by effective integration with the surrounding neural tissue surface [147], and for this reason, diamond-based MEAs are now being developed in order to improve the biocompatibility of neural MEAs. The first diamond neural electrode was implanted in 2008 into a live guinea pig's auditory cortex at Michigan State University (MSU), USA, and was successfully tested as an extracellular, *in vivo* neural recording device [148]; however, the signal-to-noise results of *in vivo* and *in vitro* experiments appeared to be negatively affected by the low conductivity of diamond [149,150]. Bergonzo et al. [151] have shown that, for a flexible diamond/polyimide MEA implanted into a rat's retina for 14 weeks, a remarkably small amount of glial scarring is present. Hess et al. [152] have fabricated diamond/polynorbornene (PNB) MEAs and found structures to be flexible in spite of diamond incorporation, with the composite structure having mechanical characteristics similar to bare PNB. Various rigid diamond-based MEAs for *in vitro* characterisation and experimentation have also been reported during the course of this thesis: Bonnauron et al. [153] have developed processes for the selective growth of conductive BNCD over 3D topographic features for improved SNR electrodes, and have fabricated transparent diamond MEAs glass for *in vitro* experimentation, made possible by an optimised low temperature PECVD process. Similarly, Colombo et al. [154,155] have fabricated transparent BNCD transparent MEAs on sapphire, and Hees et al. [156] have demonstrated the fabrication of all diamond nano-electrode arrays using BNCD and NCD materials.

3.3.3 Field-Effect Transistors

A relatively new method of recording the cell signals from neurons is using ion sensitive (or solution gate) Field-Effect transistors (ISFET/SGFET). In 1991 Fromherz et al. [157] first demonstrated the recording of action potentials from the neuron of a leech by a p-type silicon-based ISFET, where the cell was positioned directly on the ISFET gate in solution. Since then n-type silicon [158] and materials including AlGaN/GaN [159] have been used to fabricate cellular ISFETs, and materials including Si_3N_4, Al_2O_3 and Ta_2O_5 have been used as pH-sensitive insulating gates on cellular ISFETs as reviewed by Poghossian et al. [160]. Very recently, graphene has also been reported [161] to be suitable for recording the electrogenic activity of cells. Diamond is a very promising candidate for neuronal FETs due to its high biocompatibility, high pH sensitivity [162,163] and its hydrogen surface conductive channel (H-SCC) being able to form SGFET with its conductive channel in direct contact with the analyte solution [164], which allows for high cell signal transduction. Ariano et al. [165] first demonstrated the recording of neuron action potentials on H-SCC SGFET, and Dankerl et al. [166] have since demonstrated an H-SCC SGFET array recording the action potential of HL-1 cardiac cells. While H-SCC SGFET admirably record cell signals, the H-SCC is vulnerable to anodic oxidation in oxidising environments and during use [57,167] and is not suitable for chronic *in vivo* application.

Chapter 4 Experimental Methods

4.1 Cleaning of Diamond Samples

The following processes are used for cleaning diamond and other materials used throughout this thesis unless stated otherwise. All processes have been carried out with the proper safety precautions in a fume cupboard.

Piranha Etch Cleaning

Piranha etch solution is a mixture of sulphuric acid (H_2SO_4) and hydrogen peroxide (H_2O_2) that is used to clean organic residues off substrates. Piranha etchant is a strong oxidiser, hence it will remove most organic matter and also adds hydroxyl groups (-OH) to the surface of most materials, rendering them hydrophilic. Piranha etch solution is prepared as and when needed in H_2SO_4:H_2O_2 1:1 ratio by adding H_2O_2 to H_2SO_4. The reaction is exothermic and can reach 120˚C. Samples are left in Piranha etch solution for 20 minutes and thoroughly rinsed in DI water and dried by N_2 air gun. In this thesis, Piranha etching has been used to clean organic material, such as bacteria and proteins, from the surfaces of substrates used for cell culturing experiments, and to oxidise the material surfaces.

Degreasing

Degreasing treatments have been used extensively in this thesis prior to all microprocessing steps used in Chapter 6, Chapter 7 & Chapter 8. It serves to remove residues on samples and results in microfabrication processes with better adhesion and quality. Firstly, samples are submerged in an ultrasonic bath

containing acetone for 5 minutes to dissolve accumulated residues. The samples are then immediately transferred into a second ultrasonic bath containing isopropanol alcohol (IPA) (5 mins) to dissolve the acetone residue, and finally into a DI water ultrasonic bath (5 mins) to dissolve the IPA residue. Samples are then dried with an N_2 gun.

4.2 Nanodiamond Monolayer Coating Deposition

Nanodiamond (ND) monolayers can be deposited on substrates through a variety of methods, and most methods start with a hydrocolloid of monodispersed NDs [72] as a source of NDs. To sediment NDs out of colloidal suspension onto substrates, processes (listed in increasing efficacy) such as dip-coating, spin-coating, electrospray or ultrasonication can be used ([168] and containing references). All these methods rely on electrostatic attractions between the substrate and nanodiamonds to form well-adhered, continuous coatings [169]. In this thesis ultrasonication has been used to deposit ND monolayers [170]. Ultrasonic agitation of NDs increases their kinetic energy and collision rate with the substrate, giving dense monolayers with good adhesion (depending on the electrostatics of the NDs/substrate). ND monolayer deposition is performed in a clean room environment where substrates are submerged in ND hydrocolloids (0.05 g/L) and ultrasound is applied for 10 minutes. The substrate is then rinsed in DI water and blow-dried with an N_2 gun.

4.3 Primary Murine Hippocampal Neuronal Cell Cultures

The preparation of primary cell cultures was performed in close collaboration with the Schoepher Laboratory, UCL, by Agnes Thalhammer. All animal work was undertaken under the auspices of the UK Home Office Project and Personal Licenses held by the authors in their designated laboratories.

Neurons, unlike many other cell types in the body, are terminally differentiated and cannot undergo mitosis to form cell lines. Consequently, neurons must be harvested directly from animal specimens. Murine hippocampal neurons are often used as valid neurophysiological models [171] due to the relatively short breeding cycle of mice and neuronal cell types being neatly organised into layers in the hippocampus [172]. In summary, hippocampal neurons and glial cells are dissected from embryonic mice, dissociated, triturated (to shave off neurites), seeded onto substrates and incubated in various physiological media to foster development. In detail, cell cultures are prepared using a protocol adapted from [173], and can be found in Appendix A.

4.4 HL-1 Cardiac Cell line cultures

HL-1 cell cultures were performed by Vanessa Maybeck from Jülich, Germany [174].

HL-1 cells are a cell line derived from a mouse atrial heart tumour [175], capable of dividing indefinitely but also maturing when a confluent layer is formed. The mature layer forms gap junctions and begins to spontaneously send action potentials across the sheet of cells. With further maturation, the cell sheet becomes contractively active and each wave of action potentials can be seen as a movement of the cells. Thus, this system is ideal for the first validation of new electronic devices. The presence of electrical signals can be confirmed optically by the contraction of the cells in mature cultures and – since signals propagate through the sheet – by the detection of action potentials across electrode arrays with a time shift that corresponds to the propagation speed of an action potential.

HL-1 cells are maintained in Claycomb's media (Sigma) supplemented with 10 % Fetal Bovine Serum (FBS), 100 µg mL^{-1} penicillin/ streptomycin, 0.1 mM norepinephrine (NorA) and 2 mM L-glutamine in an incubation chamber at 37˚C and 5 % CO_2 atmosphere. Cells are removed from a confluent T-25 culture

flask by digestion with 1 mL 0.05 % Trypsin/ Ethylenediaminetetraacetic acid (EDTA) and one eightieth plated onto 7 mm diameter MEA devices coated with fibronectin/gelatin. The culture media is changed every day and the activity of the confluent layer is measured on day *in vitro* (DIV) 3 or DIV4. Cultures longer than DIV4 are rare but possible if the cells have not formed multilayers that reduce nutrient diffusion to the lower layers of cells. If no contraction of the cells is seen in a confluent layer, cells are stimulated with an additional 1x dose of Norepinepherine.

4.5 Immunostaining and Confocal Microscopy Imaging

The immunostaining of cells and following confocal imaging was performed in close collaboration with the Schoepher Laboratory, UCL, by Agnes Thalhammer.

Immunostaining is a procedure that allows the protein-based, biomolecular architecture of cells to be specifically labelled and visualised by imaging techniques such as fluorescent confocal microscopy. It works by exploiting the highly specific 'lock and key' binding interactions that occur between antigens and antibodies. Proteins in cells take the role of the 'key', or antigen, displaying epitope binding sites to which the appropriate paratope of an antibody can bind. In immunostaining, this primary antibody can either be labelled with a dye, or have a secondary fluorescently labelled antibody bind to it. To perform immunostaining, cells are firstly cross-linked to confer rigidity, secondly made permeable to antibodies and finally subjected to a series of media, antibodies and fluorescent dyes to make them visible under a fluorescent confocal microscope. Depending on the proteins of interest in the cell, different primary (and the appropriate secondary) antibodies are selected to specifically stain said proteins, and multiple stains can be performed on the same cell culture. For example, in this thesis the Microtubule associative protein 2 (MAP2), actin filaments (F-actin), the Glial fibrillary acidic protein (GFAP) and DNA are

stained to investigate neuron cell interaction with ND-coatings for reasons as listed as follows:

- MAP2 plays an important role in neuron microtubule assembly (regulating their structure and stability), neuronal morphogenesis and cytoskeleton dynamics [176]. MAP2 is a stringent marker for neurons, confined to neuronal cell bodies and dendrites, and is uniformly distributed throughout the cell when first expressed in cultured neurons, but becomes selectively localised as dendritic development proceeds [177].
- F-actin makes up the filopodia of growth cones, which contain the sensory, motor, integrative, and adaptive functions of growing neurites and form focal adhesions with the substratum [178]. It also is a constituent of glia cell cytoskeletons.
- GFAP is the main constituent of intermediate filaments in astrocytes and serves as a cell specific marker for astrocytes, which are characteristic star-shaped glia cells in the brain and spinal cord. They perform many functions, including biochemical support of endothelial cells that form the blood–brain barrier, provision of nutrients to the nervous tissue, maintenance of extracellular ion balance, and have a role in the repair and scarring process (gliosis) of the brain and spinal cord following traumatic injuries [7].
- DNA stains the nuclei of cells.

For each of these protein antigens the corresponding primary antibody, secondary antibody and attached fluorescent dyes are given in Table 4.1. Note that the fluorophores used here have minimal spectral overlap thus avoiding crosstalk or unintended excitation from different laser excitation wavelengths:

Antigen	Primary Antibody or stain (s)	Secondary Antibody	Dye	Ex./Em. (nm)	Ex. Source
MAP2	Mouse anti-MAP2	Goat anti-mouse IgG 115-095-003	Cy-2	488/506	Ar laser
F-actin	Rhodamine-Phalloidin (s)	N/A	TRITC*	543/570	HeNe laser
GFAP	Rabbit anti-GFAP	Goat anti-mouse IgG 115-175-003	Cy-5	637/670	Red diode laser
DNA	Hoechst 33258 (s)	N/A	N/A	353/460	Hg Lamp

Table 4.1: List of targeted protein antigens, primary antibodies, secondary antibodies, fluorescent dyes and their corresponding excitation/emission information used for the immunostaining of neuronal cell cultures. *tetramethylrhodamine-5-(and-6)-isothiocyanate. Cy=Cyanine. Ex.=Excitation. Em.=Emission. Hoechst 33258 staining was not used for all cell cultures due to fluorescence interference with NDs.

Immunostaining protocol

1. Wash cells 2x with phosphate buffered saline (PBS; 137 mM NaCl, 2.7 mM KCl, 10 mM Na_2HPO_4, 2 mM KH_2PO_4)
2. Fix cells in 4 % paraformaldehyde 4 % sucrose in PBS for 10 mins
3. Wash 2x with PBS
4. Permeablise cells with 0.2 % TritonX-100 in PBS for 10 mins
5. Wash 1x with blocking solution (BS, 5 % horse serum in PBS)
6. Incubate for 1–2 hrs in BS to minimise unspecific antibody binding (albumin in serum binds to all non-specific binding sites)
7. Incubate cells for 1–2 hrs with primary antibodies (mouse anti-MAP2, rabbit anti-GFAP at 1:500 ratio with BS)
8. Wash 3x with BS

9. Incubate for 1 hr with secondary antibodies (see Table 4.1, both goat anti-mouse IgG at 1:300 ratio with BS)
10. Wash 3x with BS and 2x with PBS
11. Stain with F-actin for 10 min at room temperature (RT) with 2 U/ml rhodamine-phalloidin and stain nuclei for 5 min at RT with Hoechst 33258 (1 mg/ml in PBS)
12. Wash 3x with PBS
13. Store at 4˚C in sterile-filtered PBS until imaging or mount for confocal imaging after wash in Gel mount (Sigma G-0918)

Confocal Microscopy Imaging

Having immunostained cells, confocal microscopy can be used to obtain 3D spatially resolved images of the fluorescent dyes stained into cell cultures. Images are obtained by rastering point-focused laser excitation sources through samples in a series of vertically stacked cross-sections, and the Stoke-shifted emission from excited fluorophores is recorded (Figure 4.1a). The spatial resolution of a confocal microscope is enhanced by point illumination and a pinhole in an optically conjugate plane in front of the detector to eliminate out-of focus signal (Figure 4.1b). As a result, only light produced very close to the focal plane can be detected and the image's resolution, particularly in the sample depth direction, is much better than that of wide-field microscopes. Confocal microscopy has been performed on a Bio-Rad Radiance 2100MP Confocal Microscope with a 20x (Nikon, Plan Flour, 0.75) water-immersion objective (Figure 4.1c). Alternatively a Leica TCS SPE confocal microscope equipped with a 40x oil-immersion objective (Zeiss, ACS APO, 1.15) has been used.

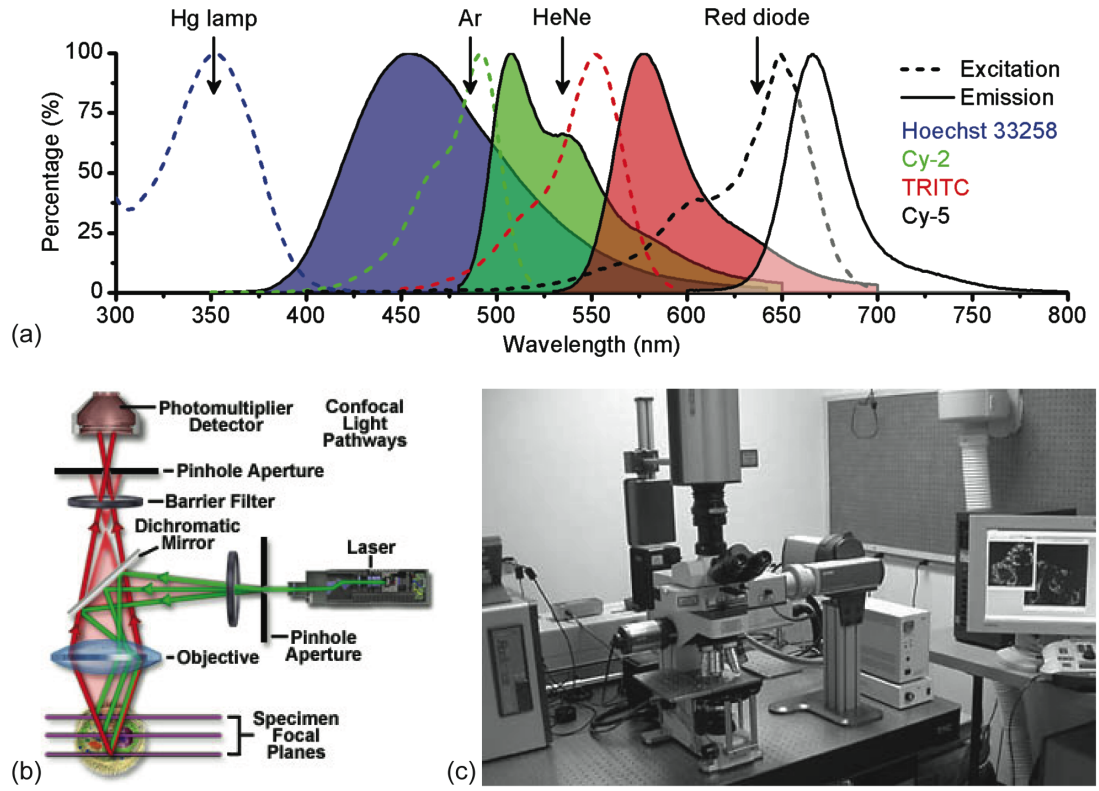

Figure 4.1: a) Spectra and excitation sources of all fluorophores used in confocal microscopy imaging. Note minimal crosstalk between dyes and excitation sources. b) Schematic of confocal microscope. c) Bio-Rad Radiance 2100MP Confocal Microscope.

4.6 Critical Point Drying of Cells and other processes for SEM imaging

Critical point drying (CPD) is a process used to dehydrate fragile objects that are susceptible to damage by the relatively enormous forces of water surface tension. CPD is commonly used to dehydrate chemically cross-linked cells for the purpose of imaging them in a scanning electron microscope (SEM), because, without CPD, cells would rupture during the evaporation process or in the vacuous environment of an SEM. Alternatively, other drying methods can be used as discussed in [179]; however, CPD is the favoured technique due to its relatively quick and quality results. It should be noted an environmental SEM can

be used to image hydrated cells, however image quality is sacrificed for easier sample handling.

CPD works by replacing the liquid in cells with an inert liquid (CO_2) that, when at or above a certain pressure and temperature called the critical point, can co-exist in the liquid and gaseous phase at the same density and therefore be vapourised with no surface tension. When exchanging liquids in the CPD process, CO_2 is not readily miscible with water, hence, a universal solvent must be used as an intermediary liquid. With cells, ethanol is commonly used and is exchanged in a gradated ethanol series as to minimise the osmotic pressure differences between the internal and external cellular solutions, and also it does not interfere in the fixing chemistry used to solidify the cells. To solidify cells and improve SEM image quality, cells are treated with various chemical processes prior to liquid exchange. The whole process is described below, and care is taken to keep cells submerged during liquid exchange:

1. Initial fixing: 4 % paraformaldehyde (linking amines and nucleic acids with methylene bridges), and 4 % sucrose (cryoprotectant) in PBS is used, as described in 4.3.
2. 10 minute wash in 0.1M sodium cacodylate buffer (SCB). SCB is used because it gives better membrane preservation and is less likely to form precipitates with other reagents (it does not react with aldehydes).
3. Protein fixing: 1 % glutaraldehyde in 0.1M SCB adjusted to pH 7.3 with HCl for 10 minutes links amino and sulfhydryl groups, which acts as a protein cross-linker.
4. 10 mins wash in 0.1M SCB.
5. Osmication: 45 minutes of Osmium Tetraoxide (OsO_4) 1 % w/v in 0.1M SCB binds phospholipid head groups in the membrane, thereof acting as a membrane fixant. Osmium also improves image contrast as it is a heavy metal and has a large electron density.
6. 10 mins wash in 0.1M SCB.

7. Graded ethanol series: cells are dehydrated with 25, 50, 75 and 90 % ethanol solutions for 5 minutes at each percentage, followed by 3x 10 minutes 100 % ethanol.
8. Critical Point Drying: liquid CO_2 is let into a cooled, pressurised chamber (Polaron Critical Point Drier, CPD 750, Figure 4.2a), flushing out the ethanol. Once complete, the chamber is gently heated to increase the temperature and pressure (ca. 20 mins, Figure 4.2b, A to B) to above the critical point (31.0˚C, 78.9 atm [180]) into the supercritical fluid phase, where it is kept for ca. 10 minutes. CO_2 is then let out slowly (ca. 25 mins, Figure 4.2b, B to C) in gaseous form from the top of the chamber, lowering the liquid CO_2 in the chamber, depressurising the chamber and thereby drying the cells.
9. Gold sputtering: To reduce charging effects during SEM imaging, samples are finally coated with a few nanometres of gold in a sputtering machine (EMScope SC 500).

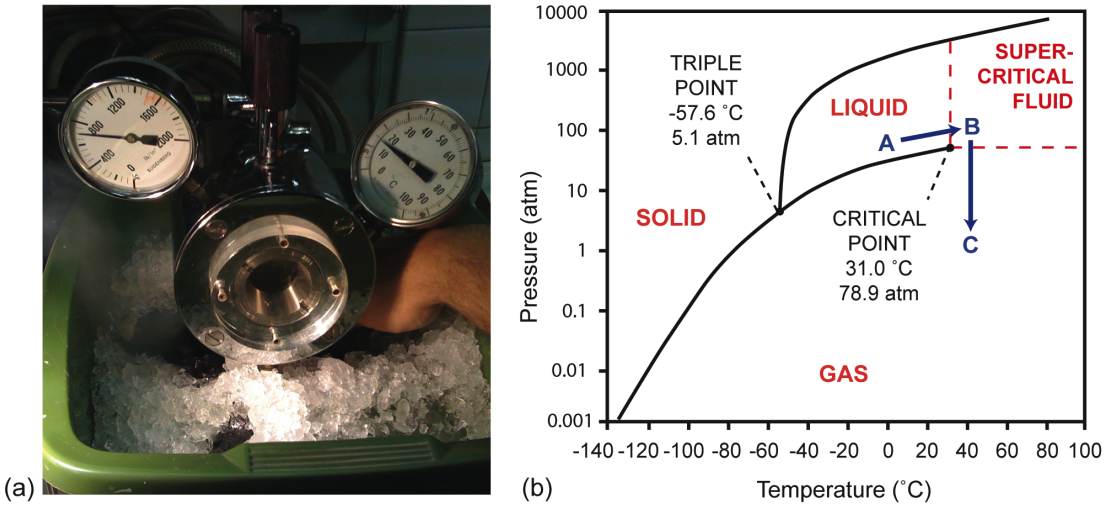

Figure 4.2: a) Picture of CPD 750 in use, b) CO_2 phase diagram adapted from [180] showing the phase path taken in CPD.

4.7 Scanning Electron Microscopy and Energy-Dispersive (X-Ray) Spectroscopy

Scanning Electron Microscopy (SEM) obtains images by, under high vacuum, rasterising a high energy beam of 'primary electrons' across a sample surface and counting the secondary or backscattered electron emission for each pixel [181]. Electron emission count is determined by the chemical composition and surface properties of a sample, allowing SEM images to convey topographic and compositional information by the contrast and spatial resolution of the image. High energy electron beams are typically generated using thermionic emission with tungsten or lanthanum hexaboride (LaB_6) filament cathodes; however, for clearer, less electrostatically distorted and higher resolution images, Field Emission Guns (FEGs) can be used. FEGs produce lower energy beams, smaller spot sizes and less sample charging in comparison to thermionic electron guns. When imaging highly insulating nanodiamond particles that charge readily, FESEM is essential for obtaining clear images.

Following electron generation, SEM works by accelerating electrons through an anode and series of magnetic lenses to focus and direct the electron beam onto the sample surface. The following components appear sequentially in the beam line of an SEM (Figure 4.3b) [181]: 1) Located before the anode, a Wehnelt cylinder (cathode electrode tunnel) shepherds electrons towards the anode which accelerates electrons down the beam path. 2) A magnetic Condenser Lens reduces the beam diameter. 3) Scan coils and a stigmator electromagnetically raster the electron beam in the X and Y direction and 4) a Final Object Lens focuses the beam into a small spot (0.4 nm possible with FESEM) on the sample surface. Upon collision with the samples, electrons interact with the first few nanometres of the sample surface and can emit other particles. These particles can be broadly classified into 3 categories: secondary electrons, backscattered electrons and energy-dispersive X-Rays.

Secondary electrons are emitted from the k-orbitals of bombarded atoms via inelastic scattering. They are approximately 1000 times less energetic than incident primary electrons and are detected by an Everhart-Thornley detector, which is a type of scintillator-photomultiplier system. The contrast of secondary electron images depends mainly on the tilt angle and topography of the sample surface.

Backscattered electrons are high-energy (>50 eV [181]) primary electrons that bounce back off bombarded atoms by elastic scattering. Backscattered electrons are detected by scintillator arrays concentric to the primary beam line, and the contrast of the resulting image is determined by the topography and the mean atomic number of the sample. In this thesis, backscattered electrons are used to image neurons and nanodiamonds due to the osmication of neurons (see section 4.6) giving them a larger mean atomic number and higher contrast image.

Energy dispersive X-Rays are a consequence of secondary electron emission. When an electron is removed from the lower k-orbital of an atom by primary electron bombardment (Figure 4.3c 1.), an electron hole is created and higher orbital electrons (for example, in the L and M shells) will energetically cascade downwards to fill the electron hole (Figure 4.3c 2.). The difference in the orbital energies is released in the form of energetically defined X-Rays, which are collected in an energy dispersive spectrometer and the resulting spectrum can be used to identify the elemental composition of the sample (Energy Dispersive X-Ray Spectroscopy (EDS)).

In this thesis, a JEOL JSM-7401F SEM (Figure 4.3a) has been used to capture backscatter SEM images of neurons on nanodiamonds with an accelerating voltage of 2 kV, and a JEOL JSM-6301F equipped with an EDS Detector has been used for elemental analysis of etched diamond structures with a 15 kV acceleration voltage.

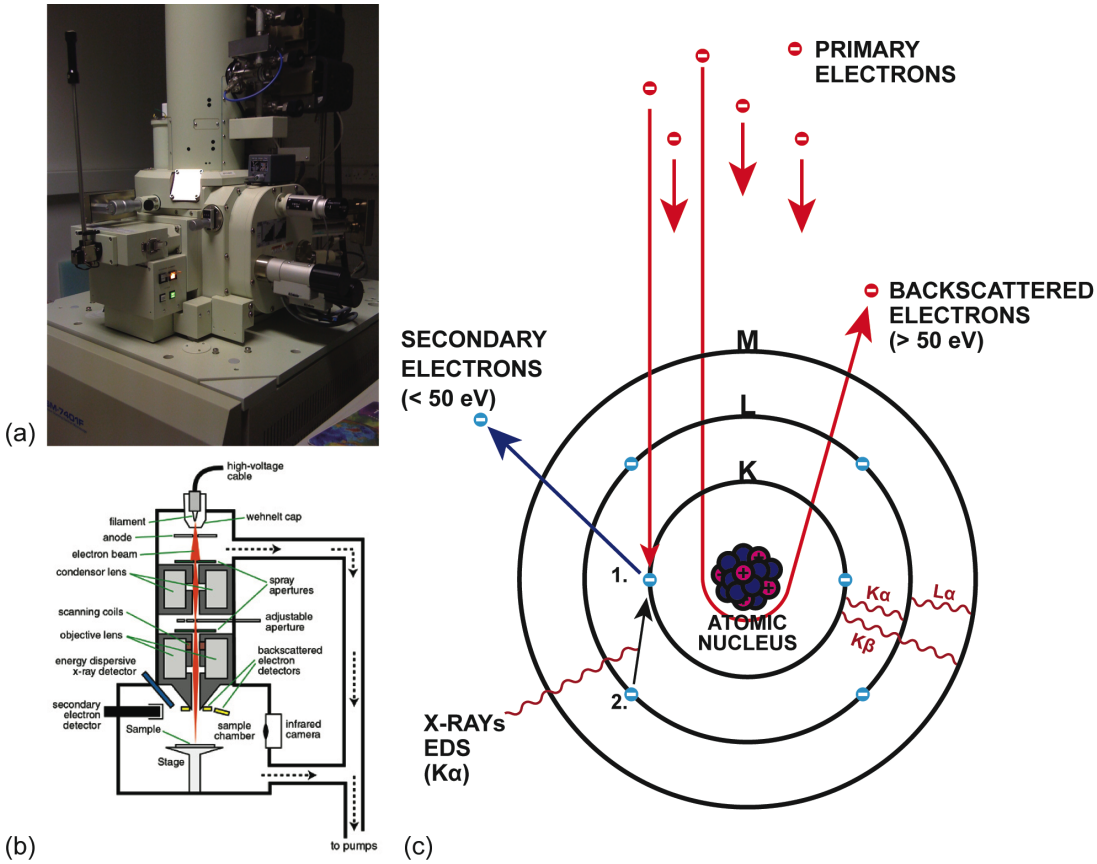

Figure 4.3: a) JEOL JSM 7401F SEM. b) Schematic of typical SEM [182]. c) Illustration of the interactions that are useful for SEM imaging and EDS, which occur upon high-energy electron bombardment of atoms. Backscattered electrons can be slingshot around the nucleus of atoms. X-Rays on the right hand side of the diagram demonstrate some the notation used to describe X-Ray emissions in atoms.

4.8 Secondary Ion Mass Spectrometry

Secondary Ion Mass Spectrometry (SIMS) was performed by Richard Morris from the Advanced SIMS Projects, Department of Physics, University of Warwick, UK.

SIMS is a technique used to analyse the composition of thin film materials by sputtering the surface of specimens with a focused primary ion beam (e.g. O_2^+, O^-, Cs^+, etc.) and collecting and analysing the ejected secondary ions [183].

Typically, a secondary ion mass spectrometer consists of 1) a primary ion gun generating the primary ion beam, 2) a primary ion column, accelerating and focusing the beam onto the sample, 3) an ultra high vacuum (10^{-10} mbar) sample chamber holding the sample, 4) a secondary ion extraction lens, 5) a mass analyser and 6) an ion detection unit. In this study an Atomika 4500 quadrupole SIMS instrument with Floating Low energy Ion Guns (FLIG [184]) have been used. FLIGs allow the use of ultra low energy primary ion beams that are essential for characterising shallow δ-like diamond samples, and produce mono-energetic ion beams in the range of 150 eV to 5 keV. FLIG Ion beams are mass filtered by a Wien filter to ensure ion beam purity and can be varied between 0˚ and 85˚ with respect to the sample holder orientation, where 0˚ is normal to the sample surface.

For ultra low energy SIMS (uleSIMS), secondary ions are typically measured with a quadrupole mass analyser in order to determine the elemental composition of the surface [185]. Quadrupole mass analysers consist of 4 circular rods set parallel to each other with RF voltages applied between opposing rods. Secondary Ions are separated by the stability of their trajectories through the resultant oscillating electric fields between the rods, which is determined by their mass-to-charge ratio (*m/z*), and ions emerging from the quadrupole mass analyser are detected with a channel electron multiplier. To obtain SIMS profiles, counts vs. time measurements are converted into concentration vs. depth profiles by comparing ion counts against similar samples of nominal concentration and by measuring the depth of the sputtered crater. SIMS is the most sensitive surface analysis technique, being able to detect elements at detection limits of 10^{12} to 10^{16} cm^{-3} [186].

One of the benefits of using uleSIMS is that primary ion energies are lower, which reduces the redistribution of atoms deeper into the sample that occurs as a result of ion bombardment. Whilst uleSIMS reduces primary ion beam mixing, mass transport cannot be fully eliminated because non-zero ion energies are necessary to sputter secondary ions for measurement; however, the redistribution of atoms in the material is predictable, whereby it is displaced and

broadened following an exponential decay of concentration on the backside of the feature [183]. This unwanted perturbation of the actual concentration profiles of samples can be mathematically represented in a simplistic form [187] by the real depth profile convoluted with a SIMS response function:

$$N(z) = \int N_0(z')\, G(z' - z)\, dz' \tag{1.1}$$

Where N(z) is the measured SIMS depth (z) profile, $N_0(z')$ is the actual depth profile, G(z'-z) is the SIMS response function and z' is the position of the a δ-doped profile feature. The mass transport response function is modelled by:

$$\begin{aligned} z' - z < -\delta, \qquad & f(z' - z) = 0 \\ z' - z > -\delta, \qquad & f(z' - z) = \frac{1}{\lambda} e^{\left(-\frac{z - z' + \delta}{\lambda}\right)} \end{aligned} \tag{1.2}$$

Where λ and δ are defined as the decay length and depth displacement of the convoluted SIMS δ-profile, and are determined experimentally from δ-layer profiles. The general SIMS response function can then be expressed as a convolution of the mass transport response function and a different convolution function:

$$G(z' - z) = \int f(t) g(t - (z' - z)) dt \tag{1.3}$$

Differentiating Equation (1.1) with respect to z and substituting in Equations (1.2) and (1.3), we find:

$$\int N_0(z_0) g\big(z - (z_0 - \delta)\big) dz_0 = N(z) + \lambda \frac{\partial}{\partial z} N(z) \tag{1.4}$$

Finally, when g(t) is a δ-function (as is the case in this thesis), an approximate solution for Equation (1.4) can be used as shown below in Equation (1.5), with its associated error in Equation (1.6).

$$N_0(z) \approx N(z + \delta) + \lambda \frac{\partial}{\partial x} N(z + \delta) \tag{1.5}$$

$$\frac{\Delta N_0(z)}{N_0(z)} = \frac{\Delta \lambda}{\lambda} \frac{\partial}{\partial z} \log\left(N(z + \delta)\right) \tag{1.6}$$

4.9 Atomic Force Microscopy

The principal of Atomic Force Microscopy (AFM) is to trace a cantilever with a nano-sharp tip across a surface and measure its deflection as it passes over the terrain. The deflection of the cantilever is measured and amplified by monitoring the deflection of a laser beam that is reflected off the back of the cantilever onto an array of four photodiodes. The array is positioned so that the laser, when reflected from an unperturbed cantilever, impinges directly onto the centre of the array, allowing subsequent deflections of the cantilever to be measured by the relative intensities measured by the four photodiodes (Figure 4.4a). AFM images are obtained by drawing an AFM tip across the sample surface in a raster pattern using piezoelectric positioners that expand and contract to sub-nanometre resolution under applied voltages. For very flat surfaces, the topography of the sample can be read by the deflection of the cantilever (variable force imaging); however, for rougher surfaces, constant force imaging can be used. In this mode the height of the AFM tip is varied as to maintain a constant deflection force on the cantilever. This is achieved by routing deflection data through a feedback control circuit that varies the tip height accordingly. Two basic modes of operation exist: 1) Contact mode, where the AFM tip is in contact with the sample in constant or variable force mode, or 2) Tapping mode, where the tip of the cantilever is driven to oscillate up and down near its resonant frequency, and the surface is sensed via the damping of said oscillations by remote forces such as Van der Waals and electrostatic forces. Tapping mode operates in a similar manner to constant force imaging in contact mode, except the amplitude of vibration is kept damped at a constant magnitude instead of a constant deflection force. Tapping mode is advantageous over contact mode for certain applications where tip contact is undesirable. Such applications include the imaging of soft biological matter (e.g. proteins, lipid membranes, etc.), which are easily damaged by AFM tips or, conversely, very hard materials (e.g. diamond), which quickly blunt sharp AFM tips, degrading image quality. Tapping mode is also beneficial for imaging unfastened particles (e.g. nanodiamond monolayers) that would otherwise be displaced during contact imaging, or stick onto AFM tips causing tip artefacts. Tip artefacts are anomalous reoccurring

shapes seen across AFM images, which are actually conveying the distorted shape of the tip rather than the shape of the sample surface. Aside from these basic modes of operation, AFM can be used in other applications including nanolithography, force spectroscopy and conductive AFM. In this thesis, tapping mode has been used to image single crystal diamond surfaces and nanodiamond-coated materials. The particle size of nanodiamonds has been estimated using the height dimension and not the lateral dimensions of scanned images in order to avoid overestimating particle size due to relatively large tip curvatures causing tip convolution in images (Figure 4.4b).

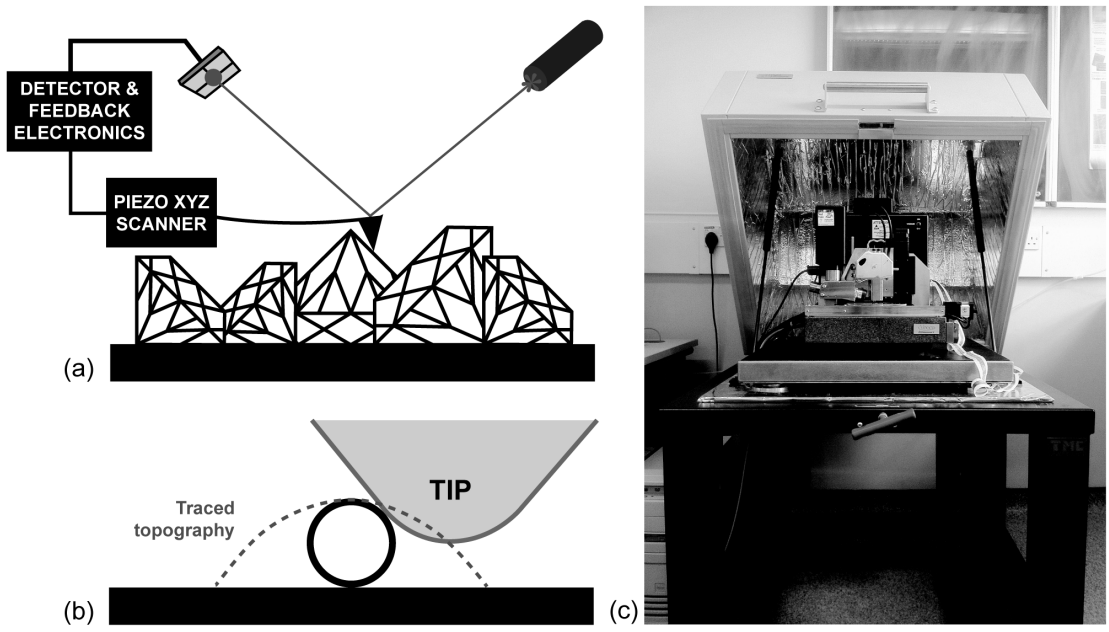

Figure 4.4: a) Schematic diagram of AFM in contact mode. b) A schematic of how tip convolution makes lateral dimensions unrepresentative of nanoparticle dimensions. c) Dimension V AFM (Veeco).

4.10 Fourier Transform Infrared Spectroscopy

Fourier Transform Infrared (FTIR) Spectroscopy is a powerful technique to probe the bonds and atoms in materials, and is particularly useful for the spectroscopy of organic bonds and molecules. FTIR spectroscopy works by measuring the molecular vibrations and rotations of a sample via its spectral absorption of infrared (IR) radiation, which is then analysed to determine the

constituent bonds and atoms in the sample. In simple approximation, intermolecular bonds can be thought of as springs in simple harmonic oscillators (they are in fact anharmonic oscillators), whereby the strength of the bond and the masses of the connected atoms (and coupled atoms) determine the vibrational resonant frequency of the system. For bonds typical to organic molecules (C–H, C–O, C=O, C–N, O–H, etc), these frequencies lie in the mid-infrared or 'fingerprint' range (400-4000 cm^{-1}) [188]. For a molecule to absorb IR, it must have an electric dipole moment to interact with the electric field of IR radiation ($U=\mu.E$, where U is the energy of interaction, μ is the dipole moment of the bond and E is the electric field component of IR) and the resultant excited state must bring about a net change of the dipole moment. Molecules can have 1) permanent dipoles, where a 1D asymmetrical distribution of atoms with different electronegativity exist, e.g. H_2O or atomic surface functionalisations; and/or 2) induced dipoles that arise from transient charge distributions caused by the vibrational fluctuations of otherwise (at-rest) centrosymmetric distributions of atoms of differing electronegativity, e.g. (CH_4, CO_2 : $O^{\delta-}=C^{\delta+}=O^{\delta-}$). Upon incidence of IR radiation onto a molecular bond, if its frequency matches the vibrational frequency of the molecule and vibrational selection rules are obeyed, then the IR radiation will be absorbed causing the molecular vibrations of the molecule to transit into an excited state. With respect to diamond, the symmetric, rigid, tetrahedral structure of bulk diamond means that diamond's bulk is largely transparent to IR, however, surface terminations can absorb IR, making FTIR spectroscopy a largely surface-sensitive technique for ND powders. Various types of vibrations are possible, each with their characteristic wavenumber, as depicted below in Figure 4.5a.

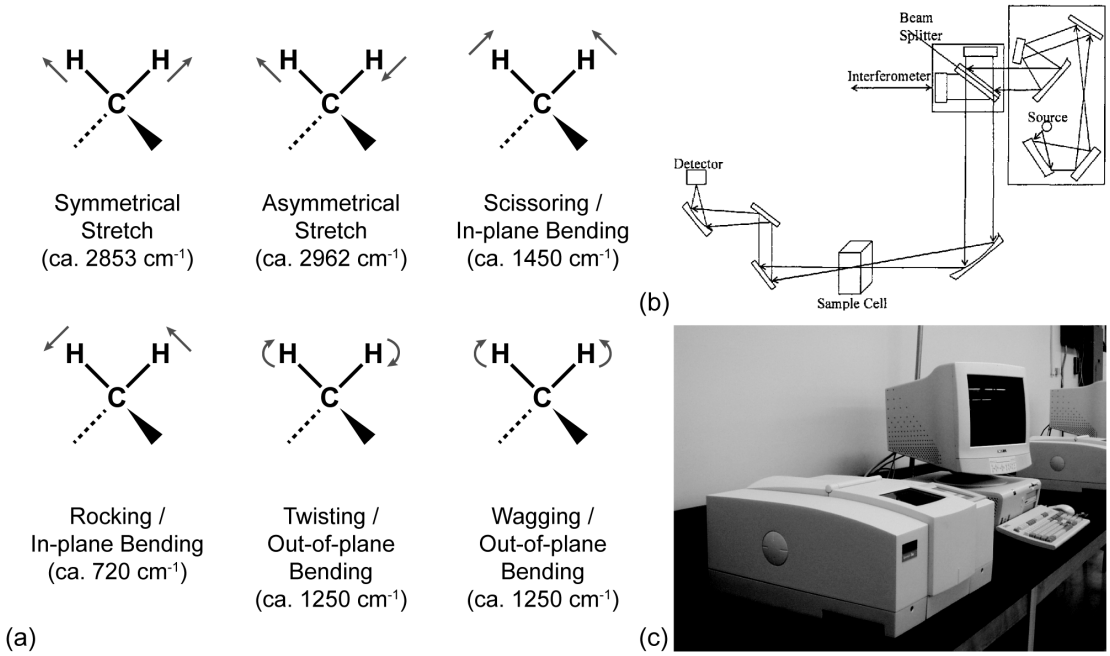

Figure 4.5: a) Depiction of vibration modes of a methyl molecule. b) FTIR spectrometer schematic. c) Perkin Elmer Spectrum One.

FTIR spectroscopy differs from standard infrared spectroscopy – where samples are exposed to successive monochromatic IR sources to make up an absorption spectrum – in that the sample is exposed to all frequencies simultaneously. Instead, light from a broadband source is directed through a Michelson Interferometer where it is split into two paths (Figure 4.5b) [189]. Whilst one path is fixed in length, the other is constantly varied by a moving mirror in the beam path. Upon recombination at the beam splitter, constructive and deconstructive interference occurs resulting in an interferogram of intensity vs. mirror position (or time). Using a Fourier Transform the interferogram can be transformed into a spectrum of intensity vs. wavenumber. FTIR spectroscopy has various advantages over diffuse IR spectroscopy: By measuring all frequencies simultaneously, measurement time is drastically reduced allowing additional co-scans, and the signal to noise ratio and energy throughput is increased. To perform FTIR spectroscopy, a sample is placed in the path of the interferometer beam and the resulting FTIR spectrum is subtracted from a background reference spectrum, which differs in content only by the sample under scrutiny. For example, for ND powders stuck onto CaF_2 windows in an N_2

purged atmosphere, CaF_2 windows in an N_2 purged atmosphere are used as background samples.

FTIR measurements can be taken in four main modes: 1) Transmission mode, where IR is transmitted and collected through a sample, 2) Spectral Reflectance mode, where IR is reflected and collected off a smooth surface, 3) Diffuse Reflectance, where IR is scattered collected from many angles off a rough surface and, 4) Attenuated Total (Internal) Reflectance (ATR), where a crystal has IR totally internally reflected through it, and the sample interacts with IR via frustrated total internal reflectance with the evanescent IR wave on the surface of the crystal. In this thesis transmission mode has been used to image ND powders, where CaF_2 windows have been used to support NDs in the IR beam path, which are IR transparent for the majority of the fingerprint spectrum (>700 cm^{-1}). CaF_2 has been used instead of the more commonly used KBr pellet method of imaging NDs because sample preparation only involves drop-coating and evaporating ND hydrocolloids on relatively robust and insoluble CaF_2 windows (Figure 4.6). KBr is soluble in water, hence cannot be used in drop-coating, and forming its very fragile pellets requires laborious sample preparation and increases sample contamination probability. In transmission mode, the amount of IR absorption is proportional to the number of bonds in the beam path (Beer's Law; Absorbance, $A=\varepsilon cd$, where ε is the molecular absorption coefficient, c is concentration and d is path length [188]), therefore determining the relative percentage of surface functionalisation of samples is possible (peak size is proportional to percentage coverage). It should be noted that FTIR spectroscopy of ND has various idiosyncrasies that manifest in non-linear baselines of FTIR spectra [189]. NDs agglomerates are comparable in size to the IR wavelengths, resulting in scattering that slopes the spectrum baseline towards higher absorption for higher wavenumbers. Conversely, NDs are primarily carbon whose large refractivity slopes the baseline in the opposite direction. Consequently, non-linear baseline correction must be used at the discretion of a user skilled in the art for quantitate analysis of spectra with varying baselines. Similarly, for interpreting spectral peaks, the organic functionalities seen on NDs will have shifted values in comparison to library values due to the relatively

large mass of the bulk ND (in comparison to organic molecules) to which the moiety is attached [188]. A Perkin Elmer Spectrum One (Figure 4.5c) with N_2 purging has been used in this thesis, where measurements have been taken after spectra stabilisation (H_2O desorption) with 4 cm^{-1} resolution and 10 minutes of co-scanning. Samples have been prepared using hot-plate evaporation of concentrated ND hydrocolloids on CaF_2 windows.

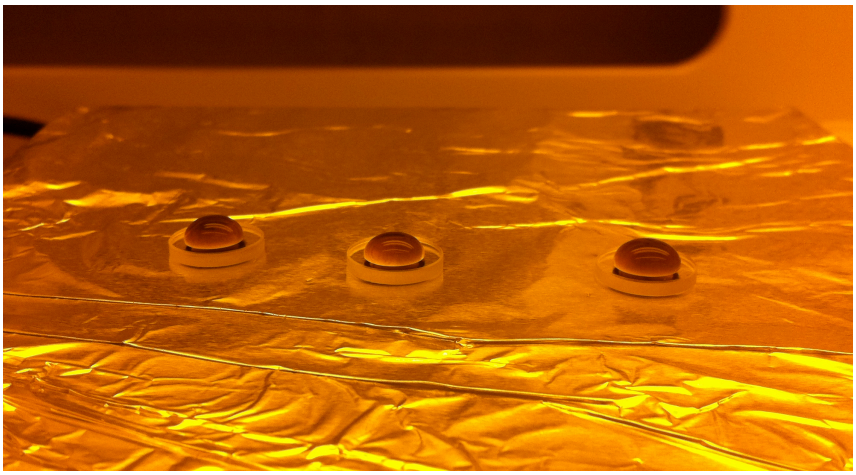

Figure 4.6: Drop-coating of NDs on CaF_2 windows using concentrated ND hydrocolloids on a hotplate at 100˚C.

4.11 Electrophysiological Recordings

Electrophysiological experiments were performed in collaboration with the MRC Laboratory for Molecular Cell Biology, UCL, by Lorenzo Cingolani and Agnes Thalhammer.

Electrophysiology is the study of the electrical properties of biological cells and tissues. The electrical activity of neurons predominantly arises from ion channels and ion pumps building up asymmetric Na^+ and K^+ ions concentrations inside and outside of the cell membrane (inside/outside: low/high [Na^+], high/low [K^+]), which produces a potential difference across the membrane (membrane potential, with a resting potential at equilibration of usually -40 to -90 mV [190]). The electrical activity of neurons is modulated by the flux of these ions (as well as Cl^-, Ca^{2+}, e.t.c.) across the membrane through gated ion channels,

which can be opened by depolarising (positive) voltages or by neurotransmitter and neurohormone release and binding at synapses and receptors. In this thesis, electrophysiological techniques have been used to probe the electrical properties of neural tissues cultured on artificial substrates. Three techniques have been employed, where each technique probes an increasingly larger scale of functionality in neuronal networks. Firstly, a technique used to determine the ability of individual neurons to fire action potentials is discussed (current clamp), followed by a technique to determine the ability of neurons to communicate with their neighbours via synaptic transmission (voltage clamp). Finally, a technique called calcium imaging that can be used to investigate the wider network functionality of electrogenic cells is discussed.

4.11.1 Whole-Cell Patch-Clamp Recordings

Conventional intracellular recording involves impaling a cell with a fine electrode; patch-clamp recording takes a different approach. To perform patch-clamping, a patch-clamp, which is a micro-electrode is a micro-pipette with a relatively large tip diameter, is placed next to a cell, and gentle suction is applied through the micro-electrode to draw a piece of the cell membrane (the 'patch') onto the micro-electrode tip, whereby the glass tip forms a high resistance 'seal' with the cell membrane [190]. This configuration is the "cell-attached" mode, and it can be used for studying the activity of the ion channels that are present in the patch of membrane; however, if more suction is applied, the small patch of membrane in the electrode tip can be ruptured, leaving the electrode sealed to the rest of the cell. This "whole-cell" mode allows for very stable intracellular recording and can be operated using the following electrical configurations. During patch-clamp measurements, cells are continually perfused with an Artificial Cerebrospinal Fluid (aCSF) containing (in mM) 130 NaCl, 2.5 KCl, 2.2 $CaCl_2$, 1.5 $MgCl_2$, 10 D-glucose, 10 HEPES-NaOH (pH 7.38; osmolarity adjusted to 290 mOsm), and additional drugs have been added to the aCSF in order to elicit different pharmacological responses from the cells. Inside the patch pipette a solution is used to mimic the intracellular medium, containing (in mM) 100 K-

gluconate, 17 KCl, 5 NaCl, 0.5 EGTA, 5 $MgCl_2$, 4 K_2-ATP, 0.5 Na_3-GTP, 20 K_2-creatine phosphate, 10 HEPES-KOH (pH 7.28; osmolarity adjusted to 280 mOsm). Recordings are performed with an Axopatch 200B amplifier (Molecular Devices, USA) under the control of Clampex 10.1 software (Molecular Devices, USA).

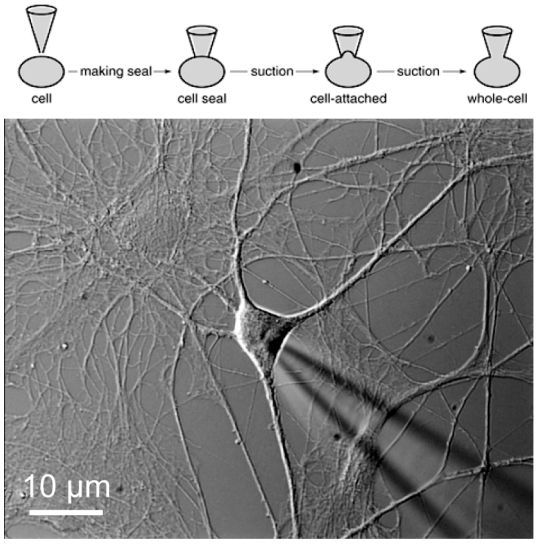

Figure 4.7: Diagram and Micrograph of micro-electrode in the whole-cell patch-clamp configuration with a murine hippocampal neuron used in this study (micro-electrode is out of the focal plane, entering the image from the bottom-right hand corner).

4.11.1.1 Current Clamp

Current clamp measurements can be used to assess the intrinsic excitability or neurons, or more specifically, determine the ability of neurons to fire action potentials. An action potential is the sudden rising (depolarisation) and falling (hyperpolarisation) of the cell membrane potential caused by ionic flux across the cell membrane, which is evoked by the application of a sufficiently depolarising voltage (threshold voltage) or current inside of the cell (Figure 4.8a) [190]. Following a threshold depolarisation, an action potential propagates through the cell, which plays a central role in intracellular communication. The current clamp technique can record action potentials by recording the membrane potential of a neuron whilst simultaneously injecting current into the

cell through the recording electrode [191]. The membrane potential is free to vary and the amplifier records whatever voltage the cell generates; either by intrinsic currents (e.g. synaptic currents) or extrinsic currents such as stimulating currents injected by the experimenter. To perform current clamp measurements, square waves of (extrinsic) current are injected into the cell via a patch-pipette at physiological amplitudes and durations in order to mimic the currents produced by synaptic inputs, and the resulting train of action potentials is recorded (Figure 4.8b). In order to eliminate unwanted intrinsic currents from neighbouring cells caused by neurotransmitter release, three receptor antagonists are added to the aCSF perfusion: NBQX and D-APV, (see below) to block excitatory stimuli and bicuculline, to block inhibitory stimuli (N.b. Na^+/K^+ ion channels are not blocked). Providing the injected current is very small (e.g. physiological) as to not cause a significant voltage drop across the recording electrode resistance, the measured potential is well approximated to the membrane potential. For functional neurons, by varying the duration and amplitude of current injections, the frequency of the elicited train of action potentials can be used to assess the neuron's intrinsic excitability.

NBQX = 2,3-dihydroxy-6-nitro-7-sulfamoyl-benzo[f]quinoxaline-2,3-dione. AMPA receptor antagonist.

D-APV = D-2-amino-5-phosphonovalerate. NDMA receptor antagonist.

Bicuculline = $GABA_A$ receptor antagonist.

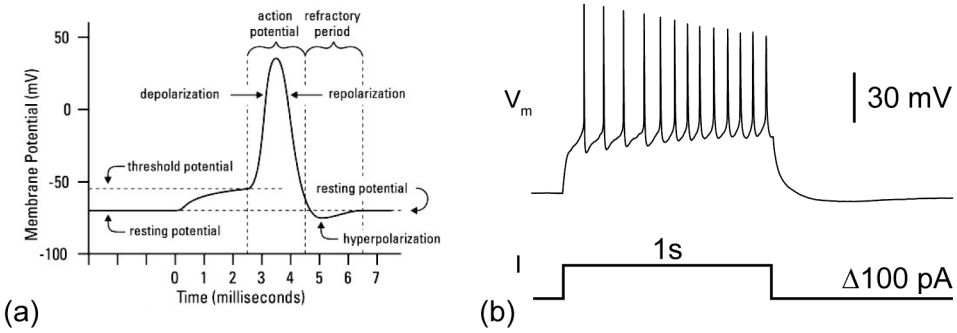

Figure 4.8: a) Diagram of the action potential of a neuron caused by a threshold depolarizing voltage. Adapted originally from [192] b) An example of action potential trains elicited from current clamp recordings on hippocampal neurons.

4.11.1.2 Voltage Clamp

Voltage clamp measurements differ from current clamp measurements in that membrane potential is held fixed. It does not mimic a process found in nature, however it allows the measurement of currents across ion channels or synaptic transmission events. By pharmacologically inhibiting action potential generation in neurons with tetrodotoxin (TTX: blocks sodium channels), voltage clamp measurements can be used to record the miniature Excitatory Post-Synaptic Currents (mEPSCs) that occur at synapses due to the spontaneous, random release of neurotransmitter vesicles by the presynaptic cell, even in the absence of stimulation (Figure 4.9a) [190]. The presence of mEPSCs in voltage clamp recordings is indicative of neurons that have developed synaptic connections with their neighbours, and multiple mEPSCs summate to cause a depolarising threshold voltage to evoke action potentials in cells. Voltage clamping works by continually adjusting the membrane potential (V_m) to a command potential set by the experimenter (usually at the resting potential, -70 mV) [191]. To do so, V_m is continually monitored and current proportional to the potential difference is injected into the cell to keep V_m at the desired value. Measuring this current against time gives mEPSCs (Figure 4.9b).

Additionally, the membrane/input resistance (R_{in}) and capacitance (C_m) of cells, which are informative on the nature of passive ion channels in cell membranes and determine the time course and distance of changes in membrane potential, can be measured using the voltage clamp configuration (Membrane Test [193]). By applying a small hyperpolarisation (5 mV) from a command potential of -70 mV, voltage-gated ion channels remain closed and only passive capacitive currents are measured. C_m is obtained by fitting a monoexponential to the decaying current to obtain its RC time constant, τ, and dividing it by the patch access resistance (R_a). R_a is obtained from the initial current, then R_{in} is obtained from the steady state current by $\Delta I=\Delta V/(R_a+R_{in})$.

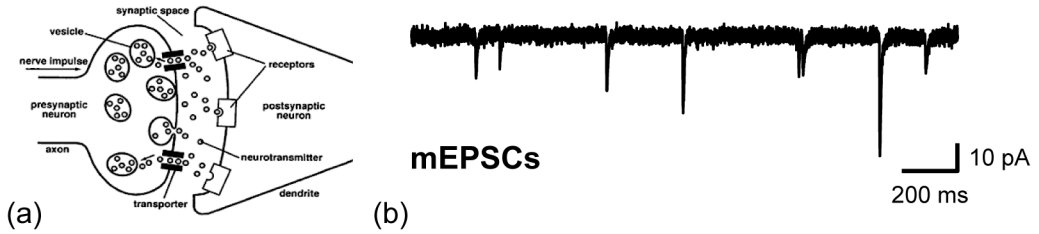

Figure 4.9: a) Schematic diagram of a neuron synapse where mEPSCs are generated in the postsynaptic neuron via spontaneous neurotransmitter vesicle release by the presynaptic neuron. b) Example of current vs. time recorded in the voltage clamp mode showing quantal mEPSCs.

4.11.2 Calcium Imaging

Intracellular calcium plays a vital role in synaptic intercellular communication. Upon depolarisation of a presynaptic terminal, extracellular calcium enters into the cell through voltage gated calcium channels and binds to calcium-sensitive proteins, which in-turn release neurotransmitter vesicles into the synaptic cleft [190]. As a result, the spatial and temporal distribution of calcium in cells closely matches the synaptic activity of neurons, and therefore can be used as an electrical activity indicator over a neuronal network by using intracellular calcium-sensitive dyes. Fura-2 is such a dye [194], and allows the accurate measurement of intracellular calcium concentrations. It is a chelator of calcium and, upon binding with calcium, undergoes a change in its fluorescent excitation spectrum in relation to the calcium concentration of the surrounding medium. Taking the ratio of emission intensity at 510 nm for 340 nm and 380 nm excitation wavelengths, the concentration of intracellular calcium can be measured (Figure 4.10). The ratio-metric readout of Fura-2 automatically cancels out certain variables such as local differences in Fura-2 concentration or cell thickness that would otherwise lead to artefacts when attempting to image calcium concentrations in cells. For intracellular imaging, Fura-2 is added in a non-chelating form of Fura-2-acetoxymethyl ester (Fura-2AM) that renders it lipophilic to allow easy entrance into the cell. Once inside the cell, cellular esterases remove the acetoxymethyl groups, regenerating the Fura-2 indicator.

In this thesis, calcium imaging has been used to study calcium waves shuttling across cultured neuronal networks. To induce shuttling action potentials across neuronal networks, cells are pharmacologically put into in an epileptic state by perfusion with bicuculline (to stop $GABA_A$ inhibitory signalling and glycine as a co-agonist of NMDA receptors. To perform calcium imaging measurements, neurons at DIV12 are incubated for 20 min with 2 µM Fura-2AM (Molecular Probes Inc., Eugene, OR), and perfused for 15 min with recording solution (in mM: HEPES, 5 (pH 7.35); KCl, 2.5; $CaCl_2$, 2; glucose, 11.1; NaCl, 126) to allow for the hydrolysis of Fura-2AM into Fura-2. Recordings are then taken using 50 µM bicuculline and 10 µm glycine in the recording solution. Fura-2 excitation (340 and 380nm) is achieved via a monochromator (Polychrom II, TILL Photonics, Martinsried, Germany) controlled by CellWorks (npi, Tamm, Germany) and emission is monitored via a photodiode (TILL Photonics).

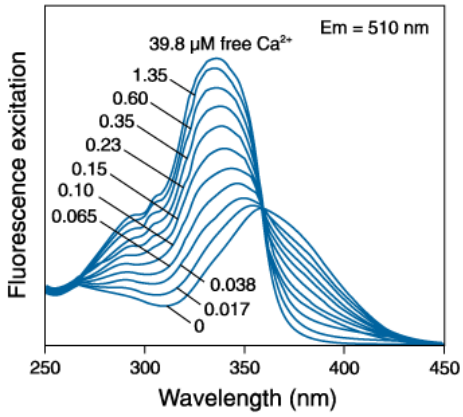

Figure 4.10: Fluorescence emission spectra vs. excitation wavelength of Fura-2 binding to different Ca^{2+} concentrations [195]. The ratio of emission at 340 nm and 380 nm excitation wavelengths gives the intracellular calcium concentration in neurons.

4.12 Plasma Processing: Plasma Enhanced Chemical Vapour Deposition and Reactive Ion Etching

Plasma Enhanced Chemical Vapour Deposition (PECVD) is a process that is used to deposit thin films on substrates. It consists of generating a plasma of

ionised reagent gases in a low pressure vacuum system in order to drive gas-phase chemical reactions that result in the deposition of reaction products in the solid phase in thin films onto substrates. Depending on the constituent precursor gases used in the plasma, different chemistries can be employed in order to deposit a wide range of materials, such as diamond and silicon-based thin films. Various methods can be used to generate plasmas for PECVD. Most simply, DC electric fields can be applied across reagent gases between parallel plate electrodes to create direct current glow discharge plasmas; however, when depositing insulating materials, discharges are quickly extinguished by the build up of insulating thin films. Instead, capacitively coupled discharges can be made using AC electric fields across parallel plate electrodes, or, furthermore, inductive discharges can be made using AC magnetic fields at microwave (MW) or radio frequencies (RF), which can be applied by AC currents in electric coils or by electromagnetic (EM) standing wave modes established in PECVD reactor cavities. (EM cavity modes can also be applied in electric modes). Inductively coupled plasmas are advantageous over capacitively coupled plasmas because the plasma discharge is completely separated from the applicator and the plasma does not make contact from the reactor chamber walls (or electrodes). This separation results in higher purity, less contaminated deposited films. In comparison to standard low pressure CVD processing, PECVD gives faster deposition rates at relatively lower temperatures with high quality films.

4.12.1 Microwave PECVD: Diamond

Diamond thin films can be deposited via a variety of methods including DC glow discharge PECVD and combustion flame CVD (etc.); however, hot-filament CVD and PECVD are the two most widely used methods [196]. Out of these two methods, hot-filament CVD was initially used by the diamond community due to its simple design, however, contamination of diamond films with filament material and subsequent improvements in PECVD technologies has lead to inductively coupled MWPECVD being the method of choice for depositing electronic-grade, high purity and high quality diamond films. MW plasma (2.45

GHz) is used instead of RF plasma because diamond PECVD requires a high density of reactive ion species with low kinetic energy to be conducive to diamond growth. At the resulting relatively high pressures required (10-100 Torr [197]), RF plasmas tend to form unstable and localised plasmas due to the reduced mean free path of electrons and, because of the lower frequency of RF plasmas (13.56 MHz), ions have higher kinetic which would not grow but etch and graphitise a diamond surface.

Diamond is deposited by MWPECVD using the precursor gases of methane and hydrogen to build up carbon atoms in a piecewise fashion into thin films of diamond. Methane (CH_4) serves as a carbon additive and, once ionised into methyl radicals ($CH_3\cdot$), attaches onto tetrahedral carbon (diamond) templates (e.g. diamond substrates or other materials seeded with diamond nanoparticles (see section 4.2)) to build up diamond (Figure 4.11). For every sp^3-bonded carbon deposited, many non-diamond graphitic allotropes of carbon are also deposited, hence, hydrogen is added to the gas mixture (ca. 99 %) to selectively etch non-diamond carbon and also catalyse the attachment of methyl radicals to the H-terminated diamond surface [27]. Hydrogen also plays the important role of preventing graphitic surface reconstruction by satisfying the dangling sp^3 bonds of diamond. For a full discussion on diamond growth mechanisms the reader is referred to the following review [198]. Other gases (e.g. O_2, CO_2, N_2, Ar, etc.) can be added to the gas mixture to effect growth properties [81] (e.g. re-nucleation, growth rate, lower temperatures) and, in particular, dopant gases (trimethylborane (TMB), $B(CH_3)_3$; diborane, B_2H_6; etc.) can be added to introduce dopants into the diamond lattice. Single crystal diamond can be grown using homoepitaxy on existing diamond substrates, or crystalline diamond can be grown via heteroepitaxy, where diamond is grown on other materials using diamond nucleation strategies such as mechanical abrasion/scratching, seeding, electrical biasing, covering/coating, ion implantation, pulsed laser irradiation or carburization, as reviewed in [81,170].

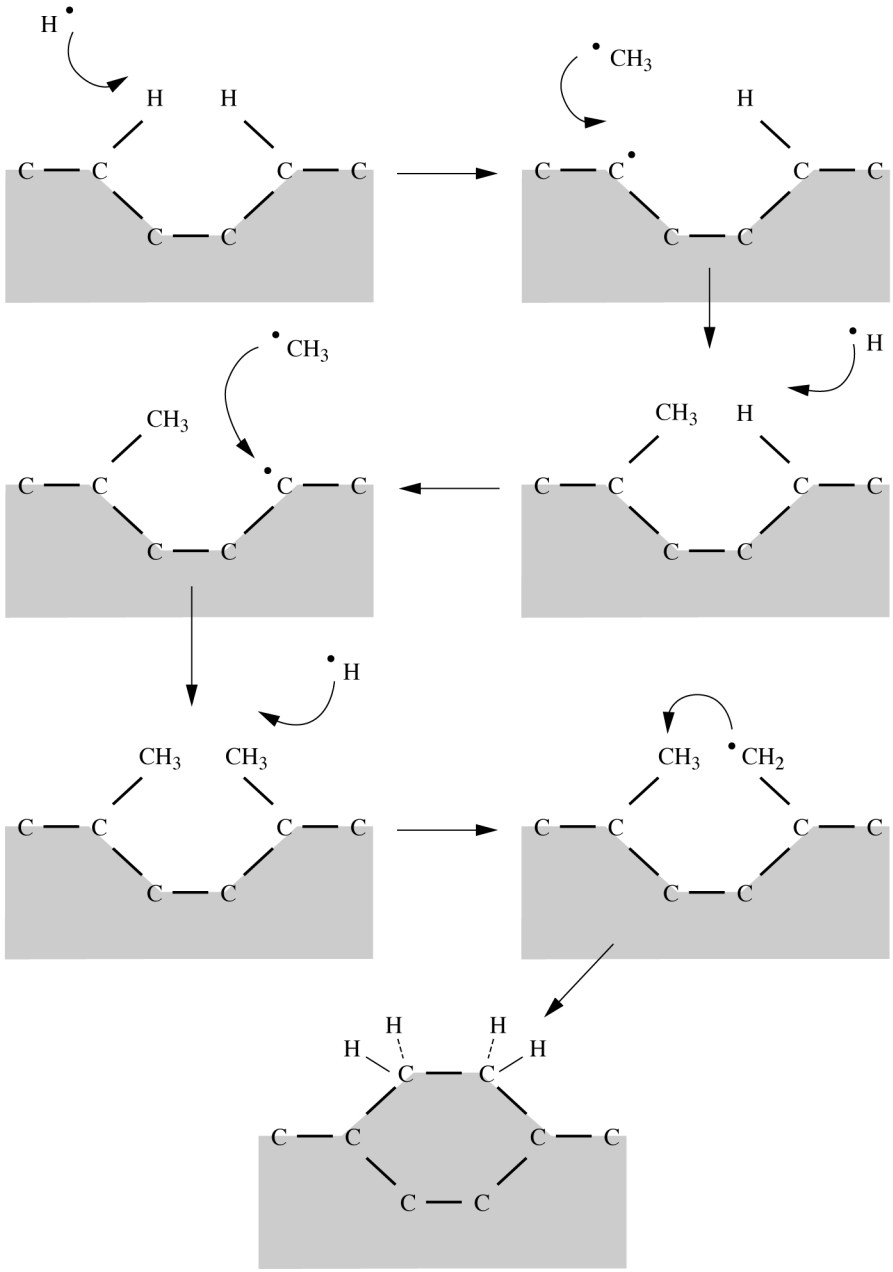

Figure 4.11: A stepwise schematic of the reactions that take place at the diamond surface that lead to diamond deposition [32].

Diamond is typically grown using MWPECVD and two major classes of reactors exist: NIRIM type reactors and ASTeX-type reactors (Figure 4.12a,b,c&d). NIRIM reactors generate plasma by setting up electric field modes in a fundamental mode rectangular MW waveguide, wherein a quartz tube reaction chamber (ca. 2 inch diameter) is positioned so that the electric field is at a maximum over the growth substrate and precursor gases [31]. ASTeX-type

reactors differ from NIRIM reactors in that the electric field modes (TE_{01}) of the MW waveguide are converted into magnetic modes (TM_{01}) using an applicator [199], and directed down into a EM cavity containing a quartz reaction chamber designed to support one large mode over the substrate holder, thereby allowing larger areas of deposition (ca. 4 inch diameter). In both reactor types, tuning stubs are used to minimise reflected power. Thereafter, both reactor types operate in the same format. A typical PECVD process is performed by initially flowing precursor gases (except the carbon additive) into a vacuous reaction chamber via mass flow controllers, whereupon the gas mixture is maintained at the desired pressure by throttle or butterfly valves and backing pumps. Following gas stabilisation, the magnetron MW generator is powered up to ignite a non-growing plasma for a short time until the substrate has increased in temperature (>600˚C), or a substrate heater can be used, whereupon methane is added into the gas mixture and diamond is deposited for the desired length of time (growth rate ~ μm/hr). After shutting off the power, samples are left to cool in hydrogen, after which the chamber is pumped down to base pressure, vented, and the sample is removed. For a high purity diamond deposition, reaction chambers are evacuated using a turbo molecular pump to pressures of ca. 10^{-7} Torr. In this thesis boron-doped layers have been deposited using a NIRIM reactor and intrinsic diamond layers with ASTeX AX2050 or Seki Technotron Corp AX5010 reactors.

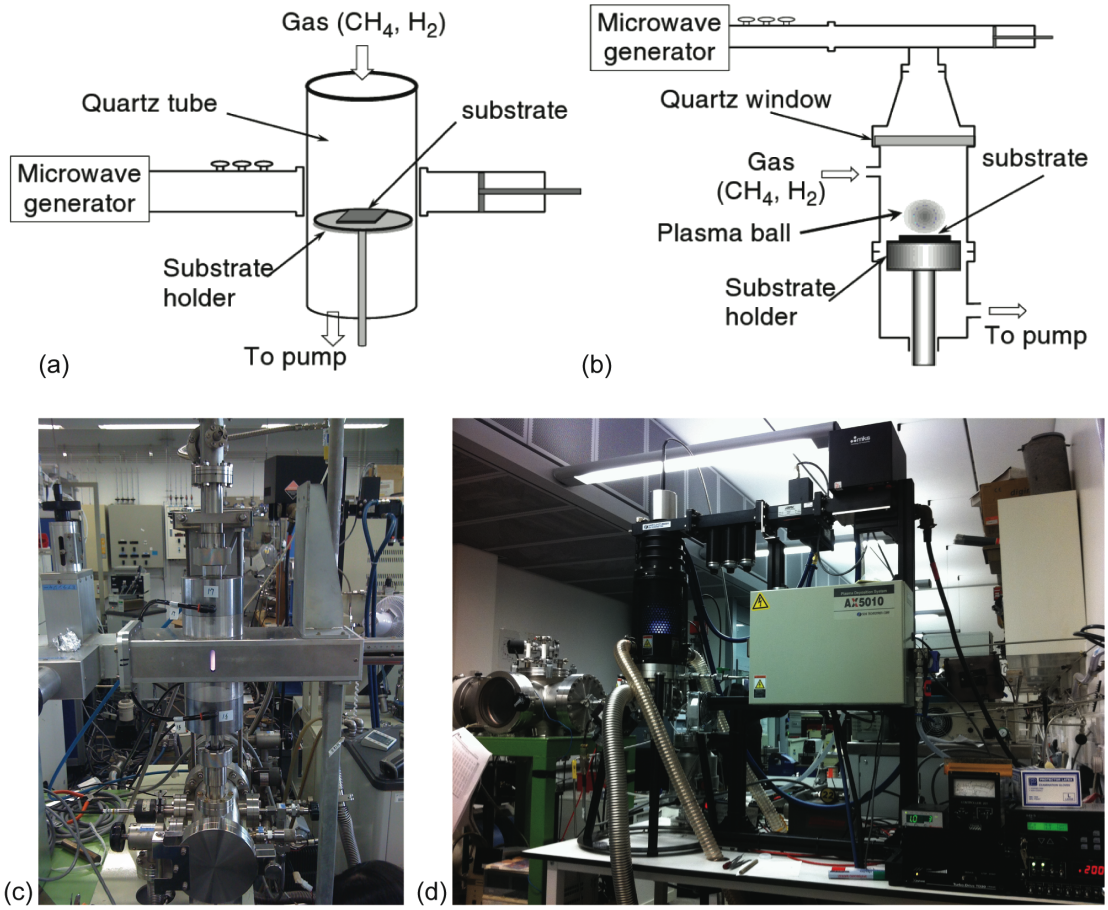

Figure 4.12: a) Schematic* and c) image of NIRIM reactor. b) Schematic* and d) image of ASTeX AX5010 reactor. *[200].

4.12.2 Radio Frequency PECVD: Silicon Dioxide and Silicon Nitride

Silicon dioxide (SiO_2) and silicon nitride (Si_3N_4) films can be deposited using AC glow-discharge PECVD, where an RF frequency is applied between parallel plate electrodes to ionise the precursor gas molecules. For silicon nitride films in particular, RF frequencies of 13.56 MHz result in films with high tensile stress; however, by intermittently switching to lower frequency plasmas of 380 kHz, tensile stress can be counteracted with compressive stress, resulting in an unstressed film [201]. This works due to the lower frequency of the plasma being sufficient to significantly accelerate not only dissociated electrons but massive ions as well. Massive ions are bombarded into the substrate causing a higher ion density in the film, thereby introducing a compressive stress into the film. With the correct interspersion (duty cycle) of high and low frequencies, film stress can

be minimised. Silicon PECVD chambers are devised so that the top electrode incorporates a showerhead that perfuses and heats precursor gases evenly across the substrate. Such rigorous application of precursor gases is applied because the heat and stoichiometry are determinant on film stress; hence, the bottom electrode is also heated. SiO_2 is deposited using silane (SiH_4), nitrogen (N_2) and nitrous oxide (N_2O). Si_3N_4 is deposited using SiH_4, N_2 and ammonia (NH_3) precursors. These materials have been used for MEA passivation in this thesis, and have been deposited using an STS Multiplex PECVD reactor.

4.12.3 Reactive Ion Etching

The experimental setup of Reactive Ion Etching (RIE) shares many similarities with PECVD (see section 4.12.2), in that precursor gases are feed into a pressure controlled vacuum chamber and a plasma is generated above the substrate, except, instead of the plasma depositing materials, the chemistry and conditions of the plasma are setup to be conducive to etching. Firstly, the precursor gas reactions are designed to result in surface reactions that produce volatile reaction products, thereby chemically etching the surface and contributing an isotropic etch process to RIE. Secondly, physical etching occurs due to ion bombardment on the substrate surface. This occurs due to the RF frequency of the plasma creating a DC voltage bias between the plasma and substrate from the accumulation of accelerated electrons on the platen (bottom) electrode. The accumulated charge and voltage bias on the platen accelerates positive, massive ions across a sheath region into the substrate, enhancing anisotropic RIE [197]. The balance of chemical and physical etching mechanisms can be controlled by the stoichiometry and pressure of the precursor gases (e.g. for diamond etching; O_2/Ar chemical/physical). RIE differs from PECVD in that the substrate is cooled (by backside helium gas), rather than heated, and the substrate stage is nearer the plasma in order to produce a larger sheath potential at the substrate surface. RIE can be performed using 1) capacitively coupled plasmas (CCP) via parallel plate electrodes, which have operational pressures of 5-500 mTorr, low ion densities and the RF power determines the ion density and

energy, or 2) by wound coils to produce inductively coupled plasma (ICP). ICP RIE shares the advantages of ICP PECVD whereby plasmas are generated away from electrodes and reactor walls, and has additional advantages for RIE processing: For quality RIE processing a high ion density (high etch rate) and low pressure (less ion collisions for better anisotropy) is desirable. ICP RIE ionises atoms throughout the plasma leading to higher ion densities, allowing lower pressure plasmas (1-100 mTorr). Furthermore, ion density can be controlled by the RF coil power source independently of ion energy, which can be increased by an RF platen power source to increase ion bombardment. In this thesis, both CCP and ICP RIE have been used to etch silicon-based and diamond films respectively (Oxford Plasma Technology RIE80; STS ICP RIE + load lock (Figure 4.13a,b)). Prior to all processes, reactors are given preconditioning runs to improve plasma stability and etching results.

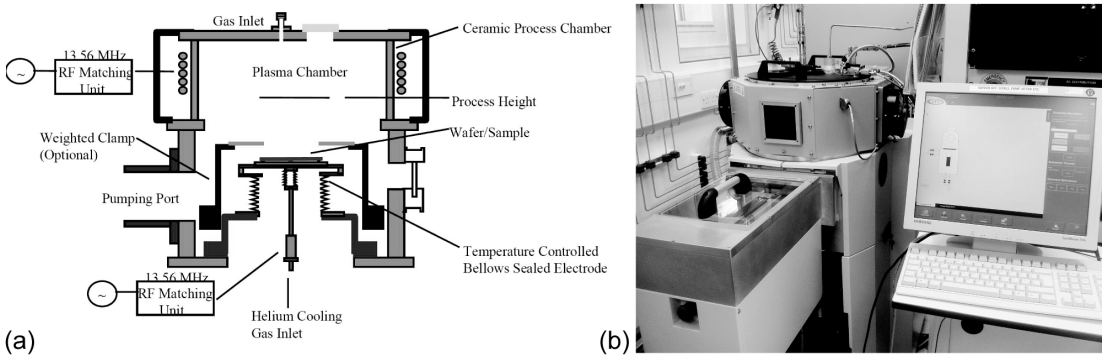

Figure 4.13: a) Schematic of STS ICP RIE [202]. b) STS ICP RIE and controller.

4.13 Metallisation

Metallisation refers to the thin film deposition of metals on other substrates. It can be used in conjunction with photolithography (see section 4.14) to deposit patterned metal films. In this thesis, two methods of metallisation have been used:

4.13.1 Thermal Evaporation

Thermal evaporation consists of vapourising a charge metal and depositing it onto a target substrate. Under high vacuum ($\sim 10^{-7}$ mbar), metals such as gold or chrome are evaporated (preferably via sublimation) using resistive heating elements made of high melting point refractory metals [203]. For different charge metals, different heating element shapes are used, such as spirals and basket filaments made of tungsten, or boats made of molybdenum. Upon evaporation, metal particles travel in a line-of-sight towards a target substrate suspended up side down above the charge metal. Colliding with the substrate, metal vapours condense and, over a short period of time, build up thin metal films [204]. The rate of metal evaporation, and thereof deposition, can be controlled by the amount of current passing through the element and monitored by a quartz crystal microbalance. Absolute control is also possible by intermediary shutters between the heater and sample inside the vacuum system. In the course of this thesis, thermal evaporation has been used when the electrical properties of the metals (Au, Cr, Al) are not of consequence to their application, e.g. hard masks for reactive ion etching, using an Edwards Thermal Evaporator II Bell Jar A306.

4.13.2 Electron Beam Evaporation

Electron Beam (E-beam) Evaporation works in a similar manner to thermal evaporation, except a focused high-energy electron beam is used to evaporate the charge metal instead of a heated filament [204]. Only a small spot on the charge metal is heated directly, avoiding heating of the supporting material, thereby minimising contamination of deposited films with filament material. Contamination is further reduced by the E-beam filament being located out of line-of-sight with the target by 270°, and electromagnets are used to bend the E-beam onto the charge metal [205]. As a result, higher purity films can be achieved, evaporation rates are easily controlled via E-beam current and lower vapour pressure metals can be deposited. In this thesis, E-beam evaporation has

been used to deposit titanium, which has been used as an adhesion layer and to impart Ohmic contacts to boron-doped diamond electrical contacts. Whilst titanium can be deposited using either E-beam or thermal evaporation, E-beam evaporation has been used over thermal evaporation due to titanium having a high melting point [203] and being prone to forming alloys with tungsten. Furthermore, E-beam evaporation produces better lift-off results and higher quality films for electrical contacts. Metal films have been deposited using an Edwards A500 Electron Beam Evaporator. This machine employs a rotating substrate holder to improve deposition uniformity.

For metal contacts with titanium adhesion layers, an annealing process is applied to induce carbide formation with the substrate, which increases adhesion strength and imparts Ohmic properties to the metallised contacts [206]. Annealing is performed in a low pressure hydrogen atmosphere via a heating element connected to a power source.

4.14 Photolithography and other device fabrication techniques

The transfer of patterns in microelectronics is commonly achieved using photolithography (PL). In brief, PL involves the creation of stencils from UV-photosensitive polymers (photoresists) that have been spin-coated onto substrates. The resulting stencils can be used as masks for the etching or patterning of deposited materials. Whilst exact protocols differ between photoresists, a typical process flow for PL is:

1. Dehydration bake: substrates are heated in an oven or on a hotplate at 150-200˚C to drive off adsorbed water.
2. Hexadimethyldisilazane (HDMS): an adhesion promoter. Can be applied by spin coating or atmospheric vapour deposition.
3. Spin coating: serves to spread the resist evenly across the substrate, and final spin speeds are typically in the order of thousand revolutions per minute

(rpm). Initial ramping steps at lower rpm are commonly used to initially disperse the resist. Higher spin speeds equal thinner resist.

4. Softbake: spun resist is heated to evaporate the remaining solvent in the resist.
5. Exposure: quartz or glass patterned with chrome serves as a stencil, or mask, for UV light exposure of the resist. UV exposure causes chemical changes in the resist according to its resist type. For 'positive' resists, exposed regions are removed during development, and vice versa for negative resists. To accurately transfer the mask pattern into the resist, the substrate is pressed closely the metallised side of the mask and then exposed to the appropriate dose of UV light.
6. Post Exposure Bake (PEB): Used for particular resists to counteract standing wave effects (localisation of photosynthetic chemical products) during exposure of thicker resists and reduce mechanical stress.
7. Development: developer chemicals are used to remove non-crosslinked areas of the resist pattern. Developers based on NaOH or KOH bases can be used, however, due to metal ions being detrimental to CMOS technologies, metal-ion free developers such as MF 26-A (containing tetramethylammonium hydroxide (TMAH)) are more commonplace in today's clean rooms.
8. Postbake: Optional. Heating the patterned resist hardens it for applications such as reactive ion etching, and can cause resist reflow that reseals small fractures.

Patterned photoresist can subsequently be used for subtractive or additive processing. Subtractive processing includes post PL processes such as wet chemical etching of metals or reactive ion etching. Additive processing is embodied by lift-off processing, wherein metal is deposited after PL and 'lifted-off' with the resist-covered regions, leaving the exposed substrate regions coated with metal. Lift-off can also involve a non-UV sensitive lift-off resist (LOR) deposited prior to the standard photoresist. During the development step, the LOR is over-etched to give an overhang sidewall profile that gives separation between the metals deposited on the resist and substrate surfaces, facilitating lift-off. In this thesis, titanium has been patterned using lift-off processing

because it forms carbides with diamond during metallisation. Lift-off processing only deposits metals on the substrate in their intended destinations (unlike wet chemical metal patterning), avoiding carbide formation on other areas of substrates. Following post PL processing, photoresists can be removed with acetone (sonicated for 5 mins) and further cleaned with oxygen barrel ashing.

In this thesis, 3 photoresists have been used extensively. SPR 220-7 μm has been used as a thick resist for oxygen/argon reactive ion etching; SU-8 2002 as an epoxy passivation layer for SGFET and AZ5214 E Image Reversal photoresist for lift-off processing. Processing parameters for these photoresists are given in Table 10.2 in Appendix B. Quintel Q4000-6 and Karl Suss MJB3 Mask Aligner are used to align and expose samples.

4.14.1 Notes on small sample processing

During spin-coating, a common observation is the unwanted build up of photoresist at the outer-most edges of substrates. These edge beads are particularly pronounced for small samples (4 mm and below) and lead to poor photolithography due to non-uniform resist thickness and diffraction effects caused large contact separations during exposure. Edge beads are standardly removed using a long exposure and development (for positive resists) at the edges of samples prior to the patterning exposure; however, for applications such as source and drain contacts on 2 mm square SGFET, an unwanted periphery of metal contacts could cause short circuits in the device. Instead, edge beads can be reduced by using higher spin speeds (> 2000 rpm) and off-central axis spinning (where samples are stuck to larger wafers), which confines edge beads to one corner of the sample. AZ 5214 E has been used for lift-off on small samples because LOR resists gave large edge beads. As well as reducing edge bead size, diffraction effects can be reduced by using a small drop of water in between the substrate and mask to reduce diffraction in a similar fashion to an immersion lens.

Figure 4.14: a) Wet bench fume cupboards in LCN Class 1000 cleanroom. b) Quintel Q4000-6 Mask Aligner (Class 100 hood). c) Karl Suss MJB3 Mask Aligner (Class 100 hood). d) Hotplates.

4.15 Ozone Oxidative Treatment

At the surface of diamond at least one of the four bonds of carbon atoms are dangling bonds. Terminating these bonds with atomic functional groups avoids reconstruction of the diamond surface, and occurs naturally during MWPECVD growth due the presence of hydrogen radicals in the plasma. Hydrogen terminated diamond is conductive and, to suppress hydrogen-based

surface conductivity, diamond is commonly terminated with oxygen moieties via processes such as anodic oxidation, acid bath, oxygen RIE or ozone treatment. Ozone treatment has been used out of these methods due to its negligible etch rate (RIE would destroy δ-layers) and dry, convenient process. Ozone is a powerful oxidant due to its ready dissociation into O_2 and O. Ozone treatment has been performed by: 1) placing samples in a sealed chamber, UV ozone cleaner NL-UV253, 2) purging it with N_2 gas (5 mins), 3) filling with O_2 gas (5 mins) and, 4) generating O radicals (15 mg/h) by UV exposure (mercury lamp, λ 184.7 nm ($2\ O_2 \rightarrow O + O_3$) & 253.7 nm ($O_3 \rightarrow O_2 + O$)) for the desired length of time. The chamber is then purged with N_2 gas and the samples are removed. Alternatively, samples have been treated in a vacuum chamber connected to an ozone generator (10 g/h) for an equivalent length of time.

4.16 AC Hall Effect Characterisation

Understanding the nature of current flow in electronic materials is very important for making electronic devices. Current flow is the density of carriers crossing an area per second under an applied electric field.

$$I = qp\mu Ewt \tag{2.1}$$

Where I is current, q is elementary charge, p is (hole) carrier density, μ is carrier mobility, E is applied electric field, and w and t are the width and thickness of the cross-sectional area of the conductor. If one considers two materials, for example, material 'A' with a high p and low μ, and material 'B' with a low p and high μ, these two materials would make characteristically very different electronic devices (A: slow responses and low mutability to gate voltage changes, B: vice-versa); however, for $p_A\mu_A=p_B\mu_B$, A and B would be indistinguishable by current measurements alone. The Hall Effect technique allows the contributions of carrier density and carrier mobility to be deconvoluted from current measurements, providing a very useful tool for the study of electronic materials.

Hall Effect works by applying a magnetic field perpendicularly through a material's conduction plane and flowing a current from one extremity to another [207]. As the carriers flow through the material and cut through the magnetic field, they are orthogonally deflected by the Lorentz force. This deflection causes an asymmetric distribution of charge through the sample that induces an electric field (E_y) and restoring force on the carriers. Reaching equilibrium, a potential difference is established perpendicular to the current direction, called the Hall Voltage (V_H). By measuring V_H, along with the resistance and current through the sample, the following derived formulas can be used to calculate p and μ of materials.

Firstly consider an x-y planar conductor with a current along the x-axis and magnetic field along the z-axis (B_z). The force along the y-axis on the moving charge, with drift velocity, $v_x=\mu E_x$, follows the Lorentz force [208]:

$$F_y = q\left(E_y + v_x \wedge B_z\right) \tag{2.2}$$

At equilibrium:

$$-E_y = v_x \wedge B_z \tag{2.3}$$

The measured hall voltage along the y-axis is:

$$V_H = -\int_0^w E_y \, dy = -E_y w \tag{2.4}$$

Combining Equations (2.3) & (2.4) gives:

$$\frac{V_H}{w} = v_x \wedge B_z \tag{2.5}$$

Then combining Equation (2.1) & (2.5), where $v_x=\mu E_{(x)}$, an expression for the carrier density (constructed from measurable or known variables) is obtained, where the sign of V_H determines the sign of the majority charge carrier in the material:

$$\frac{IB_z}{V_H} \cdot \frac{1}{tq} = p \tag{2.6}$$

Mobility can then be calculated using the resistivity, $\rho=\pi R/ln2$, of the sample, wherein R (resistance) is calculated using the four point probe method ($R_{12,34}=V_{34}/I_{12}$) [209]:

$$\mu_H = {}^{1}/_{pq\rho} \tag{2.7}$$

Where μ_H denotes the Hall mobility, which is the mobility of the sample under the assumption that scattering is energy-independent. To accurately obtain carrier mobility, μ_H must be divided by the hall scattering factor, r, which ranges from 1-2, however in this thesis r has been taken as unity due to the scattering mechanisms at play not being clearly identified in diamond.

To perform Hall Effect measurements, various electrode configurations can be used, consisting of either Hall Bar or Van der Pauw geometries (Figure 4.15a). Whilst Hall Bar geometries can have more reliable results, they require precise geometries and multiple processing steps (including mesa-etching), making subsequent device fabrication on the same sample very difficult; especially on small samples. Therefore, Van der Pauw (VdP) contacts have been used in this thesis. VdP contacts consist of 4 electrodes around the periphery of planar substrates. Arbitrary shaped samples can be used [210] and the precise positioning of electrodes is not necessary, making VdP a relatively easy method; however, the following theoretical conditions on the contacts and conductor must be met in order to reduce measurement error [209]: 1) The contacts are on the circumference of the sample. 2) The contacts are sufficiently small (c<<a, c/a<1/6; Figure 4.15a). 3) The sample is of uniform thickness. 4) The sample is singly connected with no holes. Experimentally, the contacts must be recessed from the edges of the sample to ensure surface conduction – not sample-edge conduction – is being measured. Triangular contacts (in the square geometry) can also reduce error [211]. Error can also arise whilst measuring V_H. Its value can be subject to drift, making precise measurements of V_H difficult. To counteract this, the direction of the magnetic field is switched every few seconds in a square wave, thereby changing the sign of V_H (AC Hall Effect). V_H can then be obtained by measuring half of the peak-to-peak amplitude of the resulting square wave of V_H. In this thesis, VdP triangular contacts (350 μm orthogonal sides,

Figure 4.15c) of titanium (20 nm) and gold (200 nm) have been deposited using lift-off photolithography (AZ 5214 E) (see section 4.13.2) at the corners of 2 mm square δ-doped diamond samples. Following annealing, samples have been stuck (with Crystalbond 509) onto glass slides with 4 large gold contact areas (Figure 4.15b), to which interconnects have been made using gold wirebonding (ultrasonic welding, Figure 4.15c). AC Hall Effect measurements have then been made using a Toyo Technica Resistest 8300 Hall Effect system.

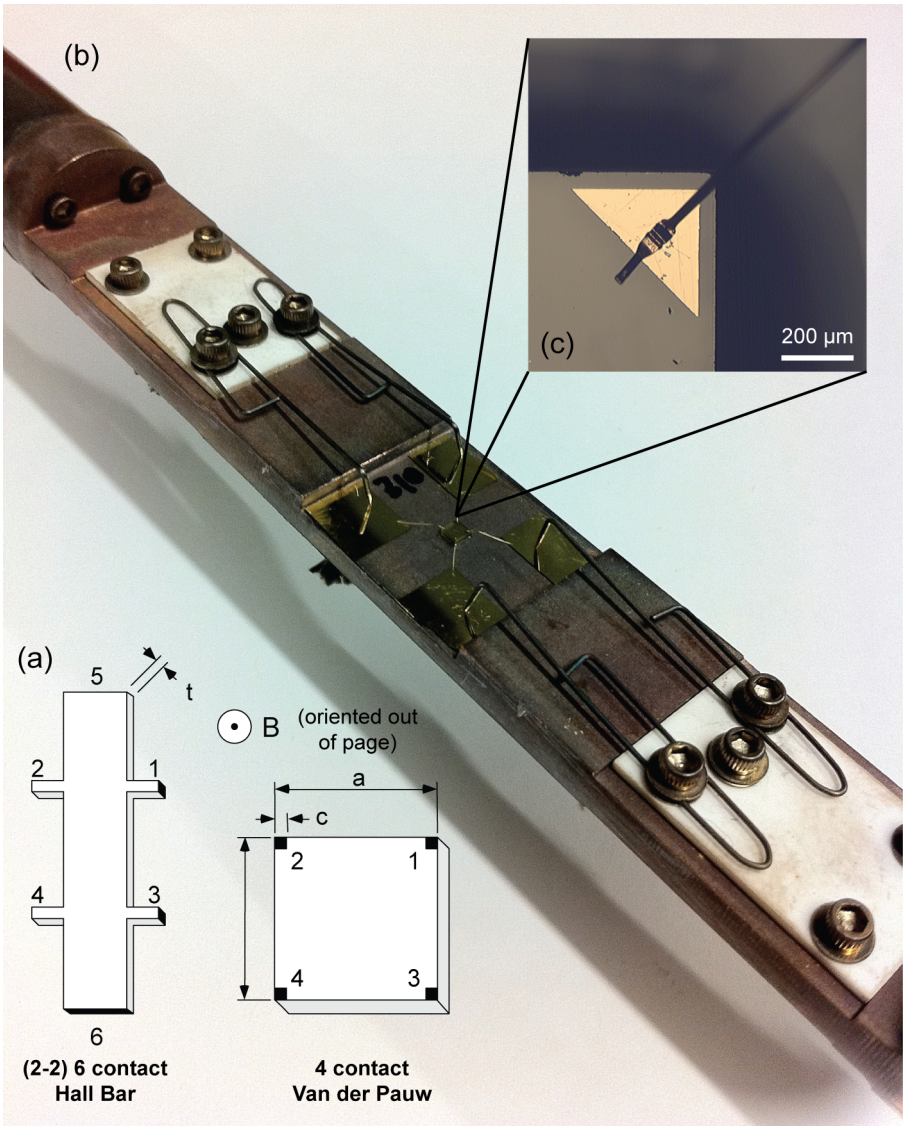

Figure 4.15: a) Diagram of Hall Bar and VdP standard configurations adapted from [209]. b) Sample mounted on glass slide onto Hall Probe in VdP configuration, with wirebonded interconnects to large contact pads for easier probe positioning. c) Micrograph of wirebonded sample.

4.17 Dielectric Impedance Spectroscopy

Whilst Hall Effect measurements allow an experimenter to investigate the fundamental properties of charge carriers in materials, Dielectric Impedance Spectroscopy (IS) can be used to investigate more idiosyncratic material properties, such as the crystallinity and interfacial properties of materials [212]. IS works by applying AC sinusoidal potentials of gradated frequency across materials and measuring the resulting phase-shifted currents. Dielectric properties such as capacitance can then be extracted from model fits to the real and imaginary components of measured impedance, which is made possible due to the inclusion of such terms in the formulated expressions of complex impedance (Z) for the material, which can be calculated (or approximated) from equivalent circuit models developed from the known structure and properties of the material. For example, consider a simple RC circuit (Figure 4.16a) that could represent an ideal dielectric material:

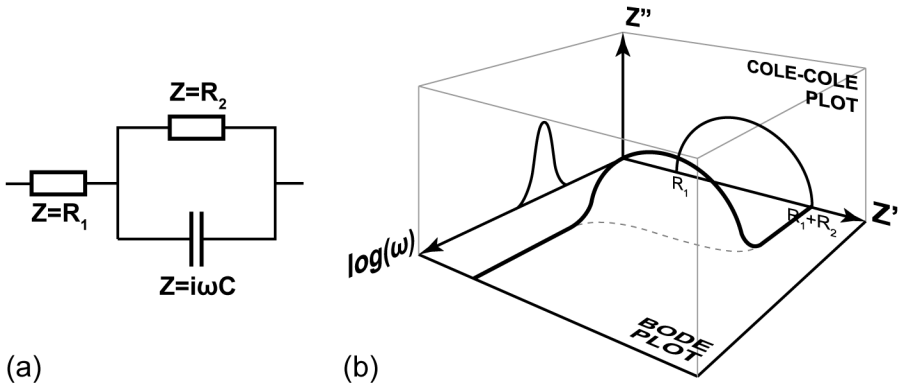

Figure 4.16: a) RC equivalent circuit diagram with reactances. b) Corresponding IS plot for RC circuit, showing the Cole-Cole, Bode and Z” vs log(ω) plots.

The sum of complex impedances and reactances for this circuit is:

$$Z(\omega) = R_1 + \left(\frac{1}{R_2} + i\omega C\right)^{-1} \tag{3.1}$$

Rearranging:

$$Z(\omega) = R_1 + \left(\frac{R_2}{1+i\omega C R_2}\right) \tag{3.2}$$

Separating into real and imaginary parts (Z' and Z"):

$$Z(\omega) = R_1 + \frac{R_2}{1+\omega^2 C^2 {R_2}^2} - \frac{i\omega C {R_2}^2}{1+\omega^2 C^2 {R_2}^2} \tag{3.3}$$

It can be seen Equation (3.3) follows the equation for a complex circle (Figure 4.16b), and by fitting circles to Cole-Cole complex impedance plots, values such as capacitance and resistance can be calculated. For $\omega=0$, $Z=R_1+R_2$; for $\omega \rightarrow \infty$, $Z=R_1$; and at the peak of the semi circle, $C=(\omega_{max}R_2)^{-1}$. If there is an inductive contribution to the impedance, this can be seen as loops in Cole-Cole plots. A common high frequency inductive effect in IS is the skin effect, and can be observed at high ω.

IS can also be used to investigate frequency and temperature dependent conduction in materials. Temperature dependence can be used to extract activation energy of impedance values, which is closely related to the activation energy of dopants in materials such as diamond.

$$\frac{\partial \ln(Z)}{\partial\left(\frac{1}{T}\right)} \cdot \frac{k_B}{q} = E_a \tag{3.4}$$

IS Frequencies of 0.1 to 10 MHz have been used, with 0.1 V_{RMS} applied voltage. In this thesis, IS has been used to investigate the temperature and frequency-dependent dielectric properties of δ-doped diamond conductive layers.

4.18 Micro-Electrode Array Recordings

Micro-Electrode Array (MEA) recordings have been performed by Vanessa Maybeck from Jülich, Germany, using a home-built, multipurpose amplifier system that allows for extracellular recording and stimulation from various chip types. The amplifier system consists of a standard main amplifier, a microprocessor, and a specific preamplifier depending on the chip type to allow for maximum flexibility. A BioMol MEA recording setup has been used. Signal-to-

noise ratios have been evaluated using signal peak-to-peak height vs. noise peak-to-peak height. Root mean square noise is not used because it does not embody and information applicable to biological measurements. MEA bandwidths are measured by applying a 4mV amplitude sine wave (1-10,000 Hz) to all 64 MEA channels simultaneously, and measuring the amplitude and phase shift of individual channels using the BioMol system. Bandwidths are then calculated using a cut-off frequency defined as:

$$A_{(v=v_{cutoff})} = \left(\frac{1}{\sqrt{2}}\right) A_{max} \tag{3.5}$$

Where A is amplitude and v is frequency.

4.19 Current-Voltage Characterisation

The relationship between the applied potential difference across an electronic device and the elicited current measured is called its current-voltage (I-V) characteristics. Typical I-V characterisation of a Field-Effect Transistor (FET) involves varying the drain-source voltage and gate-source voltage between the 3 terminals of an FET, and measuring the output currents. I-V characterisation has been performed using Labview controlled Keithley 2400 source and measurement units. For solution-based measurements, an Ag/AgCl reference electrode is used in phosphate buffered solution (PBS). Such an electrode has fast redox reaction kinetics and therefore high current can be passed through with high efficiency. The various analyses performed on I-V measurements have been accomplished using statistical routines in Excel and OriginPro software.

Chapter 5 The use of nanodiamond monolayer coatings to promote the formation of functional neuronal networks

5.1 Introduction

It is becoming increasingly clear that the interaction of nano-sized particles with living cells transgresses the framework laid down by previously known macroscopic interactions [94]. The excellent biocompatibility of diamond in different biological environments [105,132,213] and its excellent electrical properties [214] make this material a prime candidate for chronic electrical interfaces with neurons. Whilst nanodiamonds created by a detonation process have been available for some years [69], the primary particles, that have a size typically within the range 5-10 nm, aggregate during the formation process into particles with sizes on the micron scale. These particles have excellent electrical properties [75] but are not readily attached to substrate materials without complex chemical procedures. In contrast, recently developed techniques for the dispersion of the primary particles in solution [72,215], yield individual detonation ND particles and can be used to coat a given substrate by attachment through Van der Waals, electrostatic and polar forces without the need for hazardous chemical species or aggressive protocols.

Primary cultures of rodent neurons require a specifically treated surface for initial attachment and survival, and this is routinely provided by the deposition of extracellular matrix (ECM) proteins. Patterned deposition of ECM

proteins have been shown to direct ordered outgrowth of neurons on single-crystal diamonds [8], exemplifying the necessity of protein-coating for neuronal growth. Whilst protein coating is sufficient for *in vitro* experiments, *in vivo* implants, such as in neural prosthetics, will require biocompatible coatings that preferably will not introduce foreign proteins into the body.

Newly emerging biomaterials aim to mimic the physicochemical properties of ECM proteins and surrounding tissue, and the NDs' properties compare favourably to the metrics of modern biomaterials [102]. Their tissue-equivalence (carbon-based), non-cytotoxicity [76], versatile organic surface functionality [79], high affinity for protein adsorption [79] and their particle curvature and size [94,102] all present themselves as possible contributing agents to providing a nurturing environment for neuronal networks.

Given the outstanding properties of NDs, an easily implemented deposition of ND monolayers has been tested with regards to supporting functional neuronal network formation in the absence of ECM protein coatings. Here we show that ND layering is sufficient for promoting neuronal attachment and growth on four different substrate materials. Neurons grown on such ND coated materials display intrinsic electrical excitability, synaptic transmission and network function comparable to those grown under standard ECM protein coating conditions.

5.2 Experimental Methods

5.2.1 Chemicals

All chemicals were from Sigma (St Louis, MO), Tocris (Tocris Cookson Ltd, Avonmouth, UK) or Invitrogen (Carlsbad, CA), unless stated otherwise. Nanodiamonds were supplied prepared in solution by Dr Oliver A Williams (Fraunhofer Institute for Applied Solid State Physics, Freiburg, Germany) using a method described previously [215] from commercially available ultra-dispersed detonation nanodiamonds (New Metals & Chemicals Corporation, Japan).

Coatings were created by ultrasonication of the ND solution (0.05 g/L of NDs) in bath containing the substrate material for 10 min (excess time). Glass (Cover glass, VWR, UK), Silicon Si(100) p-type, commercially available polycrystalline diamond substrates (Element Six Ltd) and nanocrystalline diamond (NCD) grown by the team led by Dr Philippe Bergonzo at CEA-LIST (Saclay, France) were cleaned using a Piranha etch and rinsed in deionised water before use. In the case of the diamond substrates, strongly oxidizing solutions were used which are known to leave a contaminant free, oxygen terminated surface [216].

5.2.2 Primary Neuronal cultures

Murine hippocampal neurons were obtained at embryonic day 18, essentially as described in [217]. Cells were seeded in attachment medium (AM: MEM with Earl's salts and glutamine, 10 % fetal bovine serum, 33 mM glucose, 1 mM pyruvate) at 100,000 cells/cm^2. After 3-4 hours the AM was replaced with maintenance medium (MM, Neurobasal medium, 2 % B27 supplement, 2 mM GlutaMAX-I, 100 U/ml penicillin, 0.1 mg/ml streptomycin, 33 mM glucose). Cultures were kept for up to 12 days *in vitro*. All animal work was undertaken under the auspices of the UK Home Office Project and Personal Licenses held by the authors in their designated laboratories. For full details see section 4.3.

5.2.3 Immunochemistry and Imaging

Samples were fixed with 4 % paraformaldehyde / 4 % sucrose in phosphate buffered saline (PBS; 137 mM NaCl, 2.7 mM KCl, 10 mM Na_2HPO_4, 2 mM KH_2PO_4) for 10 min, washed with PBS before permeabilisation of cells with 0.2 % TritonX-100 in PBS for 10 min. After 1-2 hrs in blocking solution (BS: 5 % horse serum in PBS) samples were incubated for 1-2 hrs with primary antibodies (mouse anti-MAP2, Chemicon, MAB364, 1:500 in BS; rabbit anti-GFAP, DakoCytomation, Z0334, 1:500). F-actin was stained for 10 min at RT with 2 U/ml rhodamine-phalloidin (Molecular Probes R415) and nuclei for 5 min at RT with Hoechst 33258 (Molecular Probes, 1 µg/ml in PBS). Samples were washed

repeatedly and incubated with secondary antibody (Cy2- and Cy5-conjugated goat anti-mouse IgG, Jackson; 1:300, 115-095-003 and 115-175-003, respectively) for 1 hr. Samples were washed with PBS, and stored at 4°C in sterile-filtered PBS till imaging or mounted after wash in Gelmount (Sigma). For full details see section 4.5.

Confocal microscopy was performed on a Bio-Rad Radiance 2100MP Confocal Microscope with a 20x (Nikon, Plan Flour, 0.75) water-immersion objective using Bio-Rad Lasersharp 2000 software. Alternatively a Leica TCS SPE confocal microscope equipped with a 40x oil-immersion objective (Zeiss, ACS APO, 1.15) was used in combination with LAS AF software, V1.7.0. Areas for imaging were randomly chosen. 3 independent sets of experiments were performed.

5.2.4 SEM

After initial fixing as described above in section 5.2.3, the samples were post-fixed with 1 % glutaraldehyde in 0.1 M sodium cacodylate buffer adjusted to pH 7.3 with HCl (SCB), washed in SCB and then osmicated with 1 % w/v osmium tetroxide (OsO_4) in SCB for 45 min. After a 10 min wash in SCB the samples were dehydrated in a graded ethanol series (25, 50, 75 and 90 % EtOH), washed 3x 10 min with 100 % EtOH before critical point drying with CO_2 in a Polaron CPD 750 (Quorum Technologies Ltd., Ashford, UK). Once dry the samples were then sputtered with gold in an EMScope SC 500 (Emscope Laboratories Ltd., Ashford, UK) and images were taken with a JEOL JSM-7401F Scanning Electron Microscope (JEOL Ltd., Japan) using an accelerating voltage of 2 kV.

5.2.5 AFM

AFM measurements were carried out on a NanoScope V (7.0) controlled Dimension V Scanning Probe Microscope equipped with a XYZ Hybrid Scanner

(Veeco Instruments Inc., Mannheim, Germany), using aluminium-coated silicon AFM probes with a resonant frequency of 190 kHz (Nanoscience Instruments, Inc., Phoenix, USA). The AFM was operated in tapping mode with a VT-103-3K Acoustic/Vibration Isolation System and the VT-102 Vibration Isolation Table at room temperature in air. From the topographical data a first order plane fit was subtracted. Mean roughness was calculated using the following formula, where N is the number of data points and Z is the topographical data:

$$\frac{1}{N}\sum_{j=1}^{N}\left|Z_j\right| \tag{4.1}$$

5.2.6 FTIR

FTIR spectroscopy was performed on a Spectrum One Perkin Elmer FTIR Spectrometer in an N_2-purged sample chamber and instrumentation. Samples were prepared on 13 mm diameter CaF_2 windows by drop-drying concentrated ND solution on one side in a clean environment. Resulting layers were ca. 300 nm thick. Monolayers were not used due to the NDs' low IR absorption and resulting signal strength. Final spectra were acquired in transmission mode from 4000 cm^{-1} to 800 cm^{-1} for 10 minutes, only after water desorption had stabilised.

5.2.7 Electrophysiological recordings

Whole-cell patch clamp recordings were performed at room temperature from pyramidal neurons of hippocampal dissociated primary cultures as previously described [218]. In brief, cultures were continuously perfused with an aCSF containing (in mM): 130 NaCl, 2.5 KCl, 2.2 $CaCl_2$, 1.5 $MgCl_2$, 10 D-glucose, 10 HEPES-NaOH (pH 7.38; osmolarity adjusted to 290 mOsm). In current-clamp, NBQX (10 µM), D-APV (50 µM) and bicuculline (10 µM) were added to block excitatory and inhibitory synaptic currents; in voltage-clamp, tetrodotoxin (TTX, 0.5 µM) was used to block sodium currents. The intracellular solution contained (in mM): 100 K-gluconate, 17 KCl, 5 NaCl, 0.5 EGTA, 5 $MgCl_2$, 4 K_2-ATP, 0.5 Na_3-GTP, 20 K_2-creatine phosphate, 10 HEPES-KOH (pH 7.28; osmolarity adjusted to

280 mOsm). Recordings were performed with an Axopatch 200B amplifier (Molecular Devices, USA) under the control of Clampex 10.1 software (Molecular Devices, USA). Pipette resistance was 2-3 MΩ, series resistance was always below 20 MΩ, and differences in series resistances and holding currents were never statistically significant. In current-clamp, action potentials were elicited by injecting, via the patch pipette, 1 s-long rectangular pulses of current with 50 pA increments from 0 to 350 pA, every 20 s. For each neuron, the above protocol was repeated twice, and the average number of action potentials in the two trials was used to estimate the action potential frequency of a neuron. The rectangular pulses were delivered from a membrane potential of -70 mV, set by continuously injecting an hyperpolarising current; resting potentials (Vm) were, however, not significantly different between groups (-56.3 ±4.1 mV for LN/p-ORN coating vs. -56.8 ±0.9 mV for ND-coating, p = 0.93, unpaired two-tailed Student's t-test). Current-clamp recordings were filtered at 5 kHz and digitised at 40 kHz. Miniature excitatory postsynaptic currents (mEPSCs) were recorded at a holding potential of -70 mV over a period of 5 min, filtered at 2 kHz, and digitised at 20 kHz. mEPSCs detection was performed offline with Clampfit 10.1 software (Molecular Devices, USA) using a threshold crossing principle; detection level was set at -4 pA and raw data were visually inspected to eliminate false events; cells with noisy or unstable baselines were discarded. Further analysis was performed in Igor Pro 6.03 (Wavemetrics Inc., USA) using customised routines.

5.2.8 Calcium imaging

Fura-2 measurements were performed essentially as described in [219]. Cells at DIV12 were loaded for 20 min with 2 μM fura-2-AM (Molecular Probes Inc., Eugene, OR), and perfused for 15 min with recording solution (in mM: HEPES, 5 (pH 7.35); KCl, 2.5; $CaCl_2$, 2; glucose, 11.1; NaCl, 126) before taking photodiode (TILL Photonics, Martinsried, Germany) recordings. Formation of calcium waves was essentially achieved as reported previously [220]; bicuculline was used at a concentration of 50 μM in recording solution containing 10 μM of glycine. Fura-2 excitation at wavelengths of 340 and 380 nm via monochromator

(Polychrom II, TILL Photonics) was controlled by CellWorks Software (npi, Tamm, Germany). Emission data were recorded with CellWorks and analysed in Igor Pro Carbon V5.0.4B (Wavemetrics Inc., Lake Oswego, OR).

5.3 Results

5.3.1 Neuronal cell attachment on ND layers

Primary neuronal cultures were seeded onto glass, mechanically polished polycrystalline diamond (PCD), nanocrystalline diamond (NCD) and silicon (Si). All four substrates had been treated with monodispersed NDs in an ultrasonication bath to form a monolayer of NDs on the substrate surfaces. The resulting surface coatings promoted the attachment of primary murine neurons, which was absent on untreated substrate surfaces. Confocal microscopy of immunostained neuronal cultures showed comparable attachment on all ND-coated substrate materials (Figure 5.1, second column), confirming that it is the NDs themselves that are responsible for the successful attachment and growth of the neurons. None of the surfaces led to cell attachment and growth in the absence of the NDs (Figure 5.1, first column).

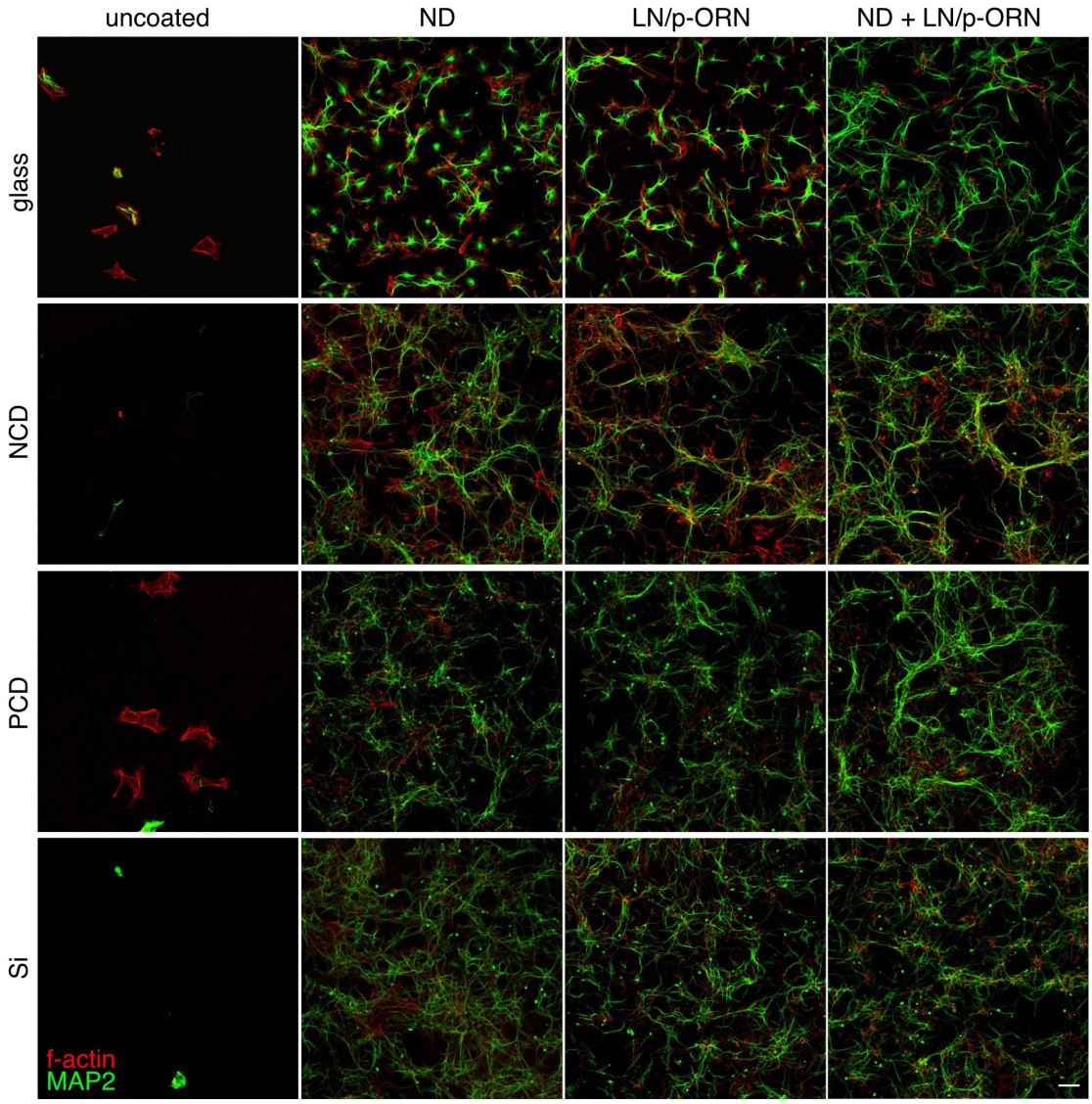

Figure 5.1: Neuronal growth on ND-coated substrates. Confocal analysis of growth of hippocampal neurons after 2 days in culture (DIV2). Substrates of glass, nanocrystalline diamond (NCD), polycrystalline diamond (PCD), and silicon (Si) were coated with nanodiamonds (ND) and/or laminin (LN)/poly-DL-ornithine (p-ORN); surfaces of uncoated substrates are oxygen terminated. Immunostaining reveals neurons via the dendrite-specific marker MAP2 (shown in green), while the cytoskeletal filaments of actin (f-actin) are stained for with rhodamine-phalloidin (red), highlighting structures rich in f-actin, such as growth cones at tips of neurites. ND-coating (2nd column) promoted neuronal attachment and outgrowth similar to conventional protein coating (3rd column), whereas the uncoated substrates displayed no significant attachment and growth of neurons, where only few cells of apparent non-neuronal origin can be detected (1st column). Scale bar: 50 µm. 3 independent batches of cultures and coatings were tested.

5.3.2 Substrate dependence of surface roughness following ND layering

Atomic force microscopy (AFM) was used to investigate the physical nature of NDs on the various substrate materials. AFM scans of the sample surfaces revealed nanoparticle structures on ND-coated surfaces in the range of 10-20 nm, which was comparable for all underlying substrates tested and did not vary substantially between different batches of ND solution used for coating (Figure 5.2a). The uncoated glass, PCD and Si surfaces were very flat with mean roughness of less than 2 nm. NCD was rougher than the other three materials with a mean roughness of approximately 8 nm. Coating the materials with NDs resulted in an increase in roughness on the glass, PCD and Si by 1.5-2 nm, whilst the NCD layer experienced a reduction in mean roughness by approximately 2 nm following ND coating. The NDs filled in and smoothed the roughness of the NCD substrate that had topographical features in excess of the ND particle size and increased the roughness of the flatter surfaces. Interestingly, all uncoated substrates showed only slight differences in mean roughness to their ND-coated equivalents (Figure 5.2c) and no clear correlation to neuronal attachment could be observed (see Figure 5.1 & Figure 5.5, first two columns). This suggests that the observed neuron adhesion and growth can likely be ascribed to other properties linked specifically to the NDs themselves.

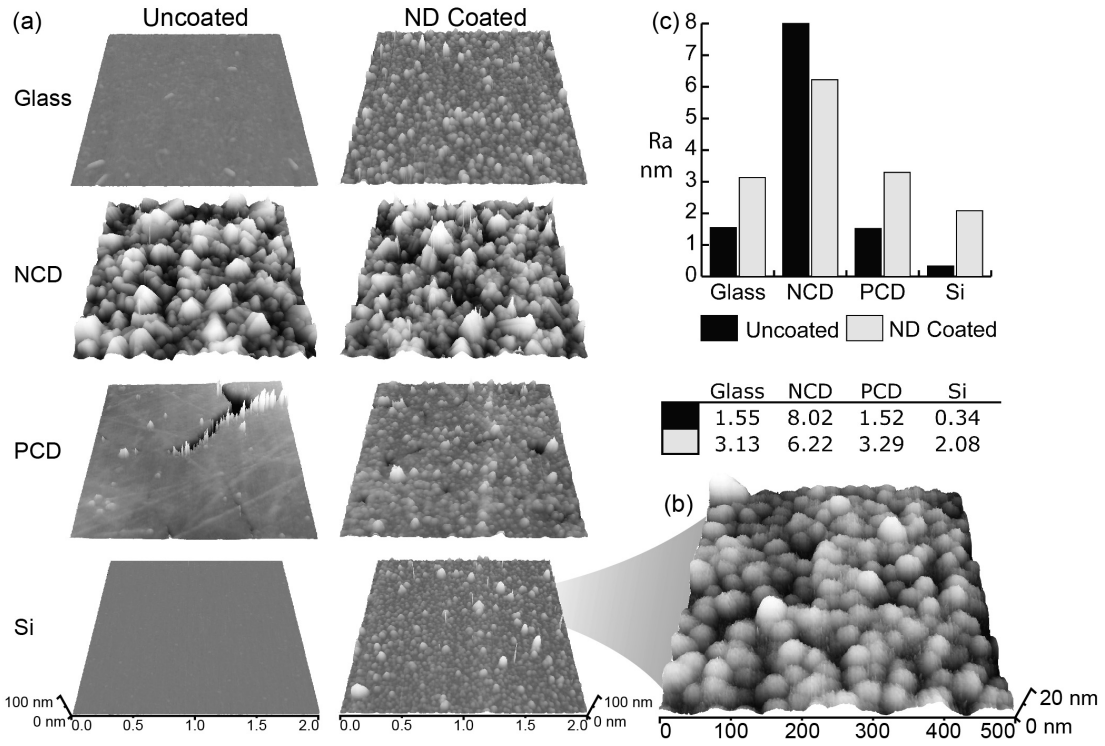

Figure 5.2: Surface roughness of ND-coated substrates that promote neuronal growth. a) AFM images of glass, NCD, PCD and Si surfaces with and without the ND coating. Scans are 2 μm x 2 μm sample areas and are presented in 25 % perspective. The scans are representative of the whole substrate areas and were selected at random over the entire substrate surface. Layer coverings of ND particles can be seen on all substrates. b) A random 500 nm x 500 nm area from the Si ND sample showed the ND layer to have particles ranging in size from 10 to 20 nm in diameter. Particle size was determined from the z-axis measurement in order to avoid AFM tip convolution effects. c) Mean roughness (R_a) data of the 500 nm square sample areas of all substrates for uncoated and ND coated samples.

Fourier Transform Infrared (FTIR) Spectroscopy was used to determine the chemical nature of the surface of the NDs used in this study (Figure 5.3). Spectra showed the NDs to have a mixed functionalisation with weak C-H_x, stronger C-O and C=O groups and adsorbed water appearing as marked in Figure 5.3. The presence of C-O and C=O groups indicated that the NDs are in a partially oxidised state, which is favourable for high-affinity protein adsorption [79]. Peak

values were ascribed with reference to literature values [221-225] with consideration given to sample nuances and peak shifts due to material phase.

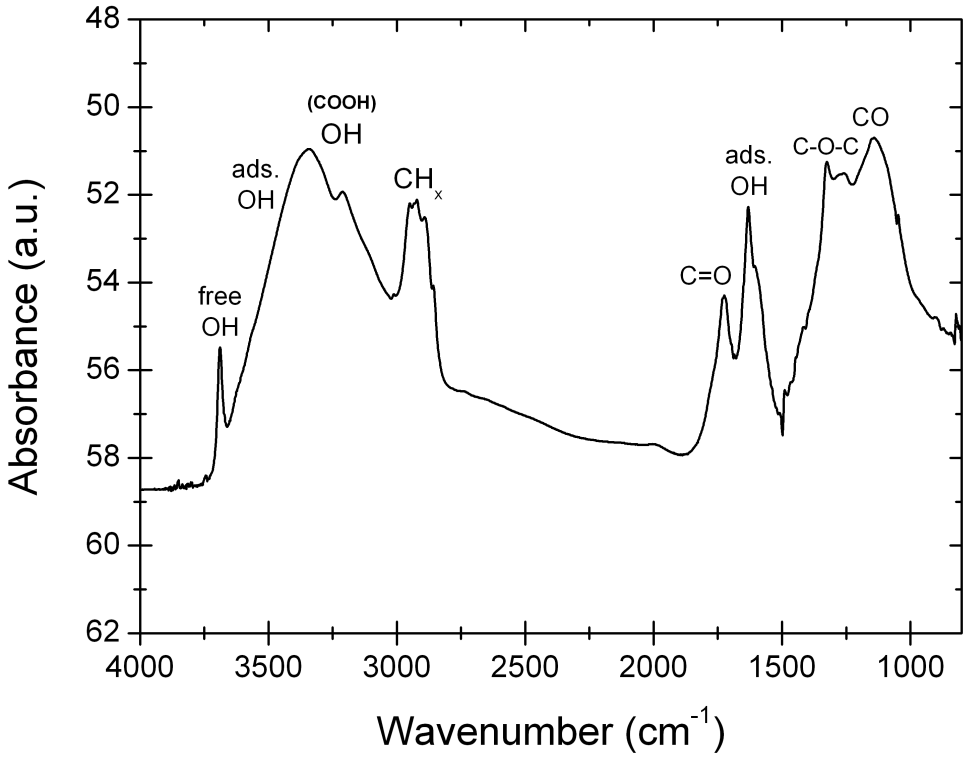

Figure 5.3: FTIR spectrum of as-received NDs. Spectrum shows the presence of oxygen and some hydrogen groups on the surface of the NDs. Ads. OH refers to adsorbed water, which can be seen to reduce during N_2 venting. Various moieties of oxygen are indicated on the NDs, including carboxyls, ethers and carbonyls. Nitrogen is also present in the low wavenumber region of the graph, however it is not clearly identified, hence not labelled.

5.3.3 Neuronal attachment and outgrowth on different materials

Our initial observation of ND-promoted neuronal attachment prompted an investigation of these neuronal cultures with respect to neurite outgrowth, direct interaction with the substrate, long-term survival and functional properties. On ND-coated substrates, hippocampal neurons displayed branched neurite outgrowth comparable to those on conventional protein-coated materials – a mixture of ECM proteins of laminin (LN) and poly-DL-ornithine (p-

ORN), (Figure 5.1 columns 2 & 3). Sequential coating with ND and protein did not result in any further improvement of cell attachment (Figure 5.1, right column), nor negative interference. The ND layer supported growth of both neurons and glia cells (Figure 5.4). This raised the possibility that neurons might not be growing directly on the ND monolayer, but on glia cells attached to the ND coating. To distinguish between these possibilities we stained the cultures with neuron- and glia-specific markers. Importantly, neurons were found to be able to grow in direct contact with the ND-coated surfaces and without interpositioned glia cells (Figure 5.4, arrow heads).

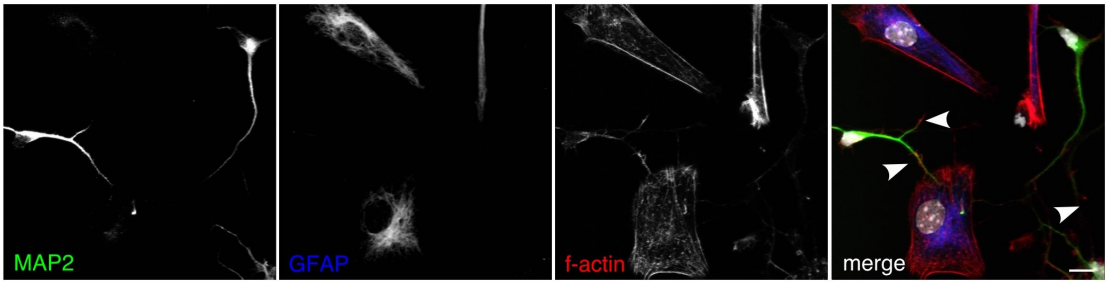

Figure 5.4: Neuronal outgrowth on ND-layered NCD. Confocal imaging of cell types and cellular compartments revealed that neuronal outgrowth can take place in direct contact with ND-layer. Dendrites of neurons (MAP-2, green in false colour merge), glia cells (GFAP, blue), f-actin (rhodamine-phalloidin, red), cell nuclei (Hoechst33258, grey values in merge). Arrowheads indicate neuronal growth cones. Scale bar: 10 µm.

5.3.4 Formation of neuronal networks

We next investigated the capability of ND coatings to support the establishment of electrically active networks in more mature cultures. The formation of electro-chemical connections between neurons via synapses takes place from about five days in culture onwards [226]. Confocal microscopy of immunostained neuronal cultures on all four substrates showed robust neuronal arborisation at 7 days *in vitro* (Figure 5.5). Scanning electron microscopy (SEM) confirmed formation of well-developed neuronal networks by day 7, and, in addition, revealed little or no degradation of the ND coating (Figure 5.6).

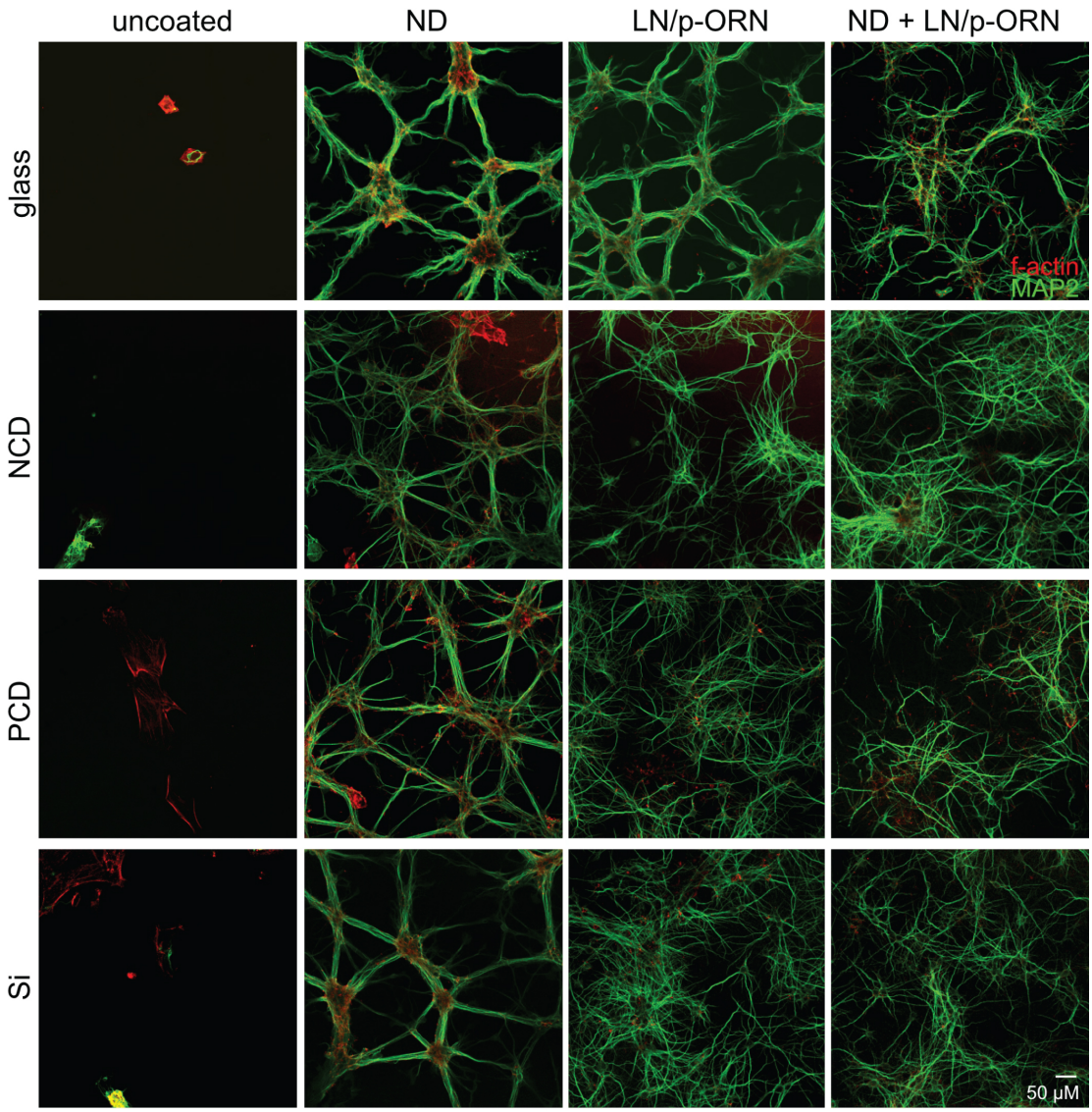

Figure 5.5: Neuronal growth on differently coated substrates after 7 days in vitro (DIV7). Substrates of glass, nanocrystalline diamond (NCD), polycrystalline diamond (PCD), and silicone (Si) were coated with nanodiamonds (ND) and/or laminin (LN)/poly-DL-ornithine (p-ORN) and the growth of hippocampal neurons was observed at DIV7. Surfaces of substrates are oxygen-terminated. Immunostaining reveals neurons via the dendrite-specific marker MAP2 (shown in green), while f-actin is stained for with rhodamine-phalloidin. Scale bar: 50 µm. The neurons have made clear physical connections between neighbouring cells.

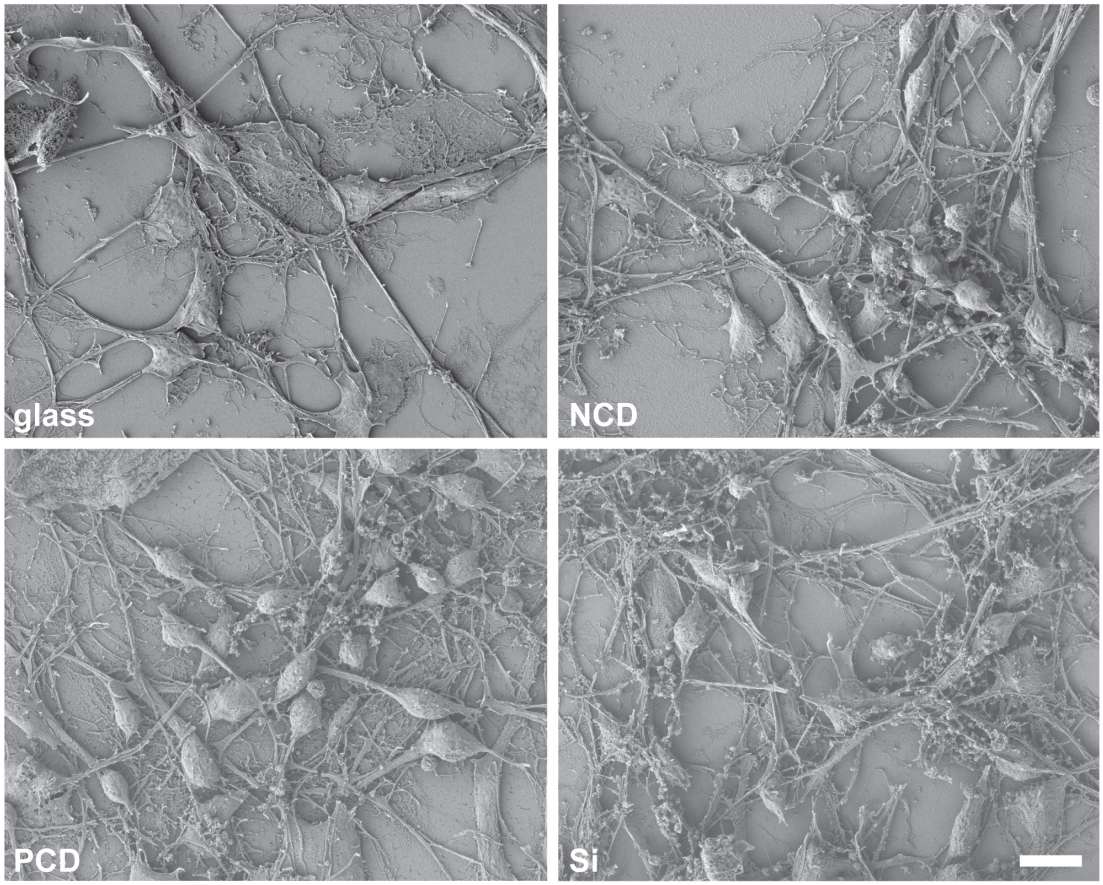

Figure 5.6: SEM images of neurons growing directly on ND-only coated material surfaces. Neurons appear highly branched and networked at DIV7. The ND layer appears intact on all supporting materials. Scale bar 10 µm.

5.3.5 Intrinsic electric excitability of ND-grown neurons

To investigate whether neurons grown on ND-layers displayed normal cell-autonomous electrical excitability, whole-cell patch-clamp recordings were performed on individual neurons in the current-clamp configuration. Graded somatic current injections successfully elicited trains of action potentials (APs) in neurons grown on ND-coated glass (Figure 5.7, right panel). This denotes that ND coating supports the development of electrically functional neurons. A comparison with recordings performed in parallel on sister cultures grown on conventional laminin and poly-DL-ornithine-coated glass (LN/p-ORN) indicates that neurons grown on the two substrates behave similarly in terms of AP frequency for injected currents up to 150 pA (Figure 5.7). Average AP frequency

at 150 pA injected currents was 28.00 ±10.04 Hz for neurons on LN/p-ORN coatings and 33.75 ±6.44 Hz for the ND-coating, p = 0.65, unpaired two-tailed Student's t-test. In order to probe to what extent the two conditions were comparable, increasingly stronger and saturating currents were injected. Only for the very high current injections, especially at the end of the pulses, did neurons grown on ND-layers display a reduced capacity to fire APs (compare lower panels of Figure 5.7). As there were no significant differences in input resistance (R_{in}) and membrane capacitance (C_m) between the two groups (R_{in} = 778 ±246 MΩ and C_m = 172 ±15 pF for LN/p-ORN coating vs. R_{in} = 735 ±118 MΩ and C_m = 156 ±31 pF for ND-coating, p = 0.88 and 0.67, respectively, unpaired two-tailed Student's t-test), the reduced number of APs in ND-grown neurons for the highest current injections (250-350 pA) is likely due to ion channel differences that make it more difficult for neurons grown on NDs to cope with strong depolarising inputs.

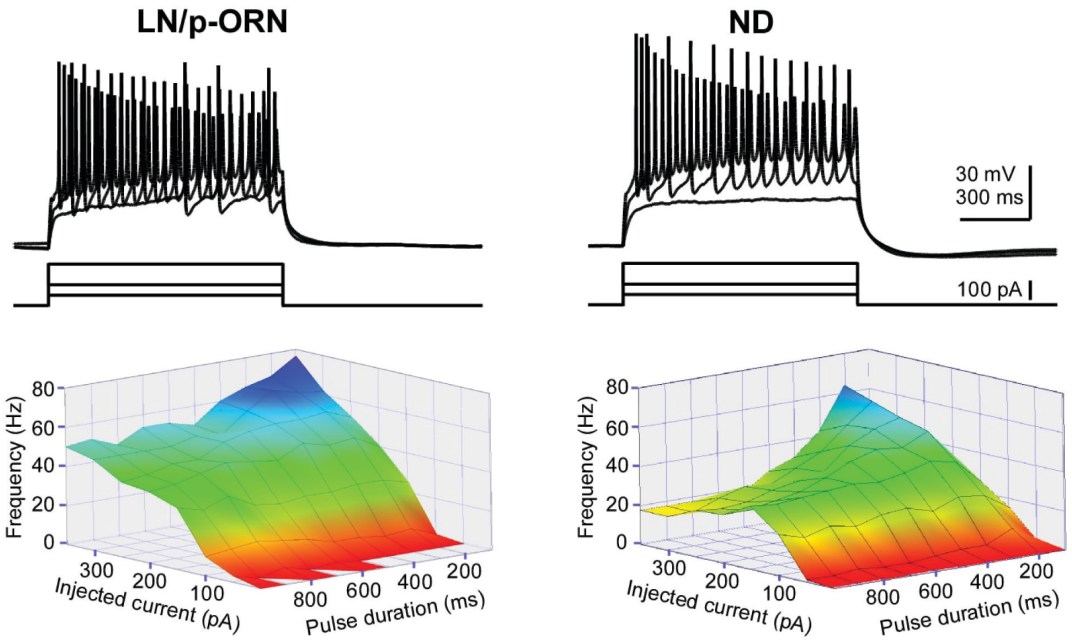

Figure 5.7: Intrinsic excitability of neurons on LN- vs ND-coated glass. Neurons from sister cultures grown on laminin ('control', left) or ND-only coated glass (right) were recorded in current-clamp mode after 7 DIV. 1 s-long rectangular pulses of current were injected via the patch pipette at the soma, with increments of 50 pA from 0 to 350 pA. Example traces recorded at 50, 100 and 200 pA are shown in top panels; middle panels depict the corresponding stimulus protocols. Summary data (n = 3 cells for control and 4 for ND) are shown in bottom panels, where action potential (AP) frequencies are plotted against pulse duration (binned at 100 ms) and intensity. Note the similarity in AP frequencies between control and ND-grown neurons for current injections up to 150 pA.

5.3.6 Synaptic connectivity

Having established the individual neuron's ability to generate APs, we next investigated the ND coating's ability to support the formation of functional synapses. To this end, whole-cell patch-clamp measurements in the voltage-clamp configuration were performed to record spontaneous miniature excitatory postsynaptic currents (mEPSCs) from individual neurons. mEPSCs are thought to represent the activation of postsynaptic glutamate receptors in response to the

spontaneous release of a single synaptic vesicle of neurotransmitter, and hence provide invaluable information on the mechanism of synaptic transmission [227]. As shown in the right panel of Figure 5.8, neurons grown on ND-layers displayed large and frequent mEPSCs, only after 7 DIV. A comparison with mEPSCs recorded in parallel from sister cultures grown on LN/p-ORN (Figure 5.8, left panel) revealed no differences in terms of mEPSC size and frequency between the two groups of cells (32.8 ±9.8 pA and 1.18 ±0.48 Hz for ND-coating vs. 22.6 ±4.0 pA and 1.73 ±0.95 Hz for LN/p-ORN coating, n = 3 cells per condition, p = 0.41 and 0.64, respectively, unpaired two-tailed Student's t-test) suggesting that ND coating supports normal synaptogenesis and synapse maturation, and possibly the formation of functional neuronal networks.

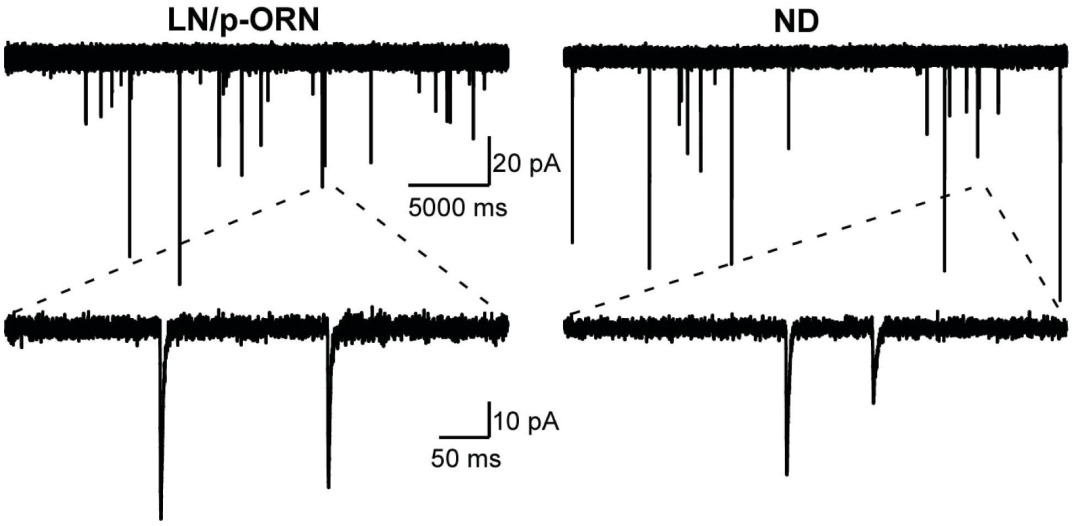

Figure 5.8: ND-coating supports formation of functional synaptic connections. Spontaneous synaptic transmission of neurons on LN- vs ND-coated glass. Spontaneous mEPSCs were recorded from neurons of sister cultures grown on laminin ('control', left) or ND-only coated glass (right) for 7 days. Note the similar size and frequency of mEPSCs in the two conditions.

5.3.7 Electrochemical network – calcium oscillations

The electrophysiological experiments above addressed cell-autonomous electrical properties of neurons on the ND-coated surfaces as well as the synaptic input an examined neuron received from contacting cells. In addition, we

examined the formation of the full neuronal network formed in the presence of ND coating via calcium imaging with the calcium dye fura-2. Following the pharmacological blockade of intrinsic inhibitory inputs, cultures grown on protein-coated glass showed the expected slow oscillatory calcium waves that are associated with the epileptic-like state induced by this treatment. Similar oscillatory activity was observed in cultures grown on the ND coating, which confirmed the formation of interconnected, electrically active networks of neurons on substrates coated with NDs (Figure 5.9).

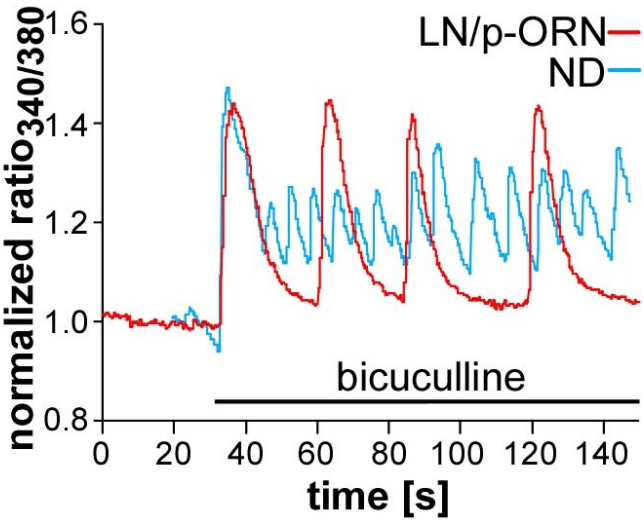

Figure 5.9: ND-coating supports formation of functional neuronal networks. Calcium measurements of neurons grown on protein or ND-only coated glass samples demonstrated network activity in primary hippocampal cultures at DIV12. Global calcium transients were elicited by bath application of 50 µM bicuculline. Fura-2 ratio$_{340/380}$ values are shown normalized to baseline.

5.4 Discussion

5.4.1 Simplicity and universality of ND coating

Previous studies have revealed that nanodiamonds are in general much more biocompatible than other carbon-based nanostructured materials, such as carbon nanotubes (CNTs) or carbon blacks [228]. Nanodiamonds are chemically inert, mechanically robust [229] and non-cytotoxic [77] in contrast to CNTs, which have been shown to induce apoptosis and therefore appear less suitable for use *in vivo* [230].

In this study, coating all the four different substrates that we tested (glass, NCD, PCD and Si) with ND layers was found to convert them from unfavourable surfaces for cell attachment, growth and maintenance, into most suitable platforms that compared well to the established culture conditions. This suggests that ND coating may be a widely applicable surface treatment to confer cell-interacting properties to various materials. Such properties are desirable for certain medical applications such as chronic implants. This is particularly interesting since ND-coating is an amazingly simple process that can coat most materials in 3D and is only limited by the size of the ultrasonic bath being used, although the long-term stability (i.e. > 2 weeks) of the ND-coating by this process has not yet been tested. Importantly, the ultrasound-mediated layering does not rely on specialised equipment or chemically-thermally aggressive protocols that are commonly used with the deposition and post-growth cleaning of other carbon materials such as CNTs [231].

5.4.2 Comparison with other growth platforms

Remarkable are the differences we observed in neuronal attachment on ND layered materials compared to uncoated NCD, which were originally grown from ND nucleation sites by microwave plasma chemical vapour deposition (MWPECVD). Whilst other studies have shown increased cell proliferation on the oxygen and hydrogen-terminated surfaces of NCD in the absence of further

coating [105,232-234], we could not detect significant cell attachment of our essentially post-mitotic neurons on the oxygen-terminated NCD substrates in the current study. This suggests that our cultures of primary murine hippocampal neurons are more demanding with respect to a suitable growth surface than cultures of renal epithelial and bone marrow cell cultures, or mesenchymal and neural stem cells. Alternatively, subtle differences in the surface properties of the uncoated NCD substrates from the previous studies compared to those used here, such as roughness or curvature of the surface topography, or propensity to protein adsorption may account for the differences in cell attachment. In the case of the successful use of ND layers (as opposed to NCD) in the current study it is possible that the ND layers led to a protein adsorption, which in turn favours cell adhesion and growth, although topographical effects may also be involved.

Neurons on ND layers were remarkably similar to those grown on traditional ECM protein coated samples. Our electrophysiological recordings suggest that there might be only minor differences in neuronal excitability. Equally, the differences in calcium wave oscillation frequency of induced epileptic activity could have been caused by these small differences in intrinsic excitability of neurons, but might reflect in addition differences in network connectivity. Such variations are in line with the known variability of primary neuronal cultures maintained under slightly variant conditions.

In contrast to electrical shortcuts observed in neurons grown on CNTs [235], the electrical excitability, and hence the ability to generate APs, seems not to be influenced by NDs, which remain electrically inert. This would allow the usage of patterned NDs on conductive biomaterials for generation of devices with spatially defined electrical properties for biological and medical application.

5.4.3 Direct attachment of neurons to ND layers

In the case of cell cultures containing different cell types, it is of interest to know whether the various cell types attach and grow directly on the ND layer, or

whether the more demanding cell types grow only on top of the less demanding ones. In the case of neuronal cultures, glia cells are known to adhere to many surfaces, and can serve as an efficient substrate layer for neurons. However, we observed direct attachment and growth of neurons on the ND layer without interpositioned glia cells. This suggests that low-capacitance and sensitive ion-sensing electrical coupling between neurons and substrate could be achieved on ND-coated materials, which is desirable for electrical interfacing between an implant and neuronal tissue.

5.4.4 Possible explanations for neuron attachment on NDs

Considering the remarkable differences and similarities in neuronal attachment observed between ND-coated, protein coated and uncoated substrates, it is tempting to entertain the possibility that NDs are mimicing the functional properties of ECM proteins, and are directly interfacing with cells and initiating cellular attachment and development. Afterall, nanoparticles can share a similar size, charge and shape as globular proteins, and have already been shown to mimic other biological processes [236]. In the particular case of NDs being anchors for the development of focal adhesions with neurons, NDs would have to mimic the function of Adhesion Molecules (AMs) of ECM proteins, which interface with cells via membrane proteins called integrins. In a similar fashion to antibody/antigen interactions, integrin receptors bind specifically to AM peptide sequences (motifs) and, thereof, initiate intracellular signalling pathways that are essential to cells' attachment, development and survival. Therefore, for NDs to mimic AMs, NDs would have to mimic AM motifs such as (for laminin) RGD, YIGSR, IKVAV, etc. [89]. In this context, similarities can be drawn between ND functionalities and the functionalities of R-groups of amino acids of AM motifs, such as the amine groups on Arginine (R) and carboxcylic groups on Aspartic Acid (D) of the RGD motif. Whilst it is not inconcievable that functionalities on NDs could be serendipitously arranged as to occasionally mimic AMs' motifs (especially considering organic RGD mimimetics exist [237]), direct ND-cell interaction is still highly unlikely. Without integrin signalling cells

die in a process called anoikis, and even slight integrin mutations cause anoikis or severe loss of function in cells [238]. Similarly, integrins show high specificity to only slight changes in motif sequence [239]; therefore, it would be surprising that NDs – crudely forged in detonation chambers – could mimic the highly specific, evolved interactions of AMs with integrins. Additionally, artificial surfaces have been shown to promote neuronal adhesion by electrostatic adhesion alone, however this is also an unlikely adhesion mechanism herein, because NCD, with similar electrostatics to NDs, does not support neuronal adhesion. It should be noted, however, that NDs are more porous than NCD films.

Instead, it is much more likely that NDs provide a substrate for the optimal adsorption of AMs, such as vitronectin from serum proteins (see section 4.3), and subsequent ECM proteins produced by cells themselves [110]. Indeed, neurons cultured without serum do not attach to ND-coated subsubstrates (n.b. serum also contains other growth factors essential to cell attachment that are not AMs), and, furthermore, the slight fasciculation of neurons observed in column 2 of Figure 5.5 (after 7 DIV) can be ascribed to neurons attaching onto their own matrix of endogenous AMs, and not the underlying surface (n.b. fasciculation is also observed on ECM coated substrates and therefore can also be ascribed to varying culture conditions). Whilst serum protein adsorption can account for neuronal attachment on artificial substrates, what is particularly remarkable here is the difference in neuronal attachment between NCD and ND coatings, which share many similarities in terms of surface chemistry and bulk consitution. Herein, we suggested that the remarkable attachment of neurons observed on ND-coatings can be explained by functional, well-orientated protein adsorption onto NDs as a result of their optimal curvature morphology – not just absolute roughness – and their high affinity for protein adsorption (Figure 5.10). The NDs used in this study have radial curvatures of ca. 5 nm, which is comparable to the dimensions of proteins, resulting in point-contact adsorption of proteins. This allows proteins to stay strongly adheered to NDs, but in their native structural and functional shape. In this context it has recently been shown that the bovine serum albumin (BSA) protein adsorbs with high affinity to NDs whilst retaining its structural features, which dictate protein function. In

consideration of which AMs could be responsible for initial attachment of neuronal cells to ND-coatings, vitronectin has been shown to absorb with high affinity to NDs from serum [135] and is known to be an important AM for initial cell attachment [110]. Furthermore, vitronectin is of similar size to BSA and is made up of globular domains that are easily denatured during absorption, which could explain increased adhesion of neurons on ND-coatings. Seeing as ND-coatings have a similar density as integrins and other structures in cell membranes (10-15 nm spacing [94]), we suggested that NDs provide an excellent substrate for neuronal growth because of the optimal adsorption of AMs such as vitronectin. With respect to the lack of neuronal adhesion on NCD layers and other substrates used in this study, the reduced curvature of these materials, which gives rise to larger contact areas and corresponding overwhelming adsorption forces, is suggested to denature some AM proteins (particularly globular proteins) [102,128], thereby reducing neuronal attachment. Alternatively, these subtrates could be adsorbing proteins in the wrong orientation with respect to the alignment of AM and integrin binding sites.

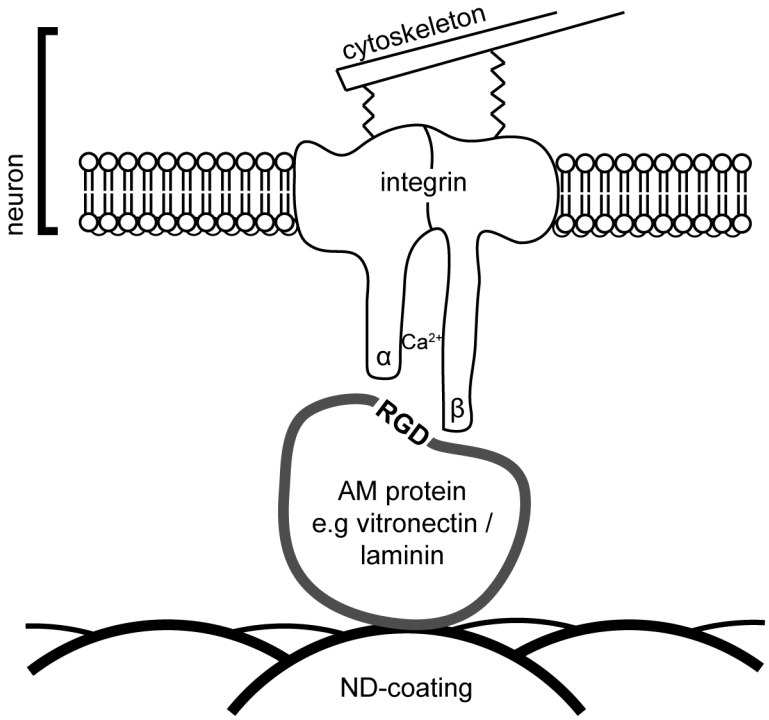

Figure 5.10: Schematic of proposed ND-AM-Integrin mediated cell attachment. Adapted from [240]. For RGD binding, R binds to the α-subunit and D to the β-subunit via salt bridges with divalent cations [237]. Not to scale.

5.5 Conclusions

The surfaces of four different materials (glass, PCD, NCD and Si) coated with monolayers of monodispersed detonation nanodiamonds displayed promising similarity to the protein-coated materials regarding neuronal cell attachment, neurite outgrowth and functional network formation. Importantly, the neurons were able to grow in direct contact with the ND-coated material and could be easily maintained in culture for an extended period equal to those on protein-coated substrates. Given the biocompatibility of NDs and their potential for surface functionalisation, ND layering might prove a valuable material technique for implants on a wide range of substrates.

Chapter 6 Nanocrystalline diamond Micro-Electrode Arrays for the recording of electrogenic cells.

6.1 Introduction

Micro-electrode arrays (MEAs) are powerful tools that allow for the investigation of the electrogenic properties of cellular networks in a non-invasive manner. Unlike patch clamp experimentation (see section 4.11.1), which addresses individual neurons and typically results in cell death, MEAs can record cell signals without damaging cells and many cells can be probed simultaneously across a network. Aside from being useful tools for electrophysiologists [241], planar MEAs are valuable for the controlled *in vitro* characterisation and evaluation of electrodes prior to their use *in vivo.* In order to achieve low-noise and faithfully reproduced action potential recordings from either long-lived cell cultures *in vitro* or chronic electrically active implants *in vivo*, MEA electrodes must display a high biocompatibility towards cells, sufficient bandwidth and high signal-to-noise measurements. At present, neural electrodes consist of materials such as noble metals (Au, Pt, Pt alloys, e.t.c.), silicon (*in vivo*), iridium oxide, tantalum and titanium nitride, as comprehensively reviewed in [242]. Whilst these electrodes are apt at stimulating or recording electrogenic activity, faradaic type electrodes (e.g. noble metals, IrO_2) react with the surrounding electrolyte, thereby damaging tissue [243] and degrade due to oxidative electrolysis reactions at their electrode surfaces (Au dissolution [244], Pt dissolution [245], IrO_2 dissolution [246,247]). Instead, capacitive type electrodes, such as titanium nitride and tantalum/tantalum oxide, can be used that do not undergo charge transfer at the electrode surface; however, the biocompatibility of these

materials is uncertain [248]. In most cases, *in vivo* implantation of electrodes ultimately results in an immunological response called gliosis or glial scarring [7], wherein neurons migrate away from electrodes, rendering the implanted electrode incapacitated. Understandably, the limited biocompatibility and longevity of electrodes is one of the main challenges faced in developing neural electrodes.

In this context, diamond could be an ideal neural electrode material. Its chemically inert nature and proven ability [8,10,249] to promote functional neuronal networks on its surface demonstrates the exceptional biocompatibility of diamond. As well as being exceptionally biocompatible, metallic boron-doped diamond [250] possesses exceptional electrical and electrochemical properties for the stimulation and recording of cells. Its strong polarisability and wide electrochemical window [11] allow for the capacitive stimulation of neurons, and its wide band gap suppresses band-to-band generation–recombination noise of carriers, which is promising for low noise devices. Additionally, due to the high biocompatibility of diamond, enhanced attachment of cells on the diamond surface should minimise the cell-electrode cleft, thereby improving signal transduction and reducing signal loss. The aim of this study, as part of the Diamond to REtina Artificial Micro-interface Structures (DREAMS) EU project, is to evaluate boron-doped nanocrystalline diamond (BNCD) as a neural electrode material. BNCD electrode MEAs with single cell resolution have been fabricated following the development of an optimised Reactive Ion Etching (RIE) recipe for etching diamond. Undoped nanocrystalline diamond (NCD), silicon dioxide / silicon nitride / silicon dioxide and SU8 epoxy have been used as passivation materials. Having fabricated and encapsulated BNCD MEAs, HL-1 cells have then been used *in vitro* as a convenient model to validate BNCD MEA performance in comparison to standard metallised MEAs.

6.2 Diamond Reactive Ion Etching

6.2.1 Recipe development

Due to the hard and chemically resistant nature of diamond, Reactive Ion Etching (RIE) diamond is not a trivial process and, in terms of its research development, is in its adolescence and does not have an established recipe. To fabricate diamond MEAs, an Inductively-Coupled Plasma Reactive Ion Etching (ICP RIE) process has been developed to give sufficiently high aspect ratio and smooth etched diamond surfaces. Whilst etch rate has been taken into consideration, considering the small thicknesses (<500 nm) of the diamond films used in this research, a high etch rate is not of primary concern. Instead, the recipe has been optimised to give well-defined photolithographic features for patterned electrodes and an etched diamond surface that is apt at supporting cellular cultures. To design the ICP RIE recipe, the parameters of coil power (CP), platen power (PP), precursor gases, pressure and mask selectivity have been considered and, as a starting point, the effect of precursor gases have been initially investigated.

Diamond is essentially carbon and, as a result, precursors gases of oxygen and argon are typically used to chemically and physically etch the diamond surface. Chemical etching, whereby precursor gas radicals chemically react with the substrate to create volatile by-products, imparts etching selectivity (Selectivity: S = Sample etch rate / Mask etch rate) and high etch rates to the RIE processes; however, chemical etching is isotropic and produces low aspect ratio etchings. On the contrary, physical etching, whereby heavy ions bombard and sputter-etch the surface, is highly anisotropic giving high aspect ratio features, but results in low selectivity due to indiscriminate bombardment of both the mask and substrate. In O_2/Ar diamond RIE, oxygen serves to chemically and physically etch diamond, producing volatile CO and CO_2 by-products, whereas argon, being an inert gas, solely physically etches diamond via ion bombardment. To investigate the effect of precursor gas ratio of oxygen to argon in diamond RIE, two single crystal (SC) Type Ib (100) diamond substrates with simple Al

hard masks were subjected to the RIE parameters shown in Table 6.1 using a STS ICP RIE system (see section 4.12.3), and the corresponding SEM images of the raw and etched diamond surfaces are shown in Figure 6.1.

Etch recipe	Ar (sccm)	O_2 (sccm)	Etch Rate (nm/min)	Pressure (mTorr)	CP (W)	PP (W)	Selectivity S
RIE.1	10	30	170	5	600	200	2
RIE.2	35	5	100	5	600	200	8

Table 6.1: ICP RIE parameters used to etch SCIb diamond to investigate the effects of changing the O_2/Ar ratio on RIE. Samples are etched for 5 mins using Al hard masks that cover half the samples. Resultant etch rates and selectivity with respect to Al are also shown.

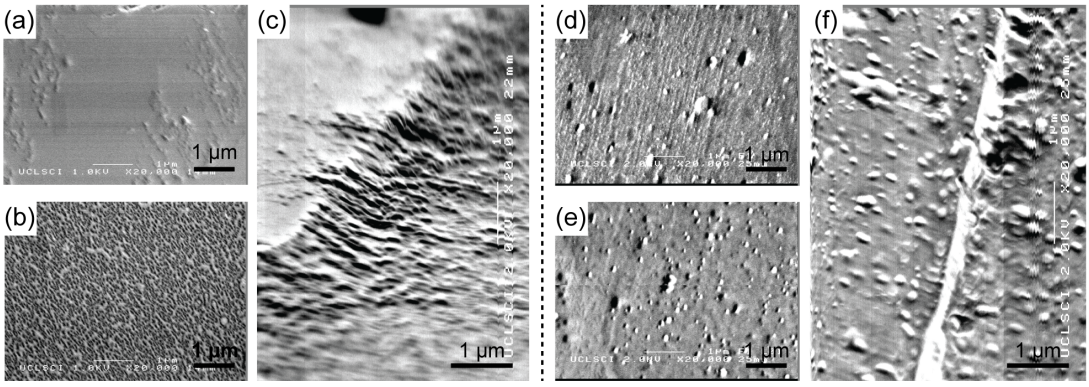

Figure 6.1: SEM images of raw and etched SCIb diamond subjected to two different O_2/Ar etch recipes: RIE.1 and RIE.2. a) Raw SCIb surface. Normal incidence. 1kV beam energy. b) Etched SCIb surface using RIE.1. Normal incidence. 1kV beam energy. c) Etch boundary showing low-aspect ratio sidewalls. RIE.1. Angle: 40˚. 2 kV beam energy. d) Raw SCIb surface. Normal incidence. 2 kV beam energy. e) Etched SCIb surface using RIE.2. Normal incidence. 2 kV beam energy. f) Etch boundary showing high-aspect ratio sidewalls with similar roughness to the un-etched surface. RIE.2. Normal incidence. 2 kV beam energy. Both samples were etched for 5 minutes using an Al hard mask, which was removed prior to imaging. SEM Images are taken with a JEOL JSM-6301F.

RIE.1 resulted in a higher etch rate than RIE.2 as expected for a chemically biased (oxygen rich) RIE recipe (Table 6.1); however, the selectivity of the etch was surprisingly reduced in comparison to RIE.2. This is ascribed to increased sputtering of the mask by O ions (see section 6.2.2). The etched surfaces of RIE.2 SCIb showed a much smoother finish than RIE.1 SCIb, more resembling its original raw surface than the pitted etched surface of RIE.1 SCIb, which is a characteristic of isotropic etching (Figure 6.1). Furthermore, the aspect ratio of RIE.2 SCIb was considerably steeper than RIE.1 SCIb. From these observations a 5:35 O_2:Ar ratio has been selected for the final RIE recipe, RIE.3. Further optimisation of gas ratios has not been performed due to the results being sufficient for our purpose.

The rest of the parameters of the forming RIE.3 recipe were then taken into consideration by conducting a literature review of diamond ICP RIE. A summary of the literature is in Table 6.2 below. It should be noted that parameter refinements based on observations made from each experiment quoted in the literature review are acknowledged to be somewhat idiosyncratic to the other parameters used by the respective experimenters, and not necessarily applicable to other experimental conditions. However, given that an exhaustive exploration of the ICP RIE parameter space was not possible with the time or sample quantity available, the extracted relationships, suggested values and trends from the review have been used as a guide in combination with empirical experimentation to formulate a sufficiently optimised RIE recipe.

Paper	Ar	O_2	Other (sccm)	Pr. (mT)	CP (W)	PP (W) / Bias	Etch Rate	S	R_a (nm)	Mask	Diamond Type
M. Karlsson 2001 [251]	8	7	-	2.5	500	140	190 nm/min	0.3	-	Photo-resist	CVD
Y. Ando 2002 [252]	CF_4:O_2 = 0 to 12.5 %			15 to 300	100 to 280	0	9.5 µm/h	-	<0.4	Al	(B)HPHT Ib 100, 111
D.S. Hwang 2004 [253]	30	90	-	15 to 50	700 to 1000	0 to 200*	40 µm/h	50	-	Al	SCIb 100
H.W. Choi 2005 [254]	10	30	-	5	250 to 1000*	0	228 nm/min	4.5	<3	SPR220	IIa
J. Enlund 2005 [255]	8	7	-	2.5	600	100 to 180 (V)	200 nm/min	-	3	Nano 495 PMMA	B-HPHT, SC-CVD 100
C.L. Lee 2006 [256]	15	40	-	5 to 30*	100 to 800	0 to 300*	0.22 µm/min	-	1.2	SPR220	Natural, HPHT
C.L. Lee 2007 [257]	15	40	-	5	400	40	0.04 µm/min	-	3	SPR220	CVD
C.F. Wang 2007 [258]	-	40	CF_4: 1	50	300	700 (V)	5.8 µm/h	-	-	Al/Ti	Ib, HPHT
T. Yamada 2007 [259]	CF_4 / (CF_4+O_2) = 2 to 100 %			15	1000	100	5.5 nm/s	10	1	SiO_2	Ib (100)
H. Uetsuka 2008 [260]	CF_4 / (CF_4+O_2) = 2 to 100 %			4.5	1000	100/ 100, 200	18.8, 30 µm/h	12/ 188, 67	-	Al/ SiO_2	(B)SCIb 100
C.L. Lee 2008 [261]	25	-	Cl_2: 40	5	400	300	1 nm/s	0.06	0.19	SPR220	IIa, HPHT, CVD
M.P. Hiscocks 2008 [262]	-	20	CF_3: 0.5	75	200	0	70 nm/min	-	-	SiO_2	SCIb 100

Table 6.2: Summarised ICP RIE recipes from a review of the literature which aim to fabricate smooth and/or high aspect ratio diamond structures. Ar and O_2 are in sccm. In the Diamond Type column, (B) denotes both intrinsic and boron doped diamond were investigated. Pr. is pressure in mTorr. R_a is average roughness. "-" denotes no data was available in the paper source. * indicates particularly influential experiments in developing RIE.3, as discussed below in Figure 6.2.

Table 6.2 demonstrates the wide span of parameter space that is used for diamond ICP RIE. The following experiments from the review were particularly insightful in identifying parameter trends, which were then applied to RIE.3:

Firstly, Choi et al. [254] investigated the effect CP has on etch rate, roughness and S on diamond etching. For ICP RIE in general, as CP is increased the density of generated ions also increases, resulting in an increased etch rate without significantly increasing ion energy (unlike parallel plate electrode systems). Choi et al. observed such a phenomenon by varying CP from 100 to 1000 W and observed an etch rate that is linearly proportional to CP (Figure 6.2a&b) and no discernable effect on S or r.m.s. roughness (R_{rms}), which are both dependent on physical, energy dependent etching mechanisms. Whilst no clear trend in S or R_{rms} was observed, a CP of 500 W has been selected for RIE.3, which gave the highest S and lowest R_{rms} in Figure 6.2a&b, and also gives a sufficient etch rate for practical processing.

Secondly, the effect of PP on diamond was considered. As discussed in section 4.12.3, PP can be applied to ICP RIE systems to cause the accumulation of negative charge on the sample, which then accelerates heavy positive ions into the substrate, increasing ion bombardment and physical, anisotropic etching. Lee et al. [256] varied PP from 0 to 300 W (at 400 W CP, Figure 6.2c) and found significantly increased etch rates for PPs greater than 100 W. Hwang et al. [253] showed 200 W PP to be sufficient to achieve near-vertical high aspect ratios, and Uetsuka et al. [260] found diamond whiskers (see below, section 6.2.2) to be removed more under higher bias (200 W, >100 W). For these reasons a PP of 200 W has been selected for RIE.3, which should give a smooth etch, sufficient etch rate and high aspect ratios without overly energetic bombarding ions.

Thirdly, Lee et al. [256] also investigated the effect of pressure on diamond ICP RIE. For low pressure, etch rate is proportional to pressure because the number of generated ions is not so effected by ion collisions and recombination events. Lee et al. found 10 mTorr (Figure 6.2d) to be the threshold at which recombination starts to determine the etch rate of diamond;

therefore, the pressure of RIE.3 has been set at 10 mTorr in order to maximise ion density in the plasma to increase etch rate without altering ion energy significantly (which can be reduced by increased collisions).

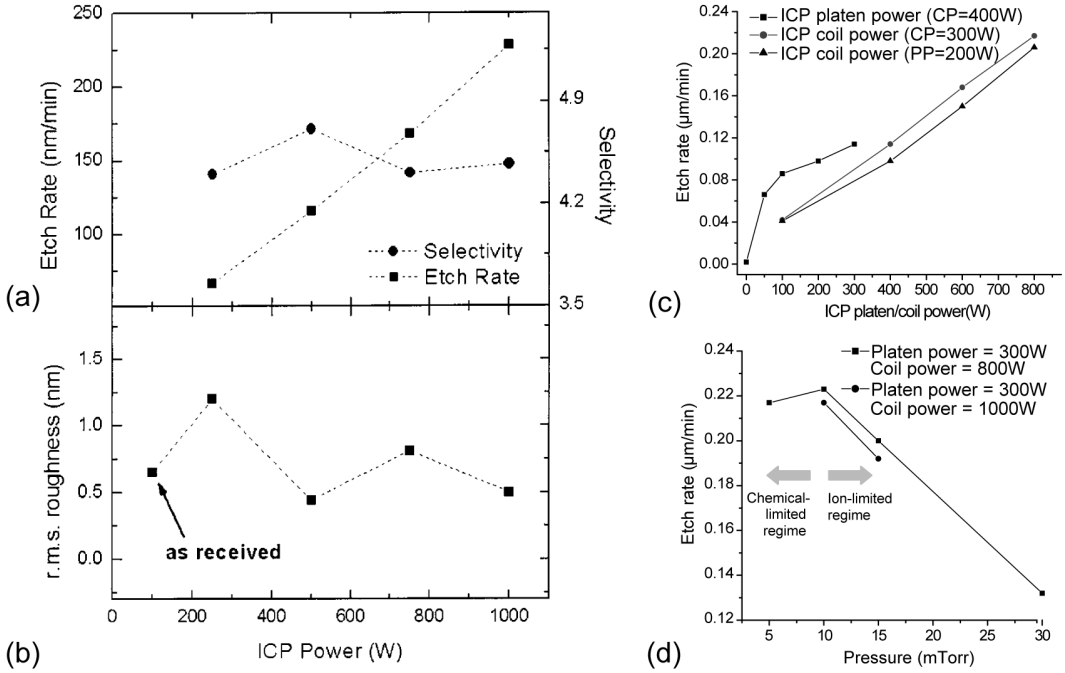

Figure 6.2: Key exerts from RIE literature review. a) Choi et al. [254] find etch rate to be proportional to CP on SCIIa diamond. 500 W CP gives optimal surface roughness b) and maximises selectivity (for SPR220). c) Lee et al. [256] find 200 W platen power (PP) increases etch rate and aspect ratio (also see [253]) without being superfluous and reducing selectivity. d) Also in [256], 10 mTorr pressure is found to give the highest etch rate, balancing chemical and physical etch processes.

Taking into account the above considerations, the optimised RIE recipe, RIE.3, is:

Etch recipe	Ar (sccm)	O_2 (sccm)	Pressure (mTorr)	CP (W)	PP (W)
RIE.3	35	5	10	500	200

Table 6.3: Optimised ICP RIE parameters for diamond etching.

6.2.2 Recipe testing and diamond whiskers

Having established a diamond recipe, a variety of diamond types have been etched using RIE.3 in order to investigate any differences in etching between diamond types. 5 diamond types have been used: 1) Hot filament CVD Black polycrystalline diamond (HFBPCD) (Diamonex, Allentown, PA, USA) 4 mm square. 2) White PCD (WPCD), (MWPECVD, ASTEX PDS18 Plasma system) 4 mm square. 3) SCIb, ca. 2 mm irregular shape. 4) SCIIa (100), (CEA-LIST, Saclay, France) 2 mm square. 5) SCIb (100), (Element Six, Ascot, UK) 2 mm square. Samples have been subjected to 10 mins etching, and etch results are presented in Table 6.4.

Diamond type	Crystallinity	Mask	Etch Rate nm/min	S w.r.t. Al	S w.r.t. SPR220
1) Black Polycrystalline diamond (PCD)	µ	Al	-	-	-
2) White Polycrystalline diamond (PCD)	µ	Al	-	-	-
3) SCIb ca. 2 mm Irregular	SC	Al	114	55	0.23
4) SCIIa 2 mm square	SC	Al	99	20	0.20
5) SCIb 2 mm square	SC	Al	108	32	0.22

Table 6.4: ICP RIE etch table for various forms and types of diamond. 10 mins etching. "-" denotes an immeasurable quantity.

Using RIE.3, all samples (bar PCD samples) showed an etch rate near 100 nm/min. Error bars are not shown but a large degree of unquantifiable error in etch rate is assumed due to sample roughness and the heterogeneous nature of

RIE across a sample making it hard to accurately measure etch depth. The etch rate of black and white PCD could not be determined using a standard profiling technique despite a subsequent extended etch time of 30 minutes. Upon optical inspection of all samples, and in particular the HFBPCD sample, unwanted whisker-like diamond structures were observed near the mask edge; hence, HFBPCD (plus WPCD, SCIIa) was further inspected using scanning electron microscopy using a JEOL JSM-6301F, equipped with an EDS Detector using an EDS accelerating voltage of 15 kV.

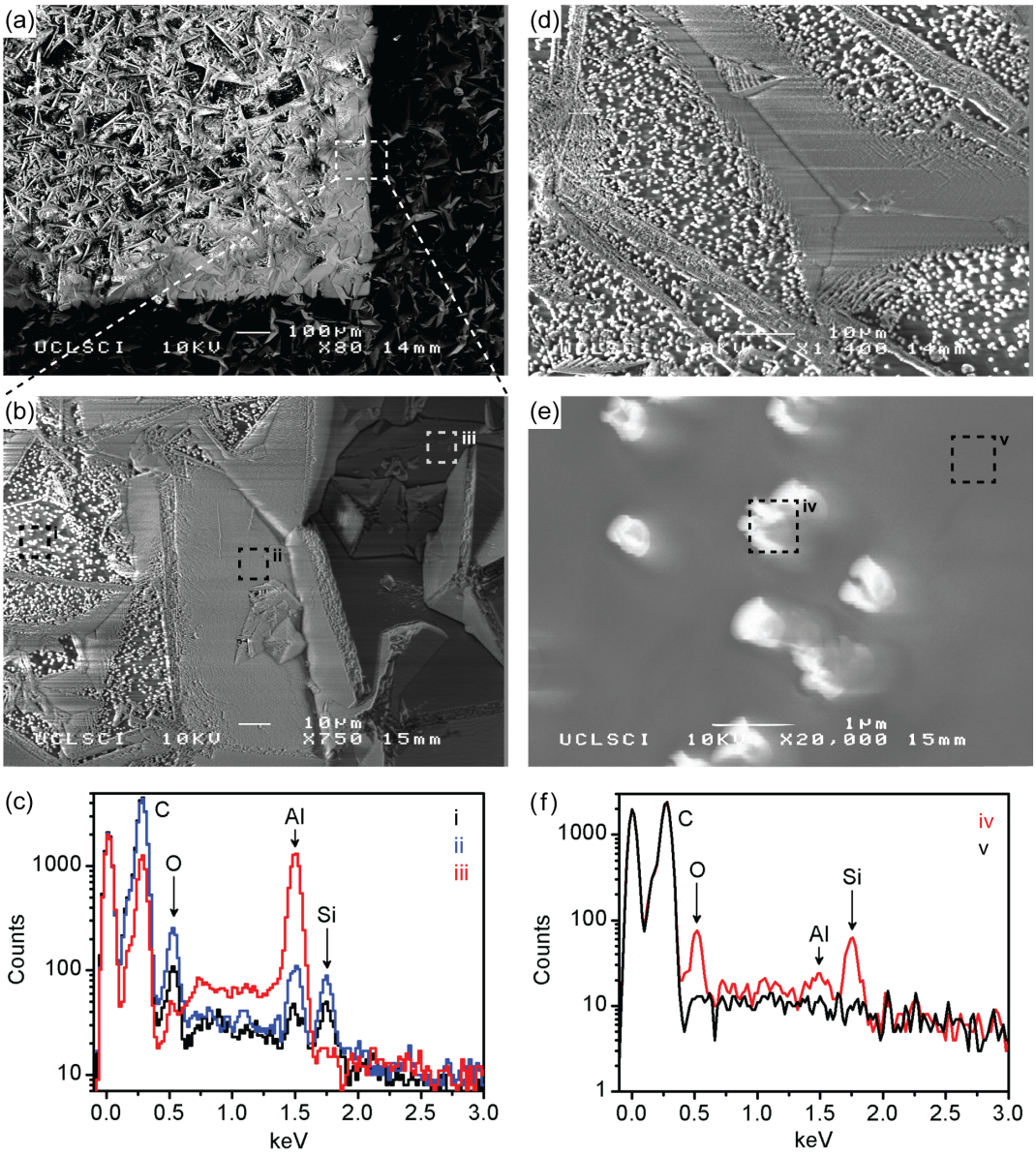

Figure 6.3: Diamond whiskers are observed on the HFBPCD sample after 10 minutes etching with RIE.3. The Al mask is kept on the sample. a) shows the Al mask (in black in a reverse L shape) to have been sputtered onto the etched surface, but to a lesser extent further away from the mask edge. b) shows a magnified area of a) selected for EDS analysis, with analysed areas indicated with dashed rectangles and roman numerals. c) EDS analysis of indicated areas in b). d) shows an area away from the mask edge on the etched sample, showing mask run off and pooling into the trenches of the PCD surface. e) Focusing on an area away from the grain boundaries and trench regions within d), individual whiskers are pictured. f) EDS analysis of marked areas in e). N.b. no Si or Al is observed at v.

SEM analysis showed the surface of HFBPCD to be heavily whiskered following RIE. Figure 6.3a shows whiskers to be at their highest density when situated close to the mask edge, and the insulating nature of the whiskers (their bright contrast is indicative of a charged insulating material, or one with a high negative electron affinity) suggested that they were due to the commonly observed effect [252,260,263,264] of mask sputtering of Al by RIE. To confirm this, EDS analysis was performed at various representative areas across the sample. Figure 6.3b shows a magnified region of Figure 6.3a, wherein 3 areas have been analysed using EDS as shown in Figure 6.3c. EDS reveals aluminium and oxygen to be present on the etched surface of HFBPCD, confirming the sputtering of Al by oxygen (and argon) onto the etched surface, whereof Al_2O_3 acts as a ceramic hard mask [264]. The amount of Al decreases as one moves away from the mask edge as expected for a sputtering process. Less expectedly, silicon was also present in the whisker regions. Inspecting whiskers located away from the mask edge (Figure 6.3d), where the whiskers themselves were located in the middle of a diamond facet (Figure 6.3e), EDS (Figure 6.3f) revealed Al to be minimally present and silicon oxide to be the main contributor to the non-diamond whisker content. Silicon could be present either due to incorporation during growth or by sputtering from the 6 inch SiO_2 wafer upon which RIE was carried out. To further investigate the origin of these whiskers in order to effectively ameliorate their creation, HFBPCD was subjected to an additional 20 minutes etching (30 mins total), and the evolution of diamond whiskers was investigated.

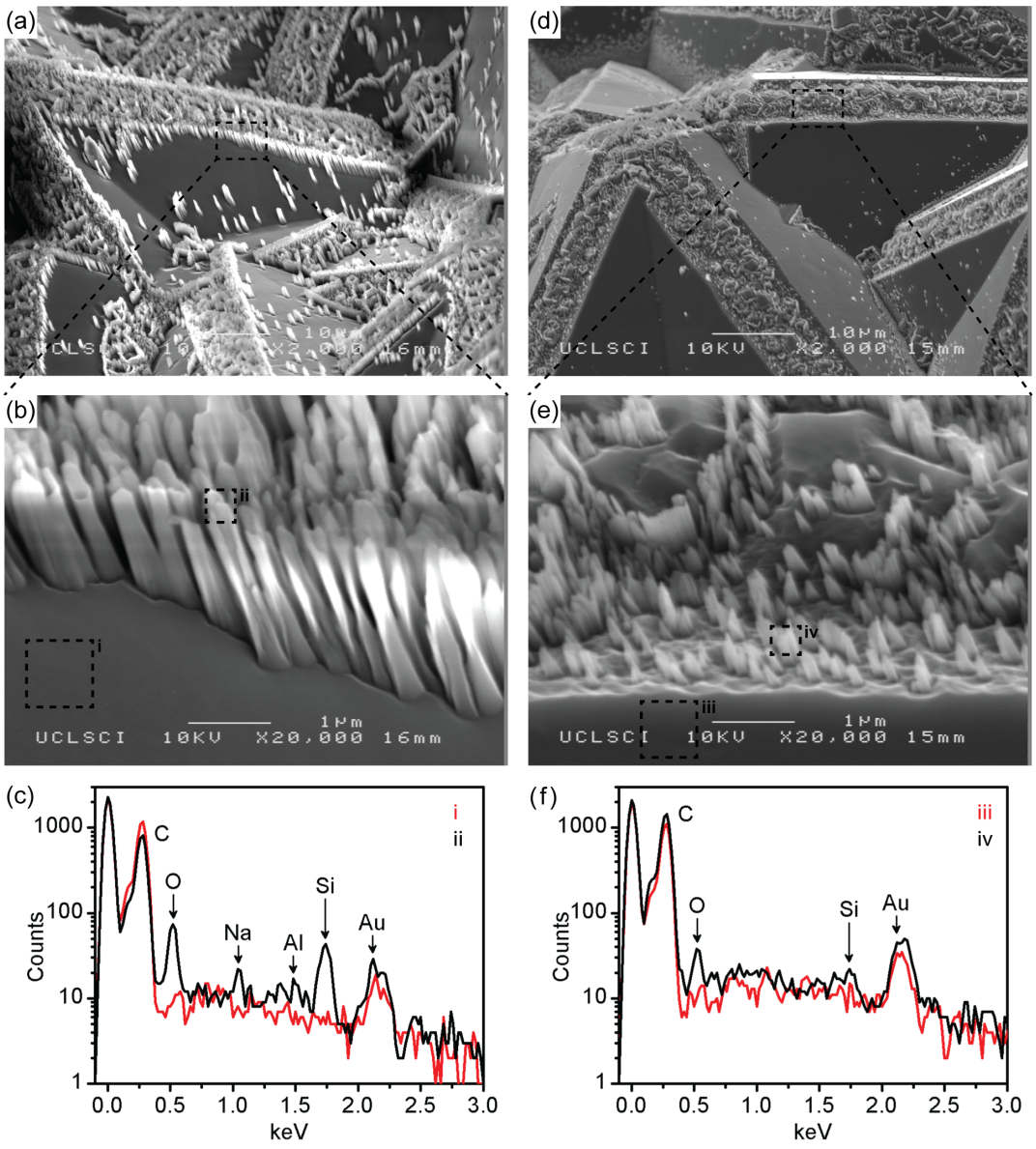

Figure 6.4: HFBPCD after 10 mins RIE is shown in SEMs a) and b), and the corresponding EDS in c). HFBPCD after 30 mins RIE is shown in SEMs d) and e), and the corresponding EDS in f). A thin layer of Au has been coated on the samples to reduce charging effects when using the higher beam energies required for EDS (15 kV). Analysis is performed away from the mask edge.

Etching HFBPCD for 10 and 30 minutes resulted in clear differences in the appearance of the diamond whiskers. Yamada et al. [259] propose there to be three types of whisker origins: 1) Located at grain boundaries – caused by sp^2 bonding and lattice mismatch; whiskers are homogeneous in height. 2) Random whiskers located mid-facet in grains – caused by imperfections and impurities

during growth. 3) Re-deposited mask material – caused by mask sputtering, unbound by location but related to mask proximity. Figure 6.4a&b show the whiskers at the grain boundaries after 10 minutes of RIE, which are homogeneous in height, to be type 1, and EDS analysis (Figure 6.4c) reveals silicon oxide (and other) impurities at the same location. After 30 minutes of RIE the type 1 peaks were much less dense, showing less homogeneity in height, (Figure 6.4d&e) and the silicon oxide contribution to the EDS spectra (Figure 6.4f) was also reduced. For both samples, little Al was observed in EDS spectra (and in particular for the 30 mins sample), suggesting the whiskers observed were of type 1 or 2, and born from intrinsic defects, grain boundary impurities and imperfections, which is reflective on the low quality and highly contaminated nature of HFBPCD samples. In this context, higher quality SEMs and EDS analysis of SCIIa and SCIb samples (data not shown) showed less whiskers and only minute traces of silicon impurities. Whilst whiskers could still be originating from sputtered silicon oxide from an RIE wafer, the observed whiskers on HFBPCD have been ascribed to intrinsic type 1 and 2 origins, and also Al-based type 3 whiskers nearer the mask edge. Type 1 and 2 can be removed by using fluorine based RIE recipes [252,259,260,262], however this was not possible for MEA fabrication due to fluorine-based chemistries not being selective to the underlying $TiSi_2$ substrates on the back contacts of the MEAs. Instead, type 3 whiskers have been removed by using a mask that does not form re-deposited oxide whisker masks. For this reason, the photoresist SPR220 (7 μm) has been used as an RIE hard mask instead of Al, which sacrifices selectivity but does not result in dense type 3 whiskers being etched onto the MEA surface.

Using RIE.3 and an SPR220 hard mask, final RIE tests were then performed on test wafers of the same NCD and BNCD [250] used for MEA fabrication, which were grown by CEA, France, using the following MWPECVD parameters as presented in Table 6.5, along with accompanying images and deposition thickness profiles as shown in Figure 6.5. BNCD has an expected boron concentration of 10^{21} cm^{-3} and conductivity of 30 Ω^{-1} m^{-1} [250].

Diamond Type	CH_4 (%) in H_2	Total gas flow (sccm)	TMB (ppm)	Power (kW)	Pressure (Torr)	Temp. (˚C)	Time (hours)
NCD	0.8	200	-	1.5	37.5	650	4
BNCD [250]	0.22	100	2000	1.5	30	750	6

Table 6.5: MWPECVD parameters of NCD and BNCD films. Films were grown by CEA, France in a custom MEPECVD reactor (Baobub).

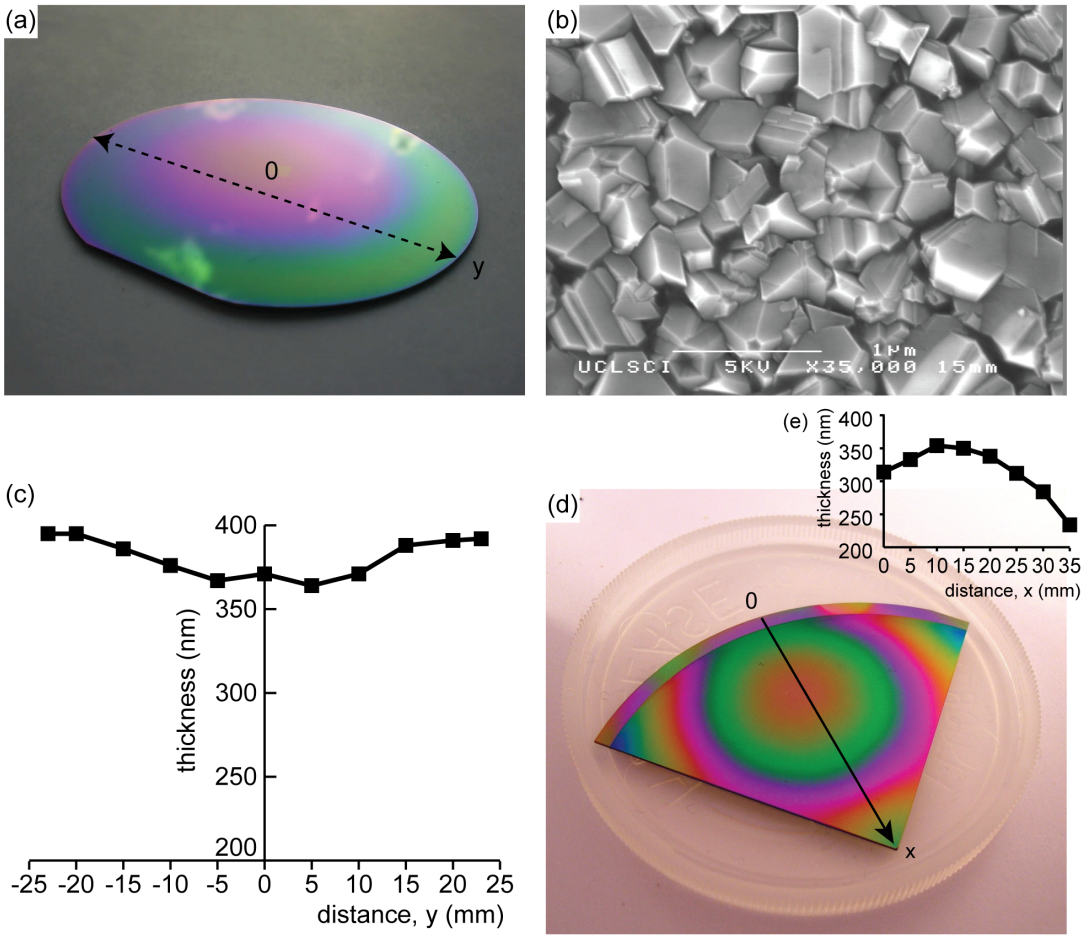

Figure 6.5: a) NCD film grown by CEA, France, for RIE.3 testing (apparent defects are clouds reflected in wafer). b) SEM confirming the NCD nature of the diamond film. c) Ellipsometry profile of NCD film across indicated line in a) (CEA). d) BNCD film grown by CEA, France with the inset, corresponding ellipsometry profile (CEA).

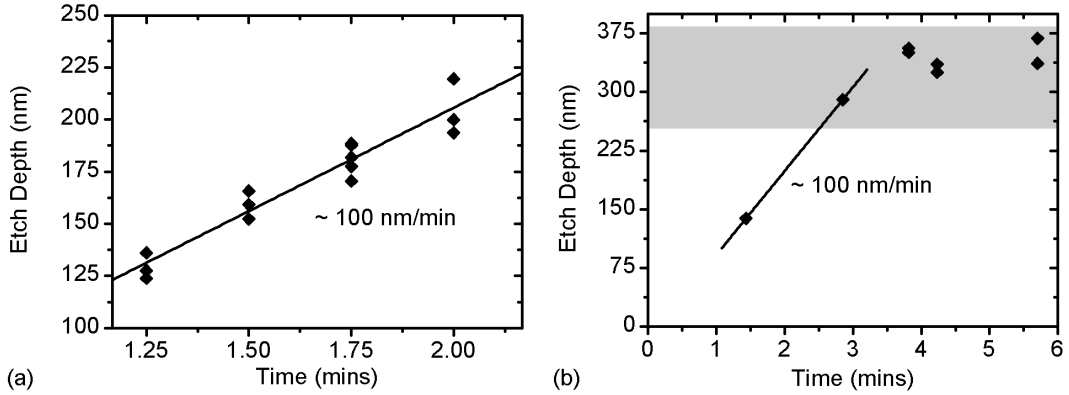

Figure 6.6: a) Etch depth vs. time of NCD using RIE.3 gives an etch rate of ca. 100 nm/min. b) Etch depth vs. time of BNCD using RIE.3 gives an etch rate of ca. 100 nm/min. The shaded grey region indicates the possible maximum etch depth for this BNCD film, hence etch rate is only fitted to the first two data points.

RIE of NCD films and BNCD films (see [250]) both resulted in etch rates of ca. 100 nm/min (Figure 6.6a&b). AFM images were then taken to investigate the evolution of roughness with respect to etch time of the NCD surface. Figure 6.7a-d show AFM images of the raw and etched surface of NCD after the same time increments as used in Figure 6.6a. Whiskers were observed at high density on the etch surface after 1.25 minutes of RIE, and to a lesser extent as RIE time proceeded, however, these images could also be erroneous data from excessive integral gain parameters in the AFM PID control circuit, especially considering whiskers appear on the raw surface of images. In this context, Figure 6.7c shows a smooth etched surface with minimal whiskers, suggesting RIE.3 on NCD to produce a smooth etch and no clear trend in roughness is observed. Taking a cross-section of the etched track in Figure 6.7d, Figure 6.7e reveals sidewalls with aspect ratio of ca. 0.16. This relatively low aspect ratio is most likely due to the postbake process of SPR220 causing reflow of photoresist that gives it a domed profile, which is subsequently transferred into the underlying substrate when the thinner edges of the resist are progressively eroded away during the etch. In actuality, a lower aspect ratio (which still gives defined features) is desirable because it allows easier seeding and regrowth of NCD over BNCD tracks when passivating BNCD electrode structures, and also presents a less sizable barrier for cells to grow onto electrodes, which could otherwise be

directed away from electrodes by electrode track sidewalls, because cells are known to be patterned by micro-scale topography on substrates [102,124].

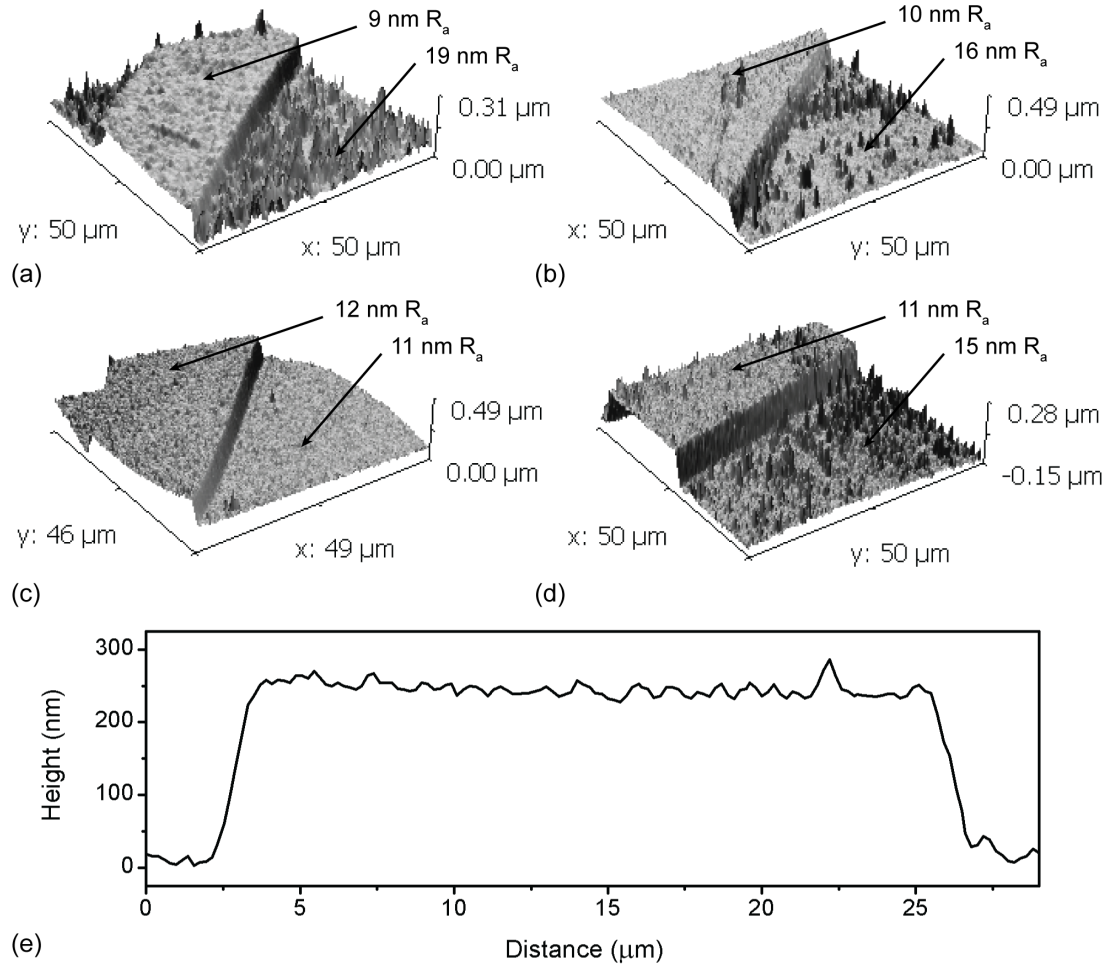

Figure 6.7: AFM scans show the higher, raw surface of NCD and the etched lower surface after different etching times of a) 1.25 mins, b) 1.5 mins, c) 1.75 mins and d) 2 mins. Average roughness, R_a, for the raw and etched surfaces are also displayed. Taking a cross-sectional profile across the track in d), an aspect ratio of ca. 0.16 is obtained. Images have been flattened by plane fitting between 3 points on the raw surface, and were taken using a Veeco Dimension V AFM.

6.3 Micro-Electrode Array Fabrication

6.3.1 MEA Design

Having established and tested a suitable diamond RIE recipe for defining electrodes and tracks, MEAs have been fabricated. The design of the MEAs is that of the Offenhäuser Group in Jülich, Germany, consisting of 64, 20 μm diameter, 200 μm spaced electrodes in a rectangular array, which allows for the single cell action potential recording across cellular networks. The structure of the MEA consists of 64 BNCD electrodes and tracks that expand radially away from the electrodes towards exposes $TiSi_2$ back contacts. These can then be electrically contacted to printed circuit board structures, as described in section 6.4. $TiSi_2$ has been used underneath BNCD in order to 1) improve BNCD adhesion onto the silicon oxide wafer via titanium silicide and titanium carbide formation and, 2) reduce the series resistance of the electrode tracks. The whole chip, except the electrodes and back contacts, have been passivated with one of three materials. 1) SU8 epoxy, 2) Silicon dioxide / Silicon nitride / Silicon dioxide stacks (ONO stacks) or 3) NCD thin films.

The following pages show blown up diagrams of the photolithography mask set used to fabricate MEAs, where Mask C (Figure 6.10) has been firstly used to etch BNCD and $TiSi_2$, then Mask B (Figure 6.9) has been used to remove BNCD from the back contacts, and finally Mask C (Figure 6.8) has been used to fabricate passivation layers. For readers viewing this manuscript electronically, the following pages are intended to be viewed together on overlayed transparent sheets in order to visualise mask alignment.

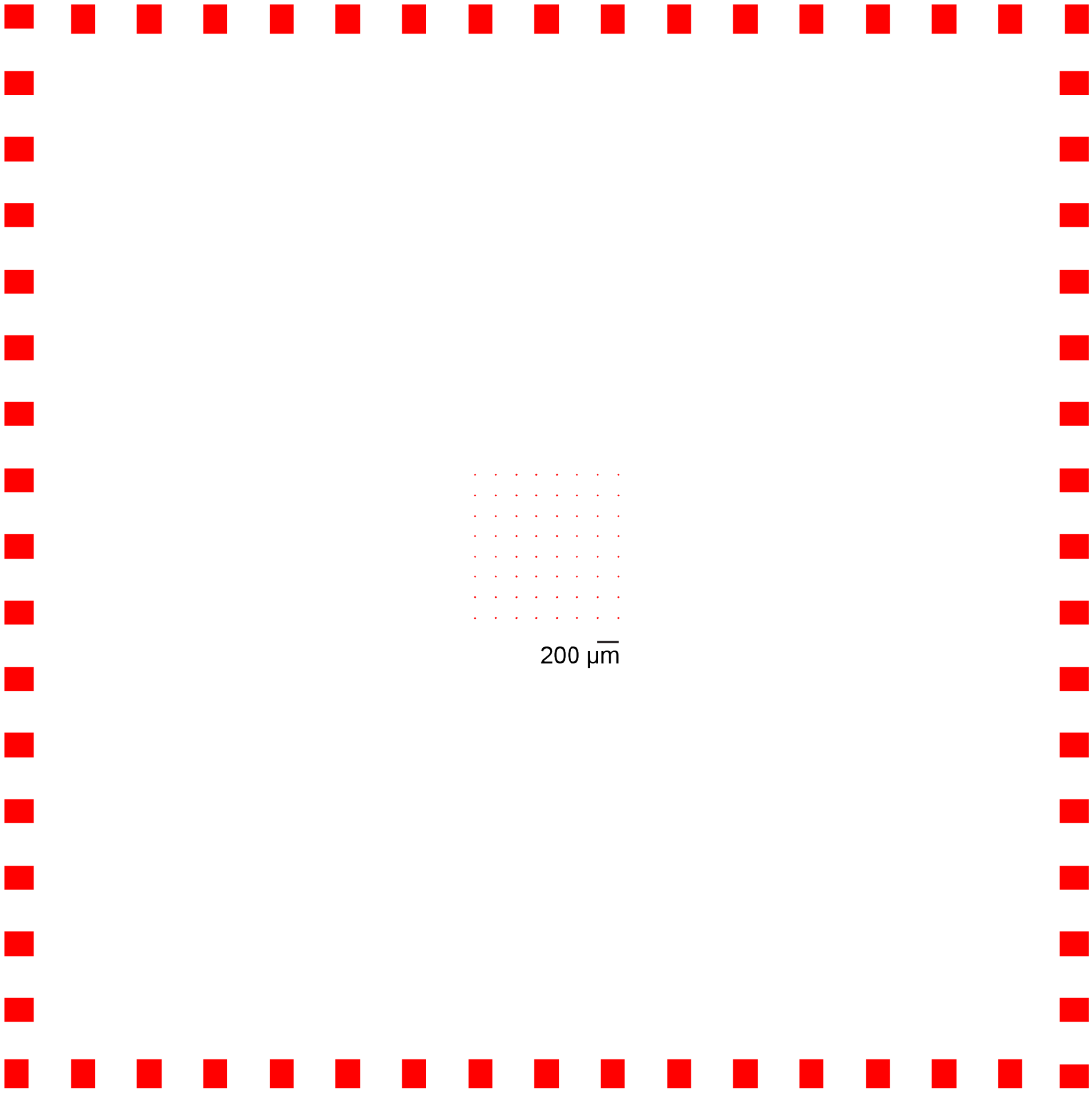

Figure 6.8: Mask A: Back Contacts and Electrodes openings. The shaded red areas show where passivation is opened to expose the BNCD electrodes in the centre and $TiSi_2$ back contacts around the edge of the MEA. Electrodes are circular openings of 20 µm in diameter with 200 µm pitch in an 8 by 8 array.

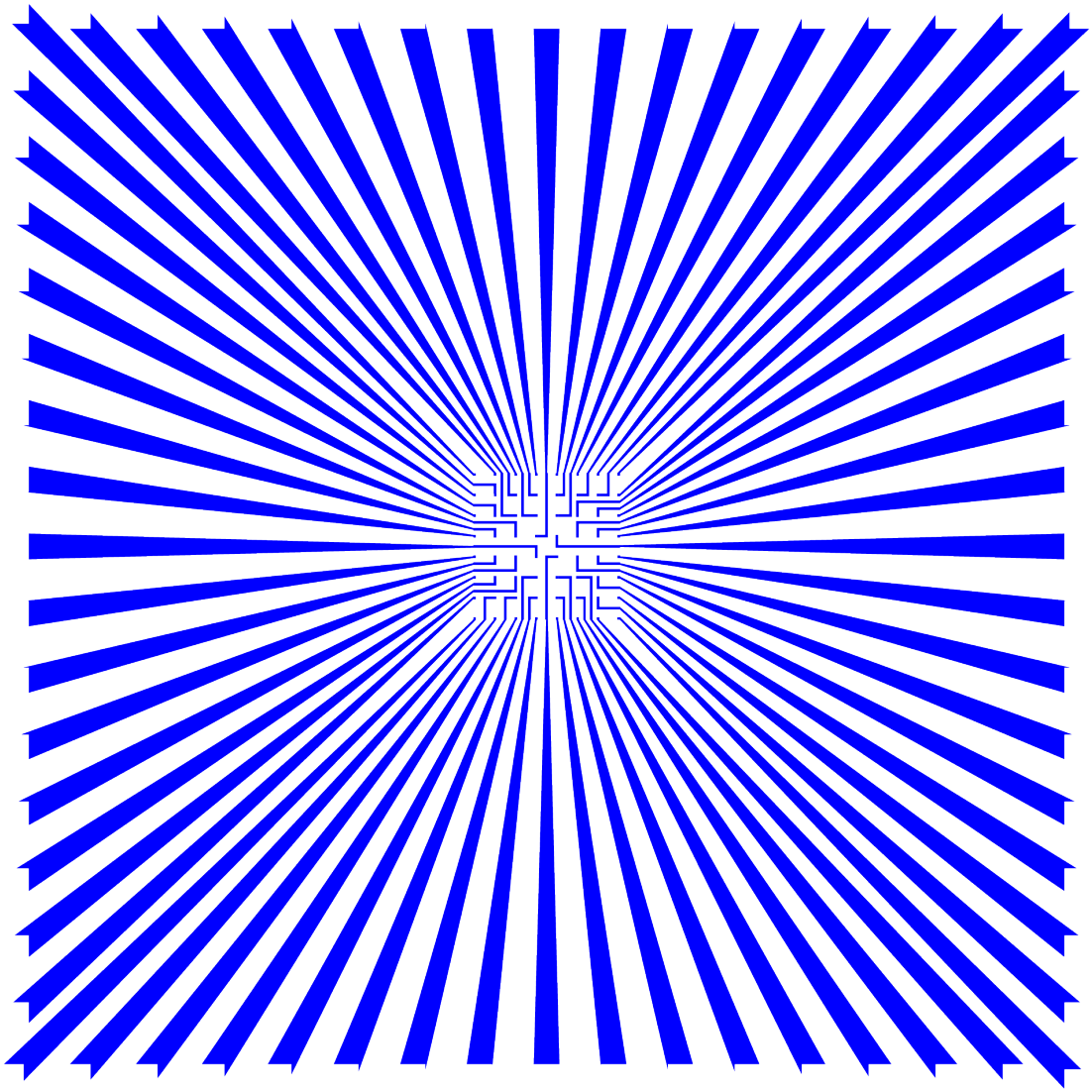

Figure 6.9: Mask B: BNCD tracks and Electrodes. This mask defines the areas of the MEA covered with BNCD. It differs from Mask C in that the back electrode areas are exposed allowing better electrical contacts to the $TiSi_2$ areas. BNCD is only necessary in the centre of the pattern, but is left across the whole device to improve BNCD adhesion. Electrode tracks in the centre pattern are 25 µm wide.

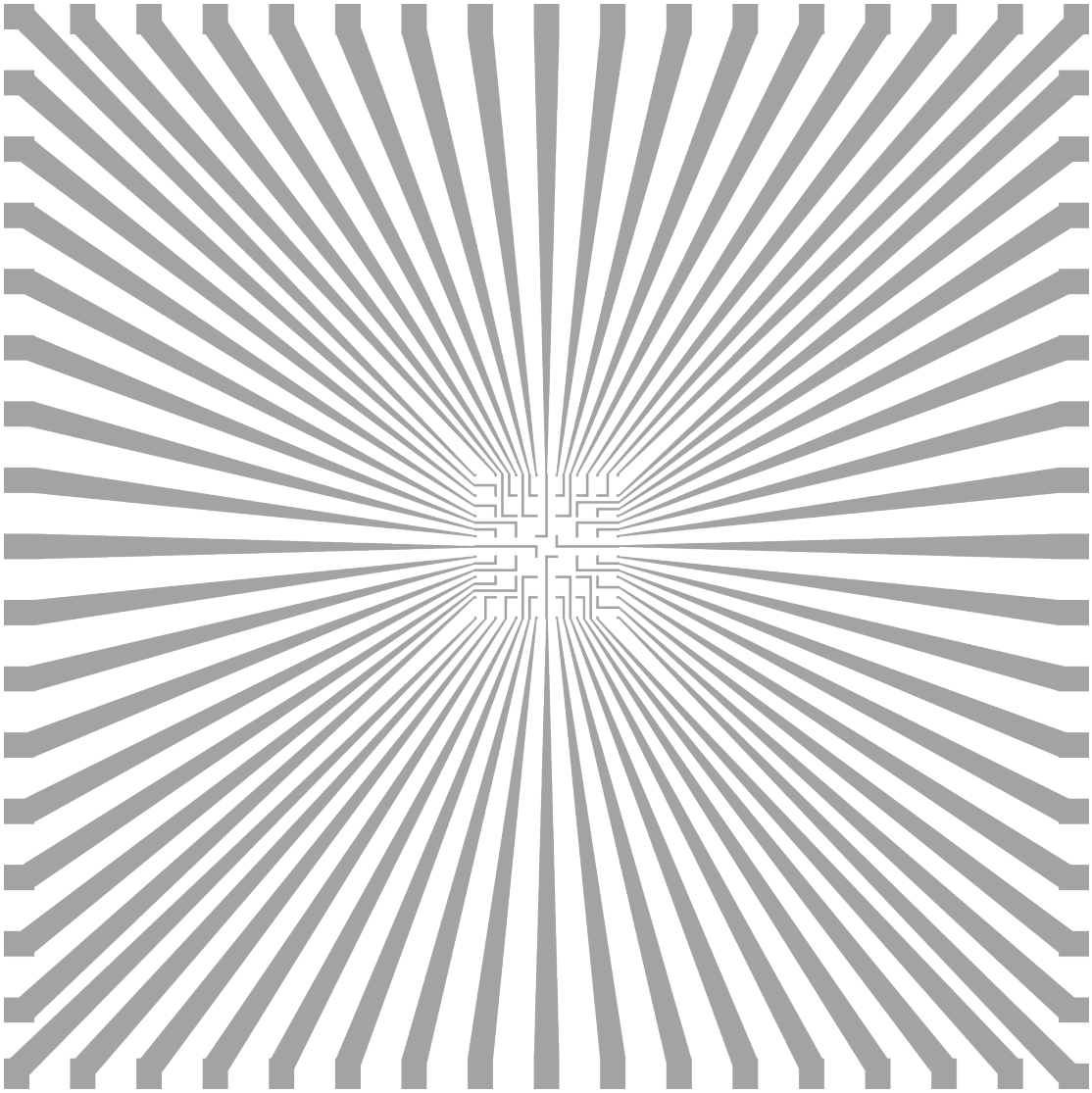

Figure 6.10: Mask C: $TiSi_2$ tracks are patterned using this mask, as are BNCD tracks prior to $TiSi_2$ back electrode opening with Mask B. The whole MEA spans 11 by 11 mm. N.b. if viewing electronically; please print Masks A to C on transparent parchment to see global alignment.

This page is left intentionally blank.

6.3.2 Electrode fabrication

$TiSi_2$ deposition was performed by Sven Ingebrandt, Jülich, Germany using the following process:

Material deposition:

1. 1 µm of SiO_2 (wet oxidation) on silicon handle wafer for capacitive decoupling
2. CVD of 100 nm n-type polysilicon (phosphorous, 10 kΩ/square)
3. E-beam evaporation of 45 nm Ti

Silicidation:

4. Heat at 670˚C for 30 s
5. Etch residual Ti in (H_2:H_2O_2:NH_4OH 5:1:1), however usually all Ti is consumed in step 4.
6. Heat at 850˚C for 30 s to form low resistance $TiSi_2$

Total thickness was ca. 140 nm and 4-10 Ω/square resistance. BNCD was then deposited by CEA, France (Alexandre Bongrain / Emilie Vanhove), as described in section 6.2.2, resulting in a wafer as depicted in Figure 6.11a (i).

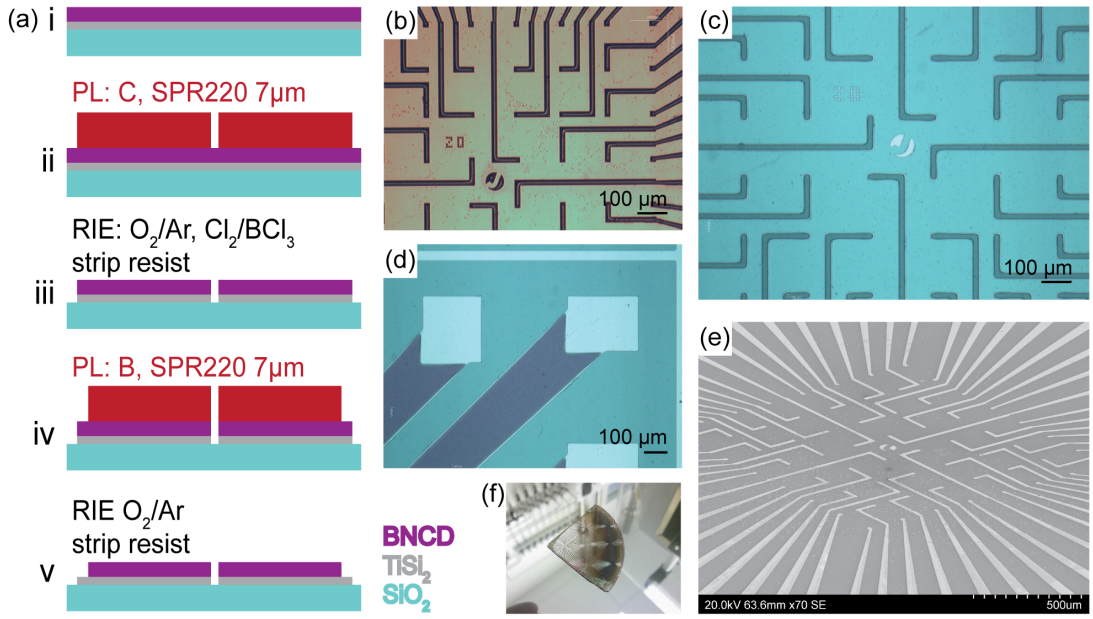

Figure 6.11: a) Process flow used to fabricate MEA electrode structures, up to before the passivation processes. 'PL: C' refers to photolithography (PL) using mask C. b) Patterned SPR220 photolithography corresponding to ii in the process flow. c) Etched electrodes (iii). d) Back contacts exposed after step iv and v. e) SEM image of MEA centre pattern still covered with resist. f) Image of MEA wafer. ¼ wafers have been used to be processable in the MWPECVD reactor; Baobub.

MEA electrodes were then fabricated following the process flow that is illustrated in Figure 6.11a. 12 wafers were processed in total:

i. $TiSi_2$ (ca. 140 nm) / BNCD wafers (ca. 350 nm +) received from CEA.

ii. SPR220 photolithography on wafers using Mask C (see section 4.14 for details). The postbake process rounded the resist, which can be seen from the centralised light sheen off the resist (Figure 6.11b).

iii. RIE of BNCD using RIE.3 for at least 5 minutes. Although etch rates had been determined, each MEA varied in required etch time (max 8 mins); however, it was possible to observe when the BNCD had been fully etched by a change in the DC bias of the plasma, and, more usefully, a colour

change to silver due to $TiSi_2$ exposure. $TiSi_2$ was then etched for an excess amount of time (75 s used, 45 s required) using RIE.4 (Table 6.6) to ensure electrodes were electronically isolated. Again, $TiSi_2$ could be seen to be removed from the MEA via a distinct colour change, serving as a reliable end point detection method. SPR220 was then removed using a 30 minute acetone soak. Slight rounding of features can be seen due to resist reflow (Figure 6.11c).

Etch recipe	Cl_2 (sccm)	BCl_3 (sccm)	Pressure (mTorr)	CP (W)	PP (W)
RIE.4	18	2	3	400	200

Table 6.6: ICP RIE parameters for $TiSi_2$ etching. STS ICP RIE.

iv. SPR220 photolithography using Mask B. Mask misalignments were hard to avoid due to nuances of the alignment equipment used (Quintel Q4000-6), however the reflow of the postbake process served to realign some of the less severe misalignments. Step iv was repeated until satisfactory alignment was achieved.

v. RIE of BNCD using RIE.3 for at least 5 mins to expose the back contacts (Figure 6.11d), and resist striping with acetone for 30 minutes. Ultrasonic bath cleaning was not used to not risk damaging the wafer.

It should be noted that complete MEAs were initially fabricated without exposing the $TiSi_2$ back electrodes; however, this resulted in poor action potential recordings and increased noise when exposed to white light. Therefore, we exposed the $TiSi_2$ back contacts in order to improve the electrical contacts to the printed circuit boards, which fixed both problems.

6.3.3 Passivation Fabrication

Following electrode, track and back contact patterning, the 12 MEA chips were allocated into 3 sets of 4 for different passivation treatments. Firstly, SU8 epoxy resist has been used as a simple, established approach to MEA passivation, which was performed by Jülich, Germany. Secondly, ONO stacks have been used to passivate MEA structures. Thirdly, NCD has been used as passivation, thereby creating an all-diamond MEA.

6.3.3.1 ONO passivation

$SiO_2/Si_3N_4/SiO_2$ (ONO) passivation is routinely used [158,265] for electrode passivation and gives a more durable coating than SU8. The first 'O' – a silicon dioxide layer in contact with the electrodes – is for good adhesion with the underlying SiO_2 and BNCD MEA surface. Secondly, a silicon nitride layer, 'N', is used for improved water resistance (SiO_2 is more permeable to water). Thirdly, a second 'O' layer is used for regaining the enhanced biocompatibility of SiO_2 in comparison to Si_3N_4. Whilst etching ONO stacks can be relatively straight forward, complications have been introduced in etching ONO stacks on top of $TiSi_2$ layers because of low etch selectivity: HF, which is routinely used for etching SiO_2, also readily etches titanium based layers [266]. Alternatively fluorine based RIE processes (e.g. CHF_3) can be used for a slower etch; however, $TiSi_2$ is still etched by F-based gases. Therefore, a precisely controlled etch has been performed using a sacrificial, protective layer of chromium, which does not quickly etch in CHF_3 RIE [266] but can withstand the temperatures required for silicon-based PECVD used to cover the $TiSi_2$ back contacts and centre electrodes.

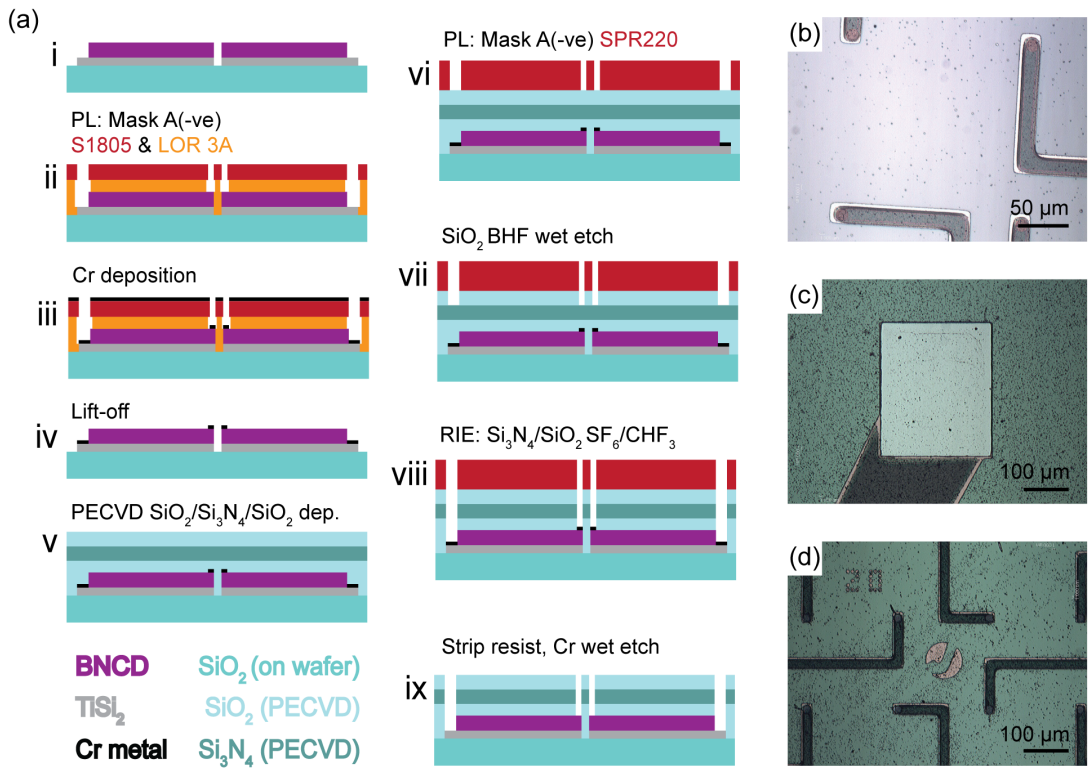

Figure 6.12: a) Process flow used to passivate BNCD electrodes with ONO stack passivation. b) Cr protective masks over the BNCD electrodes prior to ONO deposition, corresponding to process step iv. c) Back contacts and d) electrodes after process step ix.

ONO passivation was deposited as follows using the process flow that is illustrated in Figure 6.12a:

i. Start off with MEA as in Figure 6.11a (v).

ii. S1805 and LOR 3A photolithography using Mask A (see section 4.14 for details).

iii. Deposition of 70 nm of Cr using an Edwards Thermal Evaporator II Bell Jar A306.

iv. Lift-off of Cr by acetone soak (30 minutes) (Figure 6.12b) to leave Cr protective caps.

v. PECVD deposition of ONO layers, 500 nm each (1.5 μm total) using the following conditions, as shown in Table 6.7.

Mat.	N_2 (sccm)	SiH_4 (sccm)	Other (sccm)	Frequency and Power	Pressure (Torr)	Time (mins)
SiO_2	392	12	N_2O: 1420	380 kHz / 60 W	550 mT	8:30
Si_3N_4	1960	40	NH_3: 40	Dual Hz: 13.56 MHz / 20 W, 6 s & 380 kHz / 20 W, 2 s	900 mT	35

Table 6.7: PECVD parameters for depositing SiO_2 and Si_3N_4 in an STS Multiplex PECVD system. Platen and showerhead temperatures of 300˚C and 250˚C, respectively, have been used. Each layer is 500 nm thick.

vi. S1805 and LOR 3A photolithography using Mask A. N.b. alignment to the Cr caps was particularly challenging, and slight misalignments were unavoidable.

vii. BHF etch of top 'O' layer. 3 mins.

viii. RIE of 'N' and bottom 'O' layer using the following RIE recipes as shown in Table 6.8. End point detection of the last 'O' layer was achieved by monitoring fluctuations in the DC bias of the plasma in combination with observing the disappearance of thin film interference fringes of very thin SiO_2 layers, which appeared near the end of the etch. 13 minutes etching of RIE.4 was sufficient to remove Si_3N_4.

Etch recipe	Gas (sccm)	Etch Rate (nm/min)	Pressure (mTorr)	Power (W)	Rate	Time (mins)
RIE.5	SF_6: 100	170	200	100	ca. 40 nm/min	15
RIE.6	CHF_3: 200	100	200	200	ca. 70 nm/min	ca. 20

Table 6.8: Parallel plate electrode RIE parameters using an Oxford Plasma Technology RIE80. ICP RIE was not used for practical reasons.

ix. Resist stripping with 30 mins acetone soak, then 6 minutes in Cr etchant (Sigma Aldrich) (Figure 6.12c&d). Little remnant Cr was visible to be trapped under the ONO stacks near electrodes, which could have been introduced from misalignments in step vi.

6.3.3.2 NCD passivation

Two approaches for NCD passivation were possible. Either NCD could be grown on top of the entire structure, and the electrodes and back contacts could be opened via RIE; or NCD could be selectively grown around the electrodes and back contacts. Firstly, the simpler method of etching down a full NCD film was considered; however, the uneven thickness of NCD films would have resulted in different etch times being required for each electrode and back contact, risking the BNCD being etched away from electrodes whilst trying to open the thicker-covered contacts. Instead, the method of selective growth of NCD around electrodes has been used, as illustrated in Figure 6.13 and described below.

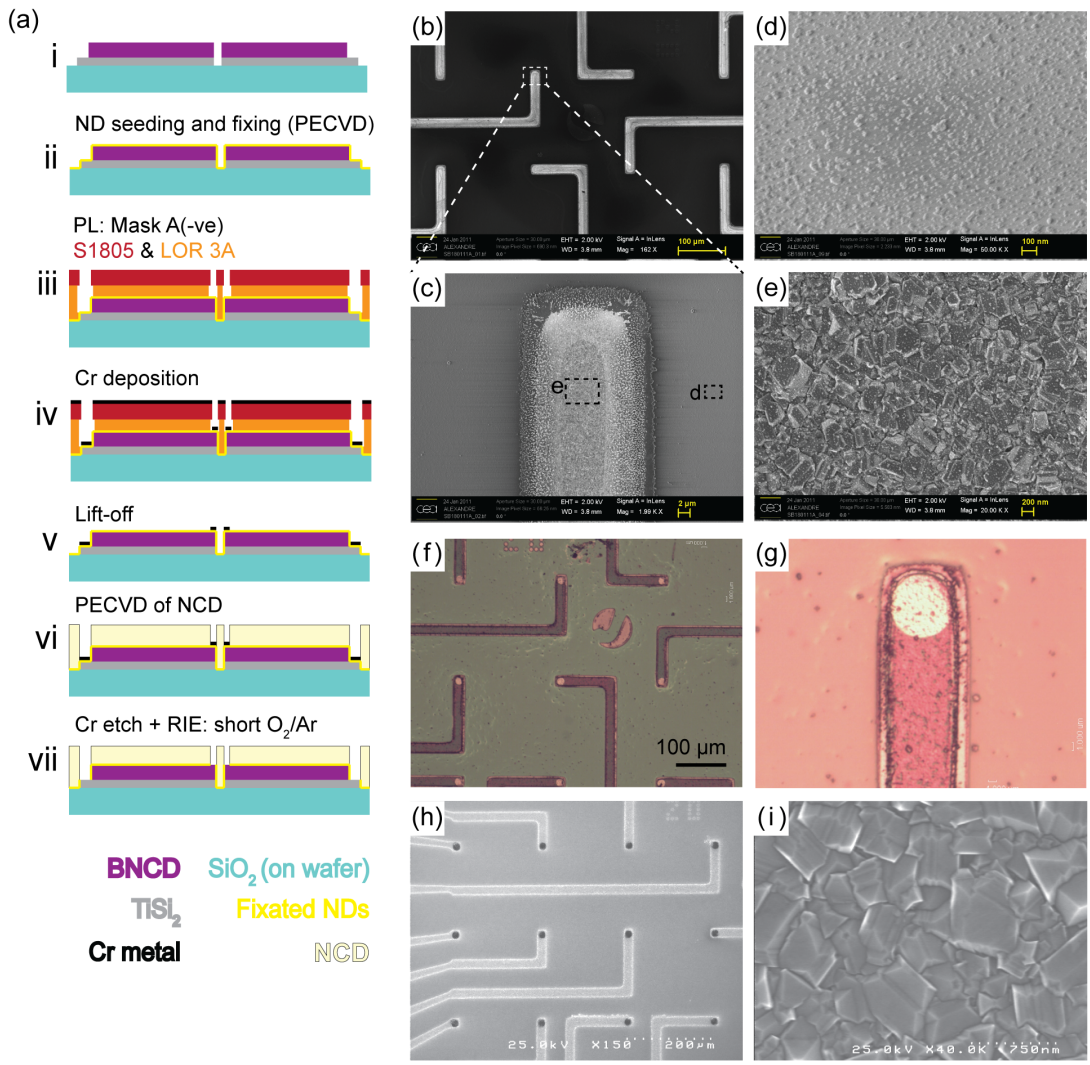

Figure 6.13: a) Process flow used to passivate BNCD electrodes with NCD passivation. b) SEM of seeded and PECVD-fixated ND layer on a MEA electrode structure, corresponding to process step ii. d) Magnification of b) at an electrode, with further magnifications showing the fixated ND layer on the d) SiO_2 substrate and e) BNCD track. f) Optical image of Cr caps deposited on ND coated MEA structures, corresponding to process step v, with g) a magnified image of a 20 µm Cr cap on the electrode. h) Shows an SEM image of NCD grown on top of the MEA, corresponding to process step vii. i) A magnified image of the NCD surface from h) confirms the NCD nature of the deposited material.

i. Start off with MEA as in Figure 6.11a (v).

ii. ND seeding: 0.05 % wt/wt ND hydrocolloid deposited on MEA, 2 mins wait, 2000 rpm 20 sec, 3000 rpm 20 sec. ND fixing: 2 kW, 25 mbar, H_2/CH_4 198/2, 15 mins, performed by CEA, France.

iii. S1805 and LOR 3A photolithography using Mask A.

iv. Deposition of 70 nm of Cr using an Edwards Thermal Evaporator II Bell Jar A306.

v. Lift-off of Cr by acetone soak (30 minutes) (Figure 6.12b) to leave Cr protective caps.

vi. ca. 500 nm NCD growth using parameters displayed in Table 6.5. Performed by CEA.

vii. 6 minutes Cr etch with ultrasonic agitation and a short RIE.3 etch (50 seconds) to remove the fixated ND layer (not masked).

Whilst performing step vii of the NCD passivation process, the problem of Cr being engrained into the BNCD electrodes became evident. Carburisation of the Cr caps during the MWPECVD process of step vi made the Cr very hard to remove from the BNCD electrodes, and it was probable that a significant CrC residue was left on the electrodes, despite the sonicated Cr etching and short RIE of the electrodes. Cr is well known to form carbides with diamond under such temperatures used in MWPECVD; however, Cr (or a similar metal such as Ti) had to be used to withstand the temperatures used in step vi. Moreover, Cr adhesion onto the $TiSi_2$ back contacts, whilst seemingly strong after step v, was in fact quite poor and Cr caps were seen to be eeling off the back contacts after step vi processing. The degree of Cr peeling between the back contacts varied from complete to not at all, and a typical example of Cr peeling, and the resultant NCD overgrowth on the back contacts that would cause electrode failure, is shown in Figure 6.14a. Similarly, an SEM image of Cr being engrained into the BNCD/NCD prior step vii is shown in Figure 6.14b.

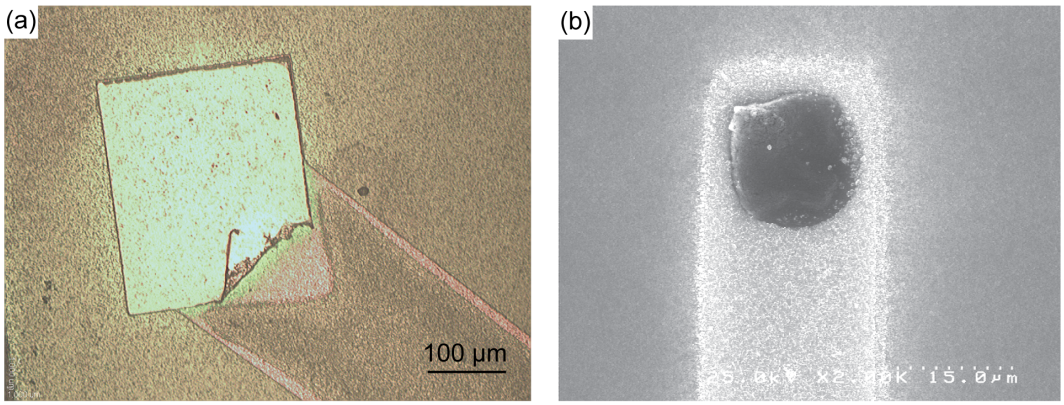

Figure 6.14: a) A typical example of Cr having peeled off the $TiSi_2$ during MWPECVD of the NCD passivation. NCD overgrowth from the exposed ND seeding can be seen in the bottom right of the contact. b) An SEM shows evidence of the dark Cr cap to be somewhat engrained into the BNCD and NCD layer, explaining the difficulties encountered in trying to remove it.

6.4 Summary of MEA recordings of electrogenic cells.

Following microfabrication, MEAs were sent to the Offenhäusser Laboratory in Jülich, Germany, where Vanessa Maybeck tested the ability of SU8, ONO and NCD passivated BNCD MEAs vs. standard metallised electrode MEAs to record the electrogenic activity of cells. For a full description of the performed testing, the interested reader is referred to Maybeck 2011 [174]. This section serves to briefly summarise those measurements. Upon receipt of MEA wafers, MEAs were mounted and encapsulated into custom chip mounts (Figure 6.15a, see [174] for full details) to facilitate cell cultures on the MEA surfaces and to interface them with the electrical measuring system. To create a well for cell culture, a glass ring (7 mm inner diameter) and PDMS sealant has been used.

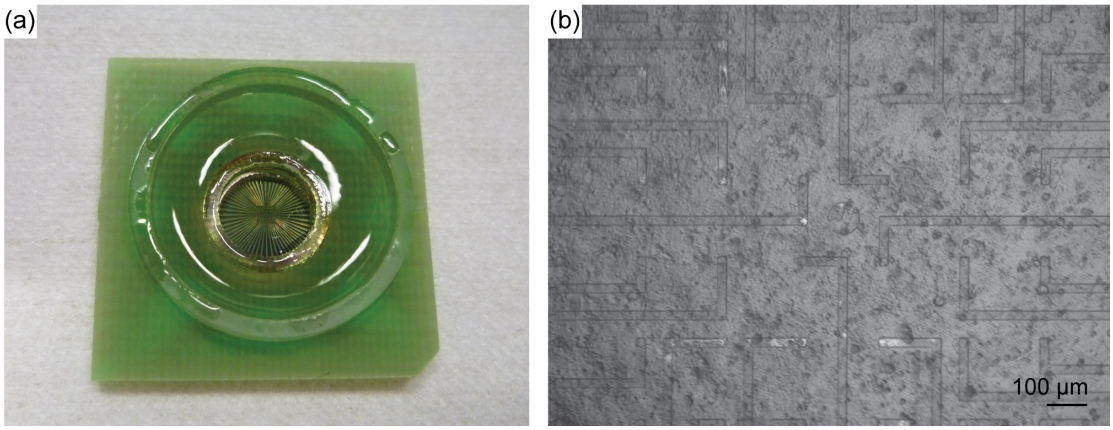

Figure 6.15: a) Encapsulated MEA (SU8), with contacts underneath the PCD board. b) HL-1 cell culture on the surface of an SU8 MEA chip.

HL-1 cardiac cells have been used to evaluate MEA performance due to their signal reliability and shape analysis, as well as the fact that HL-1 cell cultures form a confluent layer of cells. This assures that most, if not all, electrodes are covered by at least one cell (Figure 6.15b), thereby avoiding false-positive signals. False-positive signals can be further eliminated by optically confirming the spontaneous beating of HL-1 cells, by observing waves of propagating action potentials across the cellular network and by averaging superimposed action potentials (APs) over time (aligned to their sodium peak) to confirm AP shape. HL-1 cell cultures on SU8, ONO and NCD BNCD MEAs have been performed (by VM), and, firstly, the working electrode yields of the MEAs were counted.

- SU8 MEAs: 5 out of 8 finished encapsulated MEAs could detect cell signals from HL-1 cells. From these 5 MEAs, a mean of 19 working electrodes was obtained (max 33 min 3). The low yield could have been down to the stability of the SU8 passivation layer, which was seen to crack and peel after two to three cultures.
- ONO MEAs: 8 MEAs were tested that could all detect cell signals with 42 ±14 (s.d.) working channels per MEA.
- NCD MEAs: 5 MEAs were tested that could all detect cell signals, with 57 ±7 (s.d.) working channels per MEA.

Since the above MEAs were fabricated sequentially, the increasing yield of electrodes from SU8 to ONO MEAs in particular is thought to be due to improvements in the production process. The following figure series of Figure 6.16 to Figure 6.18 show representative snapshots of voltage recordings from HL-1 cells over 500 ms windows for each 64 MEA channel, and Figure 6.19 shows time averaged, superimposed APs for each MEA configuration.

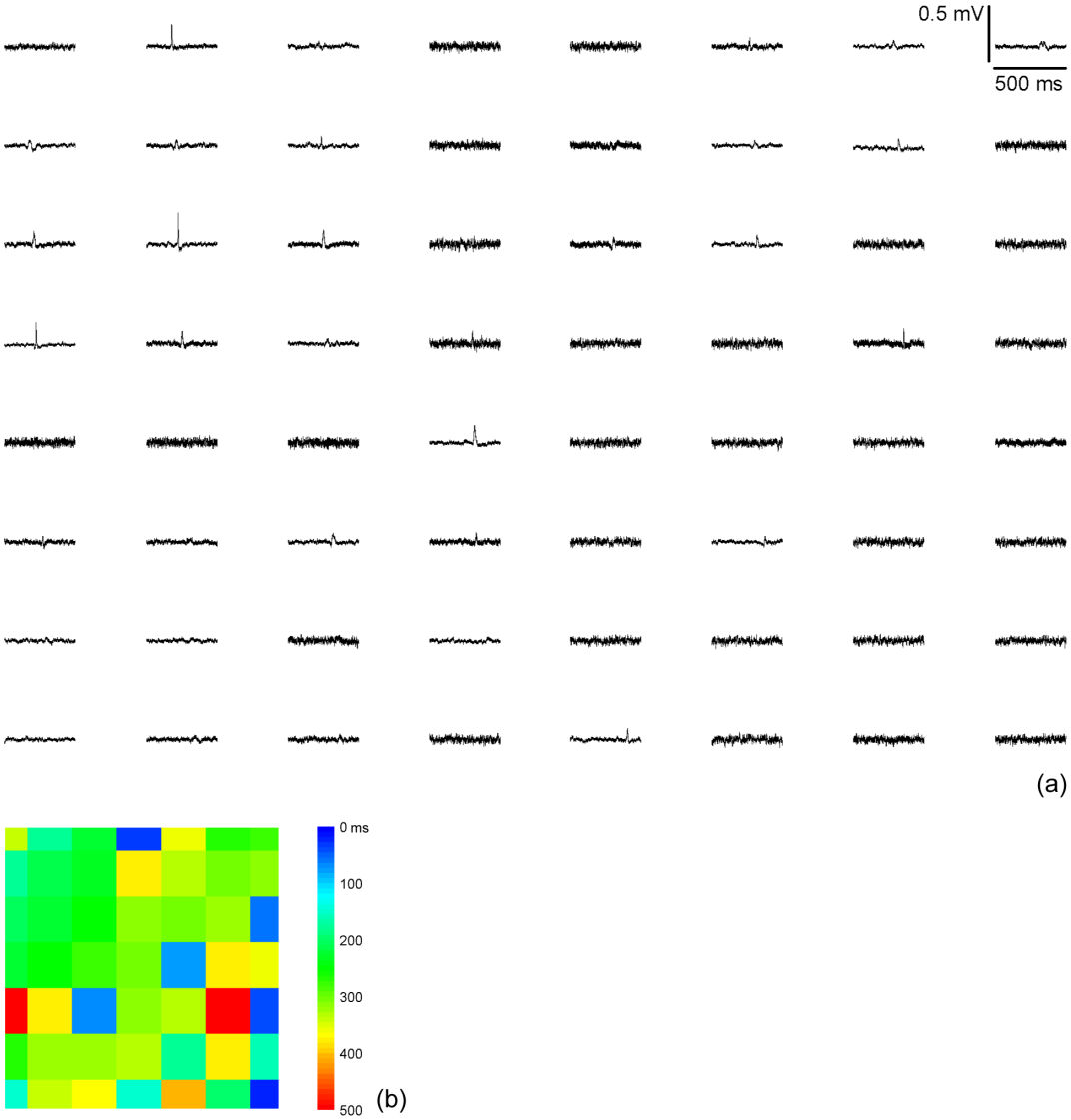

Figure 6.16: a) 500 millisecond recordings of HL-1 cells on the 64 channels of an SU8 BNCD MEA. The thick noisy recordings indicate failed electrodes. b) Time incidence of the peak voltage measurement for each channel w.r.t. the 500 ms time bin shown in (a), either corresponding to the sodium peak of an AP, or peak noise. No clear AP wave can be seen.

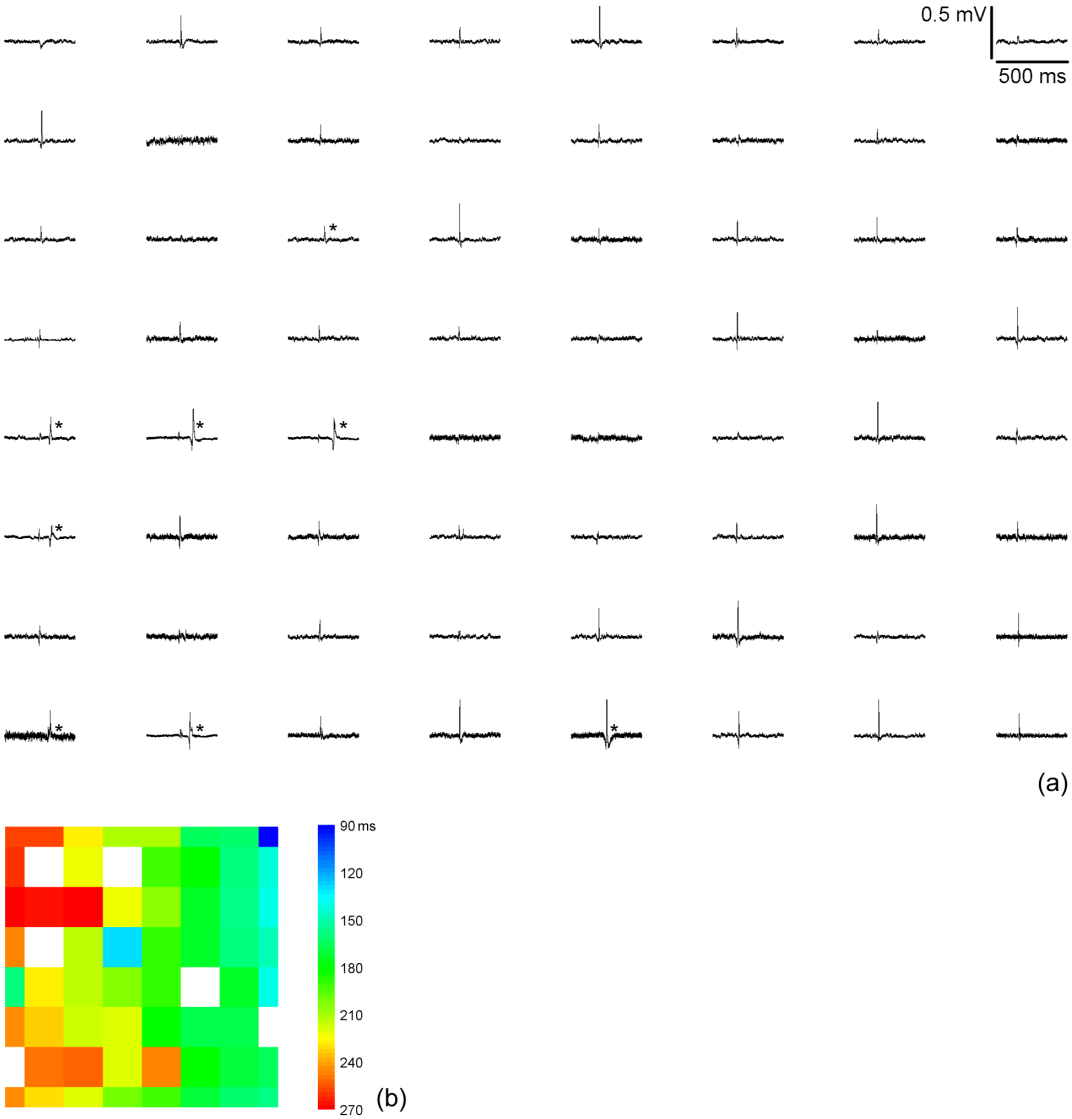

Figure 6.17: a) 500 millisecond recordings of HL-1 cells on the 64 channels of an ONO BNCD MEA. b) Time incidence of the peak voltage measurement for each channel, corresponding to the sodium peak of an AP. Failed channels without an AP have been removed from the graph (blank squares) and APs corresponding to ONO pinhole recordings (*) have been discarded in order to clearly show AP wave propagation. Pinhole recordings are identified as APs occurring close in time but out of line with the modal AP recordings of the propagating AP wave. An AP wave can be seen propagating from right to left across the MEA.

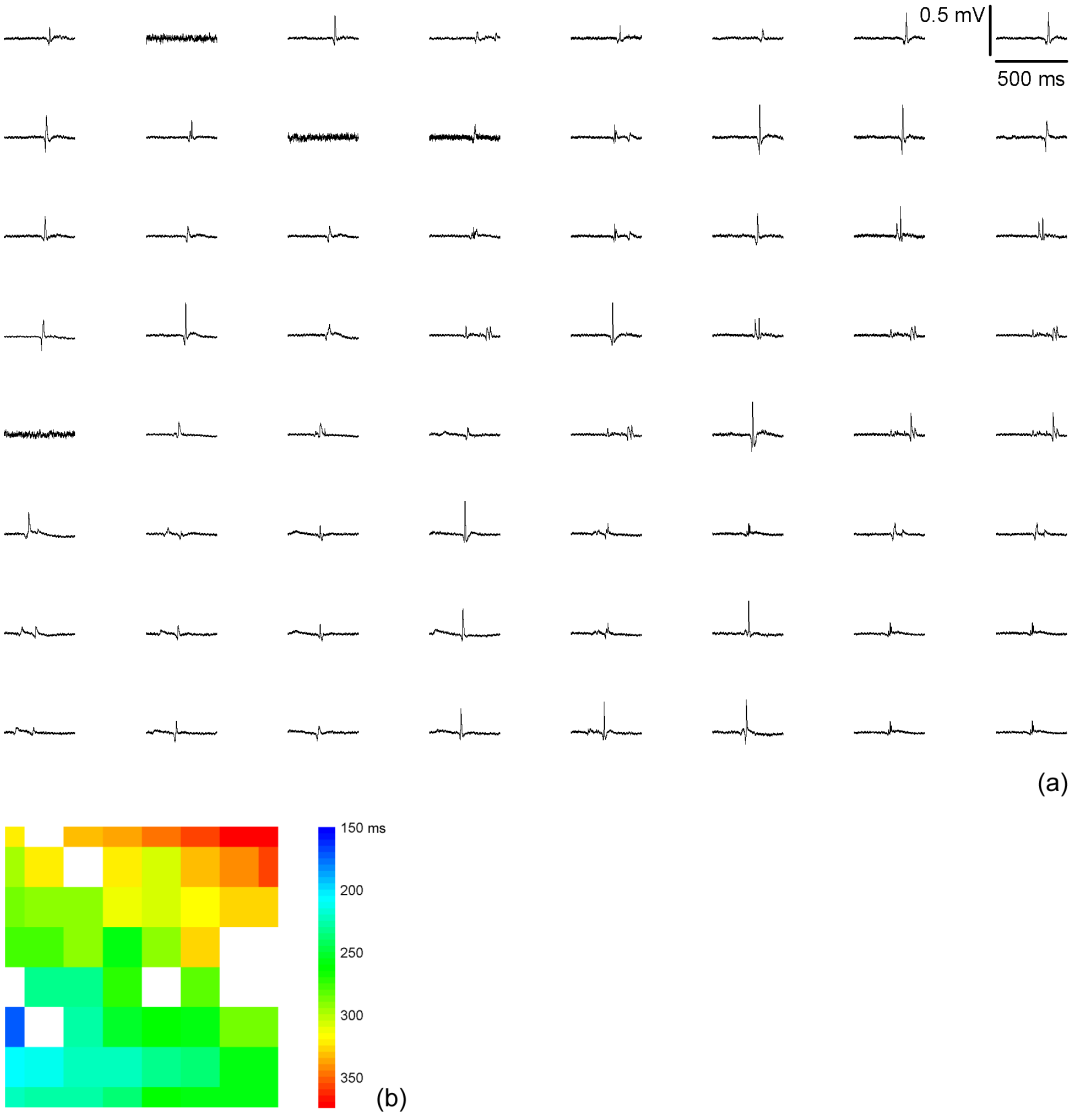

Figure 6.18: a) 500 millisecond recordings of HL-1 cells on the 64 channels of an NCD BNCD MEA. A higher yield of electrodes is evident in comparison to SU8 and ONO MEA designs. b) Time incidence of the peak voltage measurement for each channel, corresponding to the sodium peak of an AP. Channels without an AP and failed channels have been removed from the graph (blank squares). The AP wave can be seen as a graded colour sweep across the MEA from bottom-left to top-right, with a propagation speed is ca. 10-30 mm/s, which is in good comparison to the literature [174].

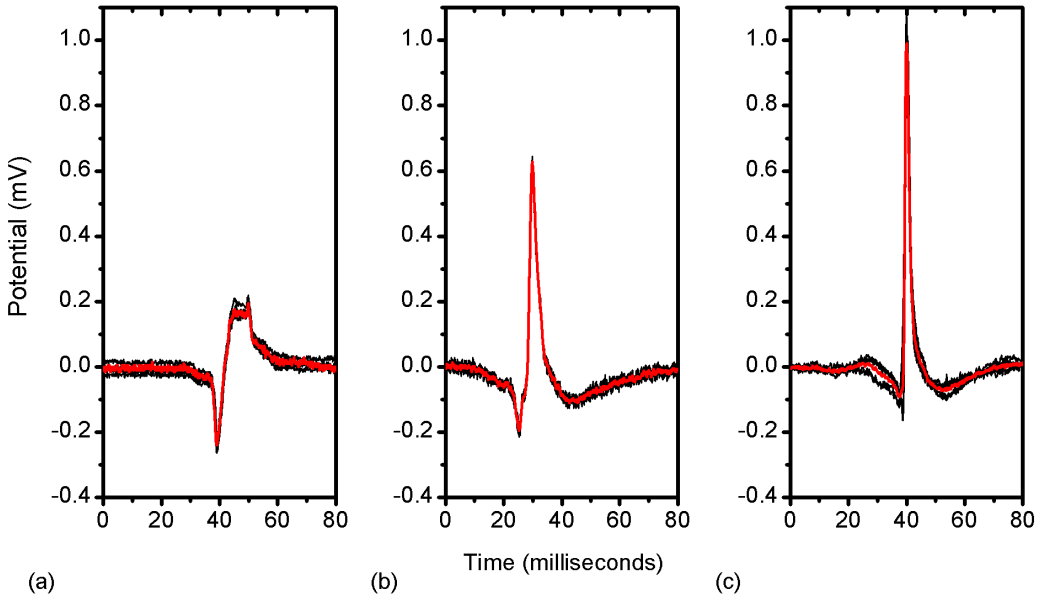

Figure 6.19: Aligning APs recorded from one channel to the sodium peak, APs are superimposed to show AP shape. The channels that were chosen for analysis were the most consistent. Averaging these APs (n=5) AP shape is confirmed, rather than random large amplitude noise. a) SU8. b) ONO. c) NCD.

SU8 MEAs have a low electrode yield (Figure 6.16a) with a signal-to-noise ratio (SNR: peak-to-to peak signal over peak-to-peak noise) that is similar to that of gold-based MEAs (Table 6.9). Inspecting the shape of recorded APs (Figure 6.19a), the sodium peak has not been fully resolved, which is probably a result of the low maximum band pass of SU8 MEAs (Table 6.9). Signal loss is smaller than gold MEAs, which could be due to the increased biocompatibility and enhanced attachment of cells on the BNCD surface.

ONO MEAs improve on SU8 MEAs showing more active channels, a higher SNR (but still similar to gold MEAs) and a fully defined AP shape (Figure 6.19b) in accordance with the larger bandwidth measured for ONO MEAs. Whilst ONO MEAs improve on SU8 MEAs, pinholes in the ONO passivation covering the electrode tracks have meant that unwanted APs are being recorded at unknown locations along the track, as can be seen in Figure 6.17a by large amplitude APs at times before or after the electrode AP, depending on the direction of AP wave

propagation with respect to the electrode in question. This has made the spatial origin of APs ambiguous, reducing our ability to distinguish AP waves; however, pinholes are scarce enough to allow the identification of pinhole recordings by their anomalous nature with respect to the AP wave propagation. In this context, by removing anomalous APs (and null channels) from the analysis, the propagation of an AP wave can be seen (Figure 6.17b) to sweep from right to left across the ONO MEA surface. To improve ONO MEA performance, pinholes could be reduced using an ONONO stack, and SNR could be improved by eliminating Cr (which could be fouling electrodes) from the process.

NCD MEAs further improve on ONO MEAs, showing a considerably higher SNR; however, a large variation in SNR has been measured between NCD MEAs. For example, two MEAs show SNR values of 40 and 36, but one shows an SNR of 4.7, resulting in a high SNR standard deviation of 16.1. Similarly, the bandwidth of NCD MEAs was subject to large variations and erratic behaviour, even for individual channels (see [174]), and as a result could not be determined. That said, for functional NCD MEAs, large SNR values have been obtained with accurate AP shape recordings (Figure 6.19c) and clearly distinguished AP waves (Figure 6.18b). The high degree of variation on NCD MEAs has been ascribed to the fabrication method of using Cr caps to achieve selective NCD growth, and the subsequent etching step after. It is probable that the BNCD electrodes have either not been fully exposed in the RIE step, or have been fouled by Cr incorporation, or both.

MEA	Signal-to-noise ratio	Bandwidth (Hz)	Signal loss (%)
SU8 BNCD	7.6 ±3.6	50±40 – 800±200	15 ±12
ONO BNCD	8.4 ±2.1	40±40 – 2000±300	26 ±5
NCD BNCD	22.6 ±16.1	N/A	N/A
ONO Gold*	10.9 ±4.7	30 – 2000	30

Table 6.9: Summary of MEA metrics. Error is ± standard deviation. * Best performance data from D. Brüggemann [174] using planar gold MEAs of 20 μm diameter electrodes.

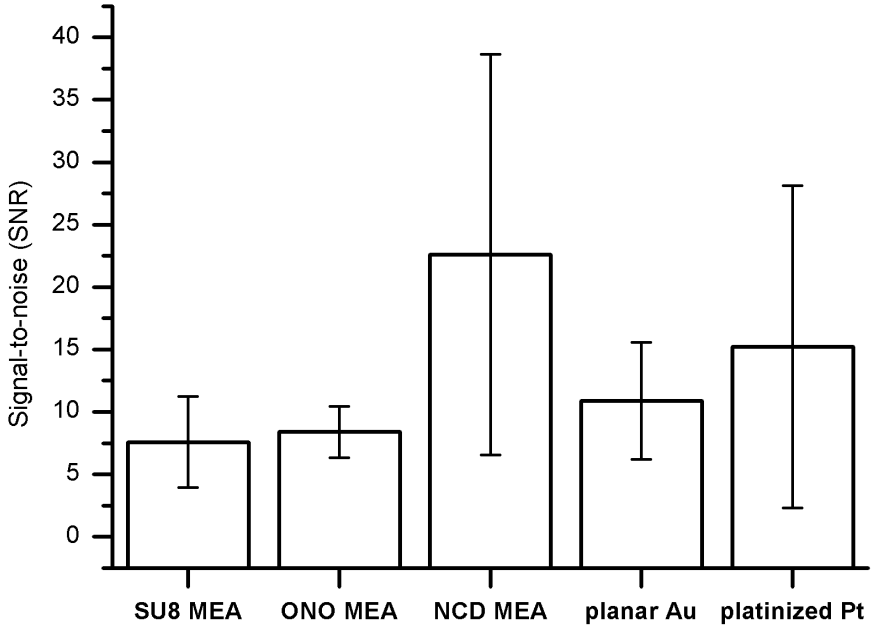

Figure 6.20: SNR for the various types of MEA tested in comparison to standard gold and platinum electrode MEAs. SU8, ONO and NCD MEAs have BNCD electrodes.

6.5 Conclusions

An optimised RIE recipe has been developed for the smooth, high-aspect ratio etching of diamond. 64 electrode MEAs have been fabricated using highly doped BNCD with SU8, ONO and NCD passivation. SNR has been improved for SU8-passivated and ONO-passivated BNCD MEAs; however, they are not statistically different from standard gold MEAs. NCD passivated chips show larger SNR ratios than standard gold and platinum MEAs, and since the variability in the NCD MEA measurements can be attributed to the production process, the high average SNR suggests that, if production can be made more consistent, the good interaction between cells and an all diamond surface can lead to a superior recording MEA.

Chapter 7 Growth and electrical characterisation of δ-doped boron layers on (111) diamond surfaces

7.1 Introduction

In comparison to other group IV semiconductors diamond possesses outstanding intrinsic electrical properties. The potential for high carrier mobilities, coupled with its high breakdown voltage and high thermal conductivity, make diamond a very attractive material for high power and high frequency electronic devices [267]. However, diamond's shortcoming as an electronic material lies in its short lattice constant resulting in few elements being suitable for substitutional doping, and those which are (boron, nitrogen and phosphorous) display large thermal activation energies [42,58]. Boron, the most commonly used diamond dopant, has the smallest activation energy of 0.37eV at low doping concentrations ($< 10^{17}$ cm^{-3}). This value still means that only a fraction of the boron present is activated at room temperature leading to relatively low concentrations of free carriers. Increasing the boron concentration reduces this activation energy, and at ca. $3x10^{20}$ cm^{-3} the concentration of boron becomes sufficient to pass the metal-to-insulator transition (MIT) point and a fully-activated impurity band is formed via the quantum tunnelling of holes between neighbouring boron acceptor states [48]. Unfortunately, as the activation energy of holes decreases, so does carrier mobility, not only because of the increased impurity scattering, but also due to the onset of a low-mobility, hopping-like conduction. The resulting material is one that has sub-unity carrier mobility and typical sheet carrier densities in excess of that which are readily controlled by a typical Field-Effect Transistor (FET) [268].

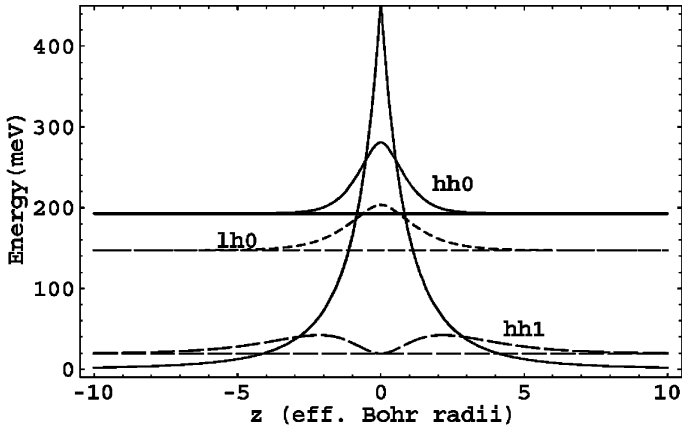

Figure 7.1: Modelled energy potential profile and hole levels of a diamond δ-doped layer with p_{2D}= 5×10^{13} cm^{-2} [269]. The probability density associated to each level is schematically shown above the corresponding energy line in the graphics. For higher energy levels the holes are more delocalised from the δ-layer.

A potential solution to this problem of doping diamond is to use a δ-doped boron layer [270]. δ-doping consists of heavily doping a metallic conductive channel in diamond on the nanoscale, with the aim of reducing its sheet carrier density whilst simultaneously enhancing its mobility. In theory, δ-doping works by reducing the thickness of a heavily doped layer to a thickness significantly smaller than the de Broglie wavelength of holes in diamond (10 nm [57]), so that the charge distribution of the carriers form a V-shaped potential well within which a 2D hole gas forms that extends into the higher mobility, surrounding intrinsic diamond [271]. The simple reduction of channel thickness also reduces the sheet carrier density of the channel to FET gate-mutable levels, whilst the partial delocalisation of carriers into the higher mobility intrinsic diamond lends the channel a higher carrier mobility [272]. In order to achieve a high degree of hole delocalisation, the δ-doped region must fulfil certain specifications. Firstly, the δ-doped region must be substantially thinner than the de Broglie wavelength of holes in diamond (ca. 100 Å [57,271]) and have an abrupt δ-function-like depth profile with boron concentration transitions shorter than the Debye length in diamond in order to allow the formation of a 2D hole gas [273]. Secondly, the

boron concentration, and thereof the hole concentration, must be sufficiently dense (>10^{20} cm^{-3}) so that its charge distribution forms a deep V-shaped potential well within which its carriers can populate more delocalised states with higher mobilities [269,272], but not be so dense that any FET subsequently fabricated would require gate voltages in excess of diamond's breakdown voltage for its control (>$4x10^{13}$ cm^{-2} [268]). This results in a requirement of ca. 1 nm, ca. 10^{20} cm^{-3} δ-layers. Thus, precise deposition of near-atomic layer thicknesses of boron doped diamond are required, but unlike III-V and Si technologies, where molecular beam epitaxy (MBE) can be used, diamond layers must be grown using the method of Plasma-Enhanced Chemical Vapour Deposition (PECVD) which does not offer such immediate levels of control over the thickness of deposited layers. Therefore, in comparison to standard diamond PECVD, δ-doping is particularly challenging. Not only must PECVD parameters be optimised for high quality, heavily boron-doped diamond deposition, but the short timescales required for ca. 1 nm of diamond growth result in the need for carefully controlled growth protocols being developed.

To date, all attempts at the growth of single crystal δ-doped boron layers on diamond have been using the (100) lattice plane due to the wide availability of high quality diamond films and the reduced lattice strain expected in comparison to the higher density (111) and (110) planes [163,270,274-276]. Whilst ultra-thin doping profiles have been achieved, relatively poor mobility values have been reported to date [273]. Instead the (111) plane is proposed for δ-layer deposition. The authors have previously shown that the (111) diamond plane can support higher doping densities for a given mobility value than diamond (100) [277] and the (111) diamond plane has also been found to be advantageous for the realisation of superconductivity in diamond [278]; similar advantages may be useful in diamond δ-doping. Firstly, the (111) crystal plane has an eight times higher boron incorporation density than the (100) diamond lattice plane [50], which could allow for thinner δ-layers with equivalent boron content. Furthermore, Kitagoh et al. [279] have shown how the (111) diamond plane outperforms the (100) plane by at least one order of magnitude in sustaining high boron dopant densities at low doping thicknesses (Figure 7.2a).

Secondly, the (111) plane brings the advantage that its carrier concentrations can exceed its boron concentrations, allowing more carriers into the channel without increasing impurity scattering [278]. This doping phenomenon may be a consequence of the formation of additional conductive channels, the distortion of the Fermi surface [280] or, less desirably, due to a larger effective mass of holes [281]. Thirdly, although (111) diamond is usually avoided as an electronic material due to its defective and dislocated crystal structure, thin layers of (111) diamond (<200 nm) can be of relatively high quality (Figure 7.2b) in comparison to (100) diamond [279] (Figure 7.2c). (111) diamond may come with the disadvantages of greater surface roughness and increased lattice strain from impurities causing increased carrier scattering [282]. However, the potential energy of anisotropic strain in (111) diamond grown by CVD may in fact be lower than that of homogeneous strain in (100) diamond [278]. This chapter addresses the use of the (111) diamond surface for the fabrication of boron δ-doped structures using PECVD. Electrical characteristics have been investigated using AC Hall Effect and Dielectric Impedance Spectroscopy, and SIMS has been used to investigate the boron concentration profiles in doped samples.

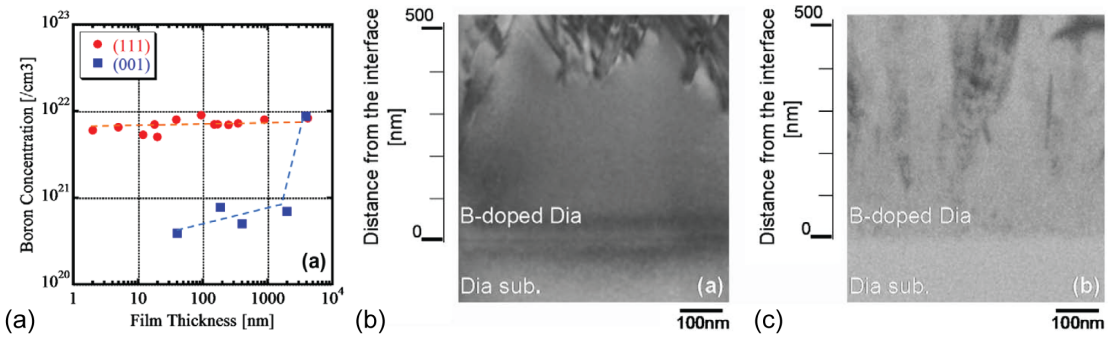

Figure 7.2: All panels from [279]. a) Boron concentration is more than one order of magnitude higher in (111) diamond than (100) diamond using the same PECVD conditions. b&c) Cross-sectional TEM images of (111) film (b) and (100) film (c). In the initial (111) growth layer a nearly defect-free structure with lattice strain is observed, however a defective structure is observed in the (100) film.

7.2 δ-doping (111) diamond

Heavily doped boron layers are required (ca. 10^{20} cm^{-3}) with abrupt 1 nm δ-doped profiles. Considering these requirements a microwave PECVD recipe was designed to give a) a high boron incorporation density via the optimization of gas ratios in the growth plasma and b) sharp boron concentration gradients with respect to layer thickness via slower diamond growth rates and a revised protocol of gas injections. The PECVD parameters of power and pressure were fixed at 600 W and 80 Torr, respectively, in order to simplify the interpretation of gas mixture changes during the iterative recipe refinement process.

Firstly boron concentration was considered. The boron incorporation density primarily depends linearly on the boron-to-carbon ratio in the gas phase, $(B/C)_{gas}$, and from multiple calibration measurements (Figure 7.3), a value of 600 parts per million (ppm) $(B/C)_{gas}$ ratio was selected to generously achieve sufficient doping of $>3x10^{20}$ cm^{-3}, without producing excessive sheet carrier densities. Whilst lower $(B/C)_{gas}$ ratios can achieve sufficient boron concentration for metallic doping, a higher $(B/C)_{gas}$ was chosen to account for the calibration measurements being from thickly doped layers and to buffer the large variance in boron concentrations for a fixed $(B/C)_{gas}$.

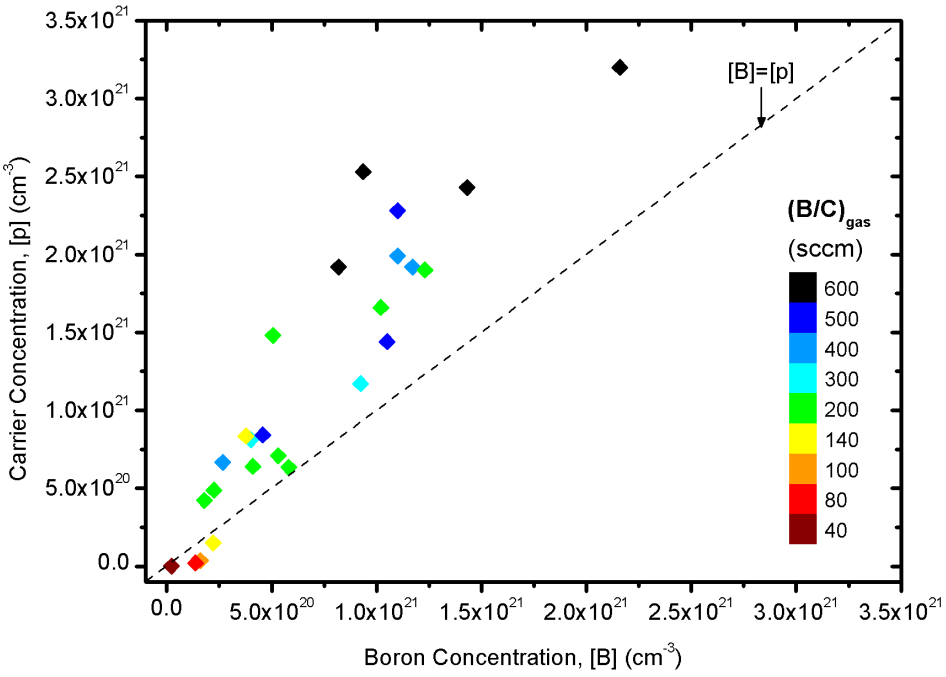

Figure 7.3: Historic data on boron-doped (111) diamond layers grown with varying $(B/C)_{gas}$ ratio. For high doping density, carrier concentration (as determined by AC Hall Effect) is superlinear with respect to boron density (as determined by SIMS) in accordance with previous findings.

Secondly the percentage of methane in the gas mixture was considered. To date δ-growth attempts on the diamond (100) plane have necessitated relatively high methane percentages (ca. 3 %) because the (100) plane of diamond is less efficient at incorporating boron at low methane percentages [48,283]. The (111) plane does not share this reduced ability to incorporate boron at low methane percentages and, as a result, lower methane percentages can be used to achieve slower, more controllable, higher quality and less graphitic diamond depositions, whilst maintaining high boron incorporation densities. A methane percentage of 0.3 % methane (with respect to total gas mixture) was selected for δ-growth, which was purposefully set above ca. 0.15 % CH_4 as to avoid hydrogen etching being dominant during δ-growth [12]. This results in a growth rate of ca. 0.015 nm/s and a 60 second growth period for a 1 nm deposition (Figure 7.4).

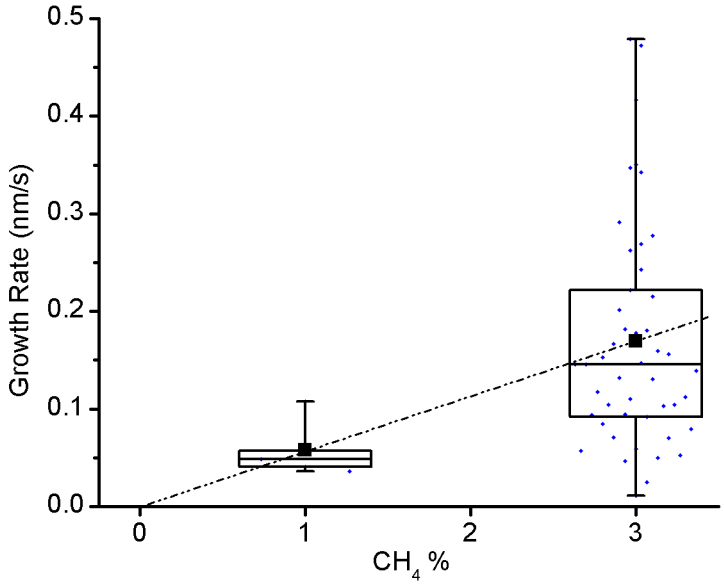

Figure 7.4: Growth rate as a function of CH_4 % in PECVD gas mixtures. The graph shows two sets of data for a series of calibration measurements performed at 1 and 3 % methane, and are represented as box charts. Box chart lines from top to bottom are 100, 75, 50, 25 & 0 %, and the solid marker is the data mean. The corresponding data points are displayed distributed around the box chart in blue and shown with the correct growth rate, but offset from their actual CH_4 % from either 1 or 3 % for ease of visualisation. Performing a linear fit of mean growth rate vs. CH_4 %, a growth rate of 0.015 nm/s is estimated.

Slower growth rates not only result in better quality diamond [284] but also allow for more abrupt doping profiles because less diamond is deposited during the transient periods of the PECVD gas mixture when $(B/C)_{gas}$ and CH_4 % are not stable. The order of gas injection was then considered to further optimise these transient growth conditions that occur at the edges of the δ-doped region. To date, δ-growth attempts have used a PECVD background plasma of hydrogen and methane with an short injection of a boron containing substance [273] (boron rod, Diborane gas or Trimethylborane (TMB)). In this work a different protocol has been used that aims to reduce residual boron doping either side of the δ-doped region, and reduce boron contamination in the underlying intrinsic diamond epilayer. Instead, methane has been pulsed into a stable plasma of

hydrogen and TMB. This method should be advantageous for depositing δ-layers, firstly, because the initial H_2/TMB plasma contains negligible carbon and so no diamond growth occurs, which, in a boron-PECVD chamber, would be contaminated with boron reducing the efficacy of the V-shaped potential well. Secondly, by injecting CH_4 instead of TMB into the plasma, during transient gas mixture periods, the $(B/C)_{gas}$ remains at high values (> 600 ppm) instead of being proportional to CH_4 %. This is particularly important for the second transient step where, in the case of injecting boron into the gas mixture, long-lived boron gas residues in the chamber would produce a lower boron concentration doped 'tail' after the δ-layer. Injecting CH_4 avoids this by the CH_4 gas residue only resulting in a slowing growth rate (and eventual slight etching of diamond) in an increasingly high $(B/C)_{gas}$ plasma, which should result in an abrupt boron concentration gradient (Figure 7.5).

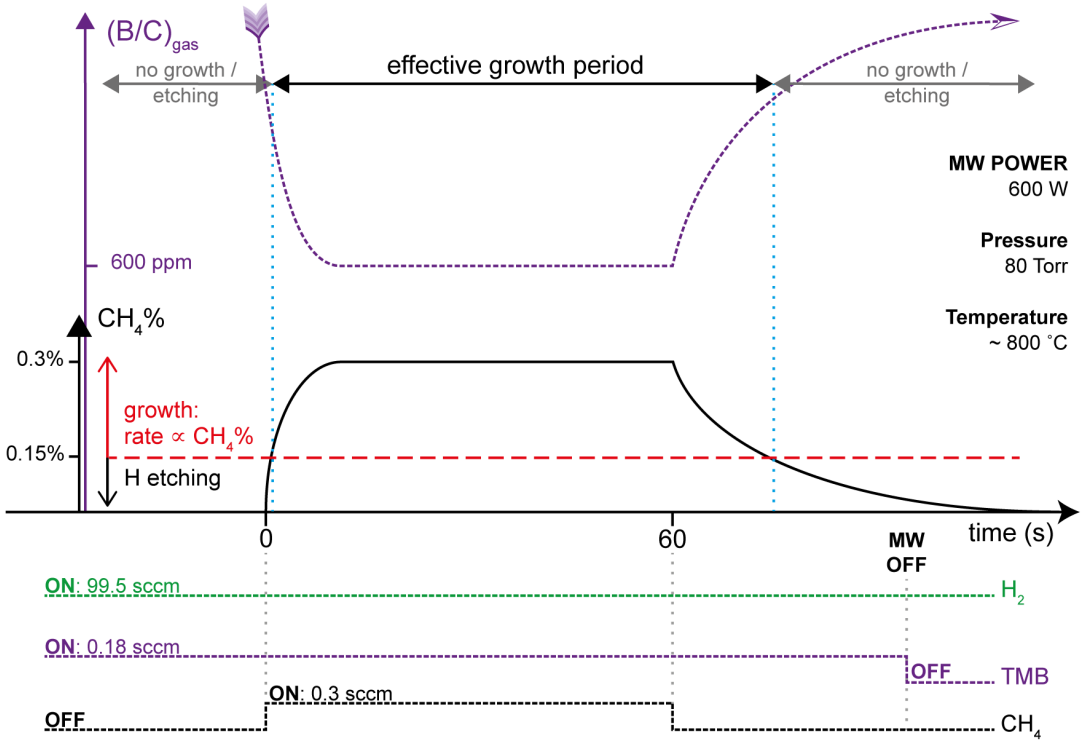

Figure 7.5: Schematic diagram of the PECVD protocol used for samples C & D in this study (see section 7.3). The bottom set of dashed lines depicts the status of the gas injections with respect to time, and the top graph shows the resulting gas mixture in the PECVD chamber. In this simplified picture, pulsing methane should result in δ-layers which have boron concentration depth profiles that

mimic in shape the $(B/C)_{gas}$ dashed line within the effective growth period abrupt drop-offs in boron concentration either side of this region. For δ-layers deposited by pulsing TMB, the depth profile of resulting δ-layers should more-resemble the CH_4 % line shape, showing less abrupt interfaces with doping tails.

7.3 Experimental methods

To fabricate heavily boron-doped δ-doped diamond layers, polished 2 mm square (111) diamond substrates (2x2mm, Suitomo Electric Ltd, Japan) were used throughout. Intrinsic undoped diamond epilayers of ca. 600nm thickness and ca. 2 nm average roughness (as determined by atomic force microscopy, AFM) were deposited using PECVD in both ASTeX AX2050 and Seki Technotron Corp AX5010 plasma reactors using the parameters shown in Table 7.1.

CH_4 (sccm)	H_2 (sccm)	Power (W)	Pressure (Torr)	Temp. (°C)	Time (hours)
0.4	399.6	750	35	500	6

Table 7.1: PECVD parameters for epilayer depositions.

Heavily-doped boron layers were deposited in a 'NIRIM-type' PECVD reactor using the conditions given in Table 7.2. δ-doped layers had average roughnesses of ca. 2.5 nm (as judged by AFM). Plasmas were extinguished 1 min after CH_4 was closed and all samples were cooled for 20 mins in 50 Torr, 400 sccm H_2 ambients. Prior to PECVD all reactors were evacuated to at least 5×10^{-6} Torr. Samples were left uncapped, i.e. without further deposition of capping, intrinsic diamond.

Sample	$(B/C)_{gas}$ (ppm)	CH_4 %	TMB (sccm)	CH_4 (sccm)	H_2 (sccm)	Power (W)	Pressure (Torr)	Temp. (˚C)	Time
A	6000	3	1.8 h	3	95.2	600	80	~800	8 hrs
B	6000	3	1.8 h	3	95.2	600	80	~800	8 s
C&D	600	0.3	0.18 l	0.3	99.5	600	80	~800	60 s

Table 7.2: PECVD parameters of heavily boron-doped diamond layers. Sample A&B use high conc. (h) TMB at 1.09 % (in H_2), and C&D use low conc. (l) at 0.0977 %.

Ohmic contacts were required for 4-point Van der Pauw AC Hall Effect measurements, which consisted of triangular Ti-Au contacts (20 nm and 100 nm, respectively) slightly inset from the corners of the samples. The contacts were subsequently annealed at 700 K in a hydrogen atmosphere (20 Torr, 100 sccm, 30 mins) [206]. Samples were oxygen terminated before and after contact formation with a UV photochemical treatment [285] in the presence of ozone for 3 hours to suppress hydrogen surface conductivity. AC Hall measurements were carried out using Toyo Technica Resistest 8300 equipment. Samples were prepared for Impedance Spectroscopy (IS) measurements in an identical method, except in a 2-point probe configuration with a source and drain of 80 μm gate length and 2 mm gate width. IS measurements were performed within the temperature range 300 to 525 K (in 25 K then 50 K increments) in air and vacuum (ca. 10^{-3} Torr) using a Solartron SI 1260 with the High Impedance Input Module 1296. Measurements were repeated 3 times at each temperature. Errors in the measurement are not shown here as they are too small to visualise. Before vacuum measurements samples were put under vacuum and subjected to a dehydration bake at 500 K. Ultra low energy SIMS measurements were performed using an Atomika 4500 Quadrupole SIMS instrument under ultra high vacuum ($5x10^{-10}$ mbar) using an oxygen primary ion beam with the following parameters: energy 250 eV, current ca. 30 nA, area ca. 180 μm by 180 μm and normal incidence. Boron concentrations were calibrated using a PECVD boron doped diamond reference sample (ref: D121, ca. 800 nm, nominal concentration $2x10^{21}$ cm^{-3}), and further analysis, such as fitting routines, were performed using Originpro software.

7.4 Results

7.4.1 Surface Topography

The surface roughness of δ-doped channels and their underlying epilayers is important in δ-growth because the lengths scales of even so-called flat materials are of the same scale as the dimensions important for inducing a 2D potential well and δ-like characteristics in channels. The (111) plane of diamond is notoriously difficult to polish, and atomic force microscopy (AFM) measurements (Figure 7.6a&b) show average surface roughness of ca. 2 nm for epilayers, and ca. 2.5 nm for grown δ-layers. Average roughness was calculated by averaging data over 4 randomly selected areas in the middle of the samples. Topological data was given plane-levelling prior to statistical analysis. The surface of the δ-channel displayed in Figure 7.6b shows a slightly inhomogeneous coverage of doped diamond growth, which could affect the electrical properties of the δ-layer. Measurements were performed on select samples only, in order to minimise surface contamination on the substrates. All samples were comparable and statistically similar. The data displayed here are for samples grown with the same recipe as C & D.

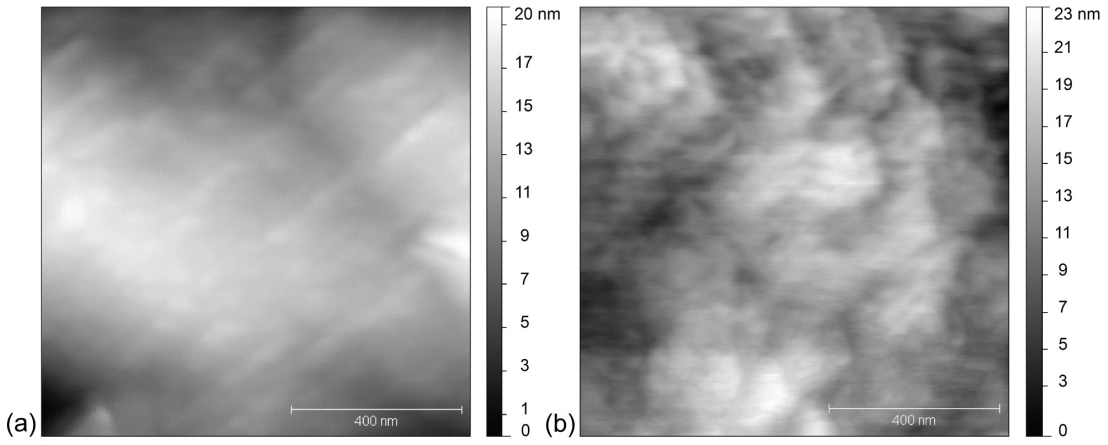

Figure 7.6: a) Epilayer surface, with a mean average roughness of ca. 2 nm. b) δ-surface, with an average roughness of ca. 2.5 nm.

7.4.2 AC Hall Effect – sheet carrier density and mobility

AC Hall measurements have been performed to measure the sheet carrier density and mobility of the boron-doped layers. Sample A represents a relatively thick heavily doped layer and B & C are δ-doped layers. AC Hall measurements reveal all samples to have positive Hall coefficients indicating that holes are the majority carriers (Table 7.3). The first δ-layer, sample B, shows mobilities in excess of what is expected for thicker heavily boron-doped diamond, as is indeed the case in comparison to sample A (< 3 cm^2/ V.s) (Figure 7.7). Similarly, the sheet carrier density of sample B is sufficiently reduced (in comparison to sample A) to be controllable by a FET gate. PECVD recipe alterations then resulted in sample C, which shows further mobility enhancement to around 13 cm^2/V.s, and again a desirable sheet carrier density. The full sets of properties determined are given in Table 7.3.

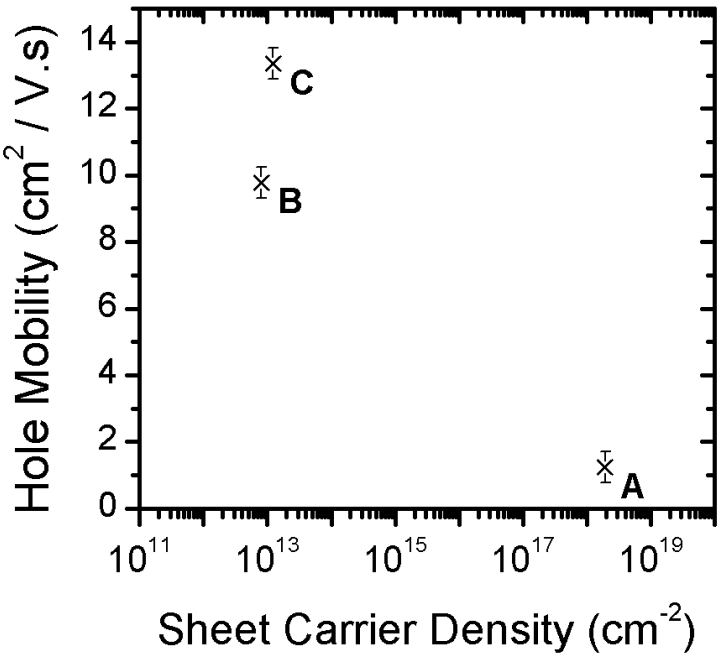

Figure 7.7: AC Hall measurements at room temperature (300 K) for samples A, B and C. Error bars: s.d.

Sample	Sheet resistance [Ω/square]	Hall coef. [cm^3/C]	Sheet Carrier Density [cm^{-2}]	Mobility [$cm^2/V.s$]	Carrier Type
A	3.32	0.43	$1.94x10^{18}$	1.24	Holes
B	$7.95x10^4$	77.77	$8.03x10^{12}$	9.78	Holes
C	$3.82x10^4$	51.05	$1.22x10^{13}$	13.35	Holes

Table 7.3: AC Hall measurements of grown layers A, B & C.

7.4.3 Impedance Spectroscopy

Impedance Spectroscopy (IS) has been used to determine the dielectric properties and activation energies of the channels in order to estimate the boron concentration of the δ-layers. Impedance Spectroscopy is used in conjunction with Secondary Ion Mass Spectrometry (SIMS) to estimate boron concentration due to SIMS being inaccurate within the first few nanometres of a sample. IS measurements are performed on samples B & D in air and vacuum from 300 K (room temperature) to 525 K, where D is of the same PECVD recipe as C. Sample temperatures have been intentionally kept below 525 K in order to maintain the oxygen coverage of the layer, which is known to affect the electrical characteristics of boron-doped surface channels [286]. 3D representations and Bode plots, shown in Figure 7.8, Figure 7.9 and Figure 7.10, give the real and imaginary impedance values (Z' and Z") vs. frequency of samples B & D in air and vacuum (10^{-3} Torr) from 300 K to 525 K. The high frequency resistance increases seen in the Bode plots are due to the high frequency skin effect from the source and drain contacts, which can also be seen as loops in the 3D and Cole-Cole plot representations of the data. The high cut-off frequency of ca. 10^6 Hz measured in samples B and D show them to have little capacitance in both air and vacuum. Similarly, the lack of a clear semi-circular shape in the Cole-Cole plots of B & D indicate a non-dielectric response that cannot be modelled using simple RC circuit elements. This suggests a metallic-like nature, which is expected for heavily doped layers [42,277]. Increasing the temperature of the samples results in their impedance reducing in a logarithmic relationship, as expected for thermally activated carriers, and by applying linear fits to the log of impedance

vs. reciprocal temperature, the gradient of the slope has been used to determine the activation energy of the conductive channels. Arrhenius plots of B & D in Figure 7.11 reveal B to have an activation energy of 22 meV in vacuum and two activation energies in air of 47 meV below ca. 400 K and 141 meV above 400 K. Sample D exhibits a reduced activation energy in comparison to B of 10 meV in vacuum and a similar dual activation energies in air of 21 meV below 375 K and 85 meV above. The low activation energies of B & D are ascribed to nearly fully activated carriers forming a metallic impurity band, indicating the channel to be heavily-boron doped. In air, the two linear fits could possibly be ascribed to thermally induced changes in the surface barrier of the uncapped channel from the onset of oxidation of the surface in air; however, the observed changes are thermally reversible.

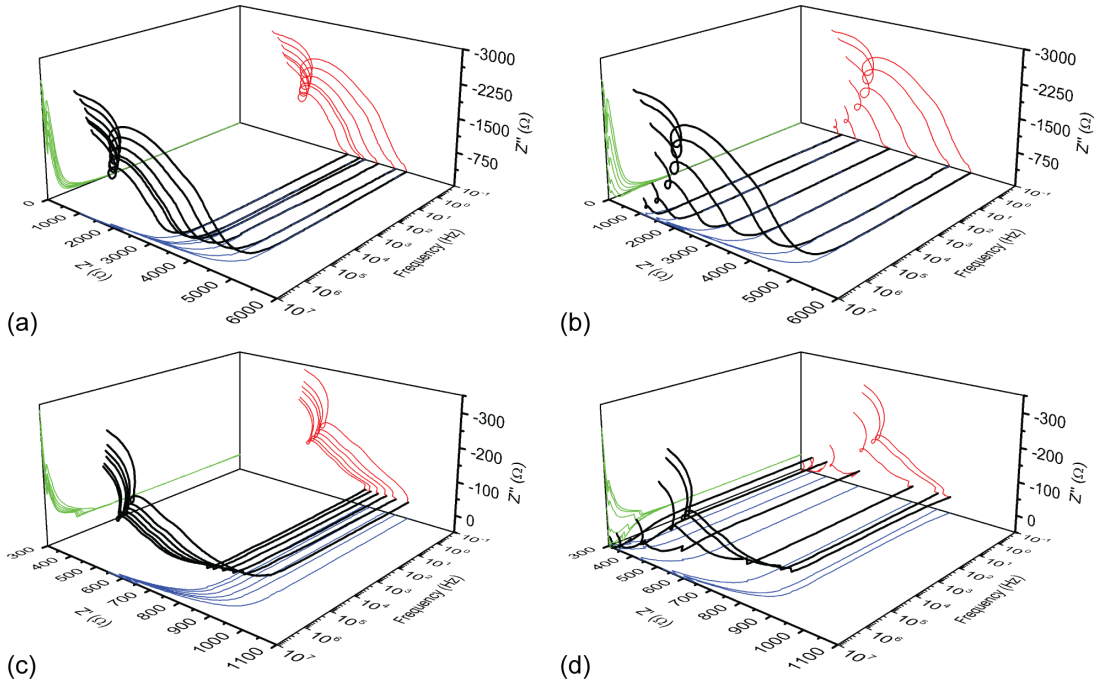

Figure 7.8: 3D representations of IS data for samples B and D. a) B in vacuum. b) B in air. c) D in vacuum. d) D in air. 3D data is projected into Cole-Cole (red) and Bode (blue) plots.

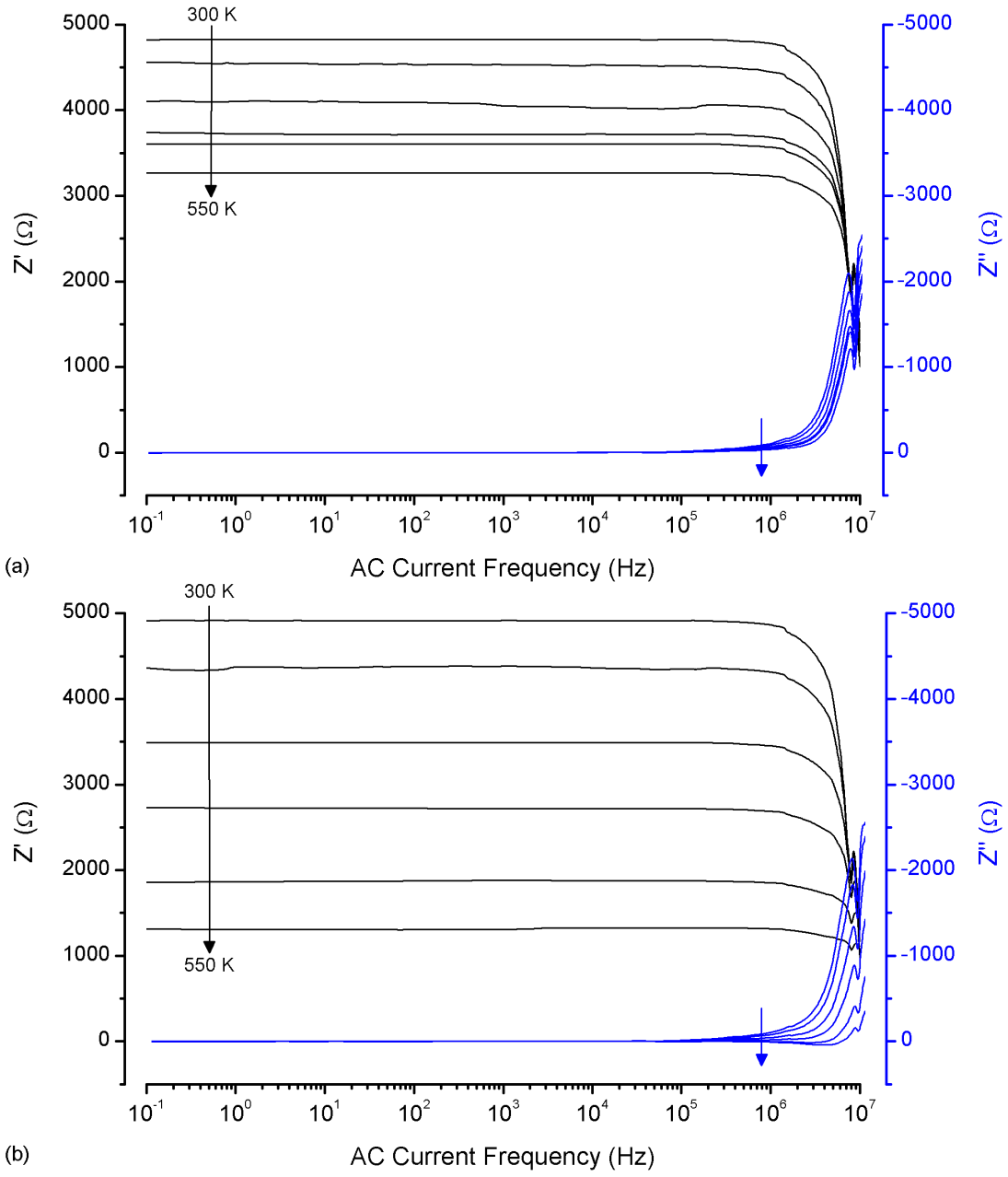

Figure 7.9: Sample B IS data in a) vacuum and b) air over the temperature range of 300 to 525 K.

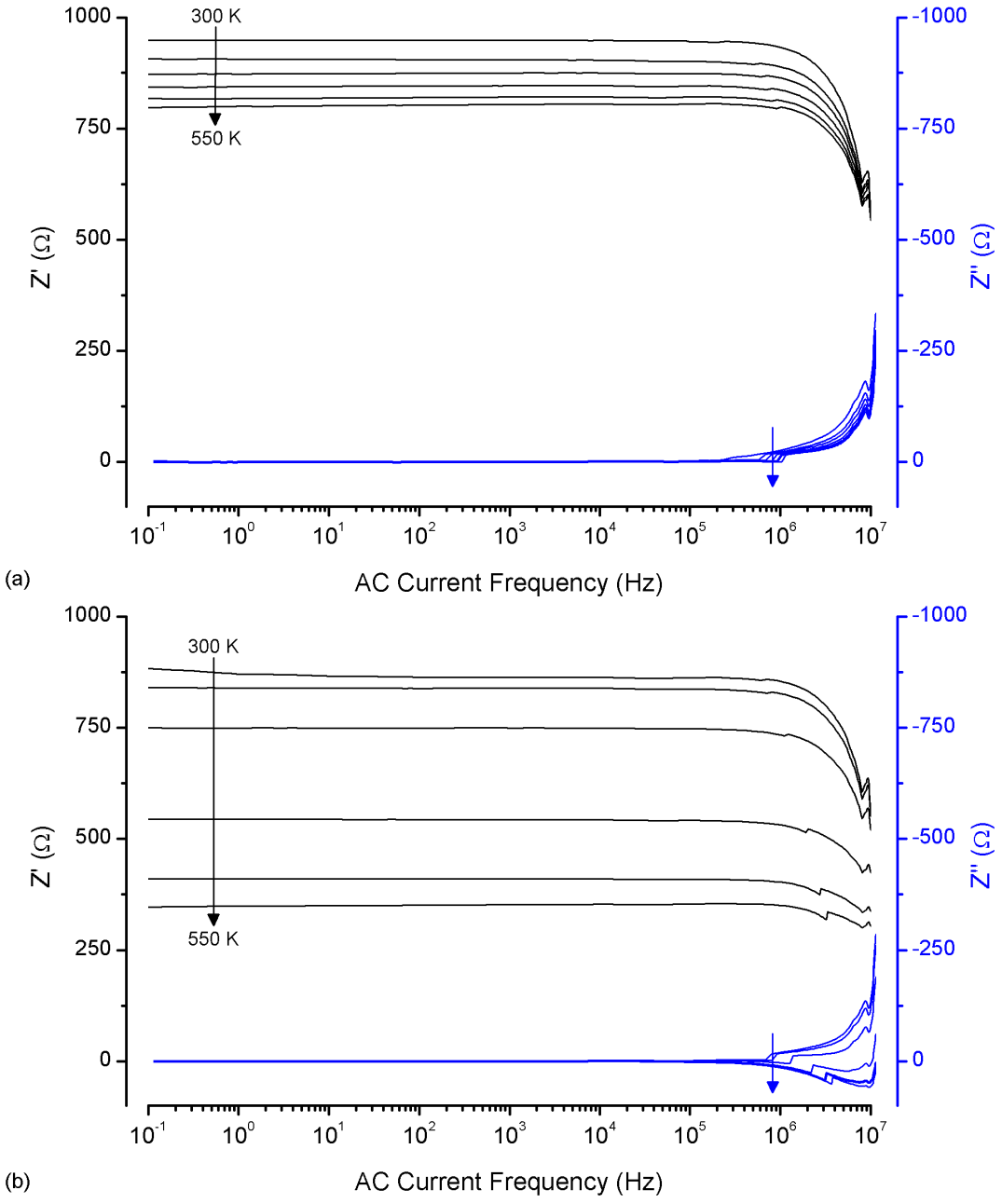

Figure 7.10: Sample D IS data in a) vacuum and b) air over the temperature range of 300 to 525 K.

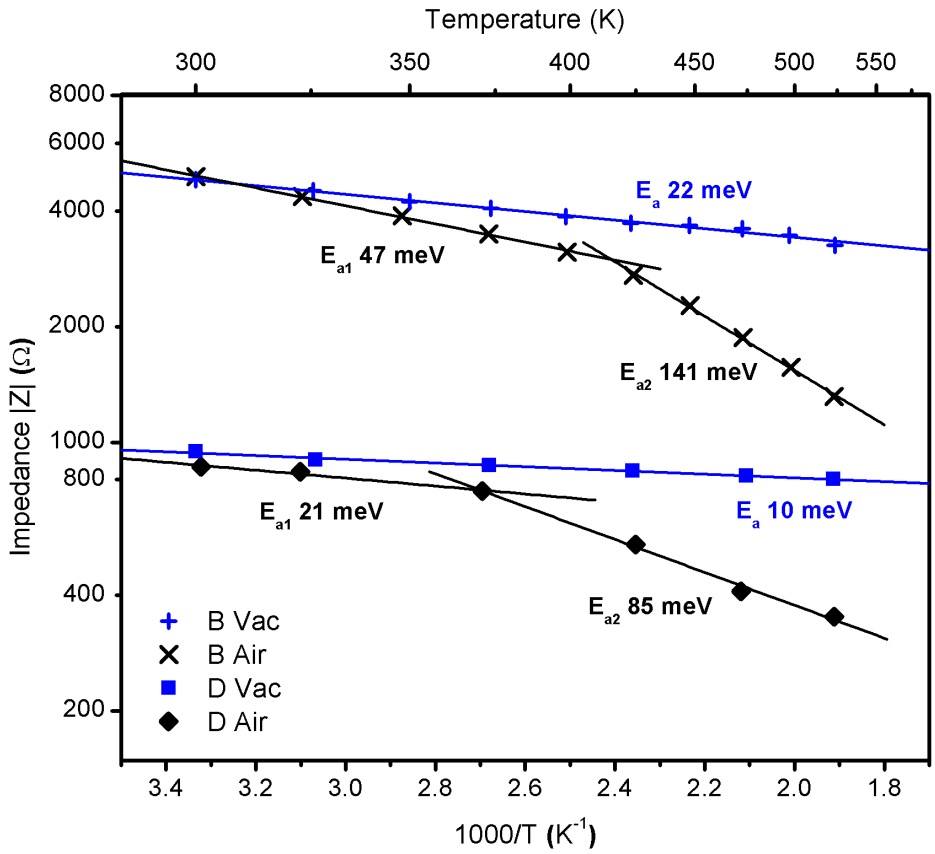

Figure 7.11: Arrhenius plots of the natural log of impedance vs. reciprocal temperature show linear relationships from which impedance activation energies are extracted.

7.4.4 Secondary Ion Mass Spectrometry

Ultra low Energy Secondary Ion Mass Spectrometry (uleSIMS) has been used to investigate the concentrations and distributions of boron in δ-doped samples B & D. Raw SIMS data reveal samples to have peak boron concentrations of $2x10^{19}$ cm^{-3} and $1x10^{21}$ cm^{-3} for B & D respectively (Figure 7.12a&b), located at the surfaces of the samples with comparable concentrations to those estimated in IS. Analysis of the substrate-side interface of the δ-layers shows the raw boron concentration to drop at slow rates of ca. 35 ±3.5 nm/decade and 9.5 ±0.1 nm/decade for B & D respectively. This is unexpected, considering the minimal boron diffusion that occurs in diamond and the PECVD method of CH_4

injection employed in this study to deposit δ-layers B & D. In fact, the close-fitting exponential decay of the boron concentration into the substrate (see Figure 7.12a&b) indicates it to be representative of a convoluted SIMS response function as a consequence of the common phenomenon of primary ion beam mixing [183] (i.e. 'knock-on' of boron). Therefore, a simple deconvolution algorithm [187] using smoothed raw data has been used to extract a better approximation of the actual boron profile in samples B & D. Figure 7.12c&d show the deconvoluted boron concentrations of B & D to have more δ-like profiles with the majority of boron segregated into the first two nanometres of the samples. Peak boron concentrations of ca. 8.2×10^{19} cm^{-3} & 1.4×10^{21} cm^{-3} and boron concentration gradients 2.0 ±0.5 nm/decade & 0.86 ±0.1 nm/decade are estimated for samples B & D respectively. A relatively high background boron concentration is recorded for both samples (Figure 7.12a&b), which is ascribed to the continual sputtering of boron from the δ-surface at the primary ion beam crater periphery, as well as boron contaminants lingering in the SIMS chamber.

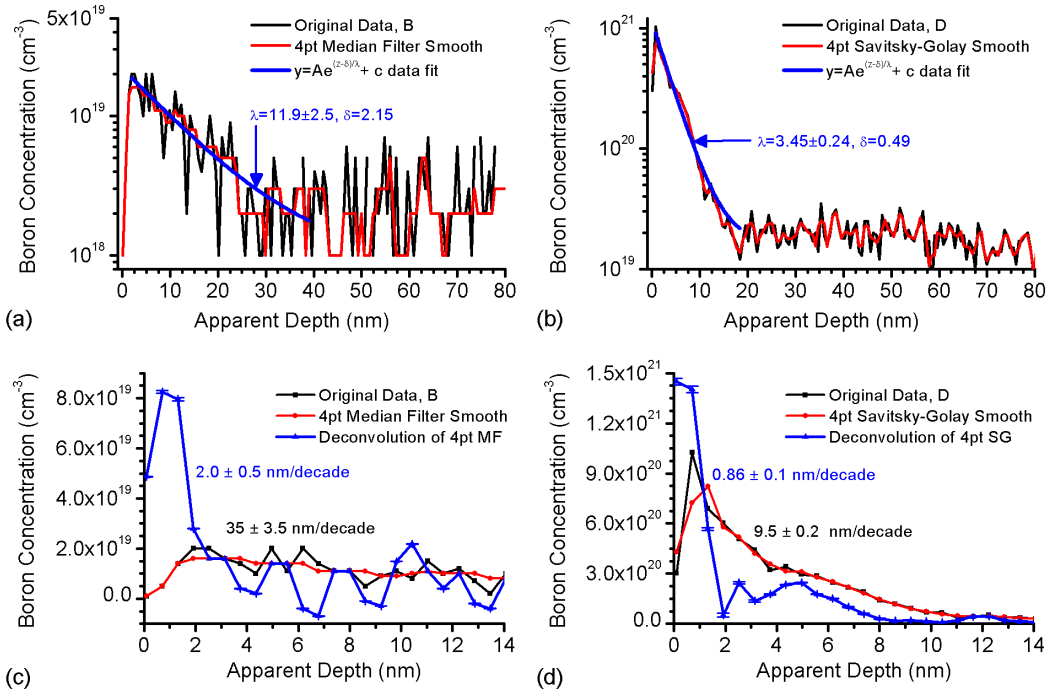

Figure 7.12: uleSIMS data for samples B and D. a&b) Exponential decay curves fit to apparent linear regions of logarithmic representations of boron concentration, [B], for samples B (a) and D (b). High frequency noise is reduced by smoothing over 4 data points (4pt) using, for B: Median Filtering (due to the low signal-to-noise ratio of the raw data) and for D: Savitsky-Golay smoothing (local 2nd order polynomial regression to retain peak data). Using λ values obtained from a&b, c&d) show deconvoluted boron profiles for B and D respectively, with error bars calculated [187] from λ errors as stated in a&b. N.b. negative boron concentrations in (c) are non-physical and are a result from a simplified deconvolution and unsmoothed noise.

7.5 Discussion

AC Hall measurements show δ-doped samples to have room temperature mobilities in excess of what is expected for thicker heavily boron-doped (111) diamond layers at metallic boron concentrations (> 10^{20} cm^{-3}) [277,287]; however, in the absence of direct measurements of boron concentration, the origin of these elevated mobilities is not immediately apparent. It is well known that diamond doped with a lower boron concentration results in carriers with

higher mobilities and larger activation energies [42,85]. This leads to the suggestion that the measured mobilities could actually be ascribed to conductive channels with lower than expected boron doping concentrations and corresponding higher mobilities. However, the mobility measured in both samples B and D do not correspond to the typical mobility of heavily boron-doped diamond with an activation energy ranging from 20 to 140 meV. Comparing the activation energy of impedance of sample B to literature values [277,287] of activation energy vs. boron concentration, the 22 to 140 meV E_a measured corresponds to boron concentrations of 10^{19} to 10^{20} cm^{-3}. Similarly for sample D, the 10 to 85 meV E_a corresponds to 10^{20} to 10^{21} cm^{-3} boron concentrations. For thick, boron-doped diamond of these boron concentrations the mobilities recorded in the literature [277,287] are 1-2 $cm^2/V.s$, as demonstrated in sample A (Figure 7.7). Vice-versa, sample B's measured mobility of ca. 13 $cm^2/V.s$ would correspond to doping concentrations of 10^{17} to 10^{18} cm^{-3}, which would exhibit activation energies in the range of 300 meV. Indeed, SIMS measurements show IS estimated boron concentrations to correspond well to measured values, and show the PECVD recipe of sample D to significantly improve on the recipe used for sample B; however, estimated boron profile gradients for samples B & D are still in excess of the Debye Length in diamond, L_D, suggesting hole delocalisation may not occur effectively in these samples [288] (L_D in B: ca. 0.3 nm, D: ca. 0.7Å). On the contrary, for such challenging SIMS samples as uncapped diamond δ-layers within the top nanometre of samples, peak displacement and broadening effects could easily be broadening and shrouding steeper-profiled δ-doped layers. Such effects include primary ion beam mixing as already discussed, and additional effects such as pre-equilibrium non-linear sputtering, topography development [183] and sample roughness.

When considering the electrical properties of uncapped δ-layers, the atomic surface termination, and thereof the energetic surface barrier of the channel, is important in determining the level of carrier depletion and surface defects. Oxygen terminating the surface of (100) boron-doped diamond is known to create a surface barrier that pins the Fermi level and, if sufficiently large (ca. 1

eV), can completely deplete thin (ca. 1 nm) channels of hole carriers [286,289]. However, it has been suggested that oxygenated (111) diamond has a low density of surface states and as a result does not have a pinned Fermi level or surface barrier [290]. The surface barrier created by the UV ozone treatment used here has not been measured directly. However, since the measured sheet carrier densities are close to the expected sheet carrier densities estimated from SIMS measurements, this suggests that little surface pinning, which causes significant carrier depletion, is occurring. See section 8.3 for further discussion.

When AC Hall measurement observations are combined with the high boron concentrations measured in SIMS and the high cut-off frequency (ca. 10^6 Hz) and low activation energies measured in IS, the nature of the mobility enhancement in the boron-doped layers can be ascribed to the onset of δ-like properties causing a fractional delocalisation of holes out of the δ-layer. Whilst the boron-doped layers display enhanced hole mobilities, further work is required to improve the carrier mobility of the channels. Firstly the δ-layers grown here are uncapped. It has been suggested that the capping layer of a δ-layer contains the largest portion of delocalised holes [272] and therefore should account for a large enhancement in the mobility value of the channel. Furthermore, the level of boron doping estimated in sample B (10^{19} to 10^{20} cm^{-3}) is not sufficient to fill the higher energetic hole states of a 2D gas which have higher mobility [272], and for both samples a sufficiently sharp boron concentration gradient has not been measured. Therefore, further mobility enhancements should be possible with sharper δ-interfaces, an intrinsic capping layer of diamond on top of the δ-layer and the use of flatter substrates. Finally, further refinements to the PECVD recipe are possible to improve the δ-layer quality.

7.6 Conclusions

Uncapped δ-doped layers have been deposited on (111) diamond substrates, wherein a revised PECVD protocol has been employed to aid abrupt

δ-doped boron concentration profiles. AC Hall Effect and Dielectric Impedance Spectroscopy measurements have been used to determine the electrical characteristics of δ-layers, and enhanced room temperature mobilities (13 $cm^2/V.s$) are reported in comparison to equivalently grown thicker heavily boron-doped (111) diamond. Impedance spectroscopy measurements show the deposited layers to have metallic-like properties with low activation energies, corresponding to estimated boron concentrations of approximately 10^{20} cm^{-3}, as confirmed by SIMS measurements. The resulting boron δ-doped diamond channels are suitable for FET fabrication with desirable sheet carrier densities.

Chapter 8 Boron δ-doped (111) diamond Solution Gate Field-Effect Transistors

8.1 Introduction

The hydrogenated surface conductive channel (H-SCC) of diamond is a unique material region for Ion Sensitive Field-Effect Transistors (ISFETs). Its strong polarisability [11], embodied by its wide band gap, strong resistance to corrosion and large surface dipole barrier mean that, unlike silicon based ISFETs, gate oxide passivation layers are not required to avoid large faradaic leakage currents and device degradation. Instead the H-SCC operates as a Solution Gate Field-Effect Transistor (SGFET) with its gate and conductive channel directly exposed to an analyte solution [164], yet does not suffer from reduced transconductance due to diminished gate potentials across the gate oxide layer or device deterioration due to trapped ions permeating into the gate oxide layer. Appropriately, H-SCC SGFETs display increased sensitivity, exhibiting large responses to pH changes near the theoretical Nernst limit of 59 mV/pH [162,291], have saturated output characteristics within the electrochemical potential window of water and can be used to perform sensitive potentiometric molecular biosensing [292] or record electrogenic activity in cells [166].

Whilst H-SCC SGFETs demonstrate excellent sensitivity and device characteristics, the H-SCC channel has proved unsuitable for long-term application due to its instabilities, including a tendency to undergo anodic oxidation during operation [167], a dependence on external adsorbates to form its conductive channel [293], differing fabrication methods resulting in H-SCCs

with differing electrical properties [57] and varying pH responses [57,162,164,167,294-296]. Instead, a more robust substitutional doping method is needed; however, few elements are suitable for substitutional doping in diamond. Those which are (notably phosphorous, nitrogen and boron) have large thermal activation energies [42,297] and, as a result, only a small fraction of boron atoms are activated as charge carriers at room temperature. Boron – diamond's lowest activation energy dopant – still has an activation energy of 0.37 eV at low doping concentrations of < 10^{17} cm^{-3}, and conductive channels from such a material result in thermally dependent, low transconductance channels that make poor FETs. To decrease the activation energy of boron in diamond one can increase the doping concentration. This continues to a point until approximately 3 x 10^{20} cm^{-3} where a metallic impurity band forms and the activation energy of the boron dopants tends to zero [48]. However, as the carrier activation energy decreases so does the carrier mobility due to increased impurity scattering [42] and the onset of a hopping-like conduction mechanism. The resultant material is one with inadequate mobilities (0.1-2 $cm^2/V.s$ [42]) for responsive FET operation with sheet carrier densities typically in excess (>4x10^{13} cm^{-2}) [268] of what is controllable by a field-effect transistor (FET).

δ-doping, as discussed at length in Chapter 7, could remedy the excessive sheet carrier density and low carrier mobility associated with metallic boron doped channels. δ-doped diamond SGFETs could improve on H-SCC SGFETs by the possibility of high channel mobilities and its surface functionalisation being less constrained by not having to maintain its hydrogenation, allowing for more versatile and tailored surface functionalisations for applications such as molecular biosensing, specific chemical sensing or electrogenic cell recording.

In practice, depositing heavily-doped abrupt δ-layers is not a simple task (as discussed in 7.1), and additional to the channel specifications required for the formation of a 2D gas, SGFETs demand further specifications on their conductive channel if they are to display saturated transistor characteristics within the electrochemical potential window of diamond and operate in the preferred enhancement mode of operation (V_T < 0, "always off"). Considering a p-type

enhancement planar-doped MESFET regime of operation, δ-layers of approximately 1 nm thickness with 10^{20} cm^{-3} boron concentration are required. To date, despite reports of 1 nm metallic δ-layers using the (100) diamond plane being reported in the literature [273], subsequent fabrications of SGFET have resulted in always-on, low gain and transconductance devices with unsaturated linear current-voltage (I-V) characteristics [163]. As an alternative, here the δ-doped (111) diamond plane as a substrate for SGFET application is investigated. Firstly, (111) diamond presents possible advantages for δ-layer growth as detailed in 7.1, and enhanced mobilities along with near-ideal sheet carrier densities are reported for δ-doped (111) diamond substrates. Additional to possible fabrication and electrical advantages, the use of the oxygenated (111) diamond plane could be of principal advantage in improving SGFET I-V characteristics and pH sensitivity. Oxygen moieties on the (100) diamond surface are known to have a high density of surface states that readily pin the surface Fermi level and permanently deplete (100) δ-layers [289]. Experimentally, in order to compensate such pinning, thicker δ-layers are typically fabricated leading to always-on, linear regime SGFETs. In contrast, it has been suggested [290] that the oxygenated (111) diamond surface is not pinned by surface states, which could allow for thinner δ-layers with lower threshold voltages, saturated output characteristics and enhanced transconductance. With respect to enhancing pH sensitivity, (111) diamond is preferentially oxidised by hydroxyl groups [298] and the density of these amphoteric oxygen moieties are thought to be responsible for determining the pH sensitivity of ISFETs in the site binding model [162,299]. The fabrication and I-V characterisation of uncapped oxidised boron δ-doped (111) diamond SGFETs is presented, and their I-V characteristics and response to different pH solutions is investigated.

8.2 Experimental Methods

8.2.1 SGFET fabrication

To fabricate SGFET, (111) δ-doped diamond layers were deposited as described in section 7.2 & 7.3. Samples B and D have been used for SGFET

fabrication. Following δ-deposition, titanium and gold (20 nm and 100 nm respectively) source and drain contacts were deposited on oxygenated uncapped δ-layers using an Edwards A500 Electron Beam Evaporator, and patterned using lift-off photolithography using AZ 5214 E image reversal photoresist. The contacts were positioned to give a 2 mm channel width and 80 μm channel length. Contacts were annealed at 700 K in a hydrogen atmosphere (20 Torr, 100 sccm, 30 mins) [206] to impart Ohmic properties. Samples were oxygen terminated before and after contact formation with a UV photochemical treatment [206,285] in the presence of ozone for 3 hours to suppress hydrogen surface conductivity and provide hydroxyl sites for pH sensitivity. Passivation of source and drain contacts was achieved using 2 μm SU-8 2002 photoresist. Three gaps were patterned into the passivation to form (1) a gate region (2 mm width, 60 μm length) and (2) source and (3) drain back contacts (Figure 8.1a). Samples were fixed onto glass slides with epoxy, and gold wires were bound with silver paste to the source and drain contacts (Figure 8.1b). Gold wires were then bound to insulated wires with CW2400 Araldite conductive epoxy and all exposed conductive regions (except the gate) were insulated with Araldite 2014 epoxy (Figure 8.1c). A dummy sample was also fabricated without boron doping, but otherwise identical processing, which resulted in highly resistive channels (> 10 GΩ).

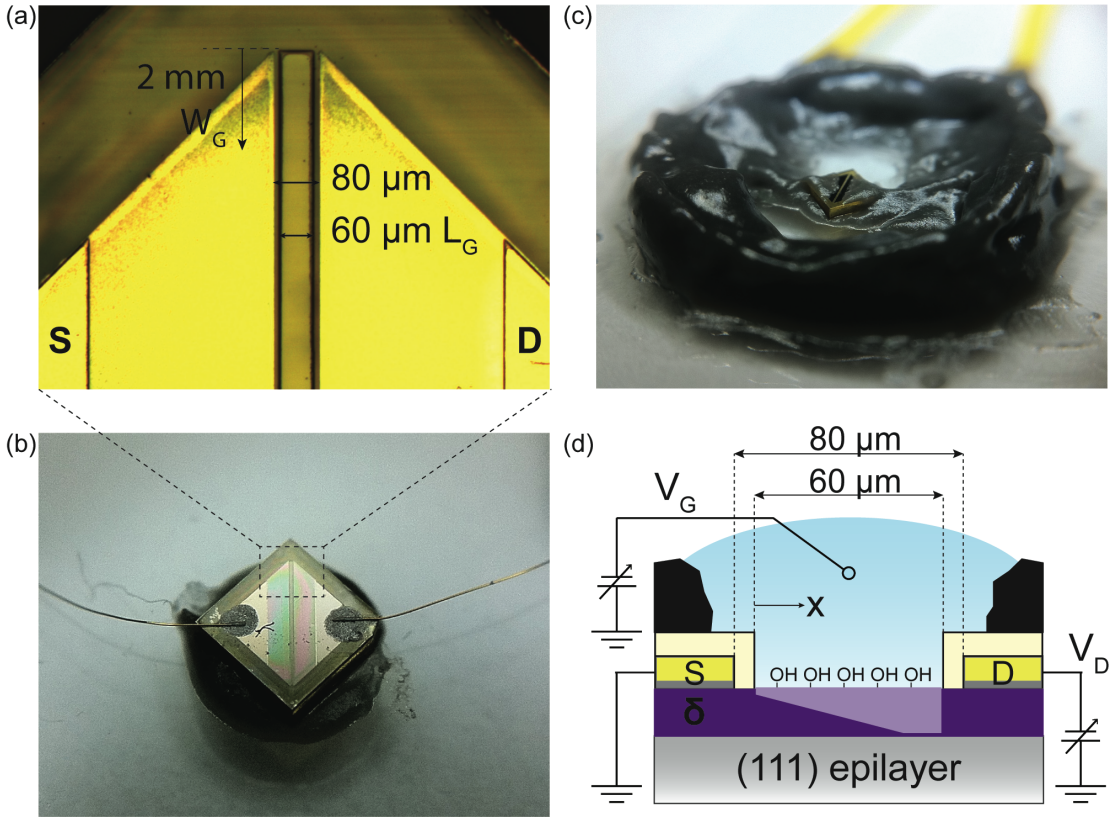

Figure 8.1: a) Micrograph of SGFET source, gate and drain showing passivation openings. b) Macro photograph of wire bonded device prior to encapsulation. Sample is 2x2 mm. c) Epoxy encapsulated SGFET. d) Experimental setup of SGFET using a MESFET analogy, depicting the channel depleted in the saturation regime.

8.2.2 I-V characterisation and pH testing

I-V characterisation of SGFET was performed using two Keithley 2400 source and measurement units interfaced with a custom Labview program, using an Ag/AgCl reference electrode in the experimental setup depicted in Figure 8.1d. Measurements were recorded in 1 mM PBS or Carmody Universal Buffer [300] solution (0.2 M boric acid, 0.05 M citric acid and 0.1 M trisodium phosphate as a pH adjuster) varied between pH 2 and 12. pH was measured using a calibrated pH meter (HS-205C TOA Electronics Ltd. Tokyo, Japan). pH transfer characteristics were taken after stabilisation with a fixed drain-source voltage of -0.6 V_{DS}. Real time pH recordings were performed at -0.9 V_{GS}, -0.6 V_{DS}.

SGFETs were rinsed before and after measurements in DI water and dried by N_2 gun, except in real time pH measurements where tri-sodium phosphate solution was added in calculated aliquots to increase the pH by 1 pH unit per addition.

8.3 Results and Discussion

8.3.1 Sample B SGFET I-V characteristics

Figure 8.2a&b show the output and transfer characteristics of the non-optimised SGFET using sample B. Output characteristics between 0 and -0.6 V_{DS} and +0.6 and -0.6 V_{GS} show the device to operate in the linear regime with no discernable channel pinch-off within the electrochemical potential window of diamond. A low transconductance (g_m) and maximum gain (g_m/G) of 20 μS/mm and 0.35 (at -0.6 V_{GS}, -0.3 V_{DS}), respectively, are measured. Positive gate voltages serve to deplete the channel, as expected for a p-type conductive channel, however the channel could not be depleted within the electrochemical window of diamond, resulting in an always-on depletion mode device. Extrapolating transfer curves (Figure 8.2b) an estimated threshold voltage (V_T) of 2 V is obtained. Using a non-optimised PECVD recipe, the I-V characteristics of B SGFET result in a linear depletion mode device with similar output characteristics to previous SGFET fabricated on (100) diamond [163]. Whilst B SGFET has a different gate length to that SGFET, both show similar transconductances of 20 μS/mm at -0.6 V_{DS}. However, B SGFET shows a higher gain of 0.35, which is irrespective of device dimensions, in comparison to the 0.16 gain extracted from the aforementioned device [163].

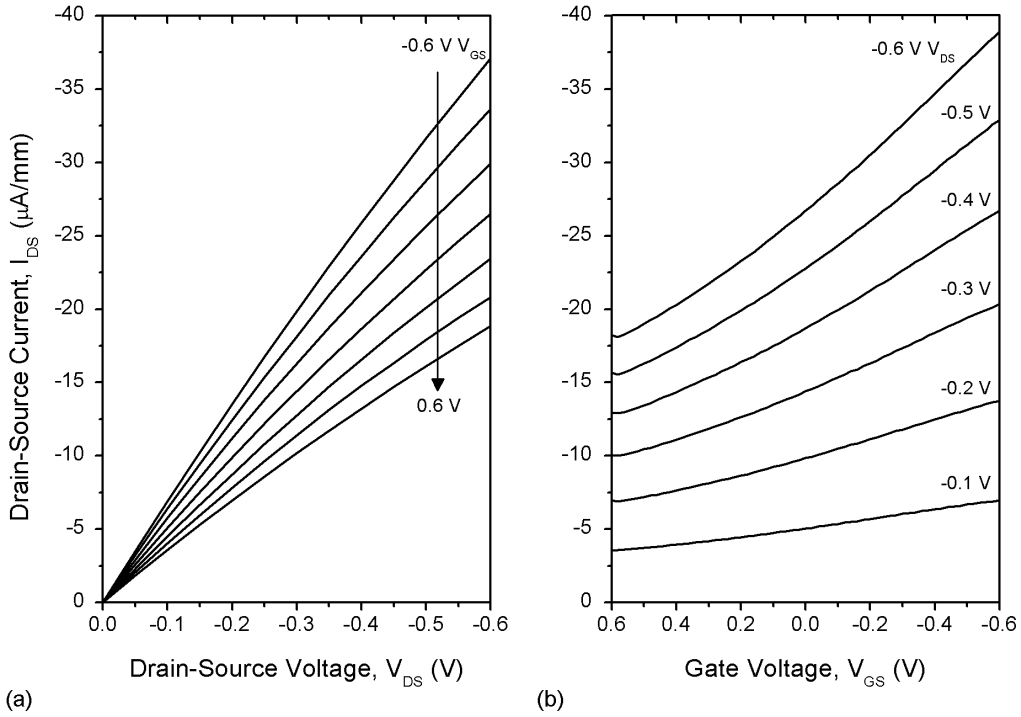

Figure 8.2: a) Output characteristics and b) transfer characteristics of B SGFET in 1 mM PBS. $Gain_{max}$: 0.35. g_m: 20 μS/mm. V_T ca. 2 V_{GS}.

8.3.2 Sample D SGFET I-V characteristics

Following I-V characterisation of sample B SGFET, the optimised sample D SGFET was investigated. Employing the optimised PECVD recipe D, the I-V characteristics of D SGFET show significantly improved output and transfer characteristics, critically operating in the favoured saturation regime and enhancement mode of operation. Output characteristics between 0 and -0.6 V_{DS} and 0.2 to -1 V_{GS} show the device to achieve channel pinch-off within the electrochemical window of diamond (Figure 8.3a), showing always-off characteristics in the enhancement mode of operation. The transfer curves of the SGFET show the current output not to be subject to variations in drain-source voltage when greater than approximately -0.5 V_{DS} (Figure 8.3b). Taking the transfer curve gradient in the saturation regime, a transconductance of 200 μS/mm and a maximum gain of 3.0 (at -0.8 V_{GS}, -0.6 V_{DS}) are obtained.

In comparison to hydrogen-based SGFETs, the measured transconductance of 50 μS/mm and gain of 1.1 at -0.2 V_{DS} and -0.7 V_{GS} for D SGFET are comparable to the 80 μS/mm and 1.6 gain reported [291] at similar operating conditions for purely hydrogenated SGFET, significantly larger than the 0.22 μS/mm and 0.01 gain reported [162] for a partially oxidised hydrogenated SGFET and similar to the 15 μS/mm and 1.0 gain as calculated from data reported [295] for another partially oxidised hydrogenated SGFET.

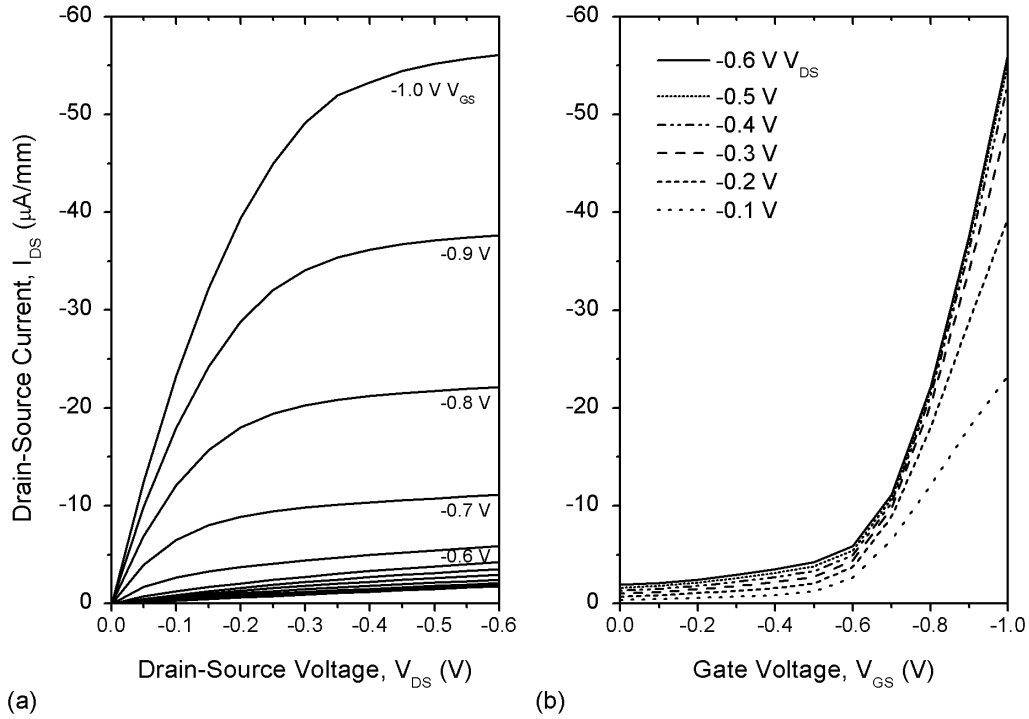

Figure 8.3: a) Output characteristics and b) transfer characteristics of D SGFET in 1 mM PBS. $Gain_{max}$: 3. g_m: 200 μS/mm. V_T -0.6 V_{GS}.

As well as improved transconductance and gain, D SGFET shows the preferable enhancement mode operation with a V_T of ca. -0.6 V_{GS}. Adapting a planar-doped FET model [301] for a uniformly doped p-type surface channel (δ-layer) with a gate reference electrode, the origin of a negative V_T can be investigated by examination of the terms of V_T, which can be expressed as follows:

$$-V_T = E_{ref} - \Psi_0 + \chi^{sol} - \frac{\phi_\delta}{q} - V_p - \frac{qN_A a^2}{2\varepsilon_s} \quad (5.1)$$

Where the first four terms constitute the equivalent of a Schottky barrier between the diamond and reference electrode (see Shinwari *et al.* [302] for further details) and are constant upon pH change, except for Ψ_0 and χ^{sol}, the electrolyte interface potential and the surface dipole potential of the electrolyte, however, changes in χ^{sol} are negligible in comparison to Ψ_0. Oxide and interface charges are not included due to the lack of a gate oxide layer. V_p is the Fermi level of bulk diamond away from the doped layer relative to the valence band and the final term is the pinch-off voltage of the channel, V_{PO}, where a is δ-layer thickness, N_A is acceptor concentration (cm^{-3}), q is the elementary charge and ε_s is permittivity. From Equation (5.1) it can be seen that the measured negative V_T can only arise from the Schottky barrier terms because the other terms are positive for p-type channels. Using estimated δ-layer parameters (1 nm δ, N_A 10^{20} cm^{-3}, ε_s 5.5 and V_p 0.37 eV (from unintentional boron doping adjacent to the δ)) and the measured V_T of -0.6 V, this gives a Schottky barrier of approximately 1.1 eV, which is comparable to typical values for oxygenated diamond surface barriers [286]. Such a positive barrier could result from either an unpinned oxygenated diamond surface equilibrating with a higher chemical potential PBS solution, or alternatively from Fermi level pinning and downward band bending from dense oxygen states on the δ-layer surface. Since the observed pH sensitivity (see section 8.3.3) of the device is indicative of an unpinned band edge, the former explanation seems most likely, i.e. an unpinned oxidised (111) surface, but with an additional low density of surface states due to an imperfectly smooth gate surface (2.5 nm R_a), that introduces binding sites favoured by more complicated, state-including oxygen moiety functionalisations [289].

Gate leakage current analysis (Figure 8.4a&b) shows that, in the operational range of the device, gate leakages are less than 25 nA with a gate resistance of 12 MΩ. Negative gate-channel voltages ($V_{GC}(x)=V_{GS}-V_{DS}(x)$) in excess of -0.8 V_{GC} and positive voltages greater than approximately 0 V_{GC} result in exponential faradaic current generation (Figure 8.4b). In terms of device

symmetry, gate leakage passes zero near the point of average zero gate-channel potential ($V_{GC}(\langle x \rangle)=(V_{GS}-V_{DS}/2)=0$), (Figure 8.4a&b), which is indicative of a device with little leakage bias to the source or drain end of the gate.

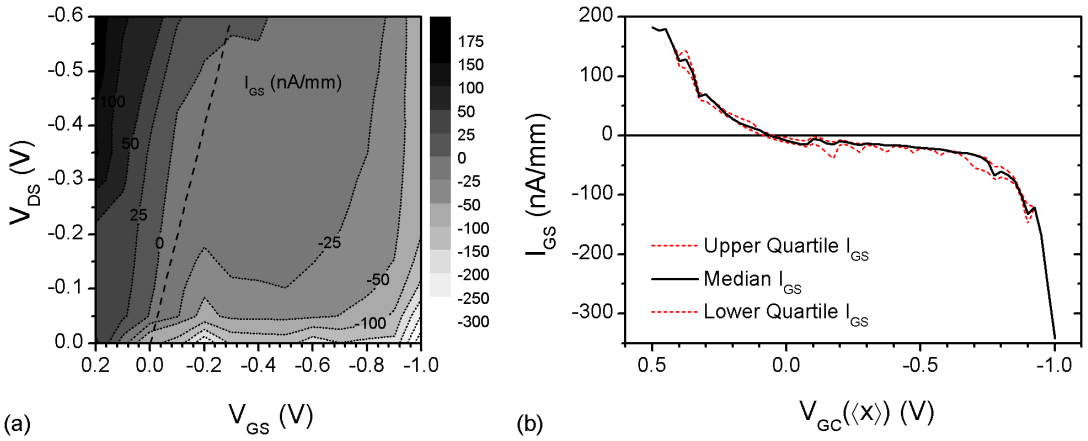

Figure 8.4: a) Gate-source current leakage (I_{GS}) contour map with respect to V_{DS} and V_{GS}, with shaded increments of 25 nA. The long-dash line represents average zero gate-channel potential (V_{GC}). b) Median I_{GS} vs. V_{GC} with upper and lower quartile error envelopes.

8.3.3 Sample D SGFET pH sensitivity

The pH sensitivity of D SGFET was then investigated using Carmody Universal Buffer between pH 2 and pH 12. Transfer characteristics of D SGFET for different pH-adjusted solutions are displayed in Figure 8.5a, wherein low pH gives a low I_{DS} output with a more negative value of V_T, and vice-versa. The pH sensitivity of D SGFET behaves as expected for a p-type oxidised SGFET following the site-binding model [57,299,303] of pH sensitivity: pH dependent protonation and deprotonation of amphoteric hydroxyl sites on the device gate – as determined by chemical equilibration with the bulk electrolyte (low pH: C-OH_2^+, neutral: C-OH high pH: CO^-) – results in the δ-channel charge density (and therefore I_{DS}) being modulated by the built up surface potential in order to maintain charge neutrality throughout the device. For example, in the case of high pH, where deprotonation of amphoteric sites occurs, the negative charge next to the δ-channel removes depletion increasing the hole current of the

channel (Figure 8.5a). It should be noted that as well as the accumulated surface charges in the Inner Helmholtz Plane (IHP), charge neutrality must be achieved for the counter charges in the Outer Helmholtz Plane (OHP), Stern and diffuse layer, which allows sensitivity to larger ion concentrations such as K^+ and Na^+, which cannot permeate (without specific adsorption) into the IHP.

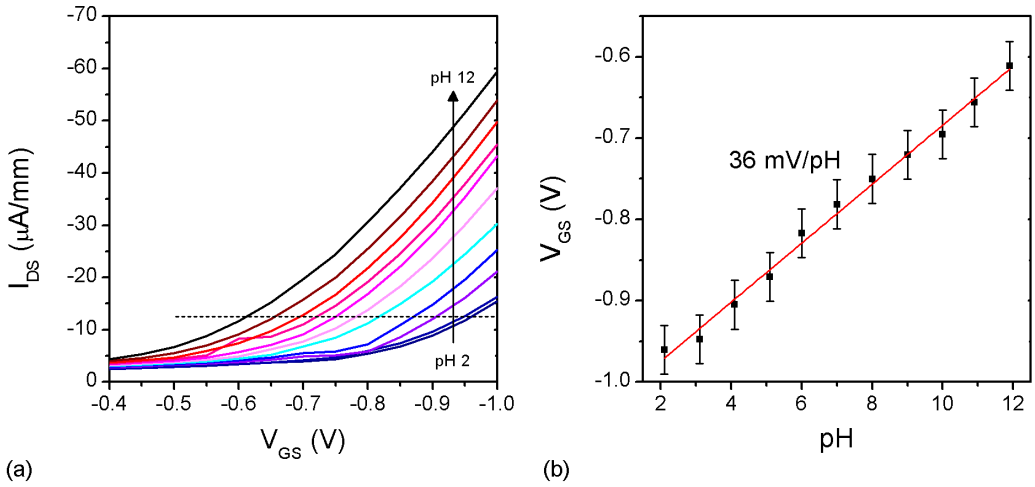

Figure 8.5: a) Transfer characteristics (V_{DS}= -0.6 V) for D SGFET at different pH. b) V_{GS} shift vs. pH for I_{DS} of -12.5 μA/mm. V_{GS} shift is calculated by performing a linear fit between the two data points above and below -12.5 μA/mm and extrapolating a value for V_{GS} at -12.5 μA/mm I_{DS} for each pH. pH is varied from pH 2 to 12 using Carmody Universal Buffer. V_{GS} error bars correspond to a generous estimated maximum variance (±0.03 V) of gate voltage drift between measurements, and pH error bars of ±0.1 pH are too small to be shown.

In terms of device I-V characteristics, the effect of pH and resultant accumulated surface charge manifests itself in a change in V_T via the electrolyte surface potential, Ψ_0, a term contained in the expression for V_T (Equation (5.1)), as can be seen in Figure 8.5a as a negative shift of V_T with increasing pH. The shift in the surface potential with respect to the bulk pH, pH_B, can be described as in Equation (5.2) [304], where the maximum V_T shift possible is the Nernstian response of ca. 59 mV/pH, α is the sensitivity parameter ($\alpha \leq 1$) associated with the oxide layer, C_{DL} is the double-layer capacitance and β_{int} is the intrinsic buffer

capacity of the surface defined by the density of surface binding sites charged per unit surface pH (pH_s) change.

$$\frac{d\Psi_0}{dpH_B} = -\alpha . 2.303 \frac{k_B T}{q} = -\alpha . 59\ mV \tag{5.2}$$

Where:

$$\alpha = \left[\frac{2.303 k_B T}{q^2} . \frac{C_{DL}}{\beta_{int}} + 1\right]^{-1} \tag{5.3}$$

Using a fixed current of -12.5 μA/mm, the gate voltage shift (and thereby Ψ_0) with respect to pH has been extracted giving a pH sensitivity (as determined by linear fit) of $d\Psi_0/dpH_B$ = 36 mV/pH (Figure 8.5b). Whilst there is slight non-linearity in the pH response, and a slight increase in g_m for a fixed I_{DS} with increasing pH (where $g_m \propto \mu$) that could possibly be ascribed to non-linear changes of mobility vs. carrier density associated with sloped conduction bands [167] (such as in a delocalised δ-layer), the drift error in measurements precludes this observation and the device exhibits a linear response to pH change with similar transconductances for different pH solutions. The $d\Psi_0/dpH_B$ of 36 mV/pH measured for D SGFET is smaller than anticipated considering the high density of amphoteric hydroxyl sites expected on the diamond surface, and the large pH sensitivities reported on similar oxidised boron doped diamond SGFETs [163,305], which report sensitivities of 50 mV/pH near the Nernst limit of 59 mV/pH. Inspecting Equation (5.3), the lower pH sensitivity could be ascribed to a large C_{DL} and/or a low value for β_{int}, which can indicate a lower density of hydroxyl sites or small surface complex dissociation constants [304]. This simplified model could imply that the conductive channel could be actually a partially O-terminated H-SCC and not an oxidised δ-doped channel; however, the dummy SGFET, fabricated identically but without the boron-doping process step, has very resistive channels (> 10 GΩ) that would not demonstrate such characteristics as presented here. It should also be noted that an uncapped, δ-doped SGFET should mimic an H-SCC SGFET due to their similarities in sheet carrier density, mobility and band structure. Alternatively a partial pinning of the valence band edge from complicated oxygen moieties could be lowering the response of D SGFET to pH change.

In order to investigate the time dependent response of D SGFET, pH titration experiments have been performed. Figure 8.6a&b show D SGFET to respond quickly to pH steps. Figure 8.6b shows an estimate of the fast response time (the initial steep response [306]), wherein I_{DS} has been transformed into pH using pH metre calibration measurements. Taking the inverse of the maximum value of the derivative of pH vs. time over a large pH step (ca. 9 pH, Figure 8.6b), an upper limit of the intrinsic fast response of ca. 33 ms is estimated. It should be noted this response time is largely reflective of the slower speed of pH titration rather than the intrinsic response of the SGFET, especially considering that, unlike other experiments [306] which employed measures to reduce this effect, standard pipette mixing was used here. It is therefore expected that the device has a considerably lower intrinsic fast response in the millisecond range. Considering this, along with the highly biocompatible nature of oxidised diamond towards cells [10,165,249] and the ability of oxidised SGFETs to sense K^+ and Na^+ ion concentration changes [307] that are in flux during electrogenic activity, oxidised δ-doped SGFET appear to be promising devices for the chronic recording of action potentials of electrogenic cells.. This could be achieved using constant current or constant voltage modes of operation. Similarly, the high specific capacitance of diamond in comparison to other materials [166] could allow the stimulation of electrogenic cells on the same device. In terms of practical use, oxidative cleaning of the device should not alter the already-oxidised device surface significantly, making it suitable for long-term application.

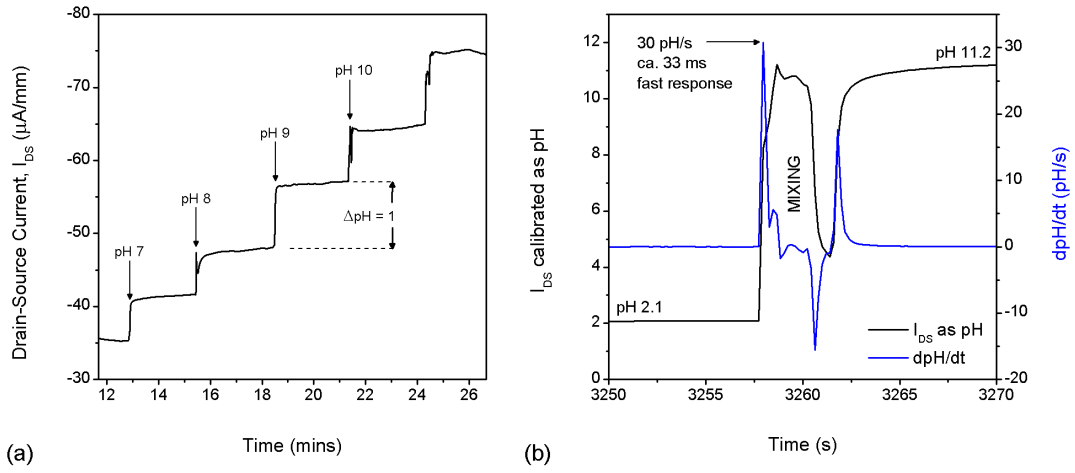

Figure 8.6: a) pH titration of Carmody buffer in pH 1 increments via the addition of appropriate aliquots of tri-sodium phosphate. b) A large addition of tri-sodium phosphate is made to give a pH 2.1 to pH 11.2 step, from which an upper limit of the fast response of 33 ms is estimated. Erratic data during the step is from solution mixing.

8.4 Conclusions

SGFETs fabricated from oxidised boron δ-doped (111) diamond channels show improved I-V characteristics in comparison to equivalent devices built on (100) diamond and are comparable to H-SCC SGFETs. Following a PECVD recipe optimisation for δ-layer deposition on (111) diamond, subsequent SGFET fabrication results in a device exhibiting the desirable always-off enhancement mode of operation (V_T -0.6 V_{GS}) with pinch-off and current saturation being achieved within the electrochemical window of diamond. The SGFET shows good maximum gain and transconductance of 3 and 200 μS/mm respectively, with a moderate pH sensitivity of 36 mV/pH and fast temporal response to pH change. The immunity of the oxidised boron-doped diamond surface to anodic oxidation, its respectable I-V characteristics, pH sensitivity and high biocompatibility make oxidised boron δ-doped SGFETs promising devices for the chronic recording of action potentials from electrogenic cells and stable pH sensors.

Chapter 9 Conclusions

In this thesis, the application of various forms of diamond at the Brain-Machine Interface have been investigated. Overall, diamond has been found to be a very suitable material for interfacing with neurons *in vitro*, which shows great promise for *in vivo* application. Whilst other materials such as titanium nitride or iridium oxide have been shown to be proficient at stimulating or recording neurons [242], ultimately it will be the most biocompatible and durable material that will perform best in chronic neural electrode applications. In this context, diamond, combined with its low signal-to-noise ratio, low signal loss recordings and its ability to be stably functionalised with biomolecules for 3rd generation biomaterial modifications [9,113], is set to be the material of choice for the BMI.

In Chapter 5 the use of nanodiamond monolayers to promote the formation of functional neuronal networks has been presented. Surfaces of four different materials (glass, PCD, NCD and Si) coated with monolayers of monodispersed detonation nanodiamonds displayed promising similarity to the protein-coated materials regarding neuronal cell attachment, neurite outgrowth and functional network formation. Importantly, the neurons were able to grow in direct contact with the ND-coated material and could be easily maintained in culture for an extended period, equal to those on protein-coated substrates. Given the biocompatibility of NDs and their potential for surface functionalisation, ND layering might prove a valuable material technique for coating implants on a wide range of substrates. Materials can be coated in 3D by a simple ultrasonic coating process in 10 minutes using bench top lab equipment and inexpensive ND hydrocolloids, which makes the ND coating process extremely integrable into production processes and scientific work flows. Whilst it could be said that the 1st generation nature of ND monolayers as a neuronal biomaterial is out-dated with respect to the tailored, biomolecular functionality

of modern biomaterials [113], Place et al. [308] suggest that the most successful biomaterials will not aim to mimic the extremely complex biomolecular functionality of biology but the field will be better served by trying to generate less complex materials that can stimulate the body to heal and improve itself using biology as a tool.

Looking forwards, initial experiments have shown patterned ND monolayer coatings to direct the patterned growth of neurons on substrates, and that cell cultures are not adversely affected by the use of different ND types or by a prior short MWPECVD fixing process to enhance ND adhesion onto substrates. Furthermore, other initial experiments [174] have shown that (due to the porosity of ND monolayers) ND monolayers do not discernably alter the bandwidth of gold electrodes MEAs, which makes patterned ND electrodes an interesting prospect for future research. Additionally, the question of why neurons attach onto NDs is to be addressed. Protein adsorption assays on NDs are to be performed in order to investigate the nature of protein adsorption from serum on ND monolayers. Knock-out mice with mutated integrins are to be used to investigate protein/integrin mediated interactions with ND monolayers substrates. *In vivo* testing of ND-coated materials is to be performed.

In Chapter 6 an optimised RIE recipe has been developed for the smooth, high-aspect ratio etching of diamond. 64 electrode MEAs have been fabricated using highly doped BNCD with SU8, ONO and NCD passivation. SNR has been improved for SU8-passivated and ONO-passivated BNCD MEAs; however, they are not statistically different from standard gold MEAs. NCD passivated chips show larger SNR ratios than standard gold and platinum MEAs, and since the variability in the NCD-MEA measurements can be attributed to the production process, the high average SNR suggests that if production can be made more consistent, the good interaction between cells and an all diamond surface can lead to a superior recording MEA. For future work, as part of the new EU Neurocare consortium, more BNCD/NCD MEAs are to be fabricated using a revised production process in order to demonstrate a statistically significant improvement in diamond-based MEA performance. Additional to repeat

experiments, MEAs with an increased number of electrodes are to be fabricated, and the possibility of improving working electrode yield by using patterned ND coatings to direct neurons onto electrode sites will be investigated.

In Chapter 7 uncapped δ-doped layers have been deposited on (111) diamond substrates for the first time, wherein a revised PECVD protocol has been employed to aid the abrupt δ-doped boron concentration profiles. AC Hall Effect and Dielectric Impedance Spectroscopy measurements have been used to determine the electrical characteristics of δ-layers, and enhanced room temperature mobilities (13 $cm^2/V.s$) are reported in comparison to equivalently grown, thicker, heavily boron-doped (111) diamond. Impedance spectroscopy measurements show the deposited layers to have metallic-like properties with low activation energies corresponding to estimated boron concentrations of approximately 10^{20} cm^{-3}, as confirmed by SIMS measurements. The resulting boron δ-doped diamond channels are suitable for FET fabrication with desirable sheet carrier densities. Whilst mobility enhancements have been achieved on δ-doped diamond channels, improvements in the MWPECVD δ-deposition recipe could further improve the sharpness of the boron and intrinsic diamond interface, thereby improving carrier mobility. However, charge screening effects may not allow much further improvements in carrier mobility enhancement. Employing a capping intrinsic layer could also improve carrier delocalisation, and a fluorine terminated surface could also lead to similar enhancements [309]. Although higher mobilities are desirable for high power and high frequency applications, which are the usual intended application for δ-doped diamond channels, the modest mobility of the channel in combination with the ideal sheet carrier density and high biocompatibility of the channel make it well suited for biosensing applications.

Finally, in Chapter 8, SGFETs that have been fabricated from oxidised boron δ-doped (111) diamond channels show improved I-V characteristics in comparison to equivalent devices built on (100) diamond, and are comparable to H-SCC SGFETs. Following a PECVD recipe optimisation for δ-layer deposition on (111) diamond, subsequent SGFET fabrication results in a device exhibiting the

desirable always-off enhancement mode of operation (V_T -0.6 V_{GS}) with pinch-off and current saturation being achieved within the electrochemical window of diamond. The SGFET shows good maximum gain and transconductance of 3 and 200 μS/mm respectively, with a moderate pH sensitivity of 36 mV/pH and fast temporal response to pH change. The immunity of the oxidised boron-doped diamond surface to anodic oxidation, its respectable I-V characteristics, pH sensitivity and high biocompatibility make oxidised boron δ-doped SGFETs promising devices for the chronic recording of action potentials from electrogenic cells and stable pH sensors. Looking forwards, in order to investigate the less than expected pH sensitivity of the device, the oxygenation of the surface will be performed using different oxidative methods. This is the first time that an enhancement mode SGFET has been fabricated using a boron-doped diamond surface channel, and opens up many research opportunities into fabricating neural recording devices. Therefore, the ability of boron δ-doped (111) diamond SGFETs to record cell signals is to be investigated, followed by the fabrication of SGFET arrays.

In lieu of the results obtained and the new neuronal devices presented in this thesis, diamond has been demonstrated as an indispensable material for interfacing with neurons.

Chapter 10 Appendices

10.1 Appendix A: Primary Murine Hippocampal Neuronal Cultures

Substrate preparation

All samples (prior to ND coating) are cleaned using a piranha etch (see section 4.1) in a clean room environment under a laminar flow hood. ND-coated substrates are used as-is, which are given as clean due to ND hydrocolloids only being opened in ultra-clean environments, and any colloid contamination is visible by ND precipitation. Protein coated substrates are treated as follows:

1. Cover substrates with 100 µL of a 3 µg/mL Poly-ornithine (p-ORN) plus 2 µg/mL Laminin (LN) solution in PBS (20 mM sodium phosphate, 150 mM NaCl, pH 7.5. Laminin from Sigma, #L2020, aliquots of a 1 mg/mL stock stored at –80°C)
2. Leave overnight (minimum 1 hr) in CO_2 incubator, 36°C
3. Take off p-ORN/LN/PBS solution
4. Float petridish with sterile water or PBS
5. Transfer substrates into culture dishes
6. Remove remaining water or PBS
7. Add attachment medium (see Table 10.1) to the culture dish
8. Keep in CO_2 incubator, 36°C, 5 % CO_2 until plating of the neurons (at least 1 hr)

Dissection

The whole preparation is done at room temperature under a laminar flow hood observing aseptic practise.

9. Obtain mouse embryos (bred at UCL) at day 18 of gestation (E18) through caesarean section
10. Decapitate embryos
11. Transfer each head into a separate well of a sterile 24 well dish containing dissection medium (see Table 10.1) (12-14 embryos can be handled in parallel)
12. Remove brains and transfer into dissection medium
13. Dissociate cortices from rest of the brain
14. Remove meninges
15. Cut out hippocampi
16. Transfer hippocampi of each animal into an Eppendorf tube containing 500 µL of dissection medium
17. Let hippocampi rest at least 10 min before continuing with trypsination (improves survival rate)

Dissociation of neurons

18. Remove excess medium and add 500 µL of trypsination solution (trypsin is a proteolytic enzyme which breaks down proteins that hold cells together) (see Table 10.1)
19. Flick tube carefully and incubate it for 9 mins in a CO_2 incubator, 36°C, 5 % CO_2 (tubes can be handled pairwise with 5 mins time difference from one pair to the next)
20. Take off solution and wash 3x for 5 mins with 500 µL of attachment medium
21. Take off wash solution and add 500 µL of attachment medium

22. Triturate with a 1 mL pipette until there are no more major lumps (approx. 20 times to cleave off neurites from the cell body, leaving just the soma)
23. Plate cells on substrate (ca. 100,000/cm^{-2})
24. Exchange medium to maintenance medium (see Table 10.1) after 3-4 hrs (take care to completely remove all serum containing medium)

Cells are then cultured up to 12 days *in vitro* (DIV), without maintenance medium replacement.

Media	Source	Volume & Conc.
Dissection medium:		
1x Hank's Buffered Salt Solution (HBBS) w/ Mg^{2+}, Ca^{2+}, glucose	(Invitrogen, #24020)	100 mL
1 M 4-(2-hydroxyethyl)-1-piperazineethanesulfonic (HEPES) acid, pH 7.2-7.5	(Invitrogen, #15630)	1 mL; 10 mM
Trypsination solution:		
1x Trypsin/ Ethylenediaminetetraacetic acid (EDTA) in HBSS	(Invitrogen, #25300)	10 mL; 1x
1 M HEPES, pH 7.2-7.5	(Invitrogen, #15630)	0.1 mM; 10 mM
Attachment medium:		
1x Minimal Essential Medium (MEM) w/ Earl's salts and Glutamine	(Invitrogen, #31095-029)	80 mL
Pyruvic acid, 100 mM	(Invitrogen , #11360-039)	0.8 mL; 1 mM
Glucose (45 %)	(Sigma G-8769)	1.06 mL; 33 mM
Fetal Bovie Serum (FBS)	(Invitrogen , #10106)	8 mL; 10%
Maintenance medium:		
Neurobasal™ w/o glutamine	(Invitrogen, #21103)	100 mL
50x B27	(Invitrogen, #17504)	2 mL; 2%
100x GlutaMAX™-I Supplement	(Invitrogen, #35050)	1 mL; 2 mM
100x Penicillin/Streptomycin	(Invitrogen, #15140)	1 mL
45 % D-(+)-Glucose solution	(Sigma, #G8769)	1.32 mL; 33 mM

Table 10.1: List of solution media used in primary hippocampal cell cultures.

10.2 Appendix B: Photolithography processing parameters

Resist	SPR 220-7	S1805	LOR 3A	SU-8 2002	AZ 5214 E
Tone	Positive	Positive	N/A	Negative	±
Purpose	RIE mask	Lift-off	Lift-off resist	Epoxy passivation	Lift-off photoresist
Dehydration Bake (Oven)	200˚C / 30mins	200˚C / 30mins	200˚C / 30mins	200˚C / 30mins	200˚C / 30mins
Spread cycle (Ramp(s), RPM, Hold(s)	Ramp 2s, 500rpm, Hold 2s	Ramp 2s, 500rpm, Hold 2s	Ramp 2s, 500rpm, Hold 2s	Ramp 2s, 500rpm, Hold 2s	1500 rpm, Hold 10s
Spin Cycle (Ramp(s), RPM, Hold(s))	Ramp 1s, 4000rpm, Hold 30s	Ramp 1s, 4000rpm, Hold 30s	Ramp 1s, 3000rpm, Hold 45s	Ramp 1s, 3000rpm, Hold 45s	Ramp 1s, 5000rpm, Hold 50s
Softbake (Hotplate)	80˚C / 30s > 115˚C / 90s	115˚C / 90s	180˚C / 90s	65˚C / 60s > 95˚C / 120s	100˚C / 60s
Final thickness (µm)	7 µm	400 nm	350 nm	2 µm	1 µm
Expose Energy mJ/cm^2	300 mJ/cm^2	20	N/A	80 mJ/cm^2	120 mJ/cm^2
Expose Time MJB3 (20mW)	16.7s	1.2s	N/A	4s	0.5s
Expose Time Quintel (10mW)	34s	1.3s	N/A	8s	1s
Acclimatise (min)	45 mins after Exposure	5 mins	N/A	N/A	20 mins after PEB
PEB (Hotplate)	80˚C / 30s > 115˚C / 90s	N/A	N/A	65˚C / 60s > 95˚C / 60s	115˚C / 180s
Flood exposure	N/A	N/A	N/A	N/A	60s
Developer	MF-26A	MF319	N/A	SU-8 Developer	AZ400K:H20 1:4
Develop time/s	80s	40s	N/A	60s	50s
Postbake (Hotplate)	130˚C / 300s	115˚C / 90s	N/A	N/A	N/A
Resist Strip	Acetone	Acetone	Acetone	Acetone	AZ100 (overnight)

Table 10.2: Photolithography parameters used for photolithography.

References

[1] J.P. Rauschecker, Science 295 (2002) 1025–1029.

[2] D. Zhou, E. Greenbaum, Springer (2009) 383.

[3] J.D. Weiland, W. Liu, M.S. Humayun, Annu. Rev. Biomed. Eng. 7 (2005) 361–401.

[4] M. Javaheri, D.S. Hahn, R.R. Lakhanpal, J.D. Weiland, M.S. Humayun, Ann. Acad. Med. Singap. 35 (2006) 137–144.

[5] I. Wickelgren, Science 312 (2006) 1124–1126.

[6] E.D. Cohen, J. Neural Eng. 4 (2007) R14–R31.

[7] V. Polikov, P. Tresco, W. Reichert, Journal of Neuroscience Methods 148 (2005) 1–18.

[8] C. Specht, O. Williams, R.B. Jackman, R. Schoepfer, Biomaterials 25 (2004) 4073–4078.

[9] A. Härtl, E. Schmich, J.A. Garrido, J. Hernando, S.C.R. Catharino, S. Walter, P. Feulner, A. Kromka, D. Steinmueller-Nethl, M. Stutzmann, Nat Mater 3 (2004) 736–742.

[10] P. Ariano, O. Budnyk, S. Dalmazzo, D. Lovisolo, C. Manfredotti, P. Rivolo, E. Vittone, European Physical Journal E (2009) 1–8.

[11] Y. Pleskov, Russ J Electrochem+ 38 (2002) 1275–1291.

[12] T. Teraji, Phys. Stat. Sol. (a) 203 (2006) 3324–3357.

[13] L. Pauling, J Am Chem Soc 53 (1931) 1367–1400.

[14] S. Thompson, J. Staley, eds. Orbitals and Molecular Representation, 2011.

[15] H.O. Pierson, Handbook of Carbon, Graphite, Diamond, and Fullerenes: Properties, Processing, and Applications, Noyes Publications, 1993.

[16] R.S. Sussmann, CVD Diamond for Electronic Devices and Sensors, John Wiley & Sons, 2009.

[17] R.F. Davis, Diamond Films and Coatings: Development, Properties, and Applications, Noyes Pub., 1993.

[18] A. Krueger, Journal of Materials Chemistry 18 (2008) 1485–1492.

[19] J.M. Zazula, Http://Lbruno.Web.Cern.Ch/Lbruno/Documents/Bibliography/LHC_Note_78.Pdf (1997).

[20] A.L. Lavoisier, Memoire Academie Des Sciences (1772) 564–591.

[21] S. Tennant, Philosophical Transactions of the Royal Society of London 87 (1797) 123–127.

[22] F. Bundy, H. Hall, H. Strong, R. Wentorf, Nature 176 (1955) 51–55.

[23] R.M. Hazen, The Diamond Makers, Cambridge University Press, 1999.

[24] D.K. Davies, Diamond, Hutchinson, 1953.

[25] I. Herbert, The Diamond Diggers: South Africa 1866 to the 1970'S, Tom Stacey Ltd., 1972.

[26] J.C. Angus, A. Argoitia, R. Gat, Z. Li, M. Sunkara, L. Wang, Y. Wang, Philosophical Transactions: Physical Sciences and Engineering 342 (1993) 195–208.

[27] J. Angus, Y. Wang, M. Sunkara, Annual Review of Materials Science 21 (1991) 221–248.

[28] W. Eversole, Synthesis of Diamond, U.S. Patent 3030187, 1962.

[29] J.C. Angus, J. Appl. Phys. 39 (1968) 2915.

[30] S. Matsumoto, Y. Sato, M. Tsutsumi, N. Setaka, J Mater Sci 17 (1982) 3106–3112.

[31] M. Kamo, Y. Sato, S. Matsumoto, N. SETAKA, J Cryst Growth 62 (1983) 642–644.

[32] P. May, Phil. Trans. R. Soc. Lond. A 358 (2000) 473–495.

[33] H. Liu, D.S. Dandy, Diamond Chemical Vapor Deposition: Nucleation and Early Growth Stages, Noyes Publications, 1995.

[34] J. Pernot, P.N. Volpe, F. Omnès, P. Muret, V. Mortet, K. Haenen, T. Teraji, Physical Review B 81 (2010) 205203–1–7.

[35] J. Isberg, J. Hammersberg, E. Johansson, T. Wikström, D.J. Twitchen, A.J. Whitehead, S.E. Coe, G.A. Scarsbrook, Science 297 (2002) 1670–1672.

[36] S. Szunerits, R. Boukherroub, J Solid State Electrochem 12 (2008) 1205–1218.

[37] J. Robertson, Mat Sci Eng R 37 (2002) 129–281.

[38] J. Luong, K. Male, J. Glennon, Analyst 134 (2009) 1965–1979.

[39] B. Rezek, E. Ukraintsev, L. Michalíková, A. Kromka, J. Zemek, M. Kalbacova, in:, Diam Relat Mater, 2009, pp. 918–922.

[40] L. Grieten, S.D. Janssens, A. Ethirajan, N. Vanden Bon, M. Ameloot, L. Michiels, K. Haenen, P. Wagner, Phys Status Solidi A 208 (2011) 2093–2098.

[41] B. Rezek, L. Michalíková, E. Ukraintsev, A. Kromka, M. Kalbacova, Sensors 9 (2009) 3549–3562.

[42] T. Borst, O. Weis, Physica Status Solidi (C) 154 (1996) 423–444.

[43] R.H. Wentorf, H.P. Bovenkerk, J Chem Phys 36 (1962) 1987.

[44] P.-N. Volpe, J. Pernot, P. Muret, F. Omnes, Applied Physics Letters 94 (2009) 092102–092102.

[45] T. Teraji, H. Wada, M. Yamamoto, K. Arima, T. Ito, in:, Diam Relat Mater, 2006, pp. 602–606.

[46] V. Mortet, M. Daenen, T. Teraji, A. Lazea, V. Vorlicek, J. D'Haen, K. Haenen, M. D'Olieslaeger, Diamond and Related Materials 17 (2008) 1330–1334.

[47] S. Yamanaka, H. Watanabe, S. Masai, D. Takeuchi, H. Okushi, K. Kajimura, Jpn. J. Appl. Phys 37 (1998) L1129–L1131.

[48] E. Bustarret, P. Achatz, B. Sacépé, C. Chapelier, C. Marcenat, L. Ortéga, T. Klein, Philos T R Soc A 366 (2008) 267–279.

[49] K. Nishimura, K. Das, J.T. Glass, J. Appl. Phys. 69 (1991) 3142–3148.

[50] K. Ushizawa, K. Watanabe, T. Ando, I. Sakaguchi, M. Nishitani-Gamo, Y. Sato, H. Kanda, Diamond and Related Materials 7 (1998) 1719–1722.

[51] F. Jia, Y. Bai, F. Qu, J. Zhao, C. Zhuang, X. Jiang, Vaccum 84 (2010) 930–934.

[52] X. Zhang, J. Guo, Y. Yao, R. Wang, G. Chen, W. Zhou, S. Yu, Applied Physics a: Materials Science & Processing 56 (1993) 425–428.

[53] R. Kalish, in:, Appl Surf Sci, 1997, pp. 558–569.

[54] M.I. Landstrass, K.V. Ravi, Applied Physics Letters 55 (1989) 1391.

[55] F. Maier, M. Riedel, B. Mantel, J. Ristein, L. Ley, Phys. Rev. Lett. 85 (2000) 3472–3475.

[56] J. Foord, C. Lau, M. Hiramatsu, R. Jackman, C. Nebel, P. Bergonzo,

Diamond and Related Materials 11 (2002) 856–860.

[57] C.E. Nebel, B. Rezek, D. Shin, H. Watanabe, Phys Status Solidi A 203 (2006) 3273–3298.

[58] R. Kalish, Diamond and Related Materials 10 (2001) 1749–1755.

[59] R. Farrer, Solid State Communications 7 (1969) 685–688.

[60] L. Wang, A. Zunger, Physical Review B 66 (2002) 161202–1–4.

[61] S. Koizumi, M. Kamo, Y. Sato, S. Mita, A. Sawabe, A. Reznik, C. Uzan-Saguy, R. Kalish, in:, Diam Relat Mater, 1998, pp. 540–544.

[62] K. Haenen, K. Meykens, M. Nesladek, G. Knuyt, L. Stals, T. Teraji, S. Koizumi, in:, Phys Status Solidi A, 2000, pp. 11–16.

[63] S. Koizumi, T. Teraji, H. Kanda, in:, Diam Relat Mater, 2000, pp. 935–940.

[64] M. Nesladek, Semiconductor Science and Technology 20 (2005) R19–R27.

[65] S. Kajihara, A. Antonelli, J. Bernholc, R. Car, Phys. Rev. Lett. 66 (1991) 2010–2013.

[66] E. Gheeraert, Solid State Communications 113 (2000) 577–580.

[67] D. Saada, J. Adler, R. Kalish, Applied Physics Letters 77 (2000) 878.

[68] D.J. Kennett, J.P. Kennett, A. West, C. Mercer, S.S.Q. Hee, L. Bement, T.E. Bunch, M. Sellers, W.S. Wolbach, Science 323 (2009) 94–94.

[69] O. Shenderova, V. Zhirnov, D. Brenner, Critical Reviews in Solid State and Materials Sciences 27 (2002) 227–356.

[70] K.V. Volkov, V.V. Danilenko, V.I. Elin, Combust Explos Shock Waves 26 (1990) 366–368.

[71] N. Greiner, D. Phillips, J. Johnson, F. Volk, Nature 333 (1988) 440–442.

[72] A. Krüger, F. Kataoka, M. Ozawa, T, Fujino, Y. Suzuki, A. E. Aleksenskii, A. Y. Vul, E. Osawa, Carbon 43 (2005) 1722–1730.

[73] S. Prawer, K. Nugent, D. Jamieson, J. Orwa, L. Bursill, J. Peng, Chemical Physics Letters 332 (2000) 93–97.

[74] M. Baidakova, A. Vul, J Phys D Appl Phys 40 (2007) 6300–6311.

[75] M. Bevilacqua, S. Patel, A. Chaudhary, H. Ye, R.B. Jackman, Applied Physics Letters 93 (2008) 132115–1–3.

[76] A.M. Schrand, H. Huang, C. Carlson, J.J. Schlager, E. Osawa, S.M. Hussain,

L. Dai, J. Phys. Chem. B 111 (2007) 2–7.

[77] A.M. Schrand, L. Dai, J.J. Schlager, S.M. Hussain, E. Osawa, Diamond and Related Materials 16 (2007) 2118–2123.

[78] A.M. Schrand, S. Hens, O. Shenderova, Critical Reviews in Solid State and Materials Sciences 34 (2009) 18–74.

[79] A. Krueger, Journal of Materials Chemistry, 18 (2008) 1485–1492.

[80] P.N. Laboratorium, Philips Research Reports, Philips Research Laboratories., 1967.

[81] D. Das, R.N. Singh, Int Mater Rev 52 (2007) 29–64.

[82] A. Gicquel, K. Hassouni, F. Silva, J. Achard, Current Applied Physics 1 (2001) 479–496.

[83] O.A. Williams, Diamond and Related Materials 20 (2011) 621–640.

[84] J.E. Butler, A.V. Sumant, 14 (2008) 145–160.

[85] W. Gajewski, P. Achatz, O. Williams, K. Haenen, E. Bustarret, M. Stutzmann, J. Garrido, Physical Review B 79 (2009) 1–14.

[86] L.L. Hench, I. Thompson, Journal of the Royal Society Interface 7 (2010) S379–S391.

[87] L. Hench, J. Wilson, Science 226 (1984) 630–636.

[88] L.L. Hench, Science 295 (2002) 1014–1017.

[89] S.S. Rao, J.O. Winter, Frontiers in Neuroengineering 2 (2009) 1–14.

[90] K. Mark, J. Park, S. Bauer, P. Schmuki, Cell and Tissue Research 339 (2009) 131–153.

[91] T. Sedaghati, S.Y. Yang, A. Mosahebi, M.S. Alavijeh, A.M. Seifalian, Biotechnol. Appl. Biochem. 58 (2011) 288–300.

[92] E. Zrenner, Science 295 (2002) 1022–1025.

[93] H. Sorribas, D. Braun, L. Leder, P. Sonderegger, L. Tiefenauer, Journal of Neuroscience Methods 104 (2001) 133–141.

[94] A.E. Nel, L. Maedler, D. Velegol, T. Xia, E.M.V. Hoek, P. Somasundaran, F. Klaessig, V. Castranova, M. Thompson, Nature Publishing Group 8 (2009) 543–557.

[95] S. Mitragotri, J. Lahann, Nature Publishing Group 8 (2009) 15–23.

[96] W.J. Streit, Toxicologic Pathology 28 (2000) 28–30.

[97] W.J. Streit, C.A. Kincaid-Colton, Sci. Am. 273 (1995) 54–5, 58–61.

[98] M.P. Ward, P. Rajdev, C. Ellison, P.P. Irazoqui, Brain Research 1282 (2009) 183–200.

[99] K. Cheung, Biomedical Microdevices 9 (2007) 923–938.

[100] C. Hassler, T. Boretius, T. Stieglitz, J Polym Sci Pol Phys 49 (2011) 18–33.

[101] S. Khan, G. Newaz, Journal of Biomedical Materials Research Part A 93A (2010) 1209–1224.

[102] P. Roach, D. Eglin, K. Rohde, C.C. Perry, J Mater Sci: Mater Med 18 (2007) 1263–1277.

[103] K. Patel, H. Tang, W. Grever, K. Ng, J. Xiang, R. Keep, T. Cao, J. McAllister, Biomaterials 27 (2006) 1519–1526.

[104] P. Ariano,P. Baldelli, E. Carbone, A. Gilardino, A. Lo Giudice, D. Lovisolo, C. Manfredotti, M. Norara,H. Shernshulte, E. Vittone, Diamond and Related Materials 14 (2005) 669–674.

[105] Y.-C. Chen, D.-C. Lee, C.-Y. Hsiao, Y.-F. Chung, H.-C. Chen, J.P. Thomas, W.-F. Pong, N.-H. Tai, I.-N. Lin, I.-M. Chiu, Biomaterials 30 (2009) 3428–3435.

[106] L. Bacakova, E. Filova, F. Rypacek, V. Svorcik, V. Stary, Physiol Res 53 (2004) S35–S45.

[107] E. Yavin, Z. Yavin, J Cell Biol 62 (1974) 540–546.

[108] R.O. Hynes, Science 326 (2009) 1216–1219.

[109] A.J. Garcia, Adv Polym Sci (2006) 171–190.

[110] A. García, Biomaterials 26 (2005) 7525–7529.

[111] C. Bokel, N. Brown, Dev Cell 3 (2002) 311–321.

[112] N.H. Romano, D. Sengupta, C. Chung, S.C. Heilshorn, Bba-Gen Subjects 1810 (2011) 339–349.

[113] K.S. Straley, S.C. Heilshorn, Frontiers in Neuroengineering 2 (2009) 9.

[114] B. Rezek, E. Ukraintsev, A. Kromka, M. Ledinsky, A. Broz, L. Noskova, H. Hartmannova, M. Kalbacova, Diamond and Related Materials 19 (2010) 153–157.

[115] R. Wenzel, J Phys Colloid Chem 53 (1949) 1466–1467.

[116] R.N. Wenzel, Ind. Eng. Chem. 28 (1936) 988–994.

[117] A.B.D. Cassie, S. Baxter, Trans. Faraday Soc. 40 (1944) 546–551.

[118] A. Curtis, C. Wilkinson, Biochem Soc Symp 65 (1999) 15–26.

[119] Y. Fan, F. Cui, L. Chen, Y. Zhai, Q. Xu, I. Lee, Appl Surf Sci 187 (2002) 313–318.

[120] Y. Fan, F. Cui, S. Hou, Q. Xu, L. Chen, I. Lee, Journal of Neuroscience Methods 120 (2002) 17–23.

[121] S.P. Khan, G.G. Auner, G.M. Newaz, Nanomedicine-Uk 1 (2005) 125–129.

[122] P. Clark, P. Connolly, A. Curtis, J. DOW, C. Wilkinson, Development 108 (1990) 635–644.

[123] D.Y. Fozdar, J.Y. Lee, C.E. Schmidt, S. Chen, Biofabrication 2 (2010) 035005.

[124] N.M. Dowell-Mesfin, M.-A. Abdul-Karim, A.M.P. Turner, S. Schanz, H.G. Craighead, B. Roysam, J.N. Turner, W. Shain, J. Neural Eng. 1 (2004) 78–90.

[125] D. Hoffman-Kim, J.A. Mitchel, R.V. Bellamkonda, Annu. Rev. Biomed. Eng. 12 (2010) 203–231.

[126] P. Roach, D. Farrar, C.C. Perry, J Am Chem Soc 127 (2005) 8168–8173.

[127] P. Asuri, S.S. Bale, S.S. Karajanagi, R.S. Kane, Curr Opin Biotech 17 (2006) 562–568.

[128] P. Roach, D. Farrar, C.C. Perry, J Am Chem Soc 128 (2006) 3939–3945.

[129] K.A. Moxon, N.M. Kalkhoran, in:, Engineering in Medicine and Biology Society, 2003. Proceedings of the 25th Annual International Conference of the IEEE, 2003, pp. 3698–3699.

[130] P.C. Georges, Journal of Applied Physiology 98 (2005) 1547–1553.

[131] R.J. Hamers, J.E. Butler, T.L. Lasseter, B. Nichols, J.N. Russell Jr, K. Tse, W. Yang, Diamond and Related Materials 14 (2005) 661–668.

[132] W. Yang, O. Auciello, J. Butler, W. Cai, J. Carlisle, J. Gerbi, D. Gruen, T. Knickerbocker, T. Lasseter, J. Russell, L. Smith, R. Hamers, Nat Mater 1 (2002) 253–257.

[133] C. Stavis, T.L. Clare, J.E. Butler, A.D. Radadia, R. Carr, H. Zeng, W.P. King, J.A. Carlisle, A. Aksimentiev, R. Bashir, R.J. Hamers, Proceedings of the National Academy of Sciences 108 (2011) 983–988.

[134] X. Kong, L. Huang, C. Hsu, W. Chen, C. Han, H.-C. Chang, Anal Chem 77 (2005) 259–265.

[135] S.C. Wasdo, D.S. Barber, N.D. Denslow, K.W. Powers, M. Palazuelos, S.M.J. Stevens, B.M. Moudgil, S.M. Roberts, Int J Nanotechnol 5 (2008) 92–115.

[136] T. Nguyen, H.-C. Chang, V. Wu, Diamond and Related Materials 16 (2007) 872–876.

[137] H.-D. Wang, C.H. Niu, Q. Yang, I. Badea, Nanotechnology 22 (2011) 145703.

[138] F. Strumwasser, Science 127 (1958) 469–470.

[139] E.M. Schmidt, Methods For Neural Ensemble Recordings (1999) 1–23.

[140] G. Kovacs, C. Storment, J. Rosen, Ieee Transactions On Biomedical Engineering 39 (1992) 893–902.

[141] K.D. Wise, J.B. Angell, A. Starr, Ieee Trans Biomed Eng Bme-17 (1970) 238–247.

[142] K. Wise, J. Angell, Ieee Transactions On Biomedical Engineering Bm22 (1975) 212–219.

[143] K.D. Wise, Ieee Eng. Med. Biol. Mag. 24 (2005) 22–29.

[144] J.J. Burmeister, K. Moxon, G.A. Gerhardt, Anal Chem 72 (2000) 187–192.

[145] A. Badi, T. Kertesz, R. Gurgel, C. Shelton, R. Normann, Laryngoscope 113 (2003) 833–842.

[146] T. Stieglitz, H.R. Beutel, M. Schuettler, J.U. Meyer, Biomedical Microdevices 2 (2000) 283–294.

[147] R.M. Rothschild, Frontiers in Neuroengineering 3 (2010) 112.

[148] Ho-Yin Chan, D.M. Aslam, J.A. Wiler, B. Casey, Journal of Microelectromechanical Systems 18 (2009) 511–521.

[149] M.W. Varney, Z. Cao, D.M. Aslam, in:, Nano/Micro Engineered and Molecular Systems (NEMS), 2010 5th IEEE International Conference on, 2010, pp. 1116–1119.

[150] M.W. Varney, D.M. Aslam, A. Janoudi, H.-Y. Chan, D.H. Wang, Biosensors 1 (2011) 118–133.

[151] P. Bergonzo, A. Bongrain, E. Scorsone, A. Bendali, L. Rousseau, G. Lissorgues, P. Mailley, Y. Li, T. Kauffmann, F. Goy, B. Yvert, J.A. Sahel, S. Picaud, Irbm 32 (2011) 91–94.

[152] A.E. Hess, D.M. Sabens, H.B. Martin, C.A. Zorman, Microelectromechanical Systems, Journal of 20 (2011) 867–875.

[153] M. Bonnauron, S. Saada, L. Rousseau, G. Lissorgues, C. Mer, P. Bergonzo, Diamond and Related Materials 17 (2008) 1399–1404.

[154] E. Colombo, Y. Men, J. Scharpf, C. Pietzka, M. Dipalo, P. Herfurth, Z. Gao, M. Schneider, V. Carabelli, E. Carbone, E. Kohn, A. Pasquarelli, Diamond and Related Materials 20 (2011) 793–797.

[155] Z. Gao, V. Carabelli, E. Carbone, E. Colombo, M. Dipalo, C. Manfredotti, A. Pasquarelli, M. Feneberg, K. Thonke, E. Vittone, E. Kohn, Journal of Micro-Nano Mechatronics 6 (2011) 33–37.

[156] J. Hees, R. Hoffmann, A. Kriele, W. Smirnov, H. Obloh, K. Glorer, B. Raynor, R. Driad, N. Yang, O.A. Williams, C.E. Nebel, ACS Nano 5 (2011) 3339–3346.

[157] P. Fromherz, A. Offenhausser, T. VETTER, J. WEIS, Science 252 (1991) 1290–1293.

[158] S. Meyburg, M. Goryll, J. Moers, S. Ingebrandt, S. Böcker-Meffert, H. Lüth, A. Offenhäusser, Biosens Bioelectron 21 (2006) 1037–1044.

[159] G. Steinhoff, B. Baur, G. Wrobel, S. Ingebrandt, A. Offenhäusser, A. Dadgar, A. Krost, M. Stutzmann, M. Eickhoff, Applied Physics Letters 86 (2005) 033901.

[160] A. Poghossian, S. Ingebrandt, A. Offenhaeusser, M.J. Schoening, Semin Cell Dev Biol 20 (2009) 41–48.

[161] L.H. Hess, M. Jansen, V. Maybeck, M.V. Hauf, M. Seifert, M. Stutzmann, I.D. Sharp, A. Offenhäusser, J.A. Garrido, Adv. Mater. Weinheim 23 (2011) 5045–5049.

[162] J.A. Garrido, A. Härtl, S. Kuch, M. Stutzmann, O.A. Williams, R.B. Jackmann, Applied Physics Letters 86 (2005) 073504.

[163] A. Denisenko, G. Jamornmarn, H. El-Hajj, E. Kohn, Diamond and Related Materials 16 (2007) 905–910.

[164] H. Kawarada, Y. Araki, T. Sakai, T. Ogawa, H. Umezawa, Phys Status Solidi A 185 (2001) 79–83.

[165] P. Ariano, A. Lo Giudice, A. Marcantoni, E. Vittone, E. Carbone, D. Lovisolo, Biosens Bioelectron 24 (2009) 2046–2050.

[166] M. Dankerl, S. Eick, B. Hofmann, M. Hauf, S. Ingebrandt, A. Offenhaeusser, M. Stutzmann, J.A. Garrido, Adv. Funct. Mater. 19 (2009)

2915–2923.

[167] B. Rezek, H. Watanabe, D. Shin, T. Yamamoto, C. Nebel, Diamond and Related Materials 15 (2006) 673–677.

[168] O. Fox, J. Holloway, G. Fuge, P. May, Mater Res Soc Symp Proc 1203 (2010) J17–27.

[169] J. Hees, A. Kriele, O.A. Williams, Chemical Physics Letters 509 (2011) 12–15.

[170] G. Cicala, P. Bruno, F. Bénédic, F. Silva, K. Hassouni, G. Senesi, Diamond and Related Materials 14 (2005) 421–425.

[171] J. Cryan, A. Holmes, Nat Rev Drug Discov 4 (2005) 775–790.

[172] P. Andersen, The Hippocampus Book, Oxford University Press, USA, 2007.

[173] G. Banker, K. Goslin, Culturing Nerve Cells, The MIT Press, 1998.

[174] V. Maybeck, Tools for Non-Invasive Communication with Electrogenic Cells: Optogenetic Stimulation and Diamond Recording Devices, 2011.

[175] W.C. Claycomb, N.A. Lanson, B.S. Stallworth, D.B. Egeland, J.B. Delcarpio, A. Bahinski, N.J. Izzo, P Natl Acad Sci Usa 95 (1998) 2979–2984.

[176] C. Sánchez, Progress in Neurobiology 61 (2000) 133–168.

[177] A. Caceres, G.A. Banker, L. BINDER, J. Neurosci. 6 (1986) 714–722.

[178] B. Geiger, J.P. Spatz, A.D. Bershadsky, Nat. Rev. Mol. Cell Biol. 10 (2009) 21–33.

[179] A. Boyde, R. Weiss, Experimental Cell Research (1972) 313–324.

[180] H. Burstyn, A. BARTLETT, Am J Phys 43 (1975) 414–419.

[181] L. Reimer, Measurement Science and Technology 11 (2000) 1826.

[182] SEM Diagram, 2011.

[183] P. Zalm, Reports on Progress in Physics 58 (1995) 1321–1374.

[184] R. Gibbons, Appl Surf Sci 203-204 (2003) 343–347.

[185] A.R. Bin CHANBASHA, A Study of the Effects of Ultralow Energy Secondary Ion Mass Spectrometry (SIMS) on Surface Transient and Depth Resolution, 2007.

[186] E. Evans Analytical Group, Http://Www.Eaglabs.com/Files/Appnotes/AN339.Pdf (2007).

[187] M. Yang, Y. Li, C. Hitzman,

Http://Eaglabs.Co.Uk/Files/Papers/PA040.Pdf (n.d.).

[188] D.H. Williams, I. Fleming, Spectroscopic Methods in Organic Chemistry, McGraw-Hill, 1973.

[189] JASCO, (2011).

[190] I.B. Levitan, L.K. Kaczmarek, The Neuron: Cell and Molecular Biology, Oxford University Press, 2002.

[191] C. Hammond, Cellular and Molecular Neurophysiology, Academic Press, 2008.

[192] A.L. Hodgkin, A.F. Huxley, Nature 144 (1939) 710–711.

[193] B. Sakmann, E. Neher, Single-Channel Recording, Springer, 2009.

[194] G. Grynkiewicz, M. Poenie, R. Tsien, Journal of Biological Chemistry 260 (1985) 3440–4350.

[195] http://www.invitrogen.com/, Fura2 (2011).

[196] S. Koizumi, C.E. Nebel, M. Nesládek, Physics and Applications of CVD Diamond, Vch Verlagsgesellschaft Mbh, 2008.

[197] P. May, M. Ashfold, K. Rosser, Chemistry.Bristol.Ac.Uk (1993) 448–454.

[198] J.E. Butler, Y.A. Mankelevich, A. Cheesman, J. Ma, M.N.R. Ashfold, Journal of Physics: Condensed Matter 21 (2009) 364201.

[199] M. Hasegawa, M. Ogura, D. Takeuchi, H. Okushi, N. Kobayashi, S. Yamanaka, Method for the Fabrication of a Diamond Semiconductor, 2002.

[200] M. Hiramatsu, M. Hori, Carbon Nanowalls: Synthesis and Emerging Applications, Springer, 2010.

[201] R.E. Sah, Silicon Nitride, Silicon Dioxide Thin Insulating Films, and Other Emerging Dielectrics VIII, The Electrochemical Society, 2005.

[202] Http://Www.Cleanroom.Byu.Edu/Sts_Icp.Phtml (2011).

[203] M. Bauccio, ASM Metals Reference Book, American Society for Metals, 1993.

[204] R.C. Jaeger, Introduction to Microelectronic Fabrication, 2nd ed. 2002.

[205] S.A. Campbell, The Science and Engineering of Microelectronic Fabrication, Oxford University Press, USA, 2001.

[206] Y. Jingu, K. Hirama, H. Kawarada, IEEE T Electron Dev 57 (2010) 966–972.

[207] E.H. Hall, American Journal of Mathematics 2 (1879) 287–292.

[208] S.M. Sze, K.K. Ng, Physics of Semiconductor Devices, Wiley-Blackwell, 2007.

[209] Lakeshore, Http://Www.Lakeshore.com/Pdf_Files/Systems/Hall_Data_Sheets/a_Hall.Pdf (n.d.).

[210] L. Van der Pauw, Philips Technical Review 13 (1958) 1–9.

[211] R. Chwang, Solid-State Electronics 17 (1974) 1217–1227.

[212] E. Barsoukov, J. Macdonald, Impedance Spectroscopy: Theory, Experiment, and Applications, 2005.

[213] K.-K. Liu, C.-L. Cheng, C.-C. Chang, J.-I. Chao, Nanotechnology 18 (2007) 325102.

[214] S. Han, L. Pan, D.R. Kania, Diamond - Electronic Properties and Applications (1995) 241–284.

[215] O. Williams, O. Douhéret, M. Daenen, K. Haenen, E. Osawa, M. Takahashi, Chemical Physics Letters 445 (2007) 255–258.

[216] B. Baral, J. Vac. Sci. Technol. A 14 (1996) 2303.

[217] C.G. Specht, C.M. Tigaret, G.F. Rast, A. Thalhammer, Y. Rudhard, R. Schoepfer, Mol. Cell. Neurosci. 28 (2005) 326–334.

[218] L.A. Cingolani, Y. Goda, Neuron Glia Biol. 4 (2008) 179–187.

[219] A. Thalhammer, Y. Rudhard, C. Tigaret, The EMBO Journal 25 (2006) 5873–5883.

[220] G. Hardingham, F. Arnold, Nature Neuroscience 4 (2001) 565–566.

[221] T. Jiang, K. Xu, K. Xu, S. Ji, J Chem Soc Faraday T 92 (1996) 3401–3406.

[222] P. Chung, E. Perevedentseva, J. Tu, C. Chang, C. Cheng, Diamond and Related Materials 15 (2006) 622–625.

[223] T. Jiang, K. Xu, Carbon 33 (1995) 1663–1671.

[224] Y.V. Butenko, V.L. Kuznetsov, E.A. Paukshtis, A.I. Stadnichenko, I.N. Mazov, S.I. Moseenkov, A.I. Boronin, S.V. Kosheev, Fullerenes Nanotubes and Carbon Nanostructures 14 (2006) 557–564.

[225] R. Martin, P. Concepcion Heydorn, M. Alvaro, H. Garcia, Chemistry of Materials 21 (2009) 4505–4514.

[226] W.M. Cowan, T.C. Südhof, C.F. Stevens, Synapses, Johns Hopkins

University Press, 2003.

[227] J.E. Lisman, S. Raghavachari, R.W. Tsien, Nat Rev Neurosci 8 (2007) 597–609.

[228] Y. Xing, L. Dai, Nanomedicine-Uk 4 (2009) 207–218.

[229] O.A. Shenderova, D.W. Brenner, Solid State Phenomena 87 (2002) 205–214.

[230] C.A. Poland, R. Duffin, I. Kinloch, A. Maynard, W.A.H. Wallace, A. Seaton, V. Stone, S. Brown, W. Macnee, K. Donaldson, Nature Nanotech 3 (2008) 423–428.

[231] Y. Abdi, S. Mohajerzadeh, J. Koohshorkhi, M.D. Robertson, C.M. Andrei, Carbon 46 (2008) 1611–1614.

[232] T. Lechleitner, F. Klauser, T. Seppi, J. Lechner, P. Jennings, P. Perco, B. Mayer, D. Steinmueller-Nethl, J. Preiner, P. Hinterdorfer, M. Hermann, E. Bertel, K. Pfaller, W. Pfaller, Biomaterials 29 (2008) 4275–4284.

[233] M. Amaral, A.G. Dias, P.S. Gomes, M.A. Lopes, R.F. Silva, J.D. Santos, M.H. Fernandes, Journal of Biomedical Materials Research Part A 87A (2008) 91–99.

[234] W.C. Clem, S. Chowdhury, S.A. Catledge, J.J. Weimer, F.M. Shaikh, K.M. Hennessy, V.V. Konovalov, M.R. Hill, A. Waterfeld, S.L. Bellis, Y.K. Vohra, Biomaterials 29 (2008) 3461–3468.

[235] G. Cellot, E. Cilia, S. Cipollone, V. Rancic, A. Sucapane, S. Giordani, L. Gambazzi, H. Markram, M. Grandolfo, D. Scaini, Nature Nanotech 4 (2008) 126–133.

[236] N. Kotov, Science 330 (2010) 188–189.

[237] M. Shimaoka, T. Springer, Nat Rev Drug Discov 2 (2003) 703–716.

[238] R.O. Hynes, Cell 110 (2002) 673–687.

[239] M.D. Mager, V. LaPointe, M.M. Stevens, Nat Chem 3 (2011) 582–589.

[240] B. Ratner, Biomaterials Science: an Introduction to Materials in Medicine, 2004.

[241] A. Stett, U. Egert, E. Guenther, F. Hofmann, T. Meyer, W. Nisch, H. Haemmerle, Analytical and Bioanalytical Chemistry 377 (2003) 486–495.

[242] S.F. Cogan, Annu. Rev. Biomed. Eng. 10 (2008) 275–309.

[243] D.R. Merrill, M. Bikson, J.G.R. Jefferys, Journal of Neuroscience Methods 141 (2005) 171–198.

[244] A.Y. Chow, M.T. Pardue, V.Y. Chow, G.A. Peyman, Chanping Liang, J.I. Perlman, N.S. Peachey, IEEE Trans. Neural Syst. Rehabil. Eng. 9 (2001) 86–95.

[245] L.S. Robblee, J. McHardy, W.F. Agnew, L.A. Bullara, Journal of Neuroscience Methods 9 (1983) 301–308.

[246] S.F. Cogan, A.A. Guzelian, W.F. Agnew, T.G.H. Yuen, D.B. McCreery, Journal of Neuroscience Methods 137 (2004) 141–150.

[247] J.D. Weiland, D.J. Anderson, IEEE Trans Biomed Eng 47 (2000) 911–918.

[248] E. Guenther, B. Tröger, B. Schlosshauer, E. Zrenner, Vision Research 39 (1999) 3988–3994.

[249] A. Thalhammer, R.J. Edgington, L.A. Cingolani, R. Schoepfer, R.B. Jackman, Biomaterials 31 (2010) 2097–2104.

[250] E. Vanhove, J. de Sanoit, P. Mailley, M.A. Pinault, F. Jomard, P. Bergonzo, in:, Phys Status Solidi A, 2009, pp. 2063–2069.

[251] M. Karlsson, K. Hjort, F. Nikolajeff, Optics Letters 26 (2001) 1752–1754.

[252] Y. Ando, Y. Nishibayashi, K. Kobashi, T. Hirao, K. Oura, Diamond and Related Materials 11 (2002) 824–827.

[253] D. Hwang, T. Saito, N. Fujimori, Diamond and Related Materials 13 (2004) 2207–2210.

[254] H. Choi, E. Gu, C. Liu, C. Griffin, J. Girkin, I. Watson, M. Dawson, J Vac Sci Technol B 23 (2005) 130–132.

[255] J. Enlund, J. Isberg, M. Karlsson, F. Nikolajeff, J. Olsson, D. Twitchen, Carbon 43 (2005) 1839–1842.

[256] C. Lee, H. Choi, E. Gu, M.D. Dawson, H. Murphy, Diamond and Related Materials 15 (2006) 725–728.

[257] C. Lee, E. Gu, M.D. Dawson, Diamond and Related Materials 16 (2007) 944–948.

[258] C. Wang, E.L. Hu, J. Yang, J.E. Butler, 07342101 25 (2007) 730.

[259] T. Yamada, H. Yoshikawa, H. Uetsuka, S. Kumaragurubaran, N. Tokuda, S. Shikata, Diamond and Related Materials 16 (2007) 996–999.

[260] H. Uetsuka, T. Yamada, S. Shikata, Diamond and Related Materials 17 (2008) 728–731.

[261] C. Lee, E. Gu, M.D. Dawson, I. Friel, G. Scarsbrook, Diamond and Related Materials 17 (2008) 1292–1296.

[262] M. Hiscocks, C. Kaalund, F. Ladouceur, S. Huntington, B. Gibson, S. Trpkovski, D. Simpson, E. Ampem-Lassen, S. Prawer, J.E. Butler, Diamond and Related Materials 17 (2008) 1831–1834.

[263] C. Li, A. Hatta, Diamond and Related Materials 15 (2006) 1122–1125.

[264] C. Li, A. Hatta, Diamond and Related Materials 14 (2005) 1780–1783.

[265] M. Lehmann, W. Baumann, M. Brischwein, R. Ehret, M. Kraus, A. Schwinde, M. Bitzenhofer, I. Freund, B. Wolf, Biosens Bioelectron 15 (2000) 117–124.

[266] K. Williams, K. Gupta, M. Wasilik, Microelectromechanical Systems, Journal of 12 (2003) 761–778.

[267] C. Wort, R.S. Balmer, Materials Today 11 (2008) 22–28.

[268] A. Denisenko, E. Kohn, Diamond and Related Materials 14 (2005) 491–498.

[269] M. Mora-Ramos, Diamond and Related Materials 12 (2003) 33–36.

[270] H. Shiomi, Y. Nishibayashi, N. Toda, S. Shikata, IEEE Electron Device Letters 16 (1995) 36–38.

[271] E. Schubert, A. Fischer, K. Ploog, IEEE T Electron Dev 33 (1986) 625–623.

[272] A. Fiori, J. Pernot, E. Gheeraert, E. Bustarret, Phys Status Solidi A 207 (2010) 2084–2087.

[273] H. El-Hajj, A. Denisenko, A. Bergmaier, G. Dollinger, M. Kubovic, E. Kohn, Diamond and Related Materials 17 (2008) 409–414.

[274] A. Aleksov, A. Vescan, M. Kunze, P. Gluche, W. Ebert, E. Kohn, A. Bergmaier, G. Dollinger, Diamond and Related Materials 8 (1999) 941–945.

[275] E. Kohn, A. Denisenko, Thin Solid Films 515 (2007) 4333–4339.

[276] H. El-Haji, A. Denisenko, A. Kaiser, R.S. Balmer, E. Kohn, Diamond and Related Materials 17 (2008) 1259–1263.

[277] H. Ye, N. Tumilty, M. Bevilacqua, S. Curat, M. Nesládek, B. Bazin, P.

Bergonzo, R.B. Jackman, J. Appl. Phys. 103 (2008) 054503.

[278] H. Umezawa, T. Takenouchi, Y. Takano, K. Kobayashi, M. Nagao, I. Sakaguchi, M. Tachiki, T. Hatano, G.Z.M. Tachiki, H. Kawarada, Arxiv Preprint Cond-Mat (2005).

[279] S. Kitagoh, R. Okada, A. Kawano, M. Watanabe, Y. Takano, T. Yamaguchi, T. Chikyow, H. Kawarada, Physica C 470 (2010) S610–S612.

[280] A. Kawano, H. Ishiwata, S. Iriyama, R. Okada, T. Yamaguchi, Y. Takano, H. Kawarada, Physical Review B 82 (2010) 1–5.

[281] E. Bustarret, E. Gheeraert, K. Watanabe, Phys Status Solidi A 199 (2003) 9–18.

[282] T. Wojewoda, P. Achatz, L. Ortéga, F. Omnès, C. Marcenat, E. Bourgeois, X. Blase, F. Jomard, E. Bustarret, Diamond and Related Materials 17 (2008) 1302–1306.

[283] S. Ri, H. Kato, M. Ogura, H. Watanabe, T. Makino, S. Yamasaki, H. Okushi, Diamond and Related Materials 14 (2005) 1964–1968.

[284] F. Celii, J.E. Butler, Annual Review of Physical Chemistry 42 (1991) 643–684.

[285] T. Sakai, K. Song, H. Kanazawa, Y. Nakamura, H. Umezawa, M. Tachiki, H. Kawarada, Diamond and Related Materials 12 (2003) 1971–1975.

[286] C. Pietzka, A. Denisenko, A. Romanyuk, P.J. Schaefer, L.A. Kibler, J. Scharpf, E. Kohn, Diamond and Related Materials 19 (2010) 213–216.

[287] C. Tavares, F. Omnes, J. Pernot, E. Bustarret, Diamond and Related Materials 15 (2006) 582–585.

[288] E.F. Schubert, Delta-Doping of Semiconductors, Cambridge University Press, 1996.

[289] A. Denisenko, C. Pietzka, A. Romanyuk, H. El-Hajj, E. Kohn, J. Appl. Phys. 103 (2008) 1–8.

[290] S.-G. Ri, C.E. Nebel, D. Takeuchi, B. Rezek, N. Tokuda, S. Yamasaki, H. Okushi, Diamond and Related Materials 15 (2006) 692–697.

[291] B. Rezek, D. Shin, H. Watanabe, C.E. Nebel, Sensor Actuat B-Chem 122 (2007) 596–599.

[292] A.R. Ruslinda, S. Tajima, Y. Ishii, Y. Ishiyama, R. Edgington, H. Kawarada, Biosens Bioelectron 26 (2010) 1599–1604.

[293] J. Ristein, J Phys D Appl Phys 39 (2006) R71–R81.

[294] M. Dankerl, A. Reitinger, M. Stutzmann, J.A. Garrido, Phys. Stat. Sol. (RRL) 2 (2008) 31–33.

[295] Y. Sasaki, H. Kawarada, J Phys D Appl Phys 43 (2010) 1–8.

[296] K.S. Song, Y. Nakamura, Y. Sasaki, M. Degawa, J.-H. Yang, H. Kawarada, Analytica Chimica 573 (2006) 3–8.

[297] R. Kalish, Carbon (1999) 781–785.

[298] F. de Theije, M. Reedijk, J. Arsic, W. van Enckevort, E. Vlieg, Physical Review B 64 (2001) 1–7.

[299] D.E. Yates, S. Levine, T.W. Healy, J. Chem. Soc., Faraday Trans. 1: 70 (1974) 1807–1818.

[300] W.R. Carmody, Journal of Chemical Education 38 (1961) 559.

[301] K. Kwok, Complete Guide to Semiconductor Devices, 2nd ed. 1995.

[302] M.W. Shinwari, M.J. Deen, D. Landheer, Microelectron Reliab 47 (2007) 2025–2057.

[303] L. Bousse, N. de Rooij, P. Bergveld, IEEE T Electron Dev 30 (1983) 1263–1270.

[304] R.E.G. van Hal, J.C.T. Eijkel, P. Bergveld, Advances in Colloid and Interface Science 69 (1996) 31–62.

[305] M. Dipalo, C. Pietzka, A. Denisenko, H. El-Hajj, E. Kohn, Diamond and Related Materials 17 (2008) 1241–1247.

[306] L. Bousse, P. Bergveld, Sensor Actuator 6 (1984) 65–78.

[307] G. Wrobel, R. Seifert, S. Ingebrandt, J. Enderlein, H. Ecken, A. Baumann, U. Kaupp, A. Offenhausser, Biophysical Journal 89 (2005) 3628–3638.

[308] E.S. Place, N.D. Evans, M.M. Stevens, Nat Mater 8 (2009) 457–470.

[309] A. Denisenko, A. Romanyuk, C. Pietzka, J. Scharpf, E. Kohn, Surface Science 605 (2011) 632–637.